LOAN DOCUMENT

PHOTOGRAPH THIS SHEET

DTIC ACCESSION NUMBER

LEVEL

INVENTORY

DOCUMENT IDENTIFICATION

DISTRIBUTION STATEMENT

H
A
N
D
L
E

W
I
T
H

C
A
R
E

DATE ACCESSIONED

DATE RETURNED

19981223 025

DATE RECEIVED IN DTIC

REGISTERED OR CERTIFIED NUMBER

PHOTOGRAPH THIS SHEET AND RETURN TO DTIC-FDAC

DOCUMENT PROCESSING SHEET

LOAN DOCUMENT

Factors Influencing Fracture Toughness and Other Properties of Aluminum - Lithium Alloys

Final Report

T.H. Sanders
Alloy Technology Division
Alcoa Laboratories

ALCOA

Naval Air Development Center
Contract No. N62269-76-C-0271
For Naval Air Systems Command

1979 June 14

FACTORS INFLUENCING FRACTURE TOUGHNESS AND OTHER
PROPERTIES OF ALUMINUM-LITHIUM ALLOYS

FINAL REPORT

T. H. SANDERS
ALLOY TECHNOLOGY DIVISION
ALCOA LABORATORIES
ALCOA CENTER, PA   15069

1979 JUNE 14

SECURITY CLASSIFICATION OF THIS PAGE *(When Data Entered)*

REPORT DOCUMENTATION PAGE		READ INSTRUCTIONS BEFORE COMPLETING FORM
1. REPORT NUMBER	2. GOVT ACCESSION NO.	3. RECIPIENT'S CATALOG NUMBER
4. TITLE *(and Subtitle)* Factors Influencing Fracture Toughness and Other Properties of Aluminum-Lithium Alloys		5. TYPE OF REPORT & PERIOD COVERED FINAL
		6. PERFORMING ORG. REPORT NUMBER
7. AUTHOR(s) T. H. Sanders, Jr.		8. CONTRACT OR GRANT NUMBER(s) N62269-76-C-0271
9. PERFORMING ORGANIZATION NAME AND ADDRESS Aluminum Company of America Alcoa Laboratories Alcoa Center, PA 15069		10. PROGRAM ELEMENT, PROJECT, TASK AREA & WORK UNIT NUMBERS
11. CONTROLLING OFFICE NAME AND ADDRESS		12. REPORT DATE 1979 June 14
		13. NUMBER OF PAGES 281
14. MONITORING AGENCY NAME & ADDRESS(if different from Controlling Office)		15. SECURITY CLASS. (of this report) UNCLASSIFIED
		15a. DECLASSIFICATION/DOWNGRADING SCHEDULE

16. DISTRIBUTION STATEMENT *(of this Report)*

Approved for publick release; distribution unlimited

17. DISTRIBUTION STATEMENT *(of the abstract entered in Block 20, if different from Report)*

18. SUPPLEMENTARY NOTES

19. KEY WORDS *(Continue on reverse side if necessary and identify by block number)*

Al-Li	Alloys	Tensile properties
Al-Mg-Li	Fracture toughness	Auger analysis
Al-Cu-Li	Fatigue crack growth	
Al-Li-Mn	Microstructure	
Al-Li-Zr	Fractography	

20. ABSTRACT *(Continue on reverse side if necessary and identify by block number)*

An investigation was made to identify the microstructural features which control the fracture behavior of Al-Li alloys. Tensile, fracture toughness, and selected fatigue tests were conducted on candidate Al-Li alloys (Al-Mg-Li, Al-Cu-Li, and Al-Li). In all three alloy systems and most aging conditions investigated, the fracture mode was low energy, intergranular failure. Three microstructural features were considered to correlate with the intergranular failure--the shearable nature of the coherent Al_3Li (δ') precipitates which leads to dislocation pile-ups at the grain boundaries; the growth of a

DD $\begin{smallmatrix} \text{FORM} \\ \text{1 JAN 73} \end{smallmatrix}$ 1473   EDITION OF 1 NOV 65 IS OBSOLETE

UNCLASSIFIED

SECURITY CLASSIFICATION OF THIS PAGE *(When Data Entered)*

20. solute depleted, precipitate free zone during aging, and the occurrence of the tramp elements sodium, potassium and sulfur presumably segregated in the grain boundaries. Furthermore, the hydrogen content of the alloys was also shown to be significantly higher than other high strength commercial alloys. All these features would contribute to the low toughness and would tend to promote intergranular failure.

SUMMARY

Microstructure

Alloys containing sufficient lithium to precipitate from the supersaturated solid solution form coherent, spherical Al_3Li (δ') precipitates. The metastable δ' was observed in the Al-Li, Al-Mg-Li, and Al-Cu-Li alloys investigated. The precipitate growth was shown to obey a coarsening law having the form:

$$r = kt^{1/3}.$$

Immediately after quenching, uniformly distributed precipitates were observed up to the boundaries. Because of the higher diffusivities in a grain boundary compared to the interior of a grain, preferential coarsening of δ' in the boundaries occurred. Along with the coarsening reaction, a solute depleted, precipitate free zone (PFZ) developed, and its growth was correlated with time and temperature. PFZ growth was studied extensively in the Al-Li-Mn system, its presence was observed in the Al-Li-Zr and Al-Cu-Li systems, and documented in the Al-Mg-Li system.

A comparison between the Al-Li-Mn and Al-Li-Zr alloys processed identically demonstrated the effectiveness of zirconium in retarding the static recrystallization process during solution heat treatment.

Strength and Modulus

The strength of an Al-Li alloy containing only lithium as the principal solute element results from the interaction of dislocations with the ordered δ' precipitates. However, grain structure also has an effect. An unrecrystallized structure

has a higher strength than a fully recrystallized structure. A small component to strength due to grain size was also observed. High strengths can be achieved through co-precipitation. For example, in the Al-Cu-Li system, the sequences:

supersaturated solid solution (SSS)$\rightarrow$G.P.I.$\rightarrow\theta''\rightarrow\theta'\rightarrow\theta$

and

SSS$\rightarrow\delta'$

were observed. The high strength in this alloy was derived from the Al-Cu precipitates and much of the deformation behavior could be attributed to the presence of δ'.

The elastic modulus benefits appear to arise as a consequence of the modulus properties of the Al_3Li precipitates. Increasing the volume fraction of the δ' precipitates would increase the absolute modulus and significantly increase the specific modulus ($E \cdot M/\rho$, where ρ is the density) as a consequence of the simultaneous reduction in density with increasing lithium.

Deformation, Fracture, and Toughness

The deformation behavior is strongly affected by the presence of the ordered δ' precipitates. The shearable nature of these precipitates results in strain localization and dislocation pile-ups at grain boundaries. When a PFZ is present, strain then becomes localized in the PFZ's. These two strain localization phenomena appear to facilitate intergranular failure in the Al-Li alloys. The higher the volume fraction of δ' the more severe the localization would be predicted to be.

The low energy intergranular failure in the Al-Li and Al-Mg-Li alloys results in a material having unacceptable fracture toughness. In the Al-Cu-Li alloy investigated, underaging results in a transgranular failure and higher fracture toughness. The increase in toughness was at a small sacrifice in strength.

The presence of the tramp elements--sodium, potassium, and surfur--which were observed on the _in situ_ fractured surfaces in a scanning Auger microscope may also account for intergranular failure. Though the mere presence of these elements does not necessarily suggest a causal relationship, the segregation of these elements at grain boundaries is worth noting.

Furthermore, the hydrogen content of the Al-Li and Al-Mg-Li alloys is significantly higher than the hydrogen content of typical commerical high strength aluminum alloys.

Fatigue Crack Growth (FCG)

The FCG performance of the Al-Cu-Li alloy was studied and compared to 7075-T651. This comparison was made because of the similarity in strength to the peak aged Al-Cu-Li alloy. Under similar test conditions, at low and intermediate regions of ΔK, the Al-Cu-Li alloy in the two tempers investigated (underaged and peak strength) had lower crack growth rates than did 7075 at the same ΔK. However, in the peak strength temper, the crack growth rate of the Al-Cu-Li alloy was greater than the 7075-T651. This increased rate of crack growth at high ΔK's is presumably due to the low fracture toughness in the peak strength temper.

FOREWORD

This work was performed for the U.S. Naval Air Systems Command under Contract N62269-76-C-0271. The research was conducted at Alcoa Laboratories. Dr. T. H. Sanders, Jr., was the project scientist, Mr. J. T. Staley supervised the work. The contract monitor for the U.S. Naval Air Systems Command was Mr. E. S. Balmuth.

TABLE OF CONTENTS

TABLE OF CONTENTS (CONTINUED)

INTRODUCTION

Aluminum-lithium alloys have demonstrated unique combinations of high moduli of elasticity, low density, and high strength, but have also shown commercially unacceptable fracture toughness for many applications.[1] The primary emphasis of the program is to understand, and thereby control, those composition and microstructural features that affect deformation and fracture toughness of aluminum alloys containing sufficient lithium to precipitate.

Precipitation in Al-Li Alloys

In the Al-Li binary alloy, the metastable phase which forms during aging after solution heat treatment and quenching is ordered Al_3Li. The structure is the Ll_2-type (Cu_3Au). A large volume fraction of this type of metastable precipitate is not found in other commercial aluminum alloys. The large solubility of lithium in aluminum and the 3:1 aluminum to lithium ratio produce a high volume fraction of ordered precipitates. The misfit of the precipitates is small and they have been shown to be spherical with a diameter approximately 0.05 μm at peak strength. With prolonged aging, Al_3Li eventually transforms to AlLi.

Precipitation in Al-Mg-Li and Al-Cu-Li Alloys

In contrast to the binary alloy, the aging sequence of ternary Al-Mg-Li has been shown to be:

$$\text{supersaturated solid solution} \longrightarrow \delta'(Al_3Li) \longrightarrow Al_2MgLi;$$
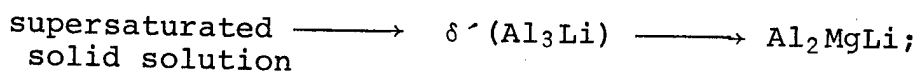
the Al_3Li metastable phase is the precipitate which is responsible for strengthening. It is essentially unaltered

by the presence of magnesium and, therefore, is similar to
the binary system. The beneficial effect of magnesium on
the mechanical properties appears to be solid solution
strengthening. In addition, it reduces the solubility of
lithium, thus promoting the development of a higher volume
fraction of the δ' precipitate at lower lithium levels. The
deleterious effect of magnesium appears to be the hetero-
geneous precipitation of Al_2MgLi on grain boundaries during
either quenching or aging.

Precipitation in the Al-4.5 Cu-1.1 Li-0.2 Cd alloy
follows the scheme:[1]

$$\text{supersaturated solid solution} \nearrow \begin{array}{l} G.P.I \longrightarrow \theta'' \\ \\ \searrow \quad (Al_3Li) \; \delta' \end{array}$$
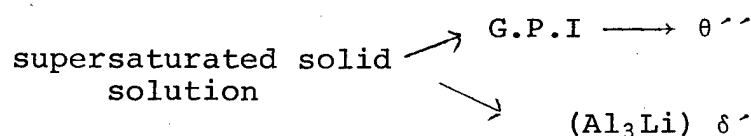
The copper precipitates independently of lithium and follows
the sequence that occurs in the Al-Cu-Cd system. The lithium
precipitates as Al_3Li (δ'). The development of high strength
in 2020 is attributed to the co-precipitation of θ'' and δ'.
The θ'' is the primary strengthening precipitate while δ'
appears to control properties such as modulus and presumably
alters the microdeformation mechanisms. Thus, the similarities
within alloys containing a sufficient quantity of lithium to
precipitate permit certain generalizations to be made.

The purpose of this program was to develop under-
standing of Al-Li alloys and determine how the structure
affects the basic deformation processes in these alloys.

This report is divided into chapters based on composition; they are:

Al-Mg-Li,

Al-Li, and

Al-Cu-Li.

A summary chapter is included to unify these properties which are attributed to the ordered Al_3Li precipitate.

LIST OF TABLES

CHAPTER 1

LIST OF FIGURES

CHAPTER 1

CHAPTER 1

Al-Mg-Li ALLOYS

Introduction

The Al-Mg-Li alloy system demonstrated in past programs the potential of providing attractive combinations of density, elastic modulus, and strength, but failed to achieve commercially acceptable absolute fracture toughness. The high volume fraction of ordered Al_3Li precipitates were thought to control the slip process. The ordered precipitates stimulate planar slip and thus create large stress concentrations at the grain boundaries. Heterogeneous precipitation of Al_2MgLi on the high angle boundaries and the possible segregation of insoluble constituent are postulated to play an important role in the low toughness by reducing the strength of these boundaries. Therefore, analysis of the fracture surface using scanning Auger spectroscopy as well as TEM of fabricated and heat treated sheet was undertaken in this program.

The influential effect of lithium on elastic modulus was shown in the previous contract.[1] Modulus was determined on a variety of Al-Mg-Li alloys aged to peak strength; however, it was not determined as a function of artificial aging conditions. Thus, a small program was developed to follow the change in modulus with aging for a particular Al-Mg-Li alloy fabricated under the last contract.

Experimental

Auger Analyses. Al-Mg-Li alloys used in the Auger spectroscopy investigation had been cast and fabricated

under a previous contract.   Remelt chemical compositions
are listed in Table 1-1.   Fracture specimens were machined
according to Figure 1-1 and heat treated according to the
practices outlined in Table 1-2.   Peak strength and one
week, naturally aged tempers were studied.   Fracture and
Auger analyses were carried out in a scanning Auger electron
microscope at Physical Electronic Industries, Incorporated,
Eden Prairie, Minnesota.   A fracture stage was incorporated
in the spectrometer vacuum system and the specimens were
transferred to the analyzing position after fracture.   The
specimens were under a constant ultrahigh vacuum, 1.33×10^{-8}
Pa (10^{-10} torr).   Auger analyses and scanning secondary
images were obtained on all fractured specimens.   The spectra
were recorded with an 8.0 KV beam incident at 30° to the
surface normal.

Elastic Modulus.   To achieve a better understanding
of the effects of ordered Al_3Li precipitates on mechanical
behavior of Al-Li alloys, elastic modulus was determined as
a function of artificial aging conditions.   An Al-Li-Mg
alloy cast and extruded to 5 cm round rod under a previous
investigation was used.   The remelt analysis is given in
Table 1-3.   The rod was given a solution heat treatment of
0.5 hour at 510°C (950°F).   Based on the hardness data shown
in Figure 1-2, five aging conditions were chosen (Table 1-
4).   The modulus values were determined using two micromeasure-
ment-type CEA-13-06UW-750 strain gauges 180° apart positioned
at the midlength of the reduced section of each specimen.

Transmission electron microscopy (TEM) was done on the most underaged specimen (0.5 hours at 149°C) and the most overaged 168 hours at 204°C). The foils were removed from the grip ends of the elastic modulus specimens and were prepared using a standard dimpling and polishing procedure. A 75% (by volume) methanol and 25% nitric acid solution was used for dimpling and polishing. To ensure a high quality foil surface, the polishing solution was cooled to -35°C and the foil was polished at 16 volts.

Grain Boundary Precipitation. A longitudinal slice, 0.63 cm (0.25"), was cut from a section of a 5.1 cm (2") diameter extrusion from three alloys cast and fabricated for Contract No. N62269-74-C-0438. The compositions are listed in Table 1-6. The slices were annealed for 0.5 hours at 510°C (950°F), cold water quenched and cold rolled to approximately 0.1 cm (0.04"). Two intermediate anneals at 510°C (950°F) for 0.25 hours were required to minimize edge cracking during rolling.

The sheets were then solution heat treated at 510°C (950°F) for 0.5 hours, cold water quenched and aged at 200°C (392°F) for 24 hours. Structures of as-solution heat treated and aged sheet were examined. TEM foils were prepared using standard polishing techniques.

Results

Auger Analyses. The four specimens fractured and analyzed in the spectrometer all had similar Auger spectra. Typically, aluminum, magnesium, and oxygen were present. A

peak which was attributed to an Auger transition for lithium was also identified. Significant amounts of potassium, sodium, and sulfur were also present on each of the fracture surfaces. A scanning secondary electron image along with an Auger electron image are shown in Figures 1-3 and 1-4. Figure 1-3 contains micrographs taken of the Al-2.3 Li-2.0 Mg alloy naturally aged for one week. The fracture appearance was ductile. Particles high in potassium can be seen on the surface when the image was formed using potassium Auger electrons. Figure 1-4 shows the fracture appearance of the same alloy aged to peak strength. Potassium, sodium, and sulfur were once again present on the surface in localized regions. The fracture appearance was considerably more brittle than that of the underaged specimen.

Elastic Modulus. The elastic moduli for the Al-Mg-Li alloy aged under different artificial aging conditions are summarized in Table 1-5. With increased aging, there was a consistent decrease in the elastic modulus. Figures 1-5 and 1-6 are transmission electron micrographs showing the size and distribution of the coherent, ordered Al_3Li precipitates. In the underaged condition (Figure 1-5), small, closely spaced precipitates were observed compared to larger, more widely spaced precipitates in the overaged condition (Figure 1-6).

Grain Boundary Precipitation. Figure 1-7 shows typical microstructures of the alloys examined immediately after solution heat treatment. The alloys were almost

completely recrystallized with a fine grain size (>ASTM 7).

Throughout the foils, small (approximately 0.2 μm) $MnAl_6$

intermetallics were observed. These precipitates were the

only precipitates observable in the foil. However, after

artificially aging the three Al-Mg-Li alloys (24 hours at

200°C, 391°F), δ´, the metastable precipitate, was observed

(Figures 1-8 through 1-10). These precipitates were ap-

proximately 0.05 μm in diameter. However, rather than

having uniform precipitation up to the grain boundaries,

precipitate-free zones (PFZ's) were present at all incoherent

boundaries, that is, grain boundaries and boundaries between

the matrix and the Al_6Mn dispersoids. Furthermore, within

the PFZ's, coarse δ´ precipitates were also observed (Figure

1-8). These precipitates produced diffraction patterns which

could be indexed on the basis of the δ´, Ll_2, structure.

In Figure 1-8b, a central dark field (CDF) image using a

$(100)_{\delta´}$ reflection shows the distribution of the small δ´

precipitates throughout the matrix and the larger δ´ in the

grain boundary region.

TABLE 1-1

REMELT CHEMICAL ANALYSES OF Al-Mg-Li FRACTURED
IN THE SCANNING AUGER MICROSCOPE

S. Number	Li	Mg	Si	Fe	Mn	Ti	Be
427599	2.30	2.03	0.04	0.04	0.28	0.02	0.004
427603	2.28	3.50	0.04	0.04	0.28	0.02	0.004
427607	2.33	4.84	0.04	0.04	0.27	0.02	0.004

TABLE 1-2

SOLUTION HEAT TREATMENT AND AGING OF Al-Mg-Li ALLOYS
FOR FRACTURE STUDIES

S. Number	Solution Heat Treatment Time (Hr)	Temperature	Aging Natural	Aging Artificial
427599	0.5	454°C (850°F)	1 wk R.T.	18 hr 190.5°C (375°F)
427603	0.5	510°C (950°F)	1 wk R.T.	36 hr 190.5°C (375°F)
427607	0.5	510°C (950°F)	1 wk R.T.	48 hr 204°C (400°F)

TABLE 1-3

REMELT CHEMICAL ANALYSIS OF Al-Mg-Li EXTRUSION USED IN
ELASTIC MODULUS EXPERIMENT

S. Number	Si	Fe	Ti	Mn	Mg	Li
427604	0.04	0.03	0.02	0.27	3.55	2.71

TABLE 1-4

AGING CONDITIONS OF Al-Mg-Li-Mn EXTRUSIONS FOR ELASTIC
MODULUS EXPERIMENT

Time, (hours)	Temperature, (°C)	(°F)
0.5	149	(300)
50	149	
1	204	(400)
50	204	
168	204	

TABLE 1-5

ELASTIC MODULUS OF Al-Mg-Li-Mn UNRECRYSTALLIZED EXTRUSIONS

Aging Condition			Modulus of Elasticity	
Time, (hours)	Temperature, (°C)	(°F)	GPa	(psi)
0.5	149	(300)	81.0	(11,750,000)
50	149		80.7	(11,700,000)
1	204	(400)	80.3	(11,650,000)
50	204		77.9	(11,300,000)
168	204		76.9	(11,150,000)

TABLE 1-6

CHEMICAL ANALYSES OF Al-Mg-Li ALLOYS ROLLED TO SHEET AND INVESTIGATED BY TEM*

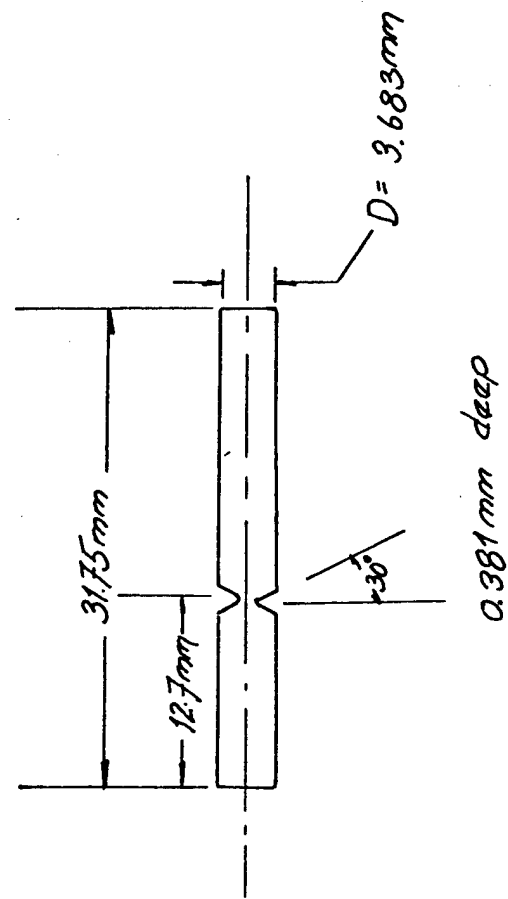| S. Number	Mg	Li	Mn	Si	Fe	Ti	Be
427599	2.03	2.30	0.28	0.04	0.04	0.02	0.004
427603	3.50	2.28	0.28	0.04	0.03	0.02	0.004
427607	4.84	2.33	0.27	0.04	0.04	0.02	0.004

*Transmission Electron Microscopy.

Figure 1-1. Specimen Design for Auger Fracture Studies.
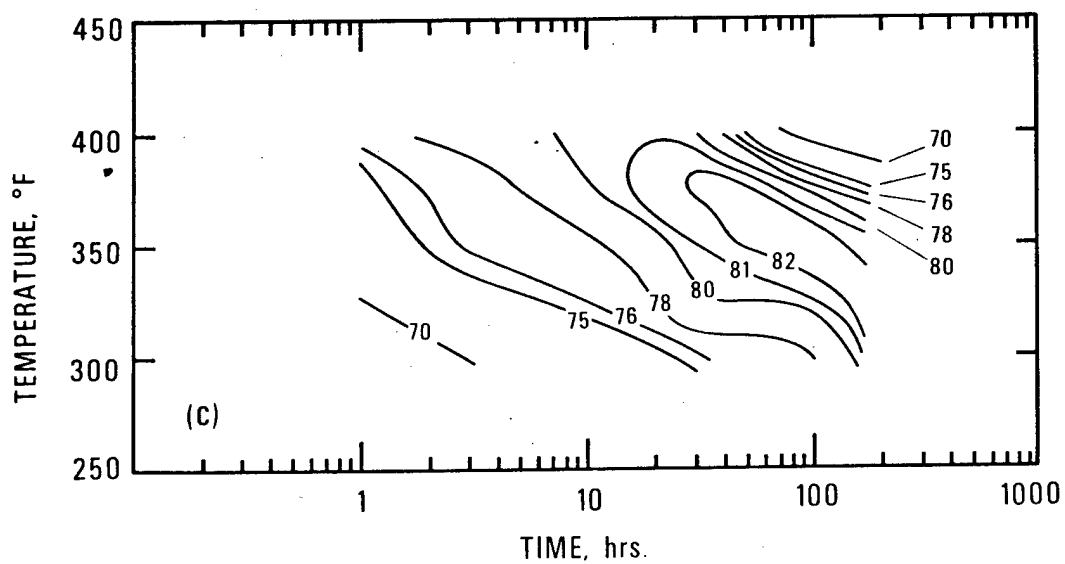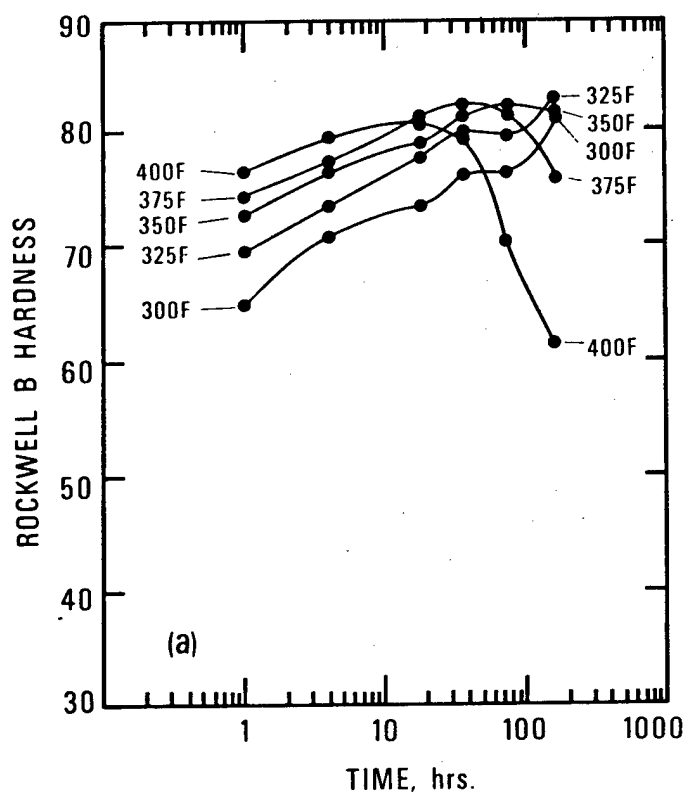
Figure 1-2.   Artificial Aging Curves for Al-Mg-Li (a)
            Isothermal, (b) Isochronal, and (c) Iso-
            Rockwell B Hardness Curves.

30 X

a

160 X

c

POTASSIUM   160 X

b
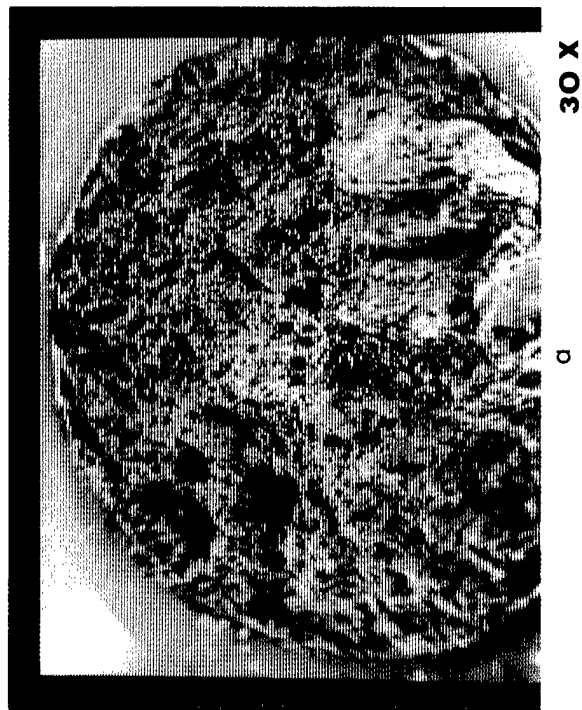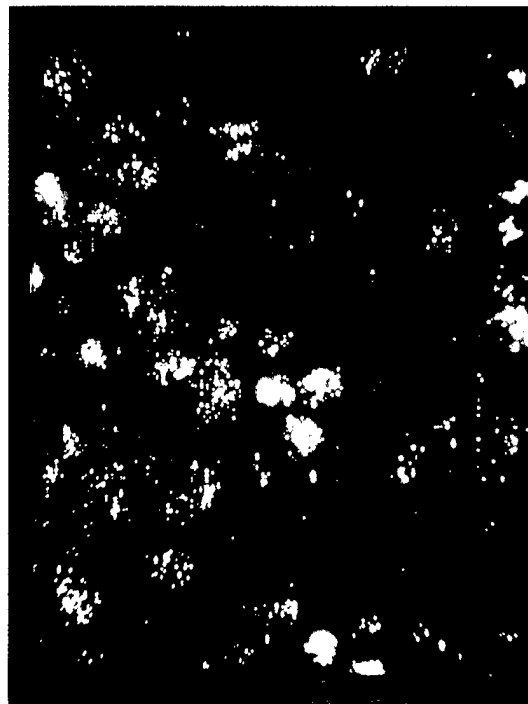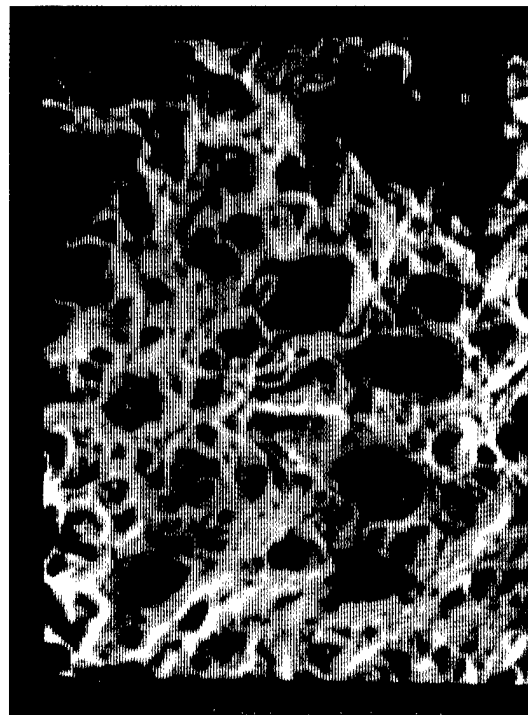
Figure 1-3.   Scanning Secondary Electron Images (a) and
(c) of the Fractured Al-2.3 Li-2.0 Mg Alloy
Naturally Aged for One Week, and (b) Scanning
Auger Image Showing Segregation of Potassium
on the Fracture Surface.

30 X
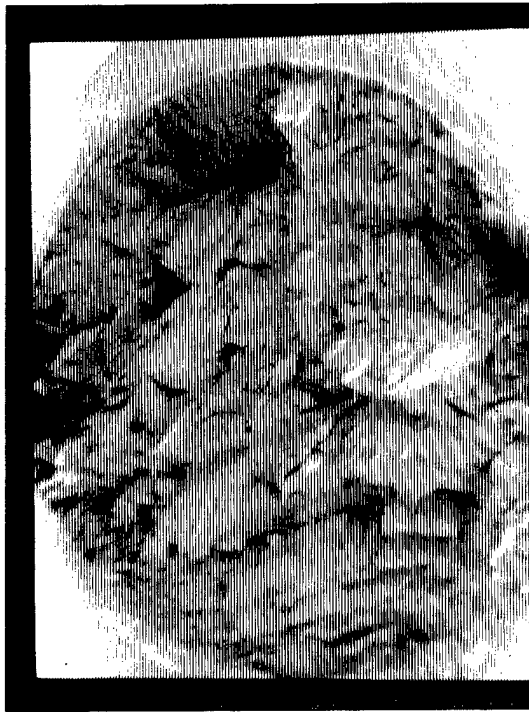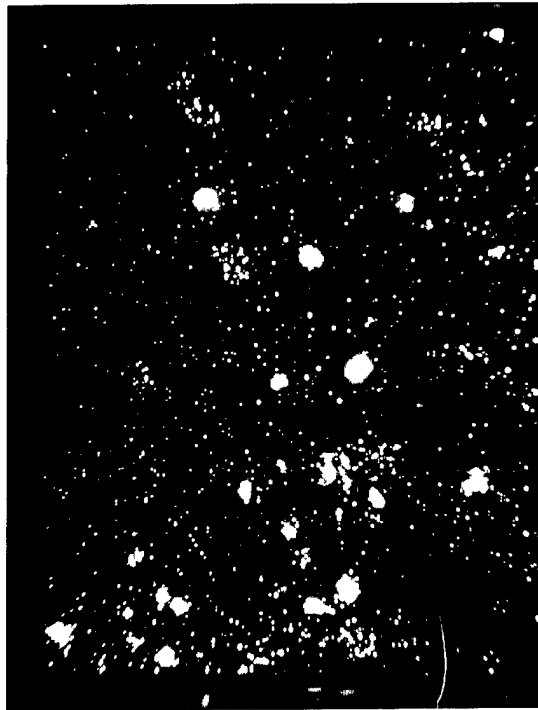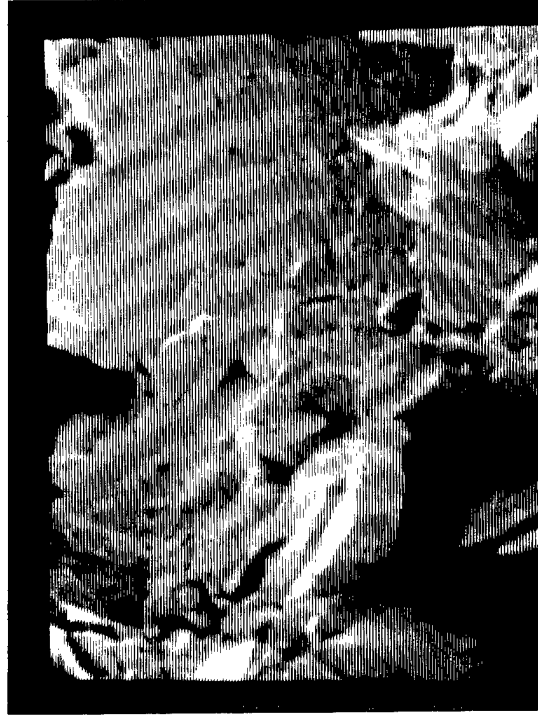
160 X

POTASSIUM   160 X

Figure 1-4.   Scanning Secondary Electron Images (a) and
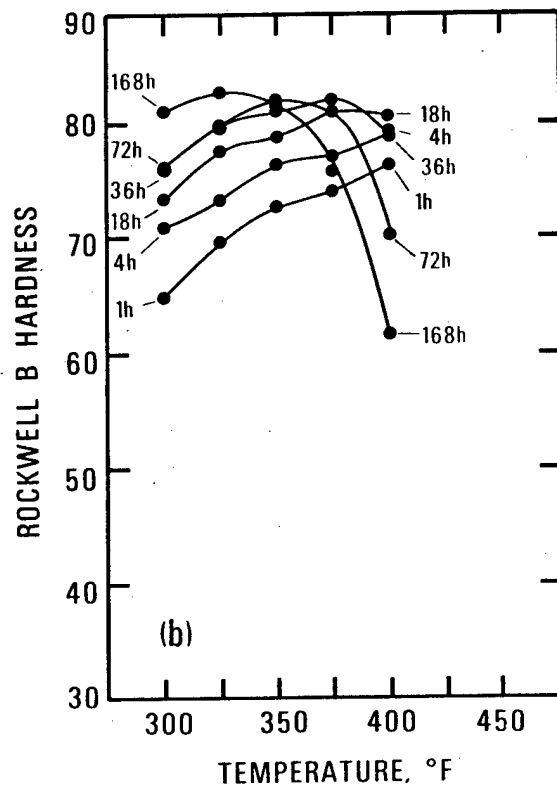(c) of the Fractured Al-2.3 Li-2.0 Mg Alloy
Aged to Peak Strength, and (b) Scanning Auger
Image Showing Segregation of Potassium on the
Fracture Surface.
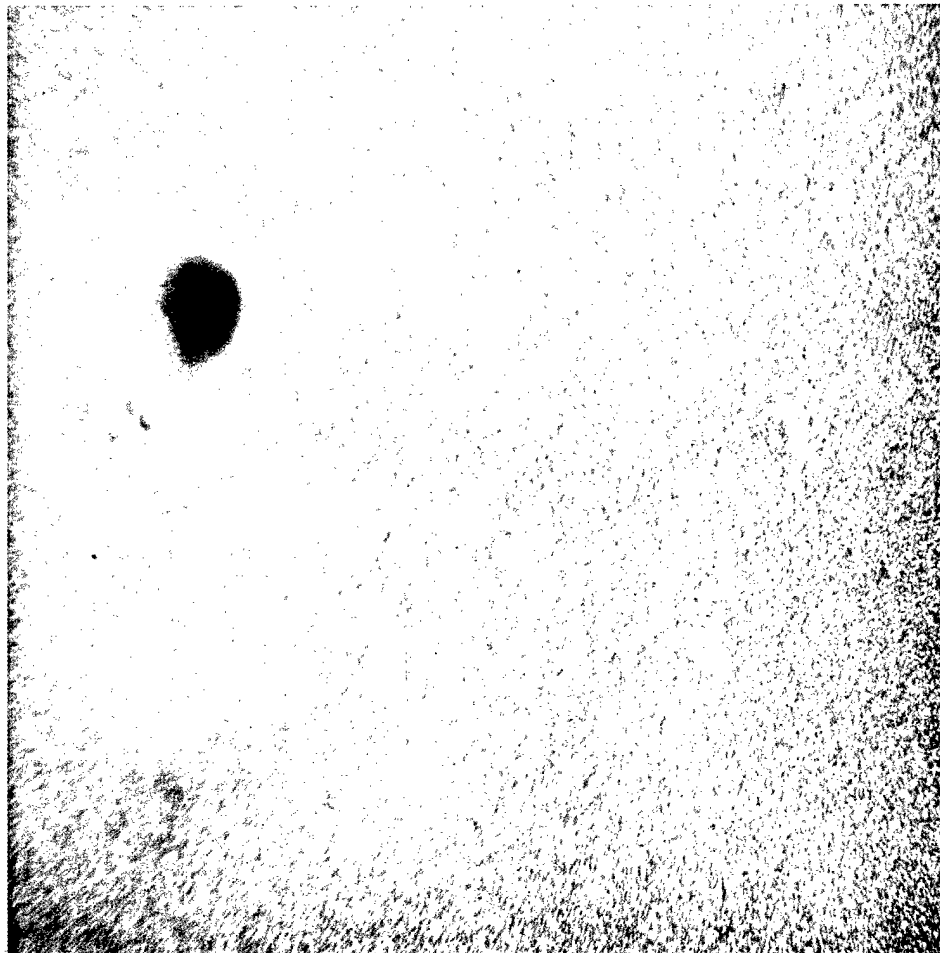
0.1 μm

Figure 1-5.   TEM Showing the Size and Distribution of Al$_3$Li
              in Underaged Al-Mg-Li.

Figure 1-6. TEM Showing the Size and Distribution of Al_3Li
in Overaged Al-Mg-Li.

0.25 μm

a

0.25 μm
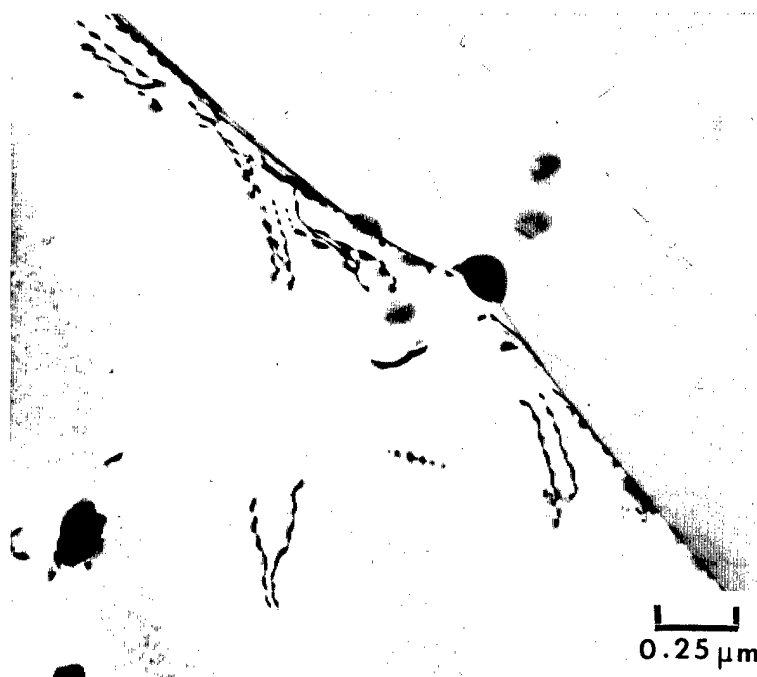
b

Figure 1-7. (a) Al-2.0 Mg-2.3 Li and (b) Al-3.5 Mg-2.3 Li
Solution Heat Treated, Cold Water Quenched, and
Immediately Examined after Foil Preparation.
The micrographs document the starting structure
in the vicinity of the grain boundaries. The
small precipitates are the Al_6Mn dispersoids.

0.25 µm

a

LIST OF TABLES

CHAPTER 2

LIST OF FIGURES

CHAPTER 2

CHAPTER 2

Al-Li ALLOYS

Introduction

Lithium is the only element with significant solubility in aluminum which simultaneously increases strength, significantly increases elastic modulus, and reduces the density. The need for this type of material for aerospace applications has been well documented. Consequently, a program to develop the basic physical and mechanical metallurgy of high solute Al-Li alloys is of paramount importance. The understanding gained from a program of this type could guide future alloy and process development programs.

Al-Li-Mg and Al-Cu-Li alloys have been successfully cast by direct chill (D.C.) methods in the past. However, certain problems such as hydrogen pickup, oxidation and lithium burn-off have been identified as potentially serious problems. Therefore, three approaches were taken to produce a 3% lithium alloy. They were conventional D.C. casting, vacuum casting and powder metallurgy approaches. These ingots were fabricated and evaluated in a variety of tempers and compared.

Experimental
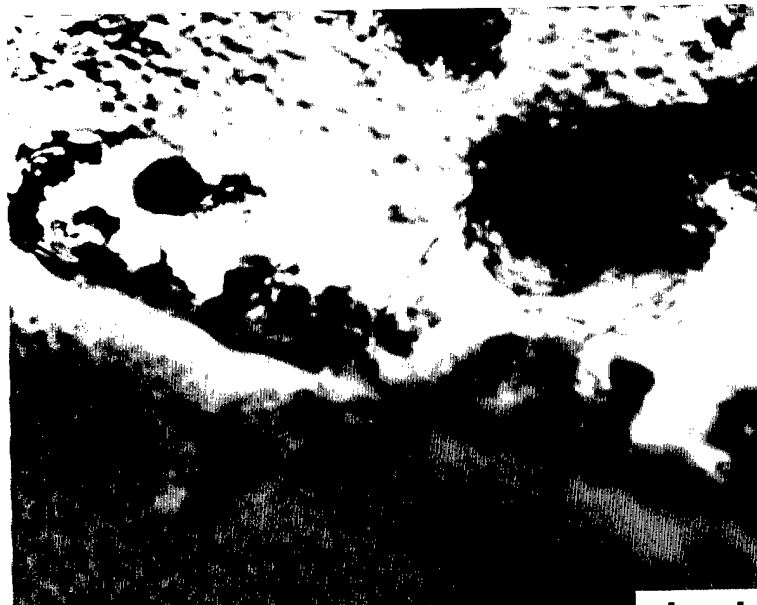
Conventional Ingot Casting. Attempts were made to cast Al-Li alloys containing either 3% or 5% Li with additions of either 0.1% Zr or 0.3% Mn as 150 mm (6") diameter DC ingots using the technique described elsewhere.[1] The lower solute alloys were cast successfully, but the higher solute alloys experienced ingot cracking. Remelt chemical analyses for the alloys are listed in Table 2-1.

Vacuum Casting. An Al-3.0 Li-0.14 Zr alloy was vacuum cast at Kawecki Berylco Industries, Inc. The casting was nominally 150 mm (6") diameter and 300 mm (12") long. The lithium was wrapped in aluminum foil and added with the aluminum and zirconium in the crucible. The furnace was evacuated and heated. A vacuum of 0.66×10^{-10} Pa (0.5 torr) was maintained during heatup and the alloy was poured at approximately 745°C (1375°F) into a steel mold with a beryllium-copper chill plate. Remelt chemical analyses are also given in Table 2-1.

Powder Metallurgy (P/M). Al-Li powder was prepared by atomizing an Al-3.0 Li melt in synthetic flue gas.* The composition and average particle diameters are given in Table 2-2. The powder was encapsulated in an aluminum can approximately 150 mm (6") diameter, then preheated five hours at 520°C (970°F) in a vacuum of 0.267 Pa (2×10^{-3} torr). It was then compacted at 427°C (800°F) with 620 MPa (90 ksi) average pressure. The hot pressed billet was scalped to 133 mm (5-1/4") diameter.

Fabrication. The ingots were preheated 12 hours at 454°C (850°F) plus 13 hours at 516°C (960°F) in an argon atmosphere.

The unscalped, conventionally cast ingot metallurgy billets and the scalped P/M and vacuum cast billets were

---

*Composition of flue gas:
  0.0% - O_2 12.6% - CO_2 Balance - N_2
  2.0% - H_2 0.6% - CO   Dew Point - -57°C (-70°F)
                                      to -68°C (-90°F)

extruded into 50.8 mm (2") diameter rod with billet and cylinder temperatures at 371°C (700°F). The butt ends of the billets were split, machined, and macroetched to reveal the structure.

Figures 2-1 through 2-3 are macroetched, longitudinal sections of the butt ends of the extrusions. The etch reveals the relative size and flow patterns of the ingot structure into the product.

Three 25 cm lengths from the Al-Li-Mn and the two Al-Li-Zr alloy extrusions were reheated in a circulating air furnace to 482°C (900°F) for 0.5 hour. The rods were flattened along the diameter into rectangular plates between two lubricated large flat dies at 204°C (400°F) to a final thickness of 1.2 cm. The final temperature of the plates was approximately 260°C (500°F). All alloys were successfully upset. The plates were then annealed in liquid metal to insure rapid heatup to 551°C (1025°F) and held at that temperature for five minutes and quenched in cold water. After this operation, large blisters were observed on the forging from the vacuum-cast Al-Li-Zr alloy ingot (Figure 2-4). A metallographic section through the blisters is shown in Figure 2-5. Chemical analysis of the trapped gas in the blisters is listed in Table 2-3. After the anneal, the plates from the conventionally cast Al-Li-Mn and Al-Li-Zr alloy ingots were cold rolled. The Al-Li-Mn alloy was cold rolled 92% and the Al-Li-Zr alloy was cold rolled approximately 50% without an anneal. After the intermediate anneal

at 50% reduction, the Al-Li-Zr was rolled to the same thickness as the Al-Li-Mn.

Recrystallization. A series of 6 mm (1/4") thick discs were machined from the extrusions and exposed at different solution heat temperatures for one-half hour. Each disc was then machined to approximately 0.46 mm (0.018") and chemically thinned to 0.2 mm (0.008"). Degree of recrystallization was determined by film technique using unfiltered copper radiation in transmission geometry. Also, pieces of the 1.6 mm (0.063") Al-Li-Mn and Al-Li-Zr sheet were solution heat treated at 552°C (1025°F) for 15 seconds and 30 minutes in molten metal, cold water quenched, and chemically thinned to 0.2 mm (0.008"). Degree of recrystallization was also determined on these specimens.

Phase Identification. Phases in as-extruded specimens were determined by using a Guinier-deWolff quadruple focusing camera.

Conventional Aging. Hardness specimens from the Al-Li-Zr extrusions were solution heat treated at 552°C (1025°F) for 0.5 hour, quenched in cold water, and artificially aged at 150, 175, and 200°C. Changes in aluminum lattice parameters were determined by measuring the displacement of the (3,3,3) and (4,2,2) Bragg reflections.

Quench Aging. Hardness specimens from the same extrusions were solution heat treated at 552°C (1025°F) in molten metal for 0.5 hour, quenched in molten metal at the desired aging temperature and aged 0.25, 0.5, and 1.0 hours.

Transmission Electron Microscopy (TEM). TEM investigations were conducted on a variety of specimens taken from solution heat treated extrusions and sheet materials. The microstructures of naturally and artificially aged tempers were studied. The nature of the different substructures and precipitate reactions occurring within and at the grain boundaries were investigated. The foils were produced using standard dimpling and polishing procedures.

Tensile/Notch Tensile/Tear. Tensile tests were conducted on the Al-Li-Mn alloy extrusion at two aging conditions; tensile and notch tensile tests were done on the Al-Li-Zr alloy extrusions and the Al-Li powder alloy extrusions aged for various times at several temperatures. The notch tensile tests were conducted using the specimen shown in Figure 2-6. Sheet-type tensile and Kahn tear tests were conducted on the Al-Li-Mn and Al-Li-Zr sheet solution heat treated in molten metal and quenched either into cold water or into liquid metal at the aging temperature. TEM and SEM investigations were conducted on specific extrusion and sheet tensile, notch tensile, and tear specimens.

Fracture Toughness. Sections of the 5 cm (2") diameter Al-Li-Zr alloy extrusions were solution heat treated at 552°C (1025°F), cold water quenched, and artificially aged 4 hours at 200°C (392°F). Compact tension specimens were machined, and toughness measurements were made according to the method outlined by ASTM E399. The specimens were 19 mm x 38 mm (0.75" thick x 1.5" wide). Two orientations were

tested, one with the crack parallel to the extrusion direction and one perpendicular to the extrusion direction.

Hydrogen Content. Hydrogen content was determined by fusion technique. Changes in thermal conductivity of a constant flow rate of dry nitrogen were correlated quantitatively to the amount of hydrogen introduced into the gas stream during melting of the specimen.

Auger Analyses. Auger specimens were prepared from both low solute conventional and vacuum cast Al-Li-Zr alloys. Specimen blanks from the extrusions were solution heat treated at 552°C (1025°F) for one-half hour, quenched in cold water, and aged 24 hours at 200°C. The specimens were machined according to Figure 1-1.

Fracture and Auger analyses were conducted at Physical Electronics Industries, Incorporated, Eden Prairie, Minnesota, as described in the Al-Mg-Li section of this report.

Strain Control Fatigue. Strain control fatigue (SCF) tests were conducted on extrusions from the conventionally cast Al-2.8 Li alloy extrusions heat treated and aged according to the practices outlined in Table 2-4. Multiple specimen SCF tests were conducted according to testing practices of ASTM E606-77T, "Constant-Amplitude Low-Cycle Fatigue Testing," SCF specimens were machined to a constant diameter reduced section of 0.914 cm (0.360") by 1.83 cm (0.720").

Total strain SCF tests were conducted on an MTS closed-loop electrohydraulic testing system using a 1.3 cm (0.5") gauge length axial extensometer attached to the reduced section of the specimen. A 44.5 KN (10,000 pound) dynamic capacity load cell in series with the specimen was used to monitor the load. The system was calibrated to a maximum strain error of 1.2 percent of reading or $\pm$0.00025 cm (0.0001"), whichever was larger, and a maximum load error of 0.5 percent of reading or $\pm$44.5 N (10 pounds), whichever was larger. The strain was applied using fully reversed, triangular wave forms with a strain rate of 0.01 sec^{-1}. Hysteresis loops were recorded directly on a DEC PDP/11 digital computer at logarithmic increments in life; load and strain extremes were recorded more frequently. Most of the SCF tests were started in the tension direction; however, for comparison, particular tests were begun in the compression direction.

Scanning electron fractographic examinations were made on particular specimens to characterize the mode of fracture. To understand the cyclic deformation behavior of Al-Li alloys, representative TEM foils were prepared from discs sectioned 0.5 cm (0.2") below the fracture surface of the SCF specimens.

Elastic Modulus. The modulus of elasticity of the Al-Li-Zr alloy extrusion from the conventionally cast ingot was determined for a variety of aging conditions. Experimental procedure was the same as previously described for Al-Mg-Li alloys.

Corrosion Resistance. Al-Li-Zr (from conventionally cast ingot) and Al-Li-Mn extrusions were evaluated for resistance to corrosion. The extrusions were solution heat treated one-half hour at 552°C (1025°F), quenched in cold water, and aged 24 hours at 200°C (393°F). Two accelerated corrosion tests were conducted on each alloy. In the first test, the alloys were exposed to a 5% NaCl solution acidified to pH 3 with acetic acid (MASTMAASIS) for one week. In the second, they were exposed to a 5% NaCl continuous spray for one week. These two exposures are considered to be aggressive tests for determining corrosion performance of aluminum alloys.

More intensive corrosion investigations were also conducted. The procedures, results, and discussions are given in Appendix 2-A.

Results

Microstructure and Degree of Recrystallization of Extrusions. Figure 2-7 shows micrographs taken of as-polished specimens which were solution heat treated at 552°C (1025°F) for 0.5 hour and cold water quenched. The micrographs show the relative amount and size of the insoluble second-phase particles. Qualitatively, the powder metallurgy product contains a greater number of insoluble particles.

Figures 2-8 and 2-9 are micrographs showing the grain structures of the solution heat treated rods from the conventionally cast Al-Li-Mn and Al-Li-Zr alloys, respectively.

Coarse, recrystallized grains are evident in the Al-Li-Mn alloy solution heat treated at 552°C (1025°F). In contrast, the alloy containing zirconium was unrecrystallized after this treatment. Increasing the solution heat treatment temperature of the Zr alloy to 593°C (1100°F) produced only a partially recrystallized structure (Figure 2-10). The grain structure of the vacuum cast Al-Li-Zr alloy was similar to that of the conventionally cast one.

Degrees of recrystallization for the extrusions and sheet as determined by X-ray are listed in Tables 2-5 and 2-6, respectively. The results confirm the metallographic examinations that the Al-Li-Zr alloy products had a lower tendency to recrystallize compared to the Al-Li-Mn alloy products. The P/M Al-Li alloy extrusion was unrecrystallized in the temperature range investigated. Also, the sheet soaked for the longer time at the solution heat treatment temperature (552°C) tended to show more recrystallization.

Phase Identification. The phases identified by the Guinier-deWolff technique on the as-extruded alloys are listed in Table 2-7.

Conventional Aging. Hardness (R_k) results are shown in Figures 2-11 through 2-13. Peak hardness was found to occur with approximately 12 hours at 200°C. A plot of lattice parameter, electrical resistivity, and hardness is shown in Figure 2- 14 for comparison.

Quench Aging. The results of the short-time arti-

ficial aging are shown in Figure 2-15. These results indicate
peak hardness can be achieved in less than 0.25 hour at
250°C.

TEM. The solution heat treated and artificially
aged Al-Li-Mn and Al-Li-Zr (conventionally cast alloy)
extrusions were examined (Figures 2-16 through 2-19).

The strengthening δ' precipitates were observed in
both alloys in the under and peak aged conditions. The high
volume fraction and the uniformity in distribution of δ' are
shown in the central dark field (CDF) images (Figure 2-16).
The precipitate is based on the ordered $L1_2$ structure having
a cube/cube orientation with respect to the aluminum matrix
and the precipitate reflections are indexed accordingly
(Figure 2-17).

The Al-Li-Mn and the Al-Li-Zr alloys dynamically
recovered during extrusion and were unrecrystallized directly
off the press. However, during solution heat treatment, the
Al-Li-Mn alloy statically recrystallized with a large grain
size. The Al-Li-Zr alloy, on the other hand, remained unre-
crystallized after solution heat treatment; the evidence of
a recovered structure can be seen in Figure 2-18.

A series of representative micrographs from foils
prepared from a variety of aging times in the recrystallized
Al-Li-Mn sheet isothermally aged at 200°C (392°F) are shown
in Figures 2-19 through 2-21. The precipitates were spherical
and the radius as a function of isothermal aging was determined

by measuring numerous δ′ precipitates, and the results are summarized in Table 2-8.

In an attempt to better understand the precipitate growth kinetics, the data were analyzed using a model having the form:

$$R = t^m,$$

where R is the radius of the precipitate in micrometers, and t is the time of aging in seconds. The data were transformed into the form:

$$\ln R = m \ln(t) + \text{constant},$$

and a linear least squares analysis of the data was completed. The regression equation was determined as:

$$\ln R = 0.338 \ln(t) - 7.689,$$

with the coefficient and the constant statistically significant at the 99.9% confidence level. Furthermore, the model was able to predict 95.2% of the variation in the data. Consequently, the data were reanalyzed using the relationship:

$$R = ct^{1/3},$$

a model whose physical significance is based on the assumption that the growth of the precipitates is diffusion controlled. The data are presented in Figure 2-22 where the radius is plotted as a function of $t^{1/3}$. This model was statistically able to acount for 95.8% of the variation in the data.

In addition to the nucleation and growth of δ′ within the matrix, other microstructural changes were also occurring during artificial aging. These changes were localized

at grain boundaries. Figures 2-23 through 2-27 show a series
of TEM's at a variety of aging conditions. After one week
of natural aging, small, uniformly distributed precipitates
occur up to the grain boundaries and the grain boundaries were
free from coarse precipitates. However, examination of
specimens from materials isothermally aged at 200°C (392°F) for
a variety of times revealed a precipitate free zone (PFZ)
which grew during artificial aging. The PFZ was measured on
grain boundaries oriented such that the plane of the boundary
was parallel to the beam direction. The PFZ half width was
determined as a function of aging time and is summarized in
Table 2-9.

A statistical treatment similar to that used on the
growth of the δ' was completed on the growth of the PFZ as a
function of aging time. A model of the form,

$$\frac{w}{2} = t^m,$$

where w is the width of the PFZ in micrometers and t is the
aging time in seconds at 200°C (372°F). The linear regression
equation was determined as

$$\ln \frac{w}{2} = 0.39 \ln(t) - 6.086.$$

The model was able to predict 87.5% of the variation in the
data. Therefore, the data were reanalyzed using the relation-
ship:

$$\frac{w}{2} = ct^{1/3}.$$

This model was able to predict 79.0% of the variation in the
data. The PFZ half width is plotted in Figure 2-28.

The presence of a PFZ occurred not only at grain boundaries but was also seen at the boundaries between the Al_6Mn and the aluminum (Figures 2-29 through 2-31). Because of the complex shapes of these boundaries, measurements of PFZ around the intermetallics were not attempted.

In addition to isothermal aging, an experiment using controlled heatup was undertaken. A heating rate of 5°C/hr to 200°C (392°F) was used and the radius and PFZ width was determined on a variety of foils prepared from specimens held at 200°C (392°F) for different times. These results are summarized in Table 2-10.

The second microstructural feature which varied with aging was the size of large precipitates in the grain boundary region. Figures 2-32 through 2-34 show successive stages in the growth of grain boundary precipitates. SAD patterns from these precipitates could be indexed based on the Ll_2 structure.

The observations made in the TEM investigations during the artificial aging of the Al-Li-Mn can be summarized as follows:

1. Nucleation and growth of the δ´ occurred within the matrix.

2. PFZ's developed and grew with aging time.

3. Preferential coarsening of δ´ occurred in the vicinity of the grain boundaries. The size increased with increasing aging time.

The nature of their interfaces and the relative shapes of the Zr and Mn precipitates are different. The Al_6Mn are incoherent with the matrix and are rod-like. Significant mechanical fibering aligns the precipitates with their long axes parallel to the direction of metal flow. The Al_3Zr precipitates are coherent and spherical. They have a definite orientation relationship to the matrix, cube/cube. Like the Al_3Li precipitates, Al_3Zr have the ordered Ll_2 structure. Figure 2-35 shows the distribution of Al_3Zr in the as-quenched Al-Li-Zr alloy.

Tensile/Notch Tensile and Tear Properties. The tensile and notch tensile properties for the two Al-Li-Zr and the Al-Li P/M alloy extrusions along with their solution heat treatment temperatures and artificial aging conditions are summarized in Tables 2-11 through 2-16. Because of the low strength and notch toughness of the powder metallurgy product, no further work was done with that material (Table 2-11).

The notch tensile data are separately plotted for each alloy and solution heat treatment and aging conditions (Figures 2-36 and 2-40) and jointly for the conventionally cast alloy on one graph (Figure 2-41). All heat treating conditions produced similar slopes in the toughness-strength relationship. A model of the form:

$$\frac{\text{Notch Tensile Strength}}{\text{Yield Strength}} = \text{Constant X Yield Strength + Constant,}$$

was used to analyze the data. Figure 2-42 is a plot of the

predicted values. All the curves for the conventionally
cast material were clustered, but the curve for the vacuum
cast material was slightly lower.

Longitudinal tensile and tear results for the Al-
Li-Mn sheet solution heat treated for 15 seconds at 552°C
(1025°F) and either quenched in cold water and aged at 200°C
or direct quenched in molten metal at 200°C and aged in the
bath are given in Tables 2-17 and 2-18 and the tensile properties
are plotted in Figures 2-43 and 2-44.

Longitudinal tensile and tear results for the Al-
Li-Zr sheet solution heat treated at 552°C (1025°F) for either
15 seconds or 30 minutes are listed in Tables 2-19 and 2-20 and
tensile results are plotted in Figure 2-45. A significant re-
duction in tensile and yield strength with an accompanying
increase in tear energy occurred when the alloys were
solution heat treated for the longer time.

Limited tests were conducted in the transverse
direction (tear only) on both the Al-Li-Mn and Al-Li-Zr
sheet solution heat treated at 552°C (1025°F) for 15 seconds,
cold water quenched, and aged at 200°C. The data are
summarized in Table 2-21. Tear results in the transverse
direction were slightly higher in the recrystallized Al-Li-
Mn sheet, but since tensile properties were not determined,
a tear/yield comparison could not be made. Valid propaga-
tion energies could not be determined in the transverse
direction of the unrecrystallized Al-Li-Zr sheet. The crack

front in these specimens was erratic (Figure 2-46). The crack always tended to move parallel to the direction of fabrication.

Fracture Toughness. The results of the fracture toughness tests are summarized in Table 2-22. The validity of the values of K_{Ic} for tests with the crack perpendicular to the extrusion direction is questionable. Figure 2-47 is a photograph of a fractured specimen with the starter crack changing direction and running parallel to the applied stress rather than perpendicular to it. For reference, a micrograph is included to show the grain morphology of the material. A number of specimens were tried, and the same change in direction resulted.

Structure/Properties. Macrographs of a tensile and notch-tensile specimen are shown in Figure 2-48. Even with the presence of the notch, the appearance of the fracture is shear. Typical scanning electron fractographs of the tensile and notch tensile specimens are shown in Figures 2-49 and 2-50, respectively. The top series of micrographs (a-c) correspond to peak strength, and the bottom series (d-f) correspond to an overaged condition. To aid in the identification of the microstructural features, the fracture surfaces were mechanically polished to reveal the underlying structure and these micrographs are included (Figures 2-49a and 2-50a and d). The intergranular nature of the failure becomes apparent. The fracture process occurs along

the elongated as-cast grains. In the overaged condition
(Figures 2-49d and 2-50d), the subgrain boundaries are
decorated by precipitate along the boundaries. Correspond-
ingly, more "dimple-like" features are apparent with in-
creased aging time. TEM from fractured tensile specimens
machined from the conventionally cast Al-Li-Zr extrusion
aged for short times (4 hours at 200°C) and longer times (24
hours at 200°C) are shown in Figures 2-51 and 2-52, re-
spectively. Planar slip occurs during deformation in both
aging conditions. A CDF micrograph using a (100) Al_3Li
reflection is included in Figure 2-52. The small offsets in
the Al_3Li precipitates indicate that the dislocations have
cut the ordered precipitates during plastic deformation.

Metallographic evidence indicated that the flow
and fracture processes for the two sheet alloys were different.
Optical micrographs of longitudinal and surface sections of
a fractured Al-Li-Mn sheet tensile specimen are shown in
Figure 2-53. The mode of failure appears to be intergranular,
and significant grain boundary separation can be seen away
from the fracture surface. Scanning electron micrographs of
the fracture surface of the most underaged and peak aged
specimens are shown in Figure 2-54. The failure is clearly
intergranular at either aging condition, as suggested by the
optical micrographs presented in Figure 2-53. Careful
attention should be directed toward the detail on the grain
faces evident at higher magnifications (Figure 2-54b, c, and

d). In Figure 2-54b and c, the most underaged condition,
ledges appear on the grain faces. The regular arrangement
of these ledges suggests a crystallographic relationship.
However, at peak strength (Figure 2-54d), the ledges are not
present, but small, "dimple-like" features can be seen on
the grain faces. Fractographs of specimens aged at inter-
mediate times at 200°C are included in Figure 2-55. The
amount of grain ledges progressively decreases while the
number of dimples increases with increasing aging time. TEM
of the most underaged specimens pulled to fracture are shown
in Figures 2-56 through 2-59. Intense planar slip bands and
their effect on grain boundaries are shown in Figures 2-58
and 2-59. Offsets at the grain boundaries can easily be
identified. These offsets occur when a slip band intersects
a grain boundary.

The observations on the Al-Li-Zr sheet contrasted
with those on the Al-Li-Mn sheet. Optical micrographs of a
longitudinal section of an Al-Li-Zr sheet tensile fracture
are shown in Figure 2-60. The mode of failure appears to be
shear, and intense bands of deformation are evident in the
photograph. Higher magnification micrographs (Figure 2-61)
show a thin, "fibrous-like" grain structure. However, small
regions of large, recrystallized grains apparently associated
with the bands of deformation can be seen. The bands of de-
formation are present in the structure prior to tensile
testing (Figure 2-62). TEM of fractured specimens of

underaged Al-Li-Zr sheet are shown in Figure 2-63. Small subgrains with planar slip were typical of the deformation structure. The subgrains were finer than in the extrusion.

Hydrogen Content. Hydrogen content for the conventionally cast Al-Li alloys and the vacuum cast alloy are listed in Table 2-23. All readings were similar and were about an order of magnitude higher than usually found in aircraft alloys.

Auger Analyses. All specimens fractured and analyzed in the spectrometer had similar Auger spectra. Aluminum, oxygen, lithium, potassium, and sodium were present on the fracture surfaces. A scanning electron image along with scanning Auger electron images of potassium and aluminum are shown in Figure 2-64. The distribution of potassium would suggest significant segregation. An Auger electron image of aluminum is included to give an indication of whether the impurity element is truly segregated or if the segregation is a manifestation of surface topography. The combination of potassium and aluminum would suggest that the potassium is segregated.

Strain Control Fatigue. The results of multiple specimen SCF tests are plotted in Figure 2-65. The data follow Coffin-Manson behavior in that the log of plastic strain amplitude versus the log of the number of cycles to failure for the two alloys and tempers are linear in the range of plastic strain amplitudes investigated.

The stress amplitude response for the structures are shown in Figure 2-66. In the case of the Al-Li-Mn alloy (Figures 2-66a and 2-66b), cyclic hardening was observed in both tempers and at all plastic strain amplitudes tested. For the sake of simplicity, only two stress amplitude response plots are included. For the Al-Li-Zr alloy, cyclic softening was found to occur at higher strain cycling and cyclic stabilization at lower strain amplitude cycling (Figures 2-66c and 2-66d).

First cycle hysteresis loops for the two alloys aged 24 hour at 200°C are shown in Figure 2-67. For comparison, two tests are plotted, one started in the tension direction and one in the compression direction. The tension and compression hysteresis loops are essentially the same except for the presence of a small deviation indicated by the arrows in Figure 2-67b.

Figure 2-68 is a plot of the half life hysteresis loops. In both cases, the curves are identical. All the SCF parameters are listed in Table 2-24.

Scanning electron fractographs of strain control fatigue specimens of the Al-Li-Mn alloy cycled to failure at an intermediate level of plastic strain cycling are shown in Figures 2-69 and 2-70. The specimens in Figure 2-69 were aged 4 hours at 200°C and the specimens in Figure 2-70 were aged 24 hours at 200°C. In both cases, the presence of a large number of octahedral facets on the fracture surface substantiates the mode of crack propagation as Stage I.

A comparison of Figures 2-69 and 2-70 indicates a greater amount of Stage I growth on the surface of the underaged structure.

Scanning electron fractographs of the conventional cast Al-Li-Zr specimens cycled to failure are shown in Figures 2-71 and 2-72. Macroscopically, the fracture appearance of these unrecrystallized alloys was similar to shear. Suggestions of Stage I growth, however, can be seen at high magnifications.

TEM on specimens cycled to failure exhibited similar deformation structure to the structures observed during uniaxial tensile deformation. In all cases investigated, intense planar slip was observed. Specimens cycled to failure which were underaged showed evidences of dislocation shearing.

Elastic Modulus. Elastic modulus for the Al-Li-Zr alloy from the conventionally cast ingot is given in Table 2-25. As in the case of the Al-Mg-Li alloy, aging slightly reduced the modulus.

Accelerated Corrosion Tests. Both the Al-Li-Zr and Al-Li-Mn alloys were exposed to the intermittent MASTMAASIS spray and the continuous 5% NaCl spray. These two exposures are considered to be aggressive tests for determining corrosion performance of Al alloys.

After one week exposure, none of the alloys showed significant corrosion in either environment. In MASTMAASIS spray, there was some staining and very shallow pitting. In

the continuous 5% NaCl spray, there were no signs of cor-
rosion damage. Photographs of the surfaces of the two
alloys after exposure in the two corrosion media are shown
in Figures 2-73 and 2-74 (see Appendix A).

TABLE 2-1

REMELT CHEMICAL ANALYSES OF Al-Li ALLOYS

S. Number	Li*	Mn	Zr	Fe	Si
454103A[1]	2.78	0.32	0.00	0.06	0.04
454104B[1]	2.76	0.00	0.14	0.07	0.04
477387 [2]	3.58	0.00	0.13	0.06	0.04

*Determined by Atomic Absorption.
[1]Conventional.
[2]Vacuum.

TABLE 2-2

ATOMIZED POWDER COMPOSITION AND SIZE

S. Number	Li	Fe	Si	Average Particle Diameter, μm
454476	3.85	0.02	0.02	21.9

TABLE 2-3

CHEMICAL ANALYSIS OF THE TRAPPED GAS
IN THE VACUUM-CAST Al-Li-Zr PLATE

Constituent	Mole (%)
Argon	45.8
Nitrogen	23.9
Oxygen	15.5
Hydrogen	9.7
Propane	4.5
Methane	0.6

TABLE 2-4

HEAT TREATMENT OF Al-2.86 Li-0.32 Mn AND Al-2.84 Li-0.13 Zr
ALLOYS FOR STRAIN CONTROL FATIGUE TESTS

Solution Heat Treatment Temperature, °C	°F	Time at Temperature, Hours	Artificial Aging Temperature, °C	(°F)	Time at Temperature, Hours
554	1025	0.5	200	(392)	4
554	1025	0.5	200	(392)	24

TABLE 2-5

DEGREE OF RECRYSTALLIZATION OF EXTRUSIONS

S. No.	427°C (800°F)	440.5°C (825°F)	454°C (850°F)	468.5°C (875°F)	485°C (900°F)	496°C (925°F)	510°C (950°F)	524°C (975°F)	538°C (1000°F)	554°C (1025°F)	566°C (1050°F)	551.5°C (1075°F)	593°C (1100°F)	610°C (1130°F)	616°C (1140°F)
454103A	unrecryx.	unrecryx.	just started	almost complete	complete	→									↑
454104B	unrecryx.	unrecryx.	← unrecrystallized		→				↑	just barely started →				just started ↑	
477387	unrecryx.	unrecryx.	← unrecrystallized	→						just barely started →				just started ↑	
454476	unrecryx.	unrecryx.	← unrecrystallized					→	↑						

454103A - Al-Li-Mn alloy.
454104B - Al-Li-Zr alloy, conventionally cast.
477387 - Al-Li-Zr alloy, vacuum cast.
454476 - Al-Li alloy P/M.

TABLE 2-6

EFFECT OF SOLUTION HEAT TREATMENT TIME ON DEGREE OF
RECRYSTALLIZATION AND GRAIN SIZE OF Al-Li-Mn
AND Al-Li-Zr SHEET

Alloy	Time at SHT	Degree of Recrystallization	ASTM Grain Size
Al-Li-Mn	15 seconds	Complete	5.
Al-Li-Mn	0.5 hours	Complete	5.
Al-Li-Zr	15 seconds	Just barely started	—
Al-Li-Zr	0.5 hours	Started	—

TABLE 2-7

PHASES PRESENT IN AS-EXTRUDED Al-Li ALLOYS

S. Number	AlLi	AlLiSi	MnAl$_6$	Mn$_3$SiAl$_{12}$	FeAl$_3$	Al$_{12}$Fe$_3$Si	Al$_4$Li$_9$	Li$_2$O
454103A	large	small	small-	small-	trace	--	--	--
454104B	large	small	--	--	v.small	v.small	--	--
454476	large	trace	--	--	--	--	trace	small
477387	large	small	--	--	v.small	v.small	--	--

TABLE 2-8

THE EFFECT OF ISOTHERMAL AGING AT 200°C (392°F) ON THE GROWTH OF δ' PRECIPITATES

Aging Time	Precipitate Radius, μm
1 hour	0.0065
2 hours	0.0098
8 hours	0.0130
12 hours	0.0230
18 hours	0.0195
1 day	0.0200
2 days	0.0230
5 days	0.0350
8 days	0.0465
14 days	0.0510

TABLE 2-9

THE EFFECT OF ISOTHERMAL AGING AT 200°C (392°F) ON THE GROWTH OF A PFZ

Aging Time	PFZ Width, μm
1 hour	0,100
2 hours	0.136
8 hours	0.272
12 hours	0.360
18 hours	0.409
1 day	0.823
2 days	0.409
5 days	0.682
8 days	0.727
14 days	1.273

TABLE 2-10

THE EFFECT OF ARTIFICIAL AGING AT 200°C (392°F)
ON PRECIPITATE SIZE AND PFZ ON MATERIAL
HEATED TO 200°C (392°F) AT 5°C/HR

Time at 200°C	Radius, µm	PFZ, µm
4 hours	0.160	0.0133
8 hours	0.220	0.0154
12 hours	*	0.0193
24 hours	0.364	0.0204
2 weeks	1.111	0.0462

*Not measured.

TABLE 2-11

TENSILE AND NOTCH TENSILE PROPERTIES OF ATC-CAST I/M Al-Li-Zr
COMPARED TO P/M Al-Li ALLOY

Alloy	Solution Heat Treatment Conditions	Aging Condition	Tensile Strength, MPa	(ksi)	Yield Strength, MPa	(ksi)	El.† (%)	Notch Tensile, MPa	(ksi)	NTS/YS
I/M Al-Li-Zr	0.5 hours at 482°C Cold water quenched	24 hours at 200°C	474	(68.8)	433	(62.9)	4.0	533	(77.3)	1.22
I/M Al-Li-Zr	0.5 hours at 593°C Cold water quenched	24 hours at 200°C	463	(67.2)	438	(63.6)	2.0	533	(77.3)	1.22
P/M Al-Li-Zr	0.5 hours at 510°C	24 hours at 200°C	387	(56.1)	301	(43.7)	6.0	231	(33.5)	0.77

†Failed outside gauge.

TABLE 2-12

LONGITUDINAL TENSILE AND NOTCH TENSILE PROPERTIES OF ATC-CAST Al-Li-Zr EXTRUSION
SOLUTION HEAT TREATED AT 552°C, 0.5 HOURS, COLD WATER
QUENCHED, AGED IMMEDIATELY AT 200°C

Aging Time, hrs	Tensile Strength, MPa	(ksi)	Yield Strength, MPa	(ksi)	Elong.† (%)	Notch Tensile, MPa	(ksi)	NTS/YS
1.0	416	(60.3)	347	(50.3)	2.9	476	(69.0)	1.37
2.0	452	(65.6)	423	(61.3)	1.0	508	(73.7)	1.20
4.0	443	(64.3)	401	(58.2)	1.4	558	(81.0)	1.39
8.0	465	(67.4)	436	(63.3)	2.9	534	(77.5)	1.22
12.0	447	(64.8)	430	(62.4)	1.0	539	(78.2)	1.25
24.0	445	(64.6)	387	(56.1)	2.9	501	(72.6)	1.30
48.0	441	(59.6)	328	(47.6)	4.3	486	(70.5)	1.48

†Failed outside gauge marks.

TABLE 2-13

LONGITUDINAL TENSILE AND NOTCH TENSILE PROPERTIES OF ATC-CAST Al-Li-Zr EXTRUSION SOLUTION HEAT TREATED AT 552°C 0.5 HOURS, QUENCHED DIRECTLY TO 200°C, AND AGED AT 200°C

Aging Time, hrs	Tensile Strength, MPa	(ksi)	Yield Strength, MPa	(ksi)	Elong.† (%)	Notch Tensile, MPa	(ksi)	NTS/YS
1.0	427	(62.0)	401	(58.1)	2.0	508	(73.7)	1.27
2.0	432	(62.7)	404	(58.6)	1.0	518	(75.1)	1.28
4.0	457	(66.3)	453	(65.7)	1.0	541	(78.4)	1.19
8.0	456	(66.2)	436	(65.3)	1.5	553	(80.2)	1.27
12.0	464	(67.3)	448	(65.0)	2.5	557	(80.8)	1.24
24.0	459	(66.6)	420	(60.9)	2.0	543	(78.8)	1.29
48.0	443	(64.2)	372	(53.9)	4.0	518	(75.2)	1.39

†Specimens failed either at fillet or outside gauge length.

TABLE 2-14

LONGITUDINAL TENSILE AND NOTCH TENSILE PROPERTIES OF ATC-CAST Al-Li-Zr EXTRUSION
SOLUTION HEAT TREATED AT 552°C 0.5 HOURS, QUENCHED
DIRECTLY TO 225°C AND AGED AT 225°C

Aging Time, hrs	Tensile Strength, MPa	(ksi)	Yield Strength, MPa	(ksi)	Elong.[†] (%)	Notch Tensile, MPa	(ksi)	NTS/YS
0.25	452	(65.5)	425	(61.6)	2.5	551	(79.9)	1.30
0.50	447	(64.9)	393	(57.1)	2.7	541	(78.4)	1.38
1.0	443	(64.3)	411	(59.6)	3.7	538	(78.1)	1.31
2.0	425	(61.6)	376	(54.6)	4.2	507	(73.5)	1.35

†Fractured outside gauge length.

TABLE 2-15

LONGITUDINAL TENSILE AND NOTCH TENSILE PROPERTIES OF ATC-CAST Al-Li-Zr EXTRUSION
SOLUTION HEAT TREATED AT 552°C 0.5 HOURS, QUENCHED
TO 275°C, AGED AT 275°C

Aging Time, min.	Tensile Strength, MPa	(ksi)	Yield Strength, MPa	(ksi)	Elong. (%)	Notch Tensile MPa	(ksi)	NTS/YS
2.5	403	(58.5)	317	(46.0)	6.0	499	(72.4)	1.57
5.0	393	(57.0)	302	(43.8)	6.0	483	(70.1)	1.60
10.0	365	(53.0)	268	(38.9)	9.0	471	(68.3)	1.76
15.0	365	(53.0)	256	(37.1)	10.0	455	(66.0)	1.78

TABLE 2-16

TENSILE AND NOTCH TENSILE PROPERTIES OF VACUUM-CAST
Al-Li-Zr ALLOY SOLUTION HEAT TREATED AT 552°C,
0.5 HOURS COLD WATER QUENCHED, AND AGED
IMMEDIATELY AT 200°C

Aging Time, hrs	Tensile Strength, MPa	(ksi)	Yield Strength, MPa	(ksi)	Elong. in 2.0", %	Notch Tensile, MPa	(ksi)	NTS/YS
0.5	405	(58.8)	355	(51.6)	*	482	(70.0)	1.36
2.0	436	(63.2)	406	(58.9)	*	494	(71.6)	1.22
8.0	465	(67.5)	444	(64.4)	*	529	(76.7)	1.19
12.0	482	(69.9)	454	(65.9)	*	531	(77.0)	1.17
24.0	480	(69.6)	454	(65.8)	2.0	503	(72.9)	1.11
48.0	467	(67.8)	422	(61.2)	*	439	(63.6)	1.04
96.0	459	(66.5)	396	(57.3)	4.0	420	(60.9)	1.06

*Fractured at fillet.

TABLE 2-17

LONGITUDINAL TENSILE AND TEAR PROPERTIES OF Al-Li-Mn SHEET SOLUTION HEAT TREATED
AT 552°C 15 SECONDS, COLD WATER QUENCHED, AND AGED AT 200°C

Aging Time, hrs	Tensile Strength, MPa	(ksi)	Yield Strength, MPa	(ksi)	Elongation, %	Tear Strength, MPa	(ksi)	Unit Prop. Energy, KJ/m²	(In.-PSI)
0.25	312	(45.2)	188	(27.2)	16	339	(49.3)	61.0	(349)
0.50	327	(47.4)	203	(29.5)	12	--	--	--	--
1.0	333	(48.3)	209	(30.3)	12	344	(50.)	41.1	(234)
2.0	359	(52.0)	228	(33.1)	10	--	--	--	--
4.0	367	(53.3)	239	(34.6)	8	329	(47.8)	16.9	(97)
8.0	379	(55.0)	252	(36.5)	7	--	--	--	--
12.0	385	(55.8)	256	(37.1)	8	--	--	--	--
24.0	376	(54.5)	264	(38.3)	5	264	(38.4)	14.3	(81)

TABLE 2-18

LONGITUDINAL TENSILE AND TEAR PROPERTIES OF Al-Li-Mn SHEET SOLUTION HEAT TREATED
AT 552°C 15 SECONDS, DIRECT QUENCHED TO 200°C, AND AGED

Aging Time, hrs	Tensile Strength, MPa	(ksi)	Yield Strength, MPa	(ksi)	Elongation, %	Tear Strength, MPa	(ksi)	Unit Prop. Energy, KJ/m²	(In.-PSI)
0.25	311	(45.1)	190	(27.5)	14	351	(50.9)	61.0	(348)
0.50	330	(47.8)	205	(29.9)	14	--	--	--	--
1.0	334	(48.4)	208	(30.2)	12	348	(50.6)	43.8	(250)
2.0	349	(50.6)	222	(32.2)	10	--	--	--	--
4.0	361	(52.4)	233	(33.8)	9	358	(52.0)	27.3	(156)
8.0	376	(54.5)	248	(35.9)	8	--	--	--	--
12.0	383	(55.6)	256	(37.1)	6	--	--	--	--
24.0	390	(56.6)	261	(37.8)	7	289	(41.9)	11.9	(68)

TABLE 2-19

LONGITUDINAL TENSILE AND TEAR PROPERTIES OF Al-Li-Zr SHEET SOLUTION HEAT TREATED
AT 552°C 15 SECONDS, COLD WATER QUENCHED, AND AGED AT 200°C

Aging Time, hrs	Tensile Strength, MPa	(ksi)	Yield Strength, MPa	(ksi)	Elongation, %	Tear Strength, MPa	(ksi)	Unit Prop. Energy, KJ/m²	(In.-PSI)
0.25	372	(53.9)	324	(47.0)	2	353	(51.3)	11.9	(68)
0.50	374	(54.3)	340	(49.3)	2	--	--	--	--
1.0	392	(56.8)	356	(51.6)	2	360	(52.2)	9.6	(55)
2.0	404	(58.6)	366	(53.1)	2	--	--	--	--
4.0	405	(58.7)	361	(52.4)	2	333	(48.3)	13.7	(78)
8.0	397	(57.6)	347	(50.3)	2	--	--	--	--
12.0	391	(56.7)	347	(50.3)	2	--	--	--	--
24.0	363	(52.7)	296	(43.0)	4	310	(45.0)	10.5	(60)

TABLE 2-20

LONGITUDINAL TENSILE AND TEAR PROPERTIES OF Al-Li-Zr SHEET SOLUTION HEAT TREATED
AT 552°C 0.5 HOURS, COLD WATER QUENCHED, AND AGED AT 200°C

Aging Time, hrs	Tensile Strength, MPa	(ksi)	Yield Strength, MPa	(ksi)	Elongation, %	Tear Strength, MPa	(ksi)	Unit Prop. Energy, KJ/m²	(In.-PSI)
0.25	336	(48.6)	271	(39.3)	2	363	(52.8)	26.6	(152)
0.50	323	(46.8)	267	(38.7)	2	--	--	--	--
1.0	336	(48.8)	264	(38.3)	4	349	(50.7)	16.4	(94)
2.0	381	(55.2)	298	(43.2)	4	--	--	--	--
4.0	374	(54.2)	301	(43.7)	4	335	(48.6)	14.0	(80)
8.0	383	(55.5)	304	(44.1)	4	--	--	--	--
12.0	391	(56.7)	303	(44.0)	4	--	--	--	--
24.0	377	(54.7)	299	(43.3)	4	318	(46.2)	13.6	(78)

TABLE 2-21

TRANSVERSE TEAR PROPERTIES OF Al-Li-Mn AND Al-Li-Zr SHEET SOLUTION HEAT TREATED AT 552°C FOR 15 SECONDS, COLD WATER QUENCHED, AND AGED AT 200°C

Aging Time, hrs	Al-Li-Mn				Al-Li-Zr			
	Tear Strength,		Unit Prop. Energy,		Tear Strength,		Unit Prop. Energy,	
	MPa	(ksi)	KJ/m^2	(In.-PSI)	MPa	(ksi)	KJ/m^2	(In.-PSI)
0.25	337	(48.9)	65.0	(371)	392	(57.0)	22.4	(128)
1.0	358	(52.0)	44.7	(255)	384	(55.7)	35.2	(201)
4.0	348	(50.6)	25.4	(145)	379	(55.1)	13.7	(80)
24.0	293	(42.6)	8.5	(50)	328	47.7	32.5	(185)

TABLE 2-22

FRACTURE TOUGHNESS RESULTS OF THE CONVENTIONAL AND
VACUUM-CAST Al-Li-Zr ALLOYS

Specimen	Orientation of Crack Relative to Extrusion	Yield Strength, MPa	(ksi)	K_Q, MPa$\sqrt{m}$	(ksi$\sqrt{in.}$)
Al-2.84 Li-0.14 Zr (conventionally cast)	Parallel	--	--	19.4	(17.7)
	Perpendicular	448	(65.0)	33.2	(30.2)†
Al-3.6 Li-0.1 Zr (vacuum cast)	Parallel	--	--	*	*
	Perpendicular	414	(60.0)	22.4	(20.4)†

†Crack turned and propagated parallel to applied stress.
*Alloy fractured during fatigue precracking.

TABLE 2-23

HYDROGEN ANALYSIS FOR
Al-Li ALLOYS

| Alloy	ml/100 grams*
454103 (Al-Li-Mn)	2.24
454104 (Al-Li-Zr, conventionally cast)	2.71
454387 (Al-Li-Zr, vacuum cast)	2.12

*ml of hydrogen/100 grams of metal.

TABLE 2-24

MONOTONIC AND STRAIN CONTROL FATIGUE PARAMETERS FOR Al-Li-Mn AND Al-Li-Zr EXTRUSIONS

	Al-Li-Mn		Al-Li-Zr	
	4 Hours @ 200°C	24 Hours @ 200°C	4 Hours @ 200°C	24 Hours @ 200°C
ε_f	6%	5%	3%	3%
σ_y	188 mPa	232 mPa	424 mPa	422 mPa
ε'_f	4.5%	4.5%	3%	6%
C	-0.64	-0.90	-0.66	-0.58

TABLE 2-25

ELASTIC MODULUS OF CONVENTIONALLY CAST AND EXTRUDED
Al-Li-Zr ALLOY
(SHT 552°C, 0.5 HRS, CWQ, AND AGED IMMEDIATELY @ 200°C)

Aging Time, hrs	Modulus of Elasticity, GPa	ksix10^3
1	81.5	11.82
2	81.5	11.82
4	81.5	11.82
8	81.0	11.75
12	81.0	11.75
24	80.5	11.68
48	79.5	11.53
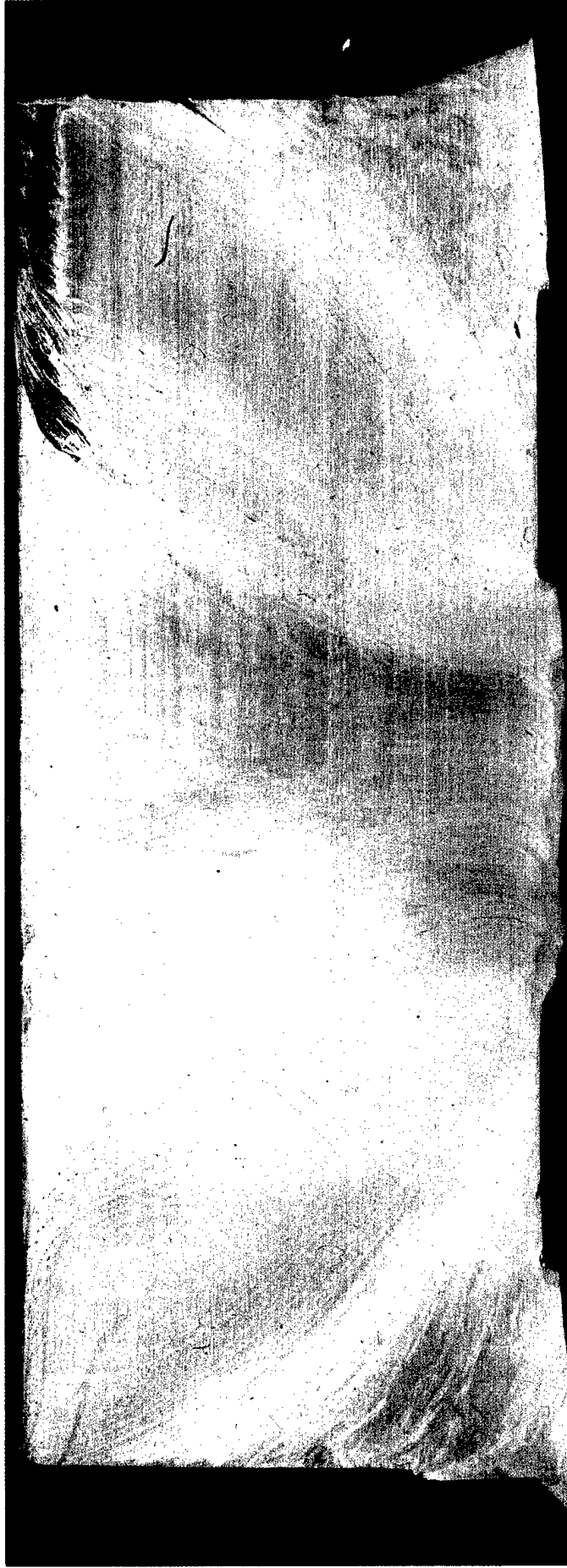
2.5 cm

Figure 2-1. Longitudinal Section, Macroetched, of the Butt
End of the Conventionally Cast Al-Li-Mn Alloy.

2.5cm

Figure 2-2.   Longitudinal Section, Macroetched, of the Butt
End of the Conventionally Cast Al-Li-Zr Alloy.
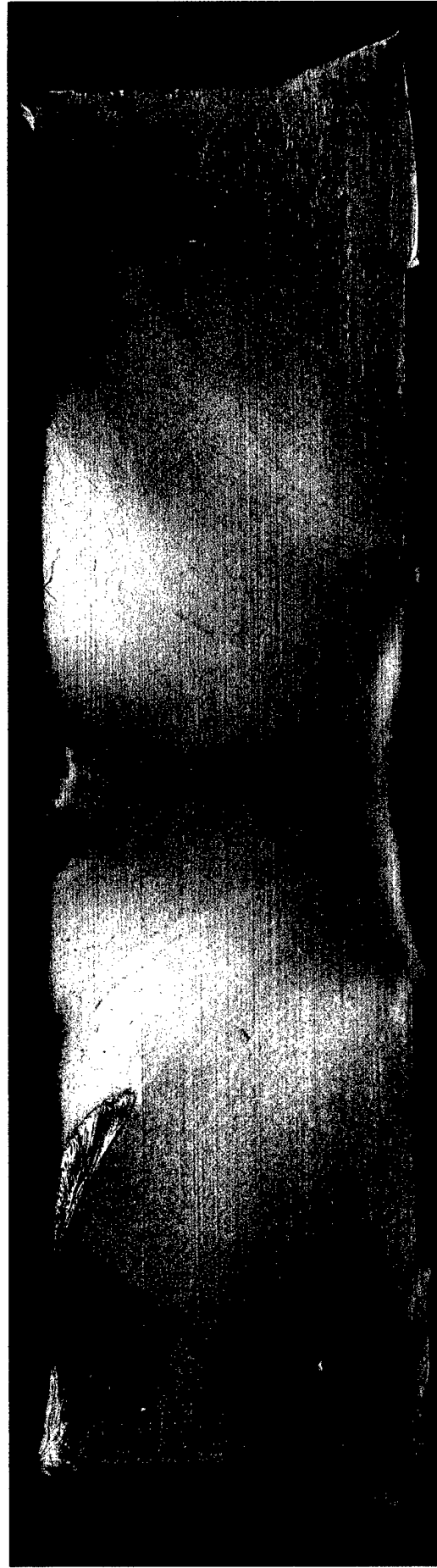
2.5 cm

Figure 2-3. Longitudinal Section, Macroeteched, of the Butt
End of the Al-Li Powder Alloy.
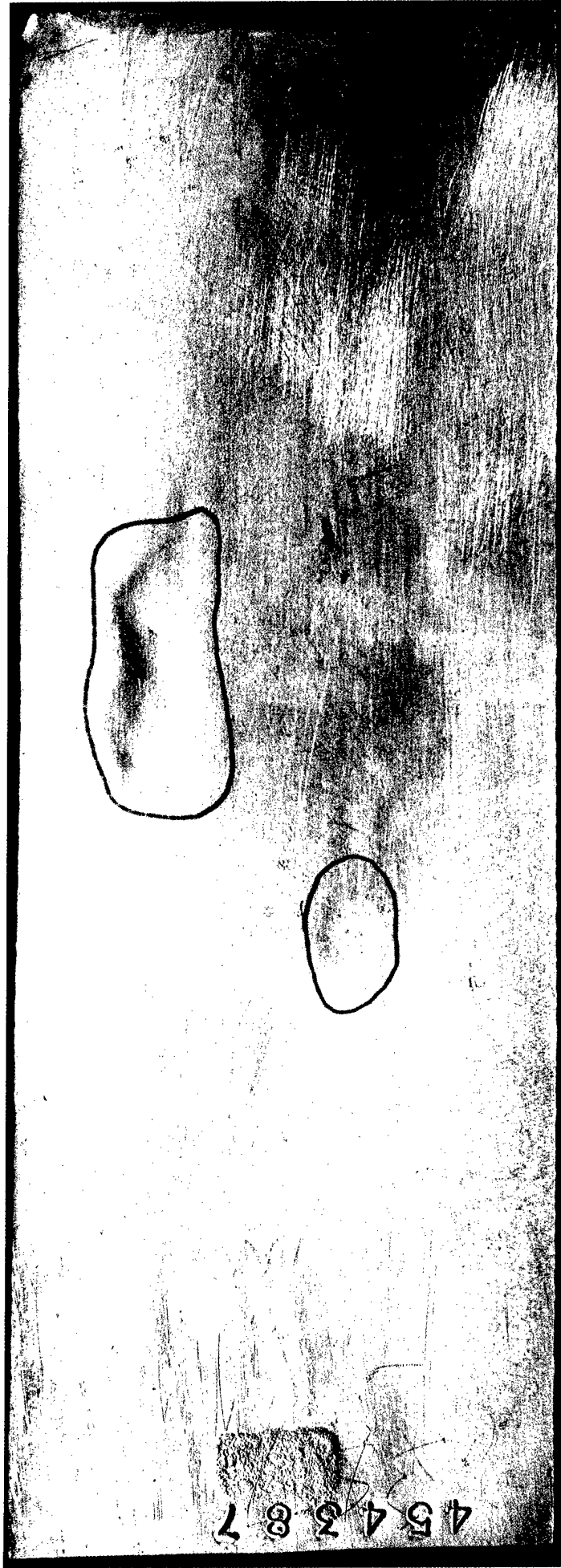
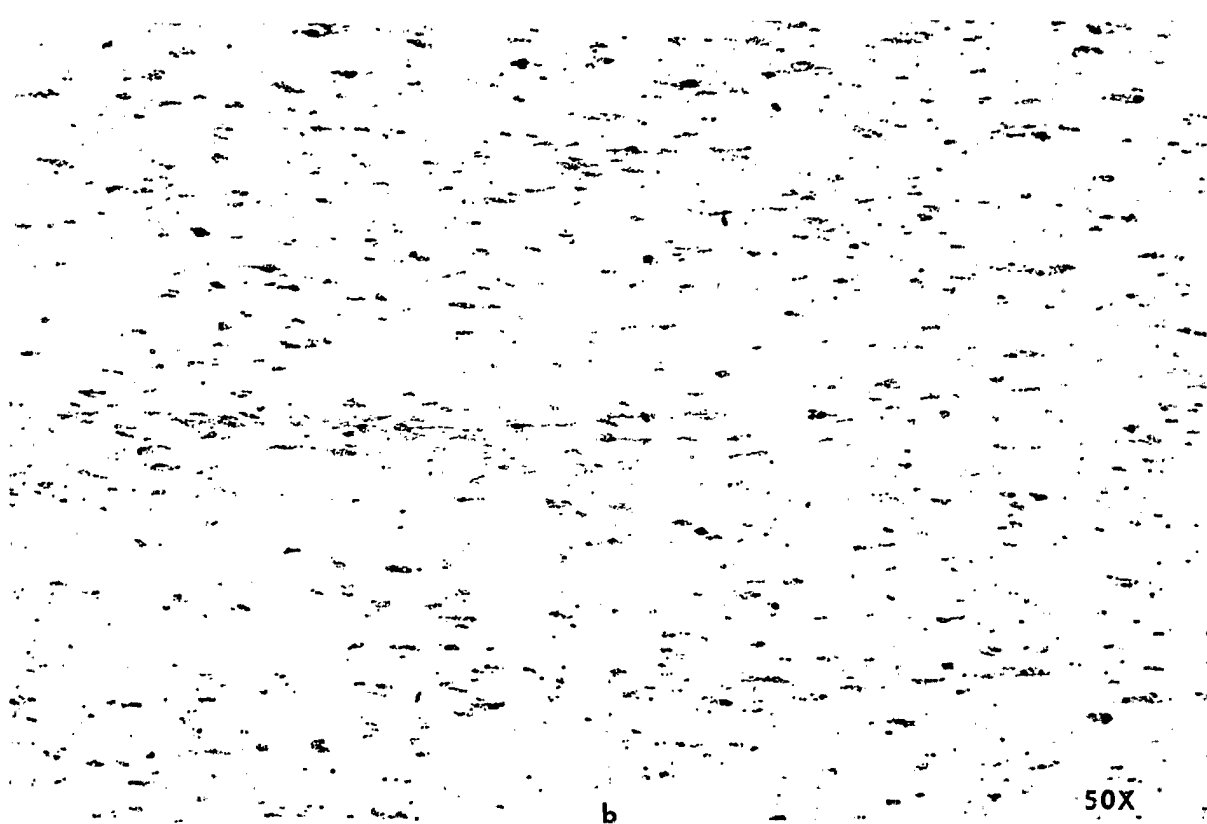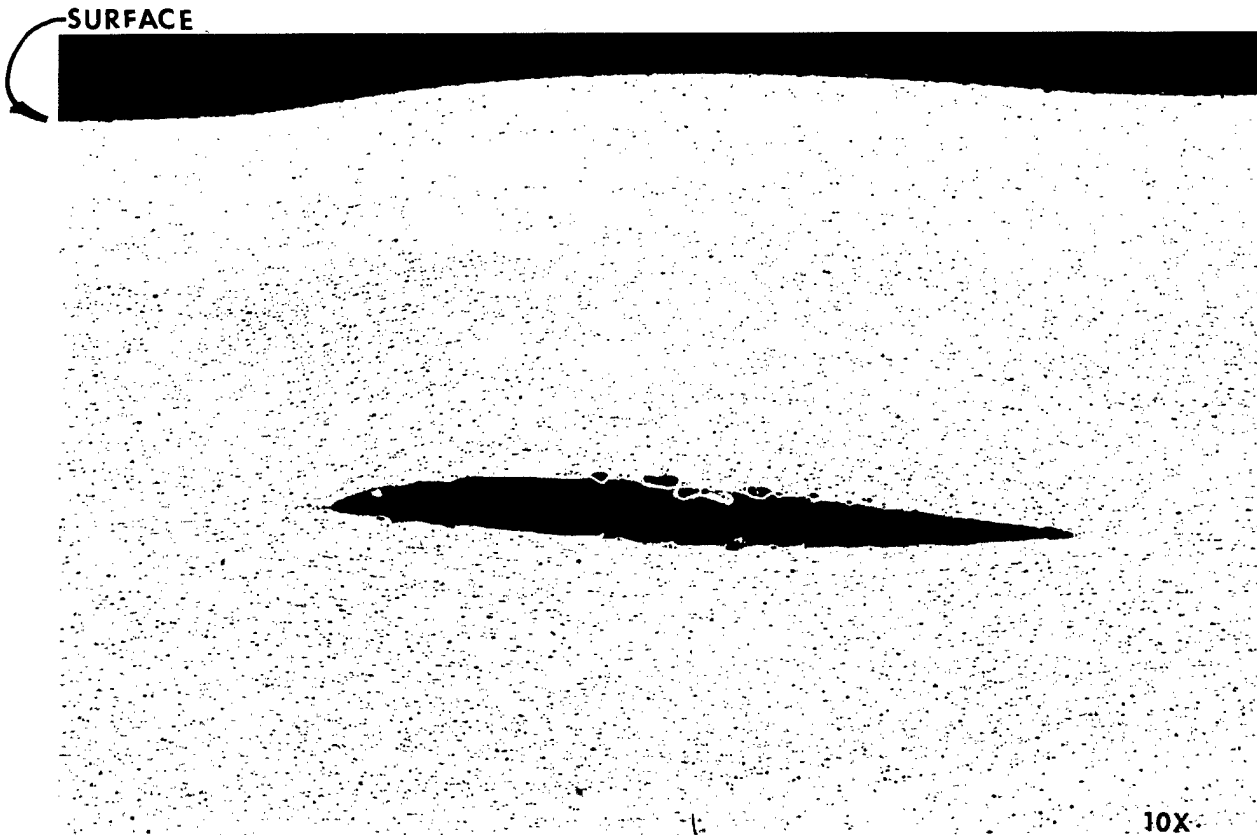Figure 2-4. Macrophotograph Showing the Blisters in the Vacuum Cast Al-Li-Zr Alloy After Upsetting and Liquid Metal Annealing.
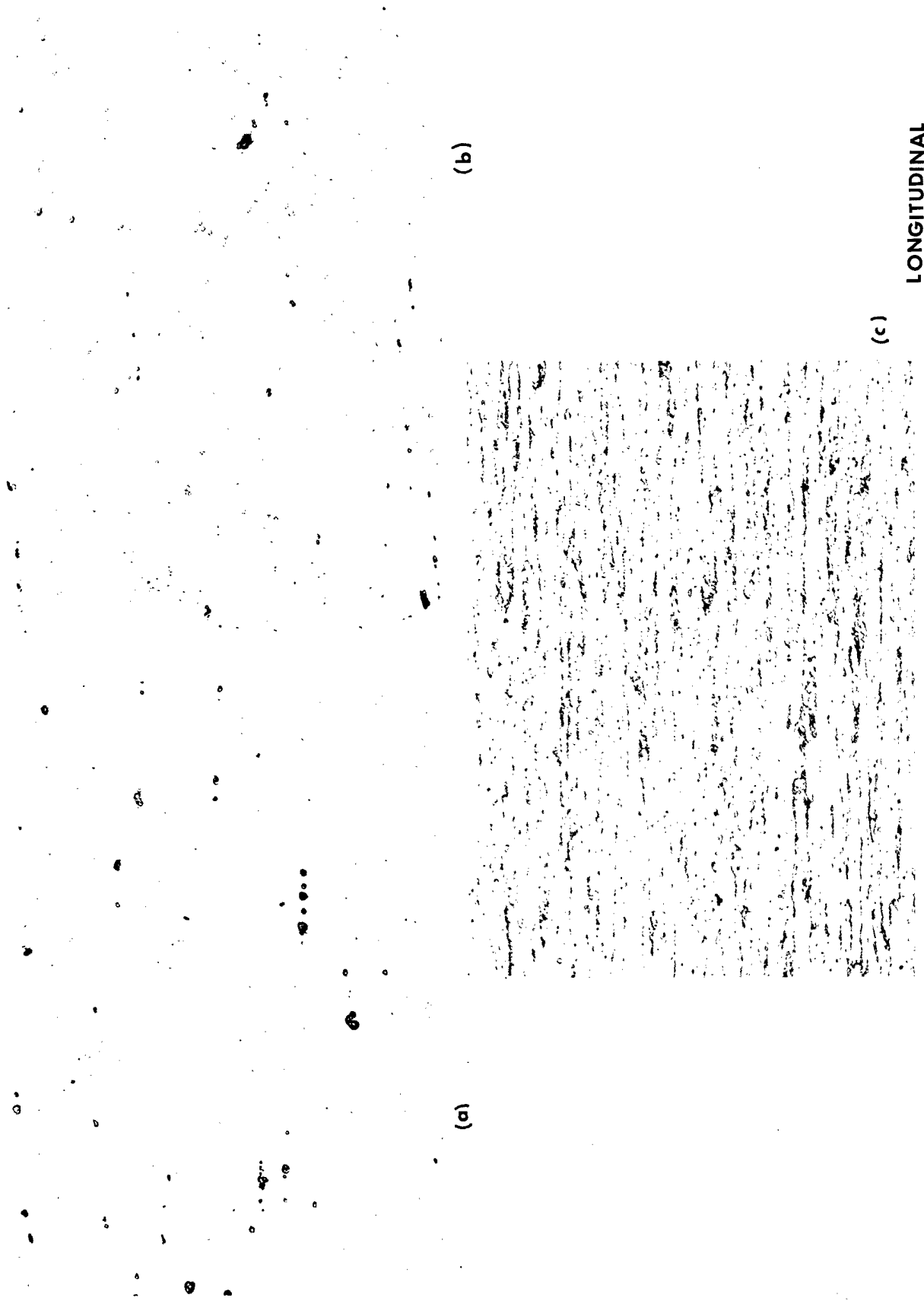
SURFACE

10X

a

50X

b

Figure 2-5. (a) Macrograph Showing a Transverse Section Through a Large Blister. (b) As-polished Micrograph in the Vicinity of the Large Blister in (a). The small black areas are fine porosity.

NOTCH TENSILE SPECIMEN

NOTE: TO OBTAIN SHORT-TRANSVERSE SPECIMENS,
THE OVERALL LENGTH MAY BE REDUCED BY
SHORTENING THE REDUCED SECTION

Figure 2-6. Notch Tensile Specimen Geometry.

Figure 2-7. Photomicrographs of As-polished Extrusion
Sections: (a) Conventionally Cast Al-Li-Mn,
(b) Conventionally cast Al-Li-Zr, and (c)
Al-Li-Powder Showing the Relative Size and
Amount of Insoluble Phases in the Heat
Treated Materials. (500X)

Figure 2-8. Al-Li-Mn Solution Heat Treated at 552°C (1025°F), Cold Water Quenched, Electropolished (EP), and Photographed Using Polarized Light (PL). Coarse, recrystallized grains were observed. (100X)

Figure 2-9.   Conventionally Cast Al-Li-Zr Solution Heat Treated at 552°C (1025°F), Cold Water Quenched, EP, and Photographed Using PL. The structure is un- recrystallized. (100X)
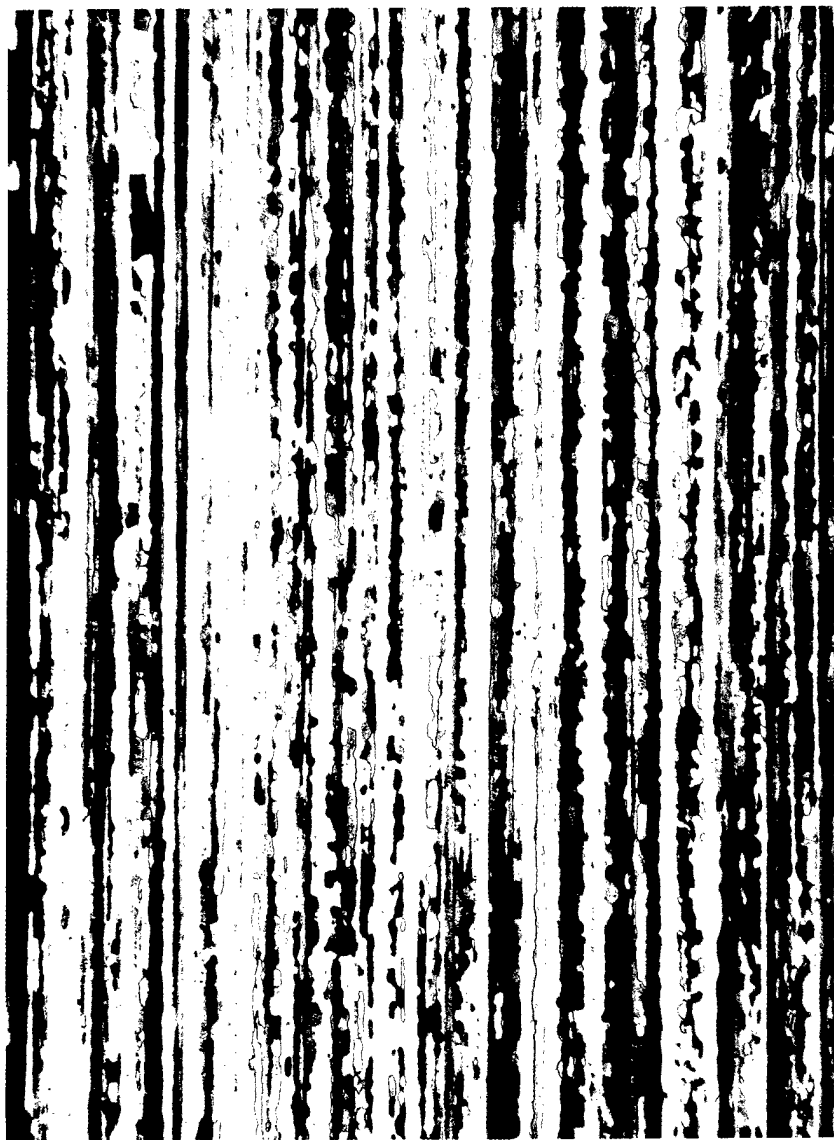
Figure 2-10. Conventionally Cast Al-Li-Zr Solution Heat Treated
at 593°C (1100°F), EP, and Photographed Using
PL. Partial recrystallization is evident. (100X)
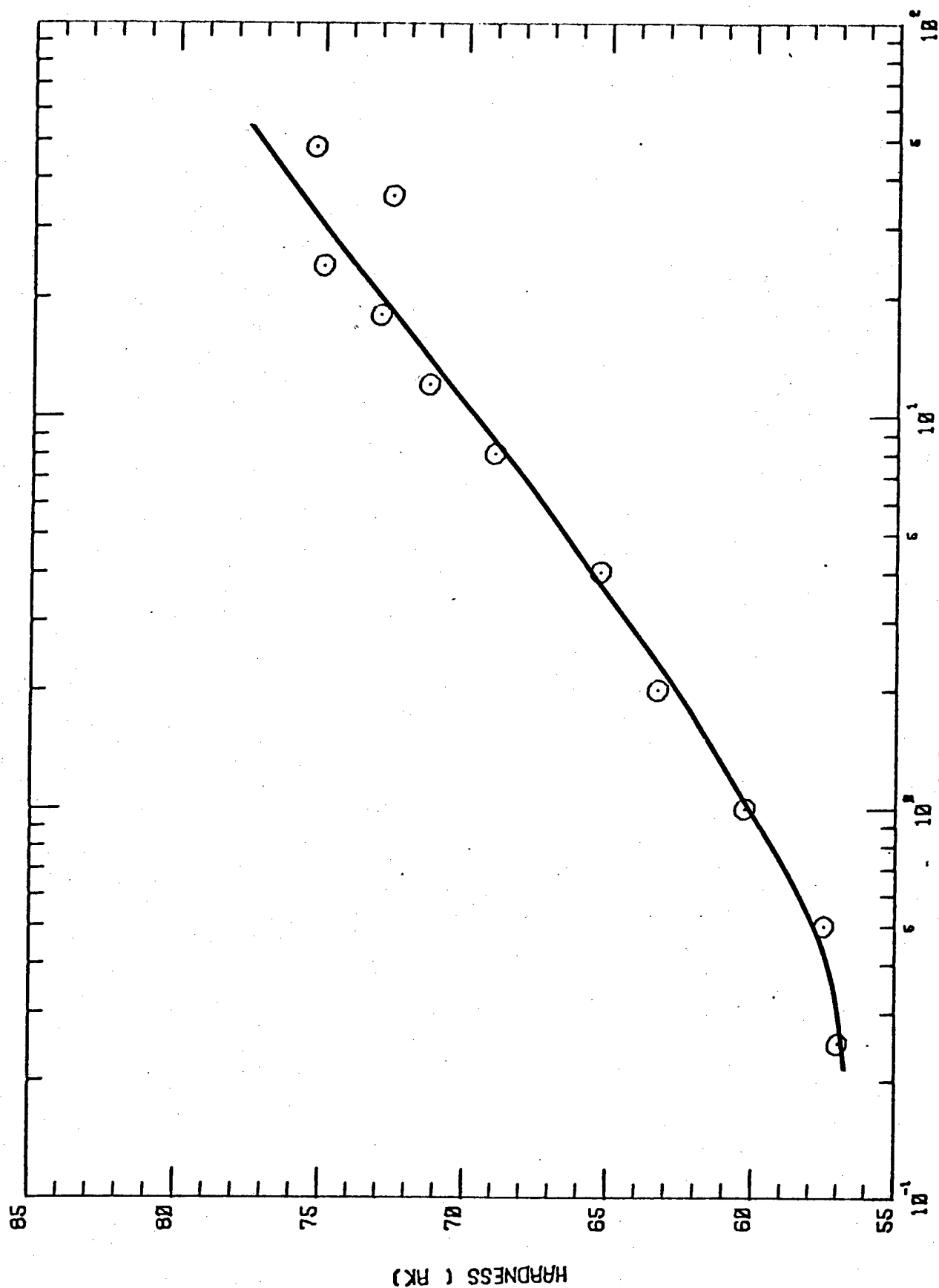
Figure 2-11. Hardness Response of Conventionally Cast
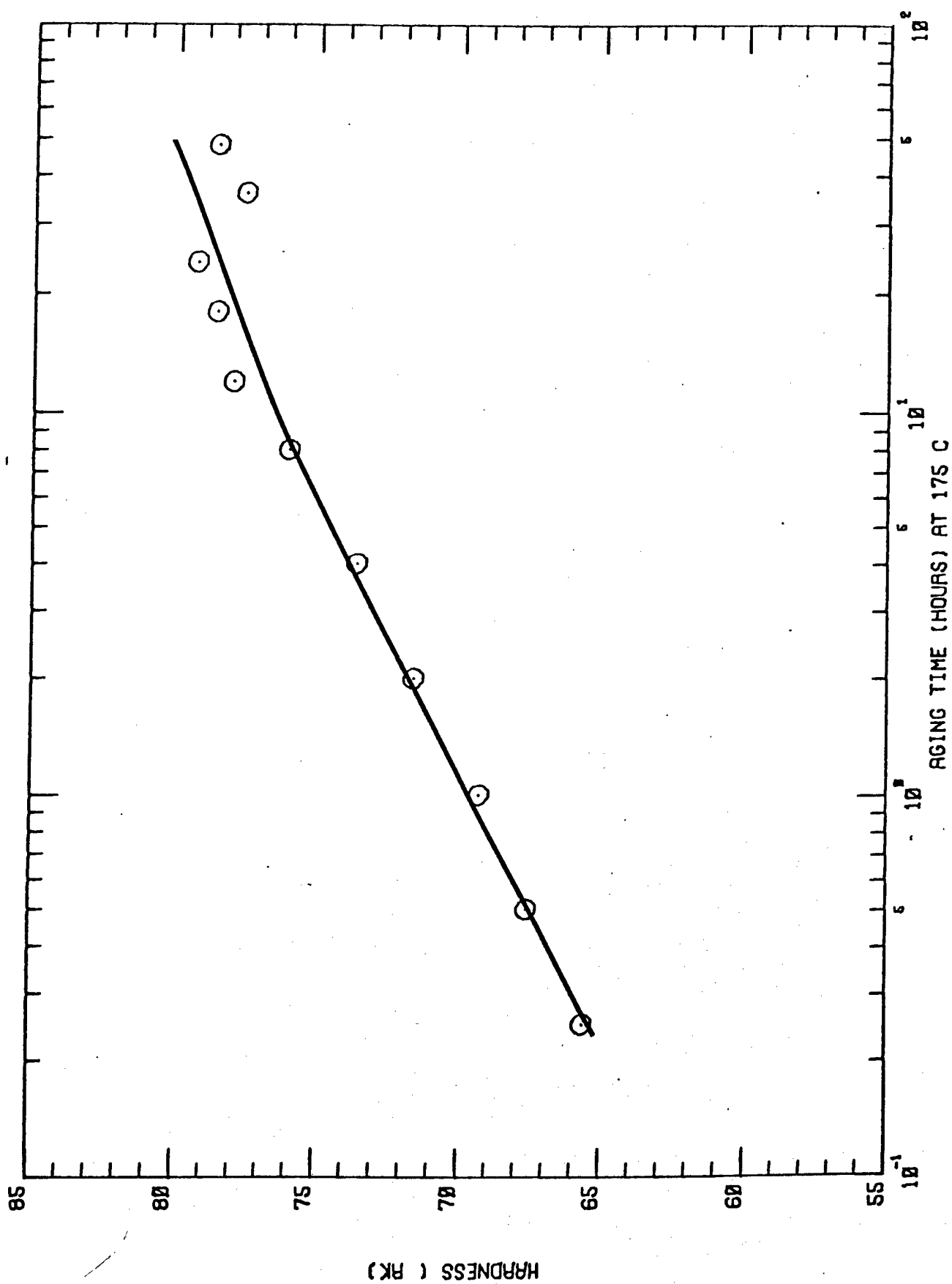Al-Li-Zr Unrecrystallized Extrusion Aged at
150°C.

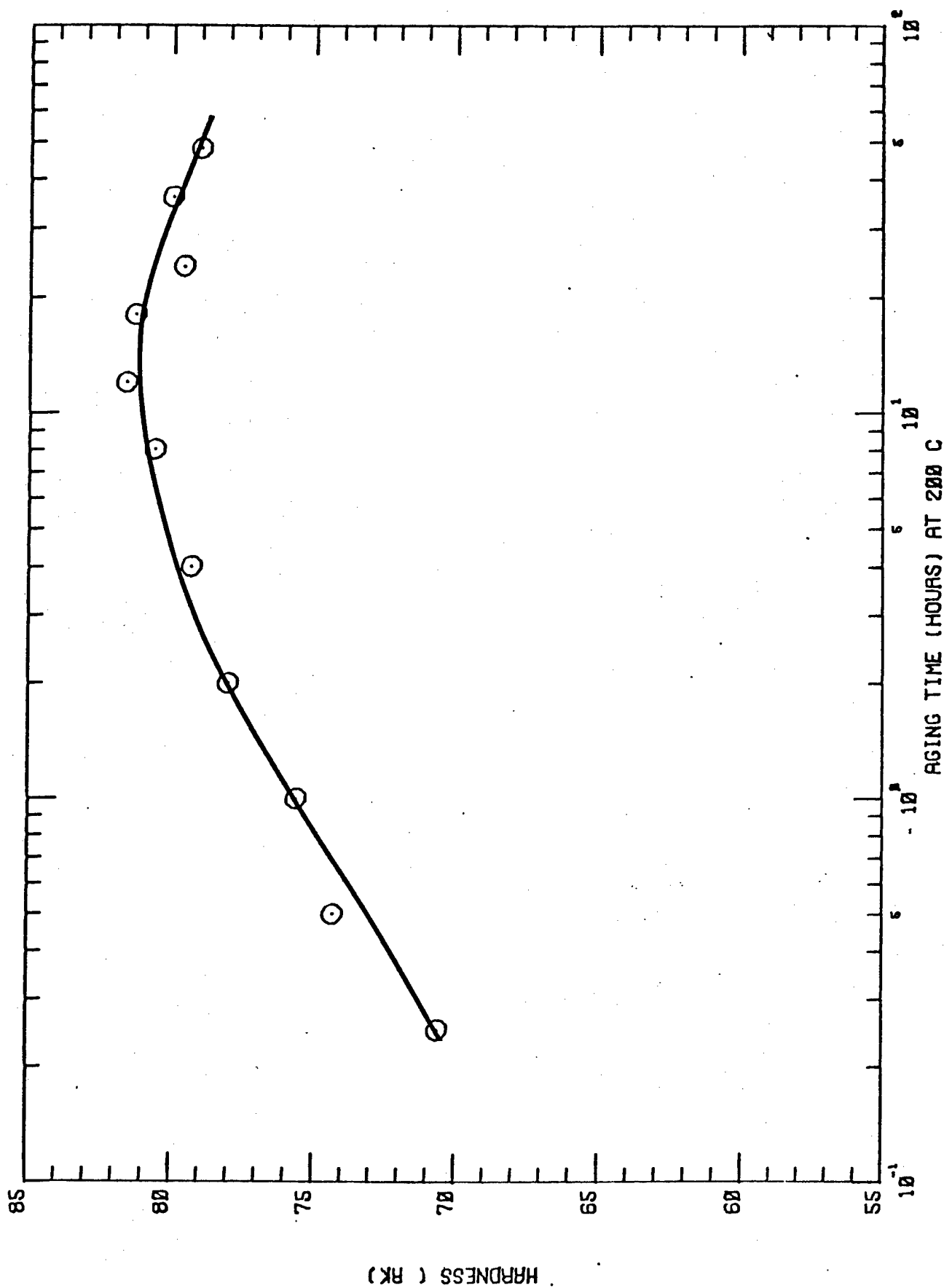Figure 2-12. Hardness Response of Conventionally Cast Al-Li-Zr Unrecrystallized Extrusion Aged at 175°C.

Figure 2-13. Hardness Response of Conventionally Cast Al-Li-Zr Unrecrystallized Extrusion Aged at 200°C.
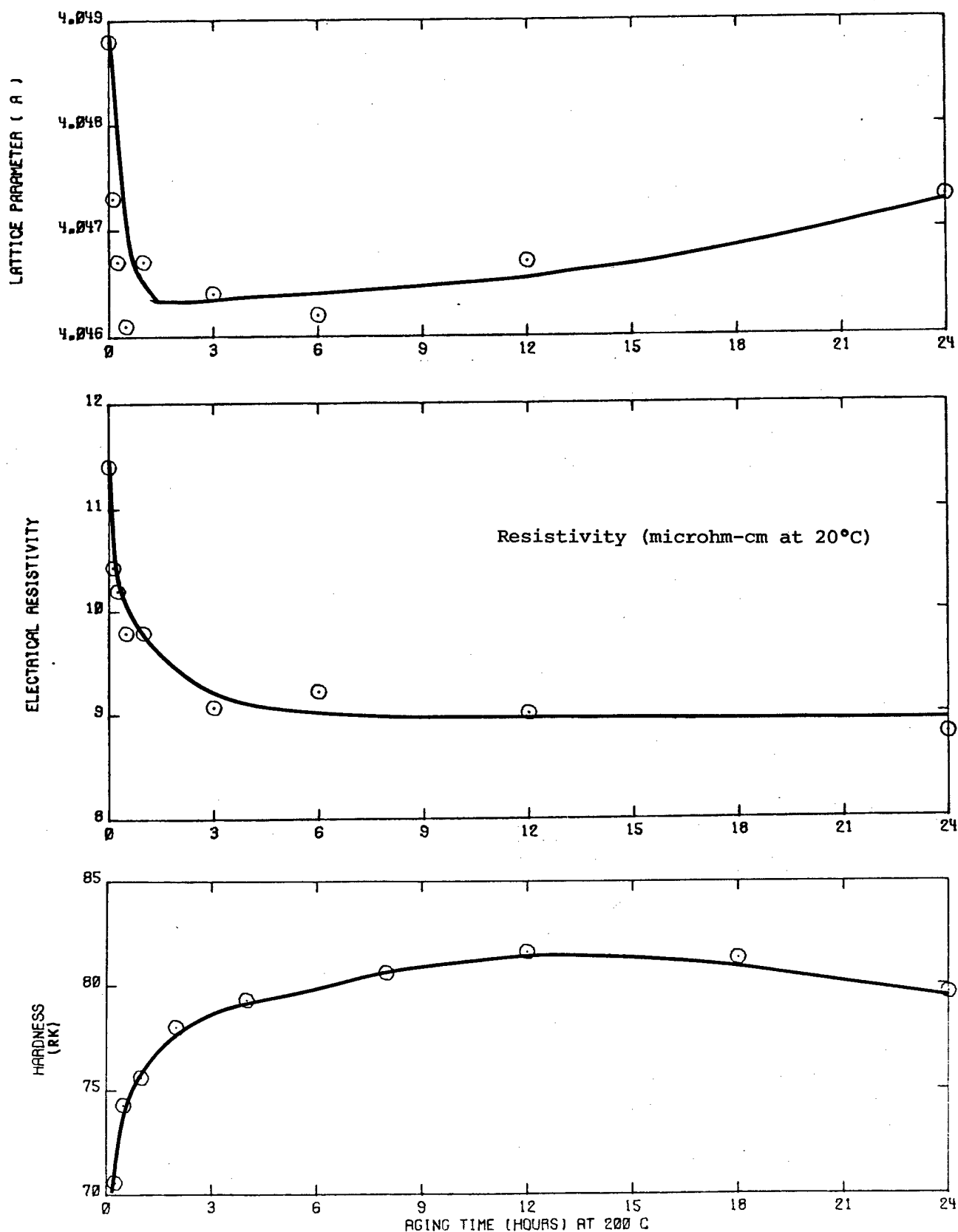
Figure 2-14.   Changes in Lattice Parameters, Electrical
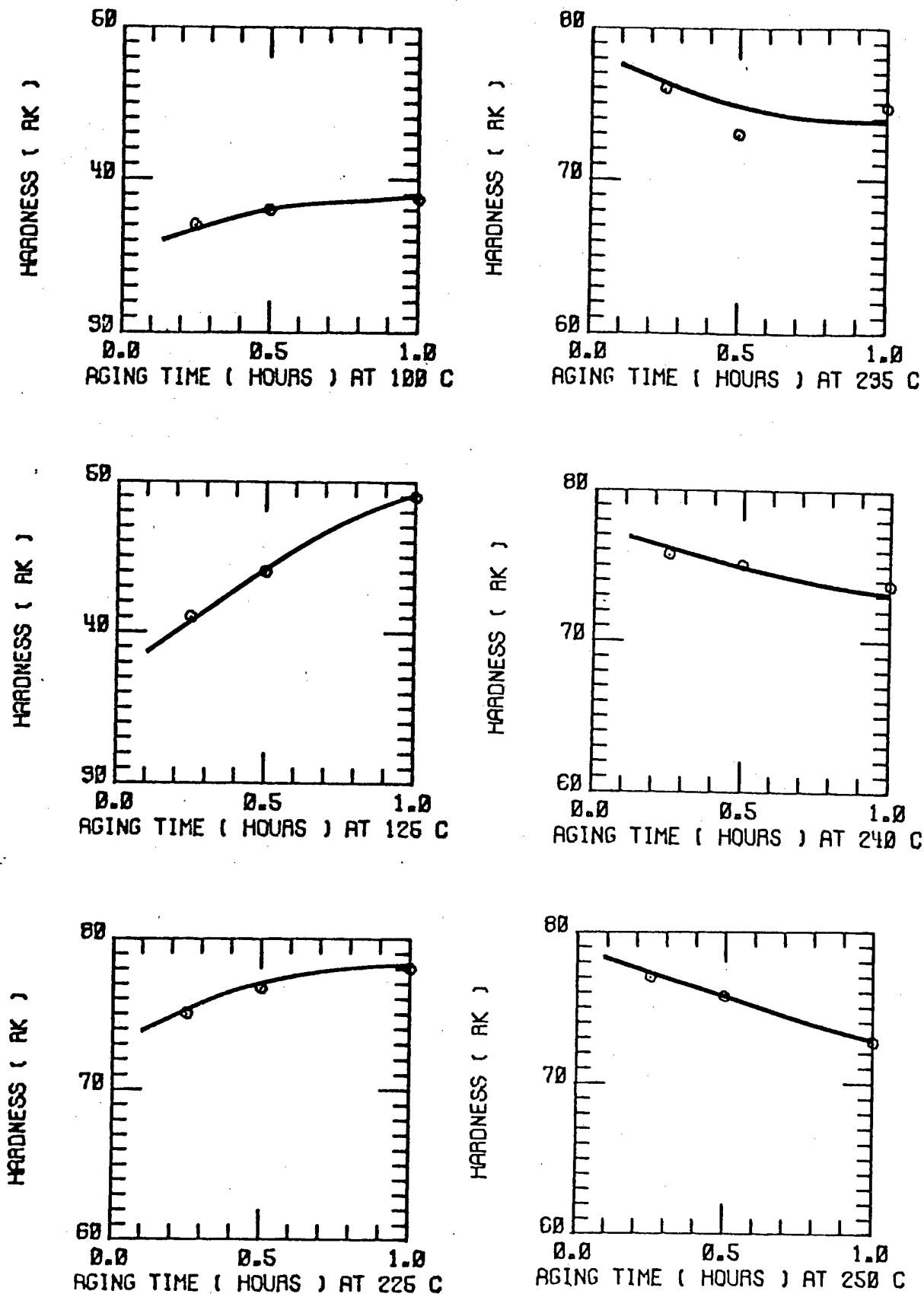Resistivity, and Hardness with Artificial
Aging at 200°C.

Figure 2-15.   Short-Time Hardness Responses of Conventionally
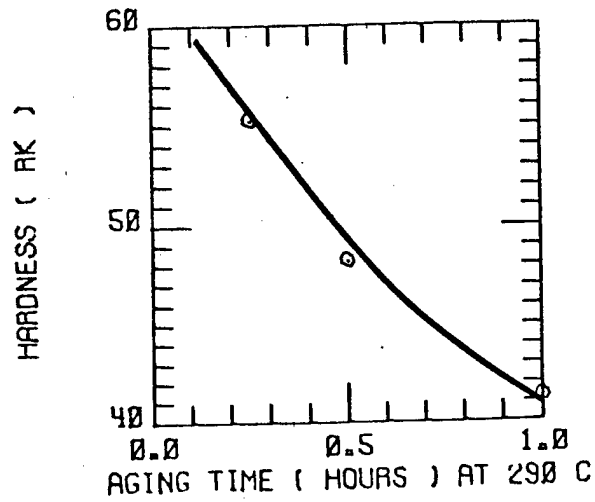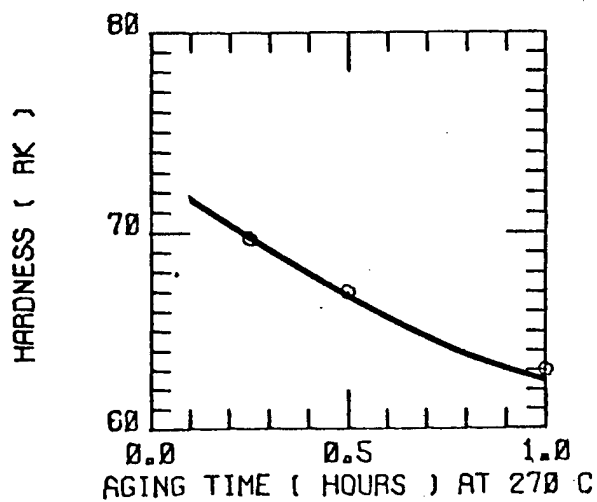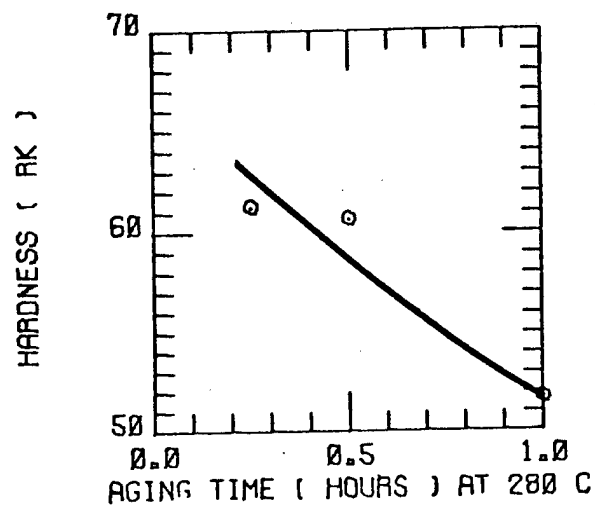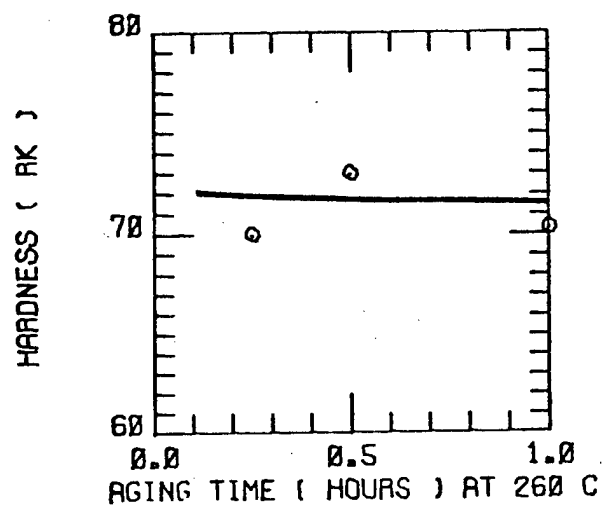Cast Al-Li-Zr Alloy Aged at Various Temperatures.

Figure 2-15 continued

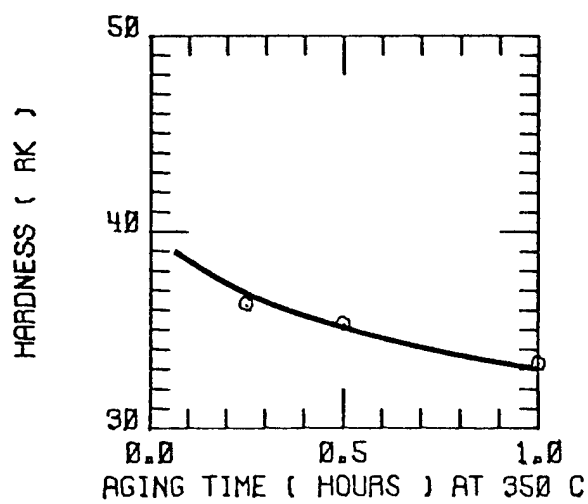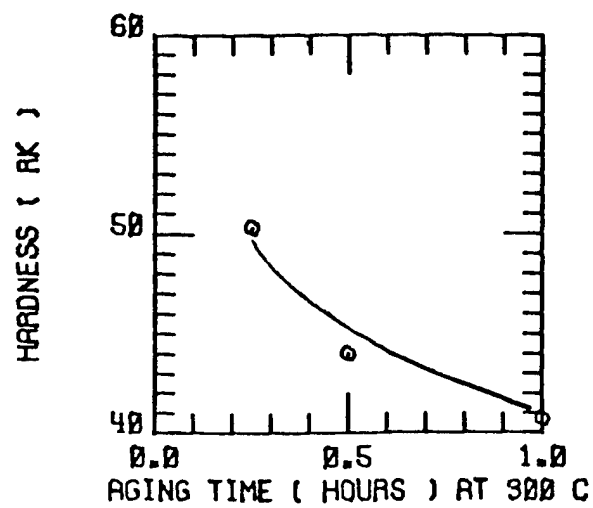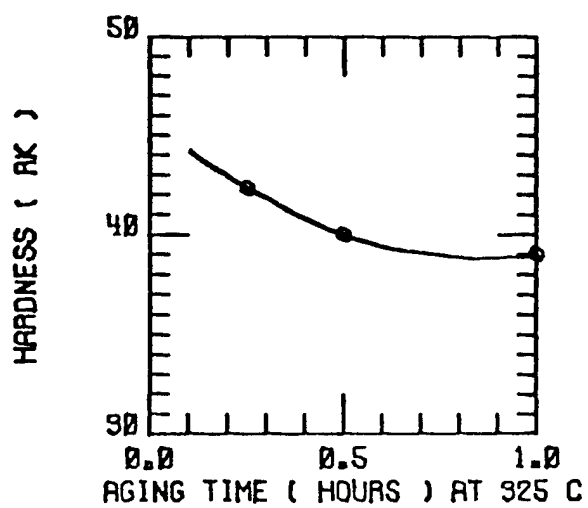Figure 2-15 continued
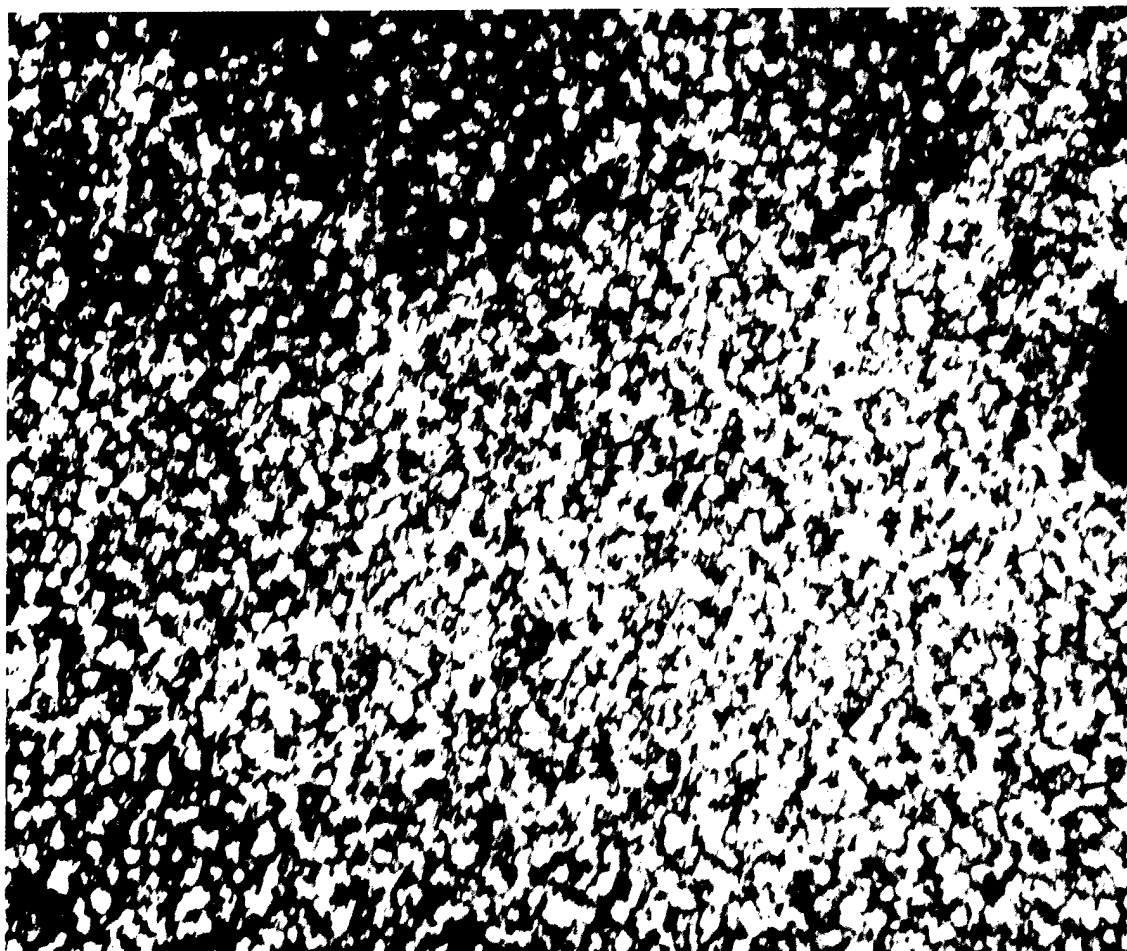
0.1 μm

Figure 2-16. Central Dark Field (CDF) Image of (100) Al₃Li
Reflection in Peak Aged Al-Li-Zr Alloy.
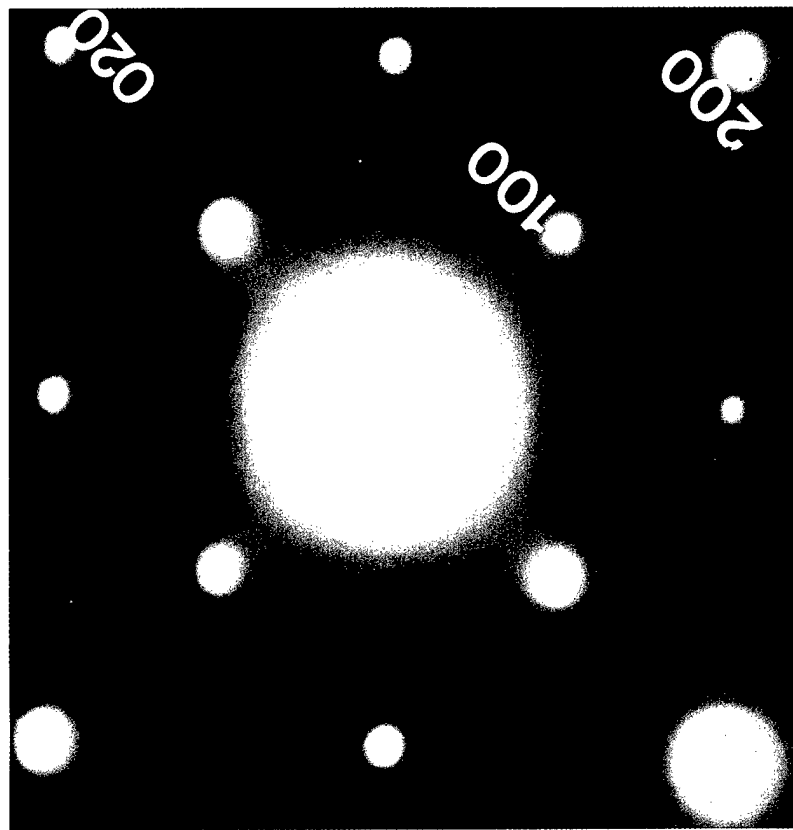
Figure 2-17.   Selected Area Diffraction (SAD) Pattern Showing
the Indexed Matrix and Precipitate Reflections.
The precipitate reflections are indexed on a
cube/cube orientation relationship with respect
to the matrix.

Figure 2-18. Recovered Structure of Al-Li-Zr Alloy.
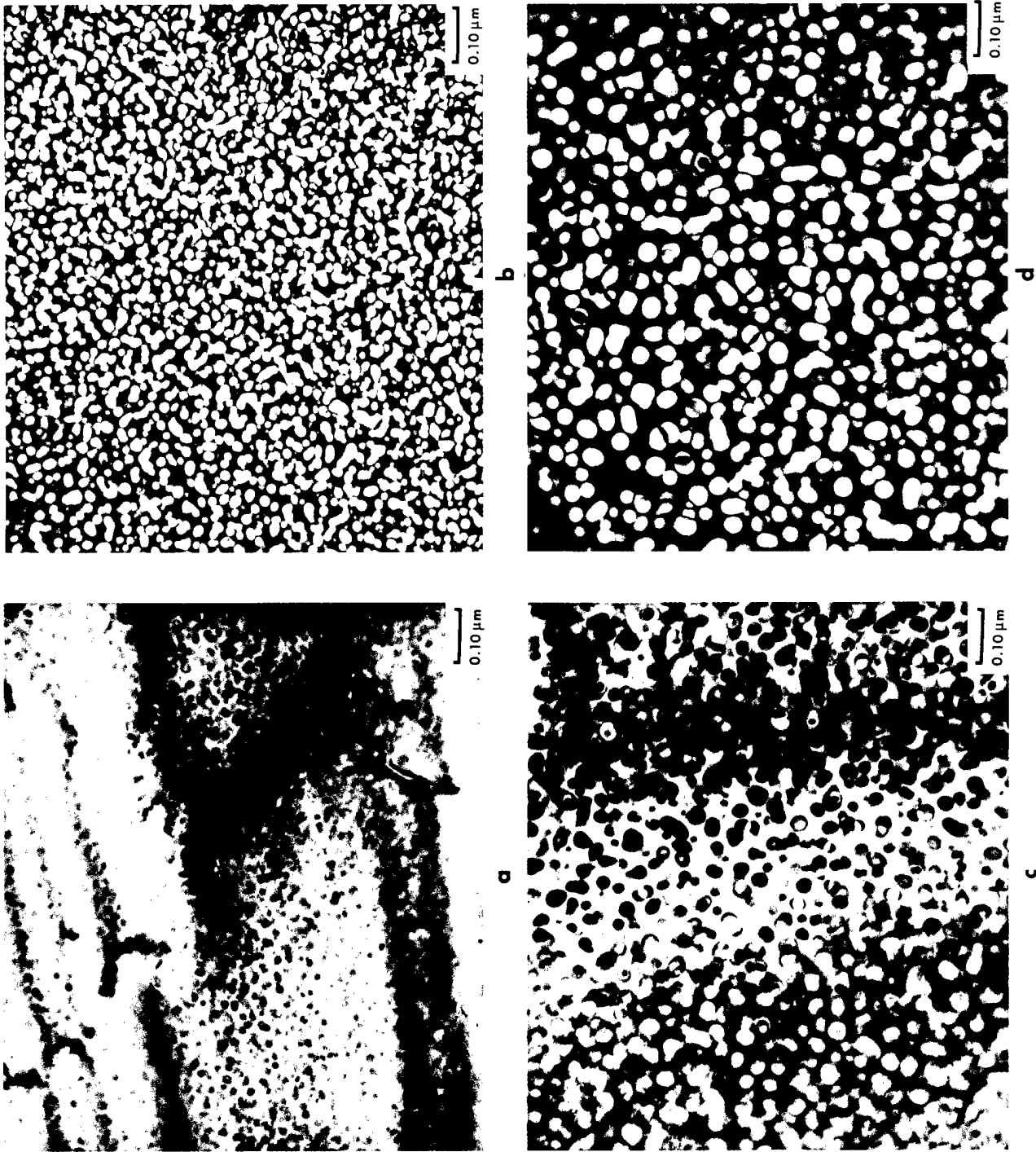
Figure 2-19. TEM's Showing the Morphology of δ' as a Function of Isothermal Aging Time at 200°C in Al-Li-Mn Sheet (a) 18 hours, (b) 24 hours, (c) 48 hours, and (d) 120 hours.
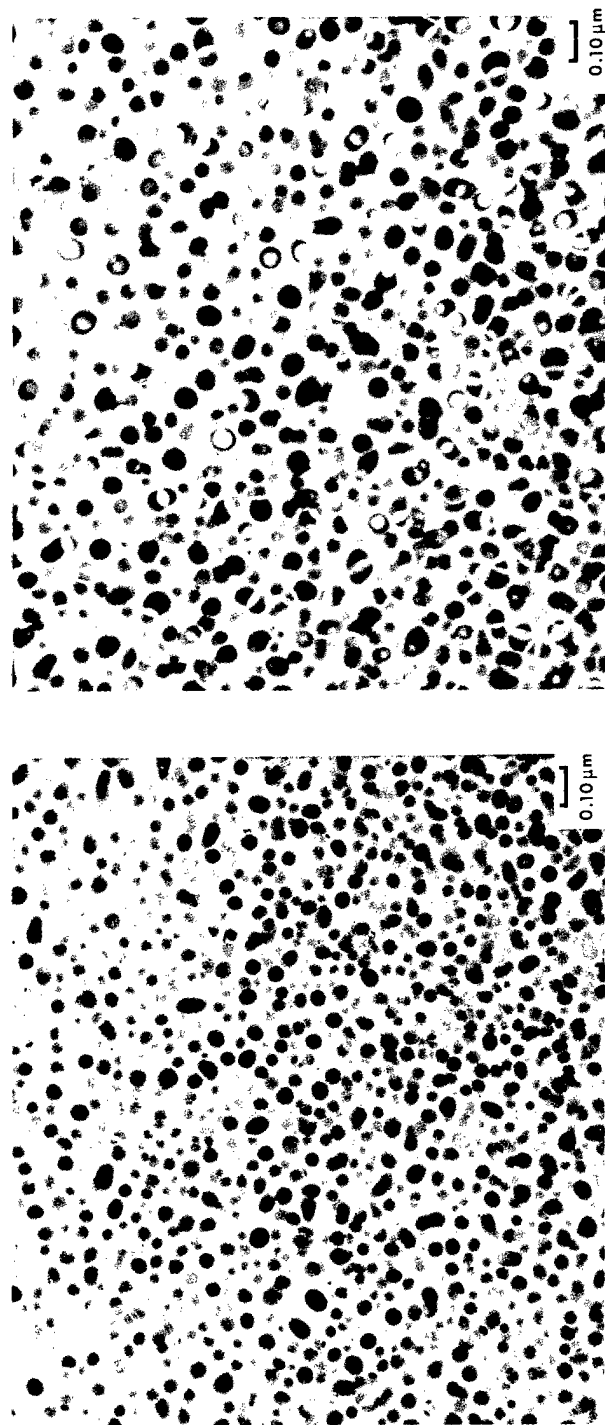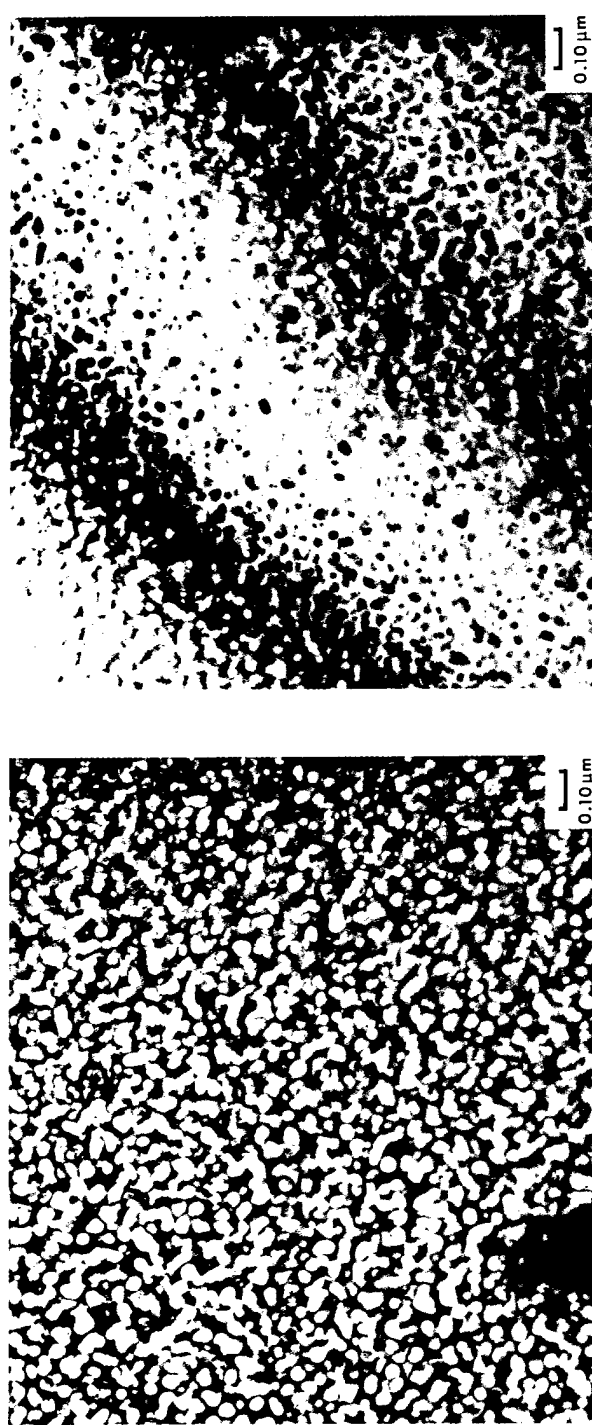
Figure 2-20. TEM's Showing the Morphology of δ' as a Function of Isothermal Aging Time at 200°C in Al-Li-Mn Sheet (a) .75 day, (b) 1 day, (c) 2 days, and (d) 5 days.
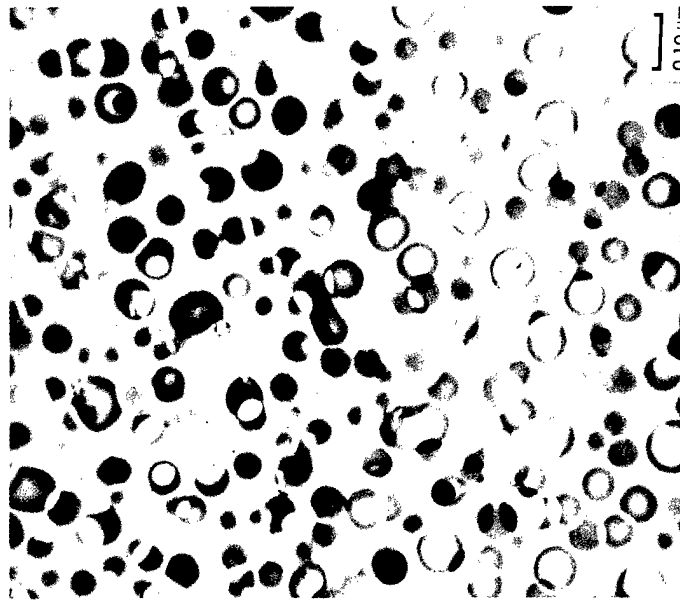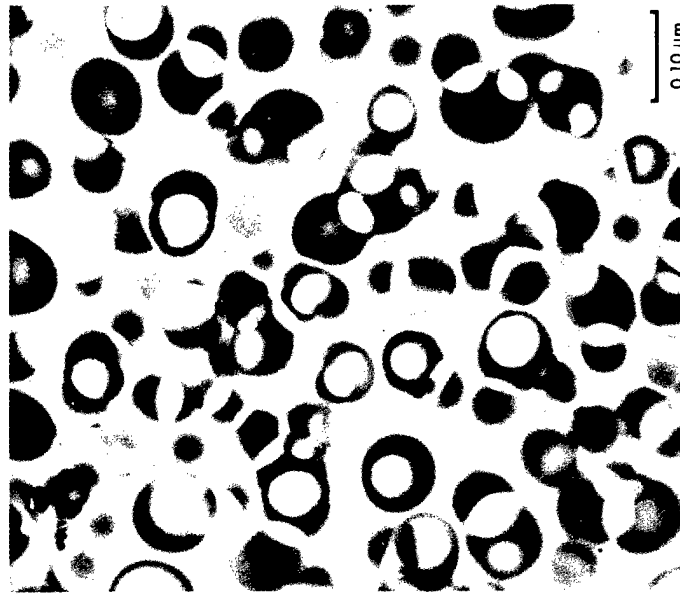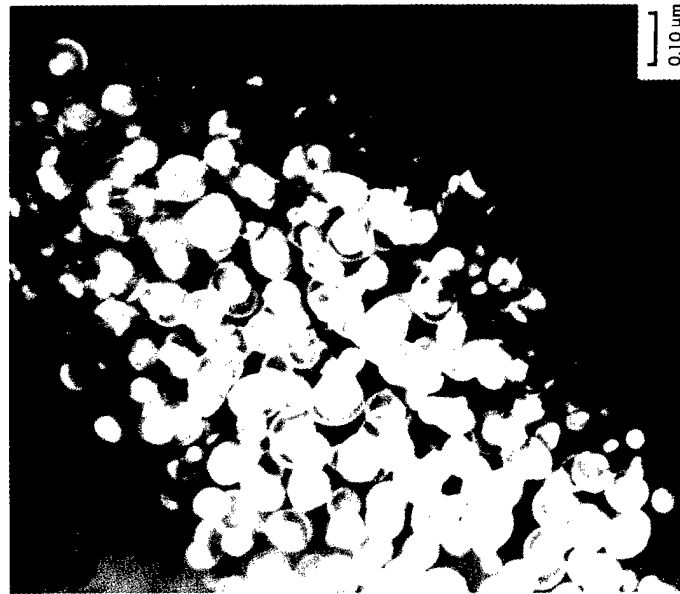
Figure 2-21.   TEM's Showing the Morphology of δ′ in Al-Li-Mn Sheet Isothermally Aged at 200°C for Two weeks.
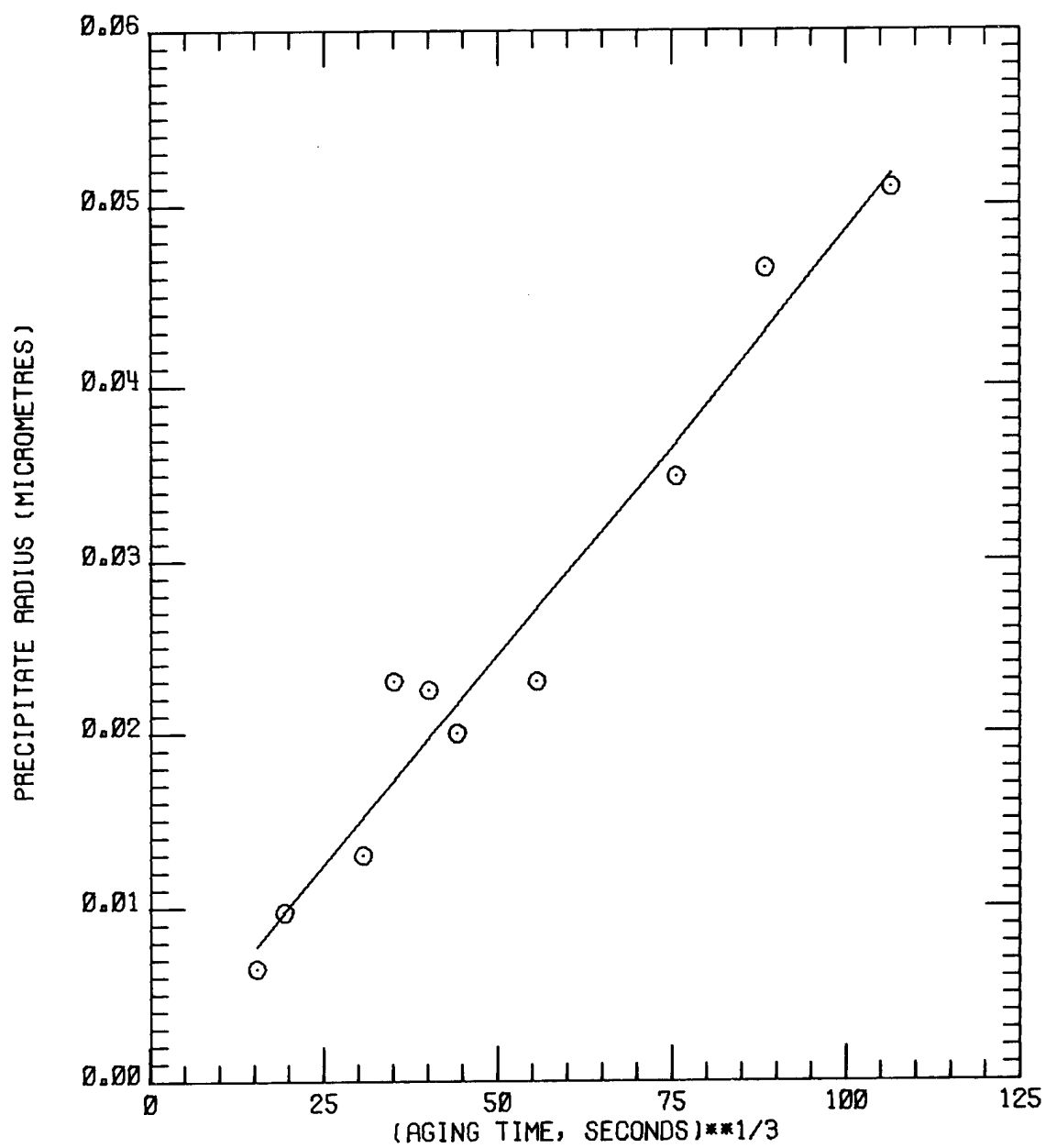
Figure 2-22.   Average Precipitate Radius as a Function of the
               Cube Root of Isothermal Aging Time at 200°C.

Figure 2-23. Matrix and Grain Boundary Area in Al-Li-Mn Sheet Naturally Aged for 1 Week. Uniform precipitation of δ´ up to the grain boundary with no coarse precipitates in the grain boundary area can be seen.
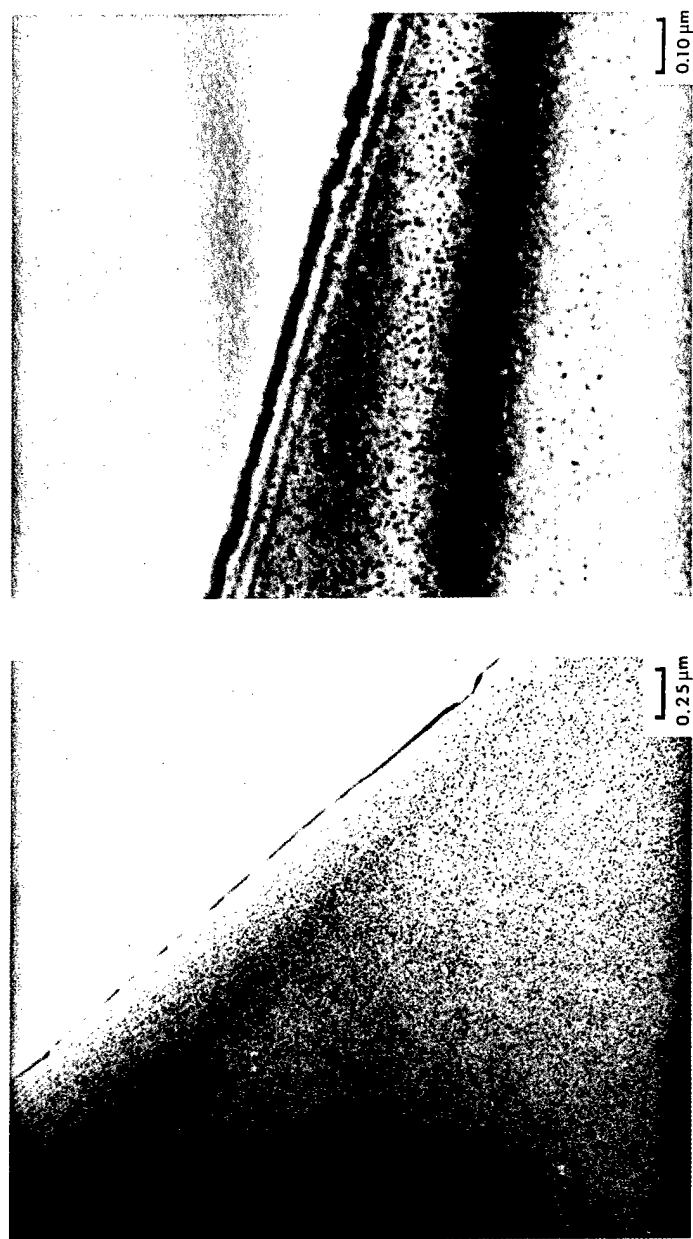
Figure 2-24. Matrix and Grain Boundary Area in Al-Li-Mn Sheet
Naturally Aged for 1 Week. Uniform precipitation
of δ´ up to the grain boundary with no coarse
precipitates in the grain boundary area can be
seen.

Figure 2-25. Triple Point in Al-Li-Mn Sheet Isothermally Aged for 1 Hour at 200°C. Note the presence of a narrow PFZ.
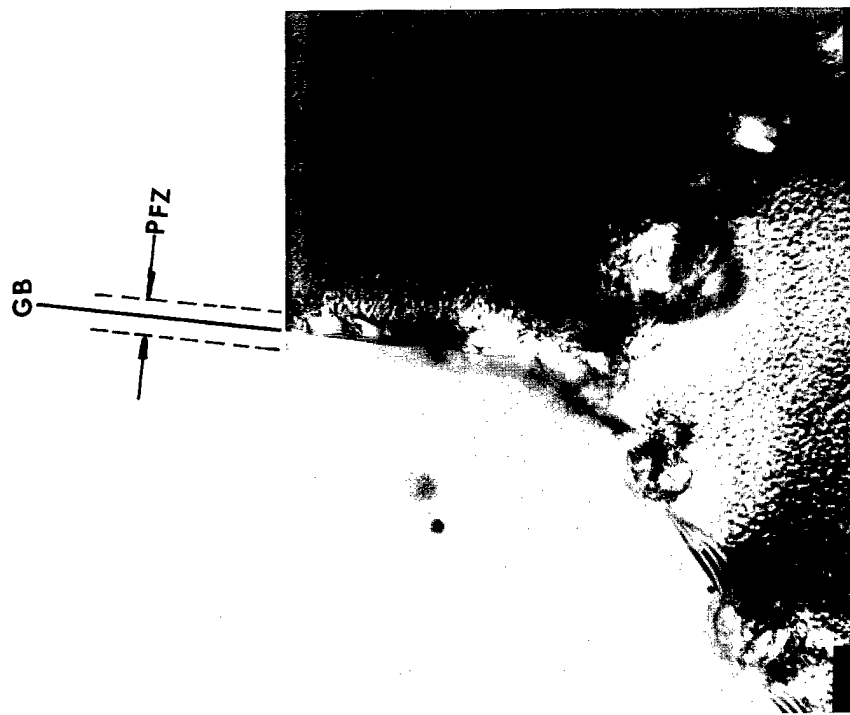
0.5 μm

Figure 2-26.   Grain Boundray Regions in Al-Li-Mn Sheet Iso-
thermally Aged for 8 Hours at 200°C. Note the
increased width of the PFZ as compared with
Figure 2-25. Also, numerous precipitates can
be seen in the grain boundary regions.
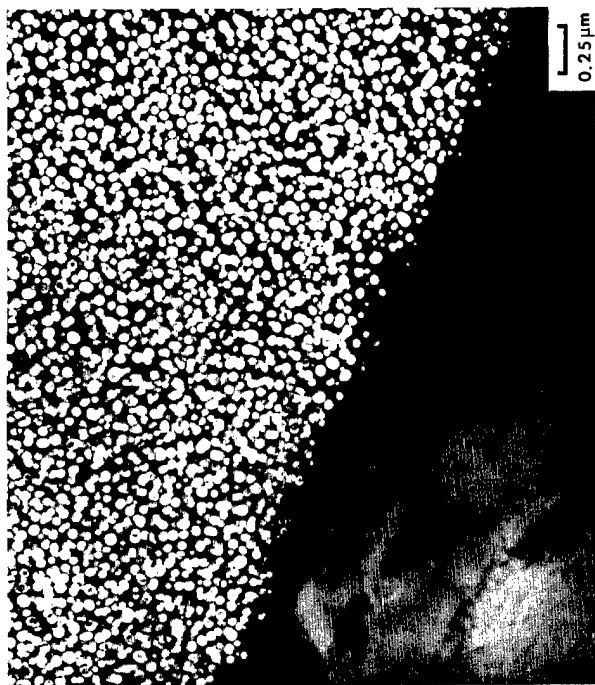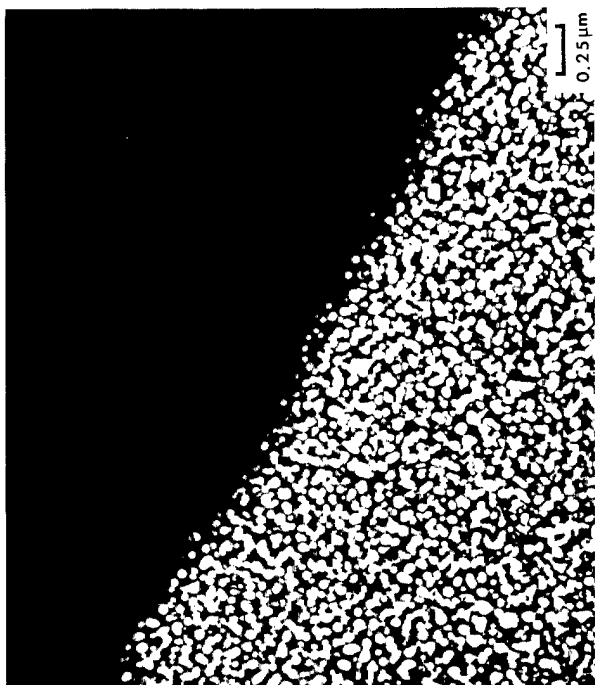
Figure 2-27. A Series of TEM's Using Different Orientations and Imaging Conditions Showing the Very Large PFZ after 5 Days of Isothermal Aging at 200°C.
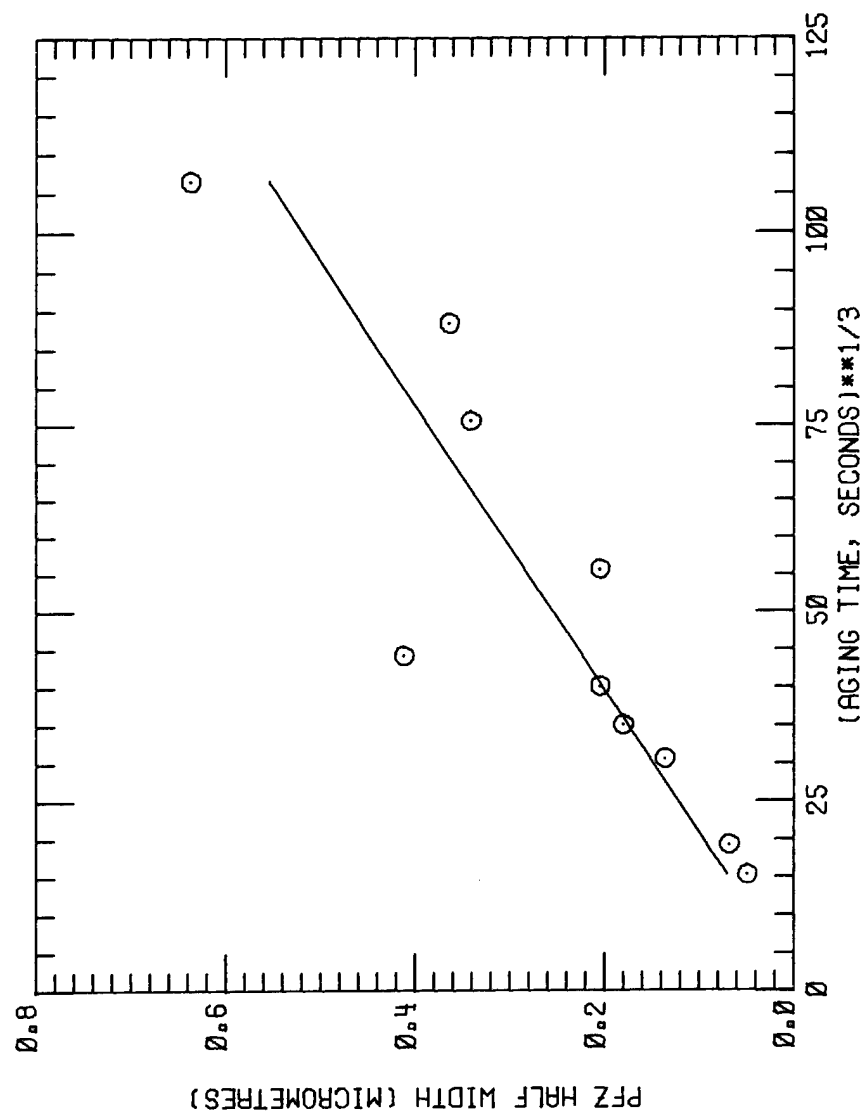
Figure 2-28. PFZ Half Width as a Function of the Cube Root of the Aging Time During Isothermal Aging at 200°C.
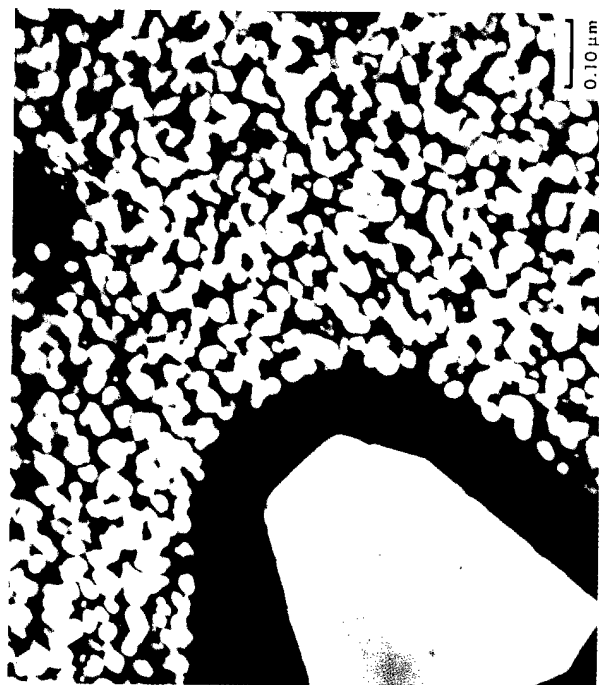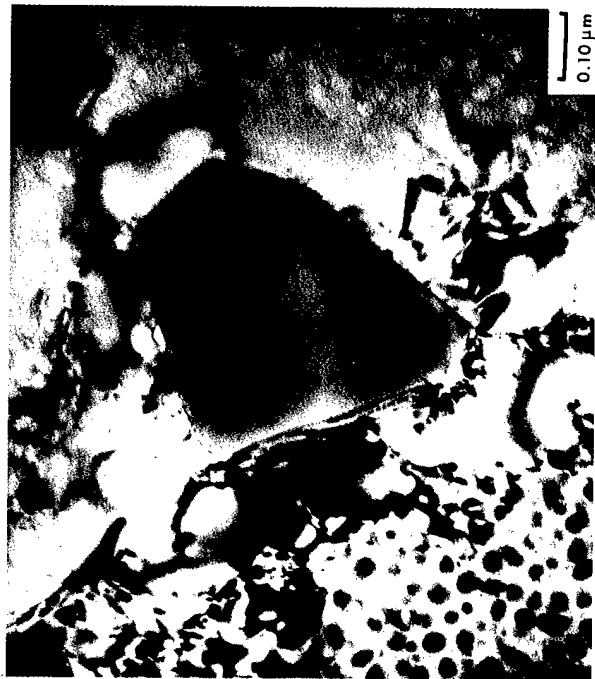
Figure 2-29. A series of TEM's Using Different Orientations and Imaging Conditions Showing the Presence of a PFZ Around an Al_6Mn Precipitate. The foil was prepared from a specimen of Al-Li-Mn sheet aged 8 hours at 200°C.

Figure 2-30. A BF and CDF Pair Taken of the Same ARea in
Al-Li-Mn Sheet Aged 18 Hours at 200°C. A PFZ
can be seen around the Al_6Mn and at the grain
boundary. The CDF image was produced using a
$(100)_{\delta'}$ reflection.
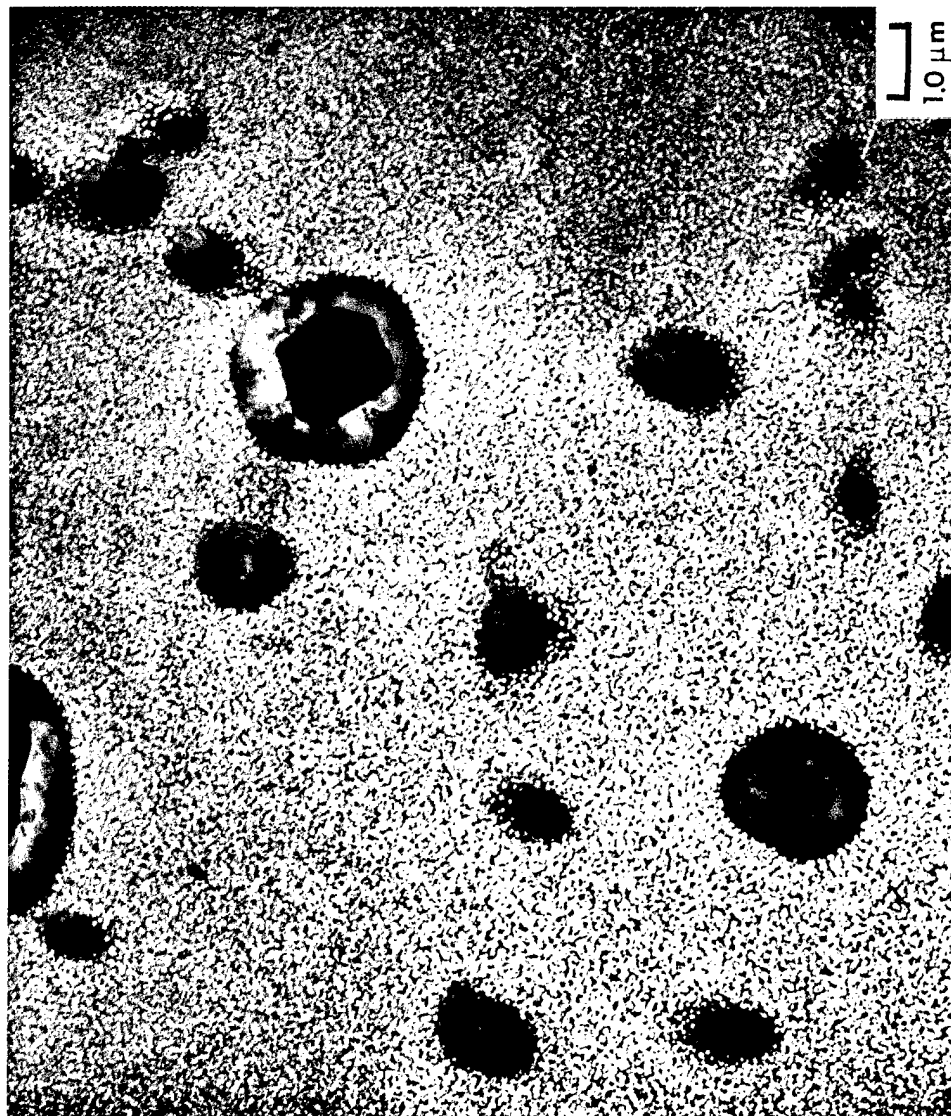
Figure 2-31. A Lower Magnification CDF Image Showing the Distribution of δ' in an Area Having Numerous Al_6Mn Precipitates. The CDF image was produced using a $(100)_{\delta'}$ reflection.
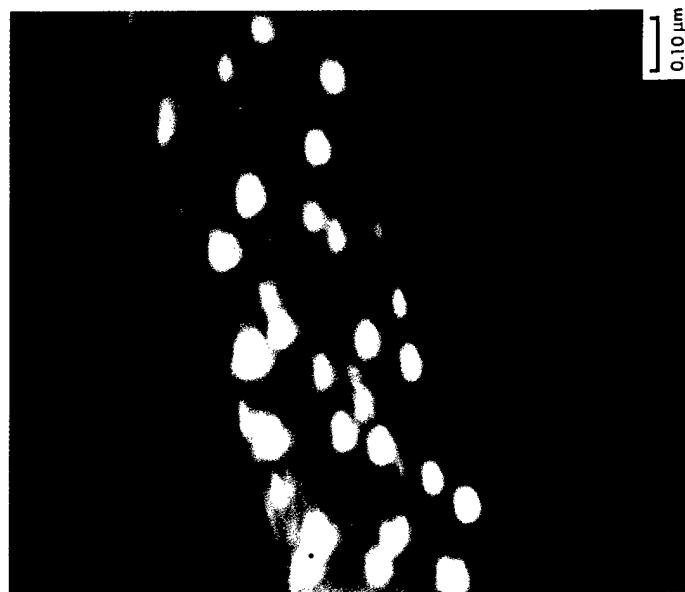
Figure 2-32. CDF Images of Coarse δ′ Precipitates in the Region of a Grain Boundary. The foil was prepared from a specimen heated to 200°C at a rate of 50°C/hour. The CDF image was produced using a (100)_{δ′} reflection.
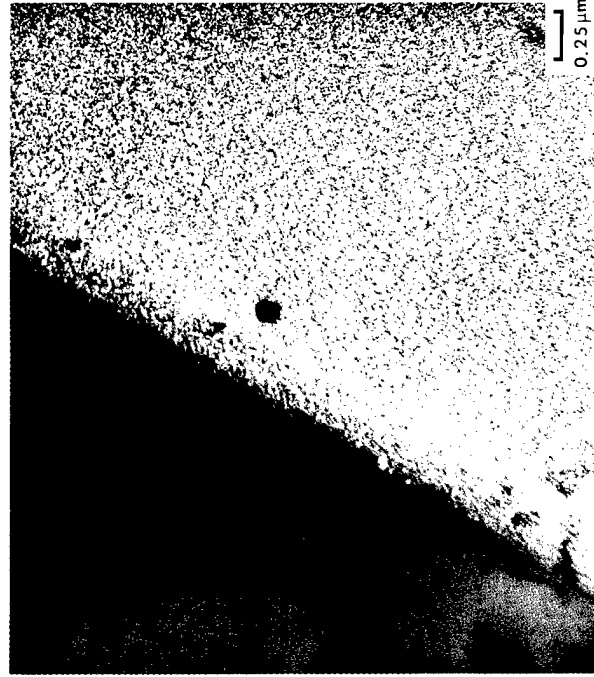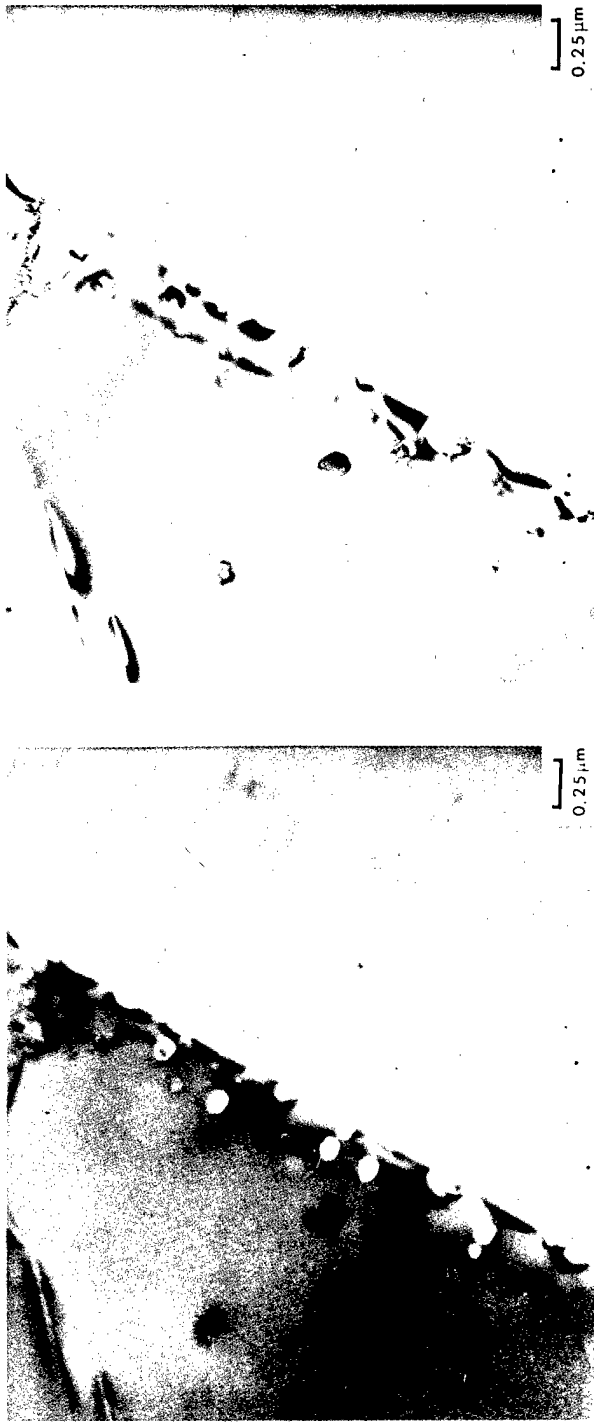
Figure 2-33. A Series of TEM's Using Different Orientations and Imaging Conditions to Illustrate the Relative Size of the Precipitates in the Matrix and in the Grain Boundary Region. The foil was prepared from a specimen of Al-Li-Mn sheet isothermally aged at 200°C for 10 minutes.
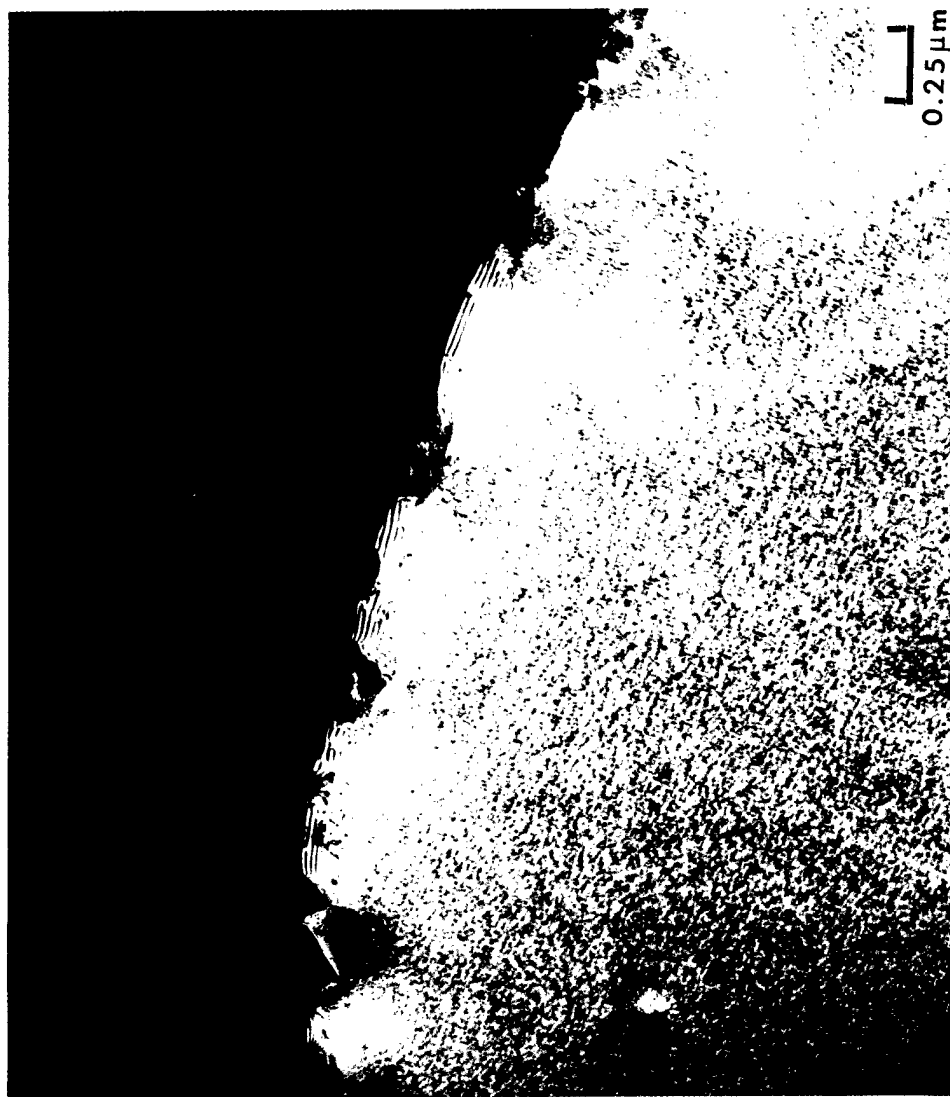
Figure 2-34. A CDF Image Showing the Presence of Coarse Precipitates in the Grain Boundary Region. The CDF image was produced using a (200) Al reflection.
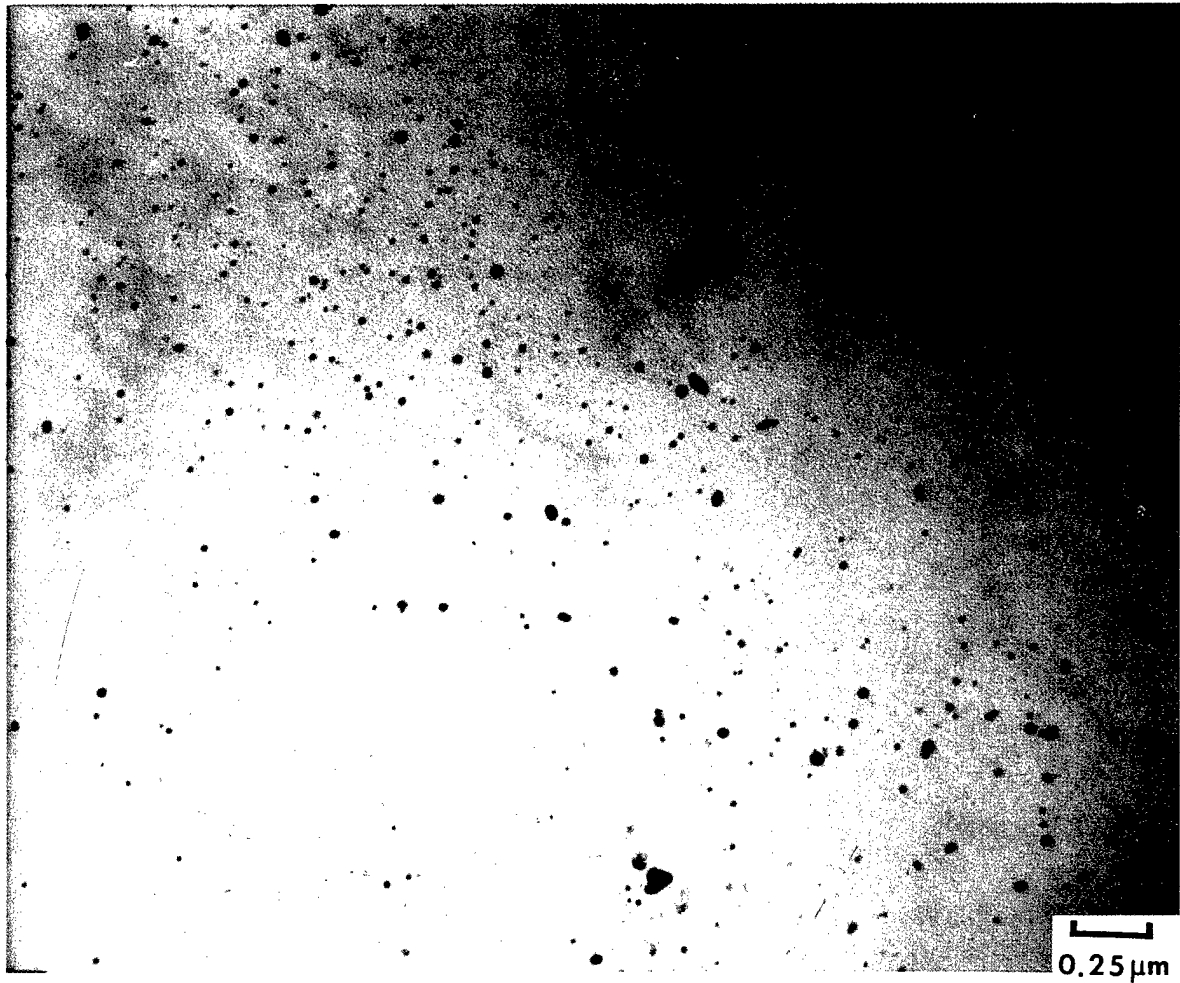
Figure 2-35. BF Image Showing the Distribution of Al_3Zr in Underaged Al-Li-Zr.
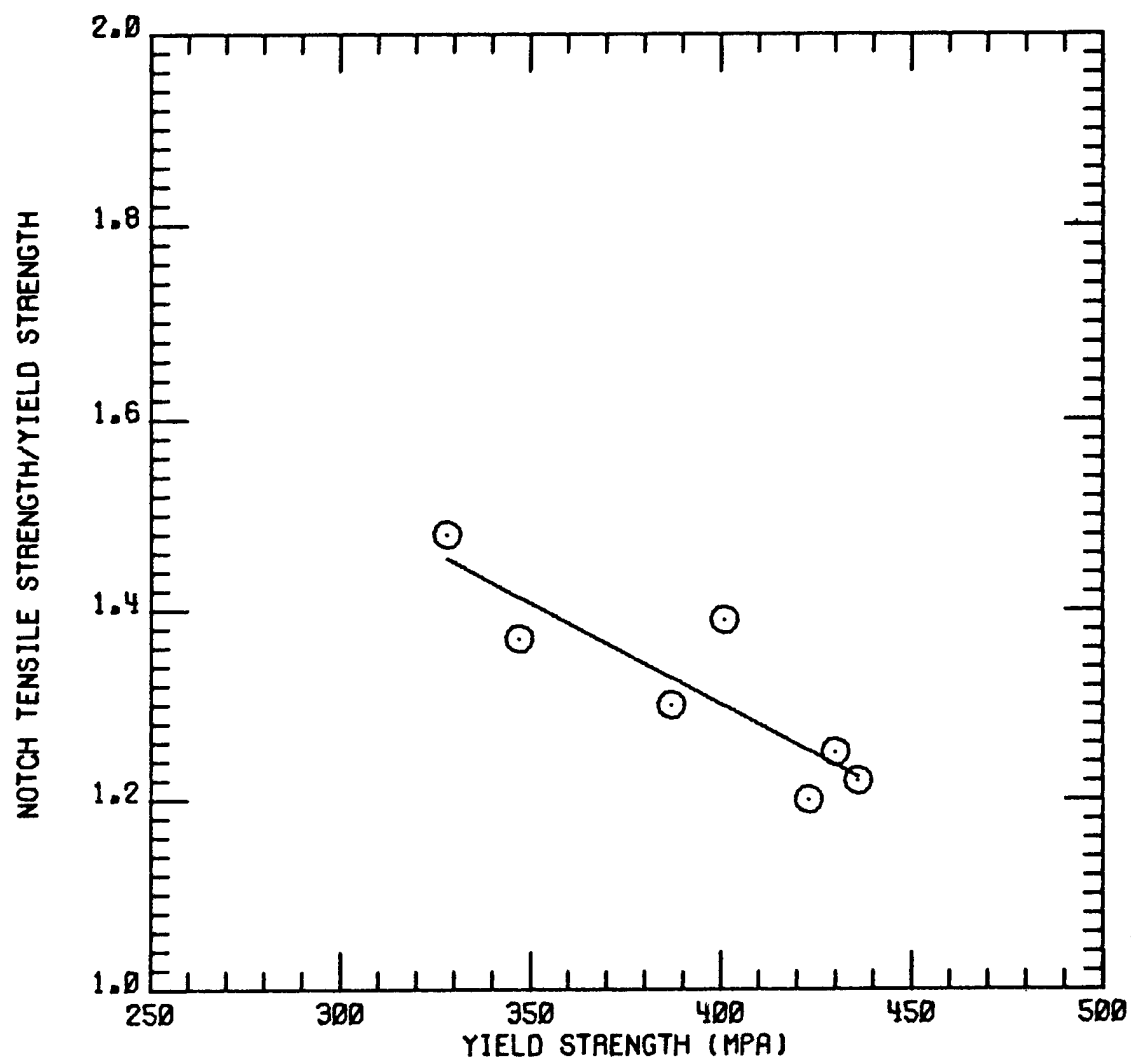
Figure 2-36. Notch Tensile Strength/Yield Strength Ratio
Versus Yield Strength of Conventionally Cast
Al-Li-Zr Extrusion Solution Heat Treated (SHT)
at 552°C for 0.5 Hours, Cold Water Quenched,
and Aged Immediately at 200°C.
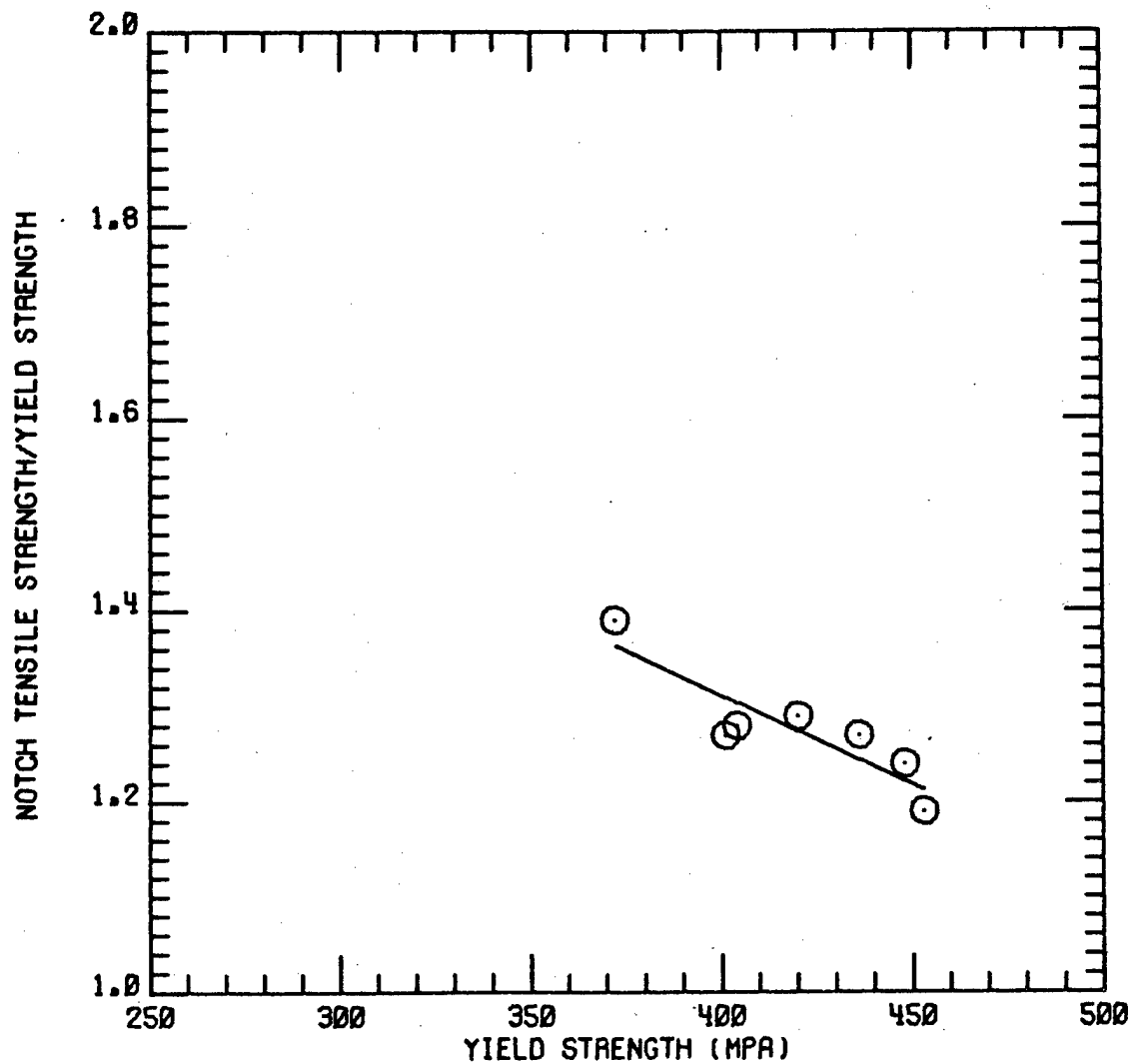
Figure 2-37.   Notch Tensile Strength/Yield Strength Ratio
               Versus Yield Strength of Conventionally Cast
               Al-Li-Zr Extrusion SHT at 552°C for 0.5 Hours,
               Quenched Directly to 200°C, and Aged at 200°C.
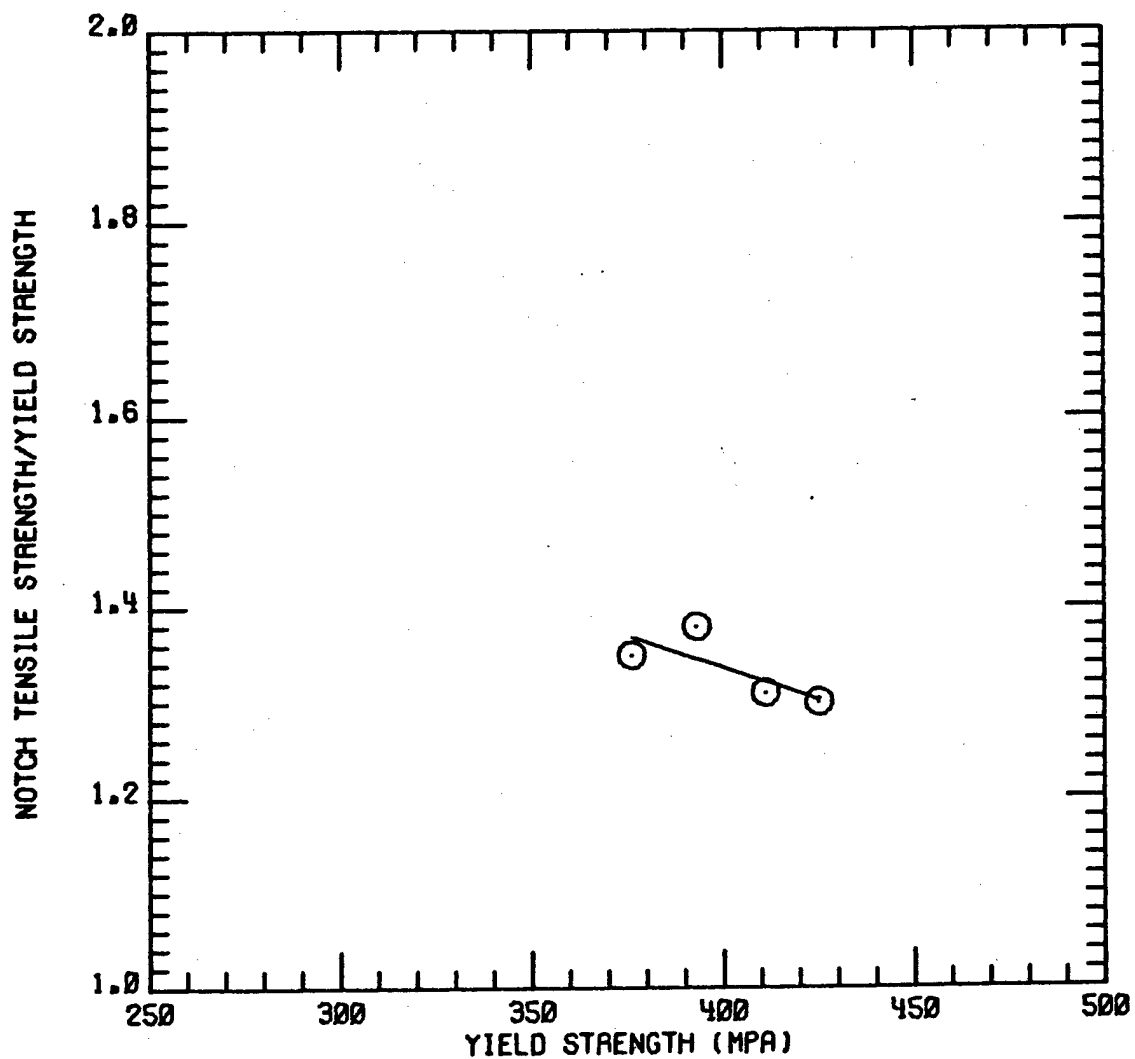
Figure 2-38.   Notch Tensile Strength/Yield Strength Ratio
              Versus Yield Strength of Conventionally Cast
              Al-Li-Zr Extrusion SHT at 552°C for 0.5 Hours,
              Quenched Directly to 225°C, and Aged at 225°C.
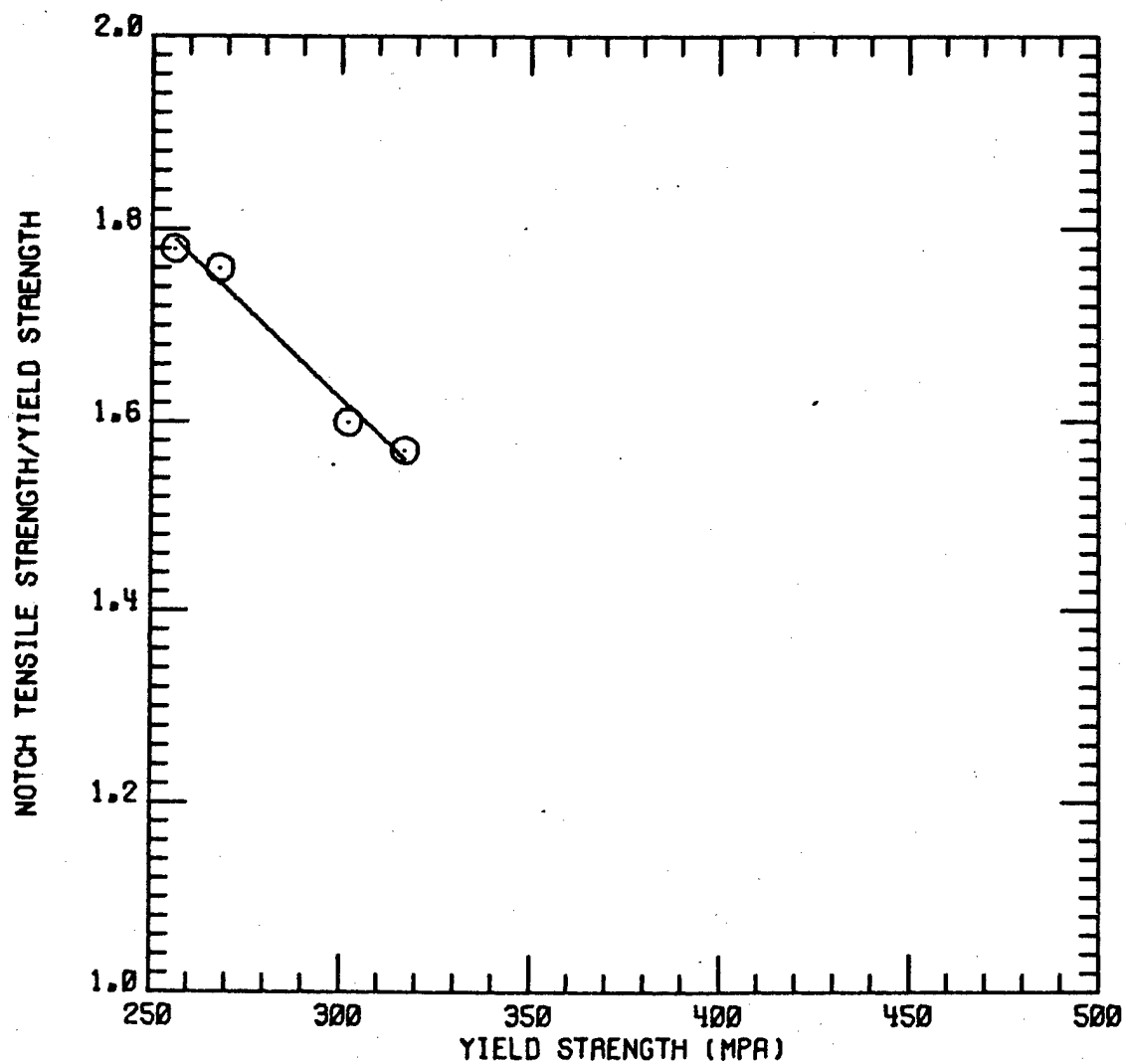
Figure 2-39. Notch Tensile Strength/Yield Strength Ratio
Versus Yield Strength of Conventionally Cast
Al-Li-Zr Extrusion SHT at 552°C for 0.5 Hours,
Directly Quenched to 275°C, and Aged at 275°C.
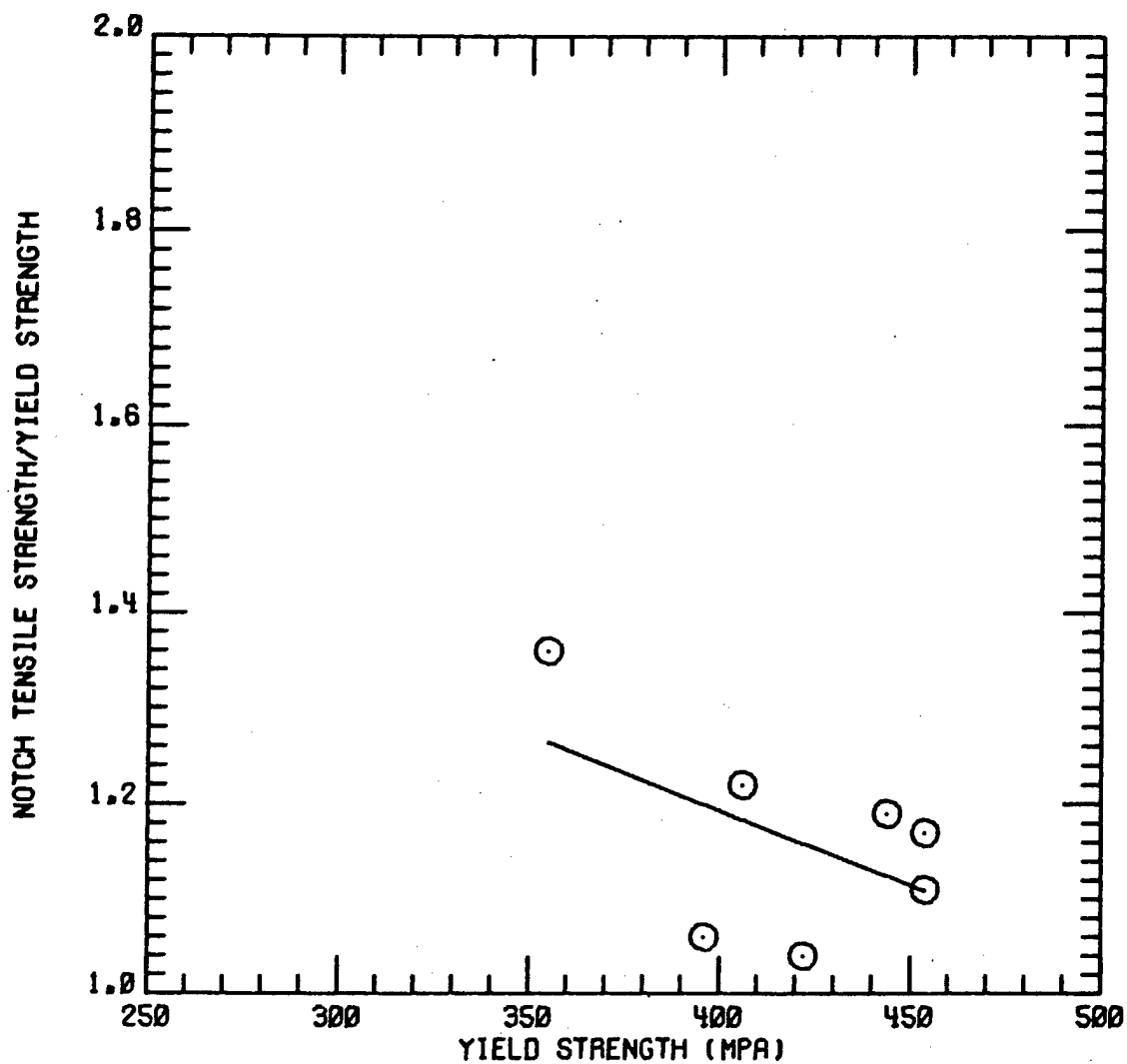
Figure 2-40. Notch Tensile Strength/Yield Strength Ratio
Versus Yield Strength of Vacuum Cast Al-Li-Zr
Extrusion SHT at 552°C for 0.5 Hours, Cold
Water Quenched, and Aged Immediately at 200°C.
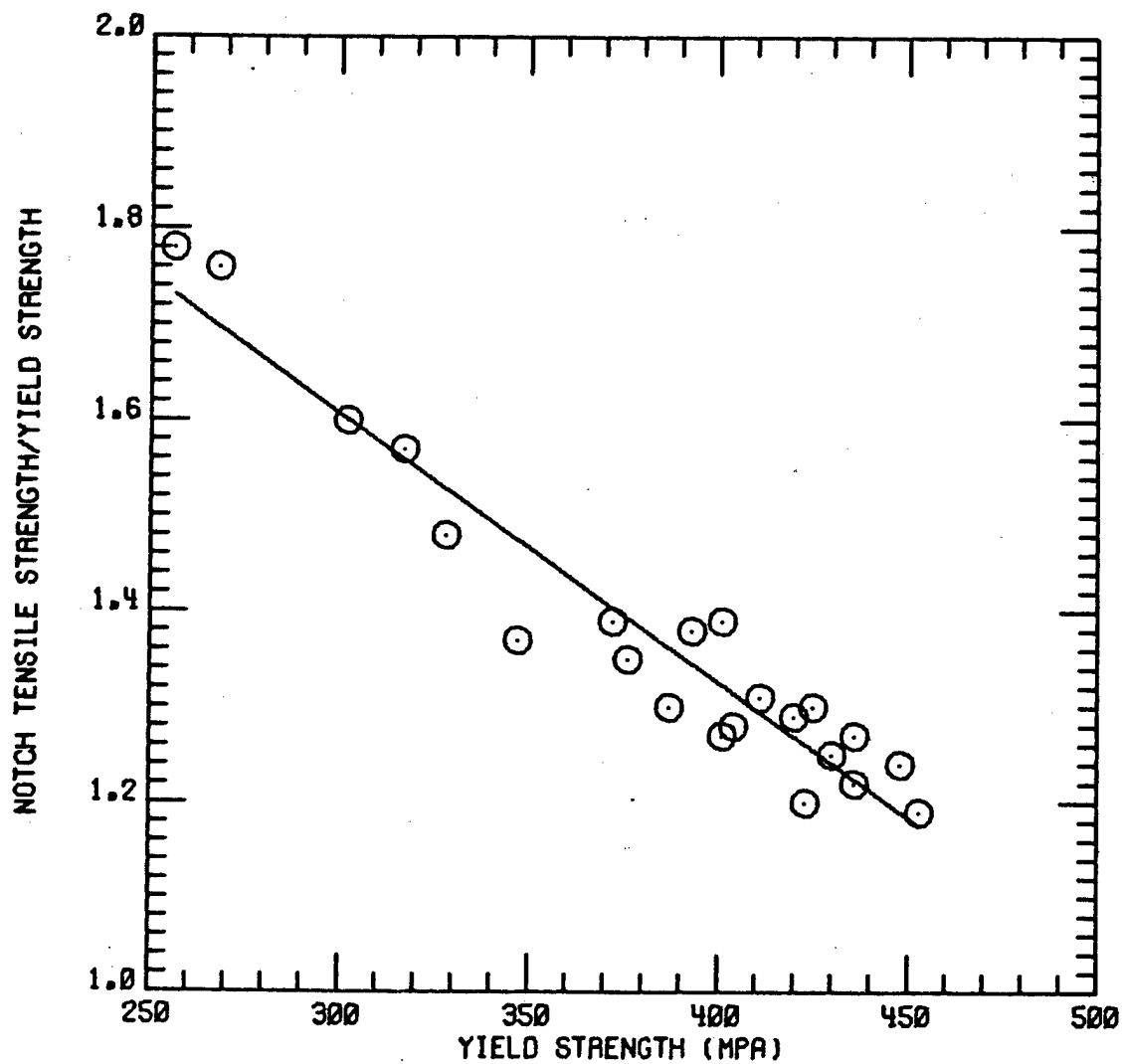
Figure 2-41. Notch Tensile Strength/Yield Strength Ratio
Versus Yield Strength of Conventionally Cast
Al-Li-Zr Extrusion SHT at 552°C for 0.5 Hours
and Artificially Aged at the Different Conditions.
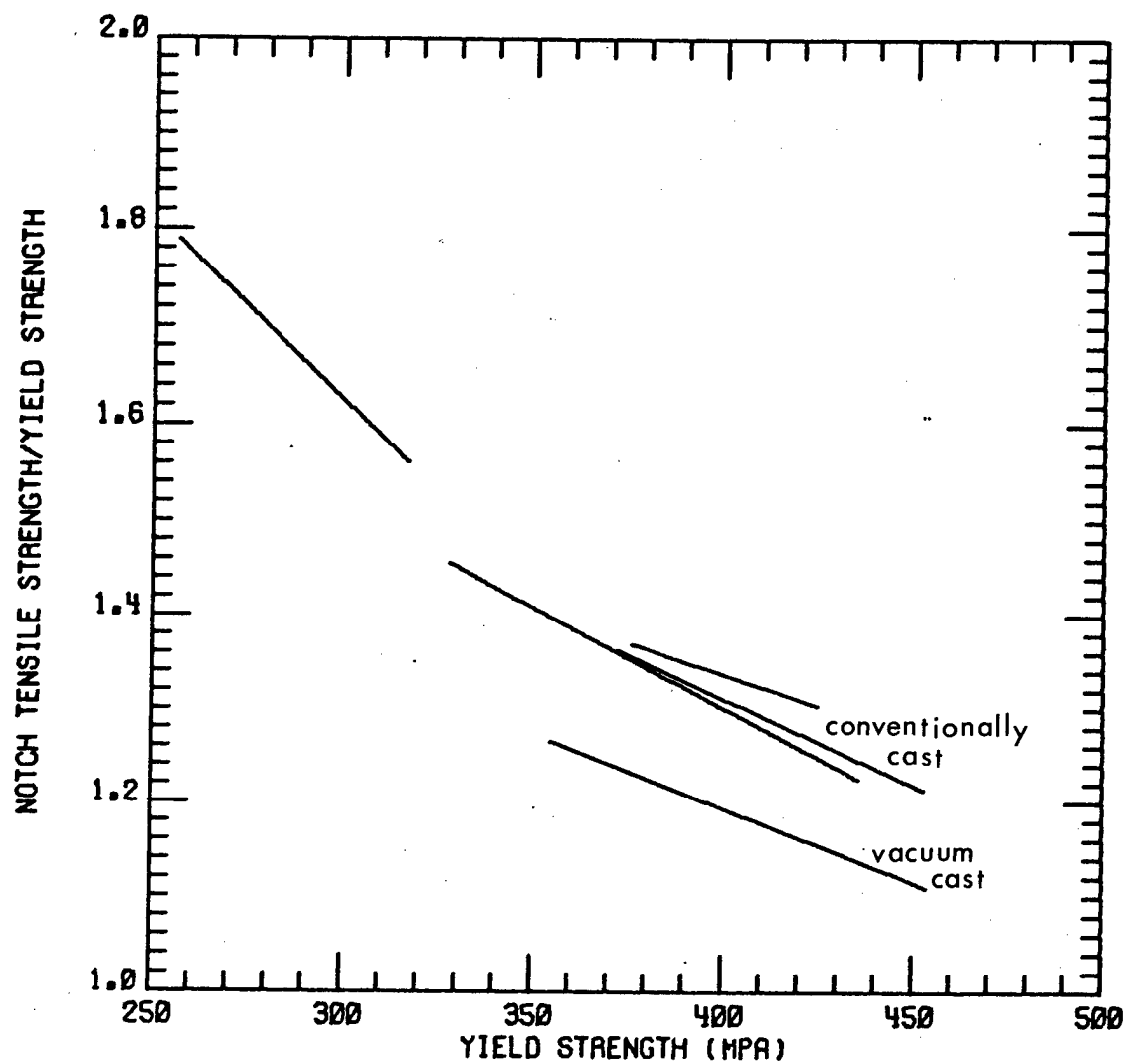
Figure 2-42. Notch Tensile Strength/Yield Strength Ratio
Predictions for SHT and Aged Al-Li-Zr Alloys.
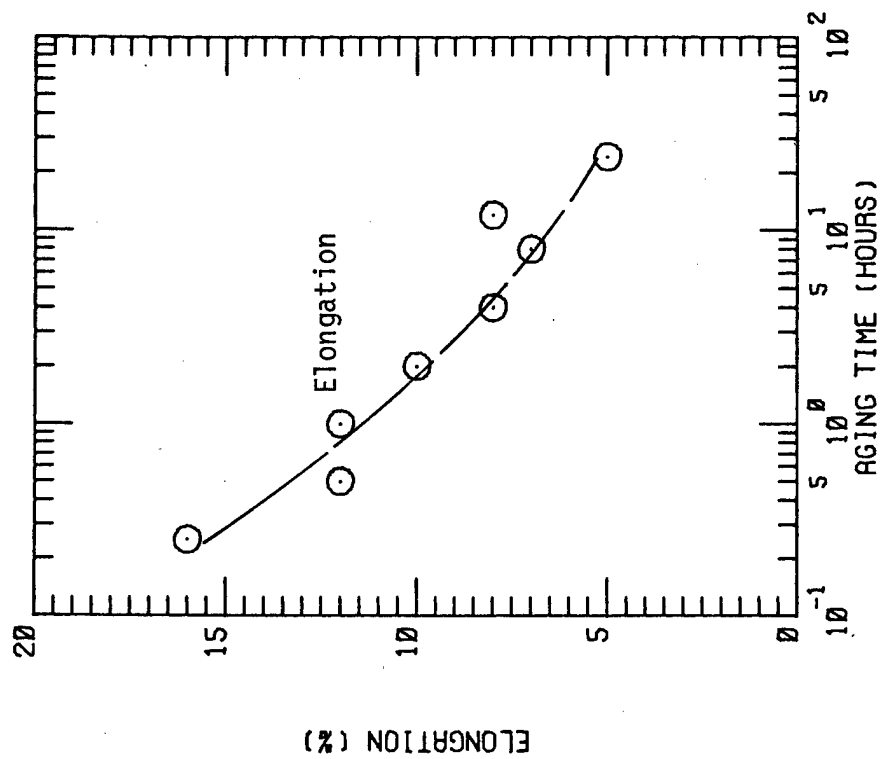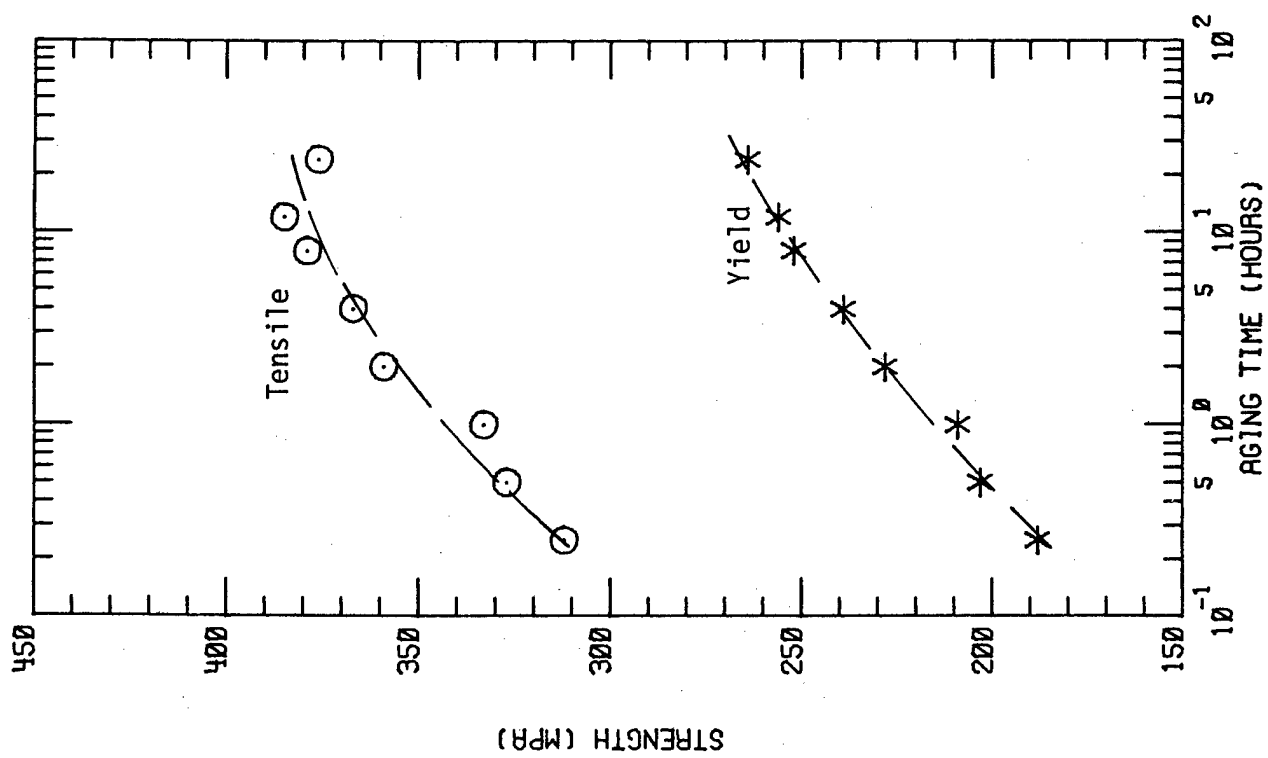
Figure 2-43. Tensile Properties of Al-Li-Mn Sheet SHT at 552°C for 15 Seconds, Cold Water Quenched, and Aged at 200°C.
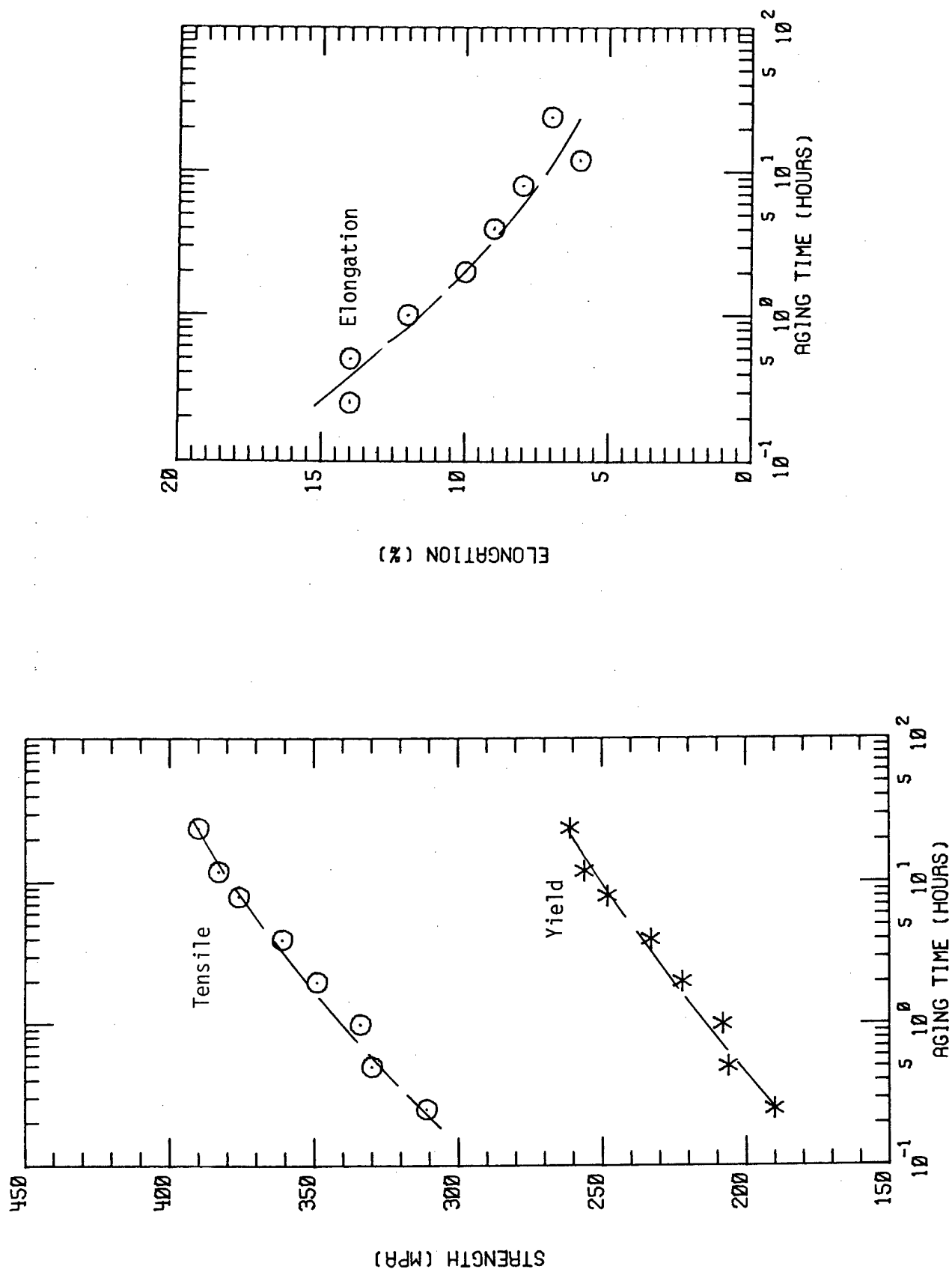
Figure 2-44. Tensile Properties of Al-Li-Mn Sheet SHT at 552°C for 15 Seconds and Quenched Directly to Aging Temperature of 200°C.
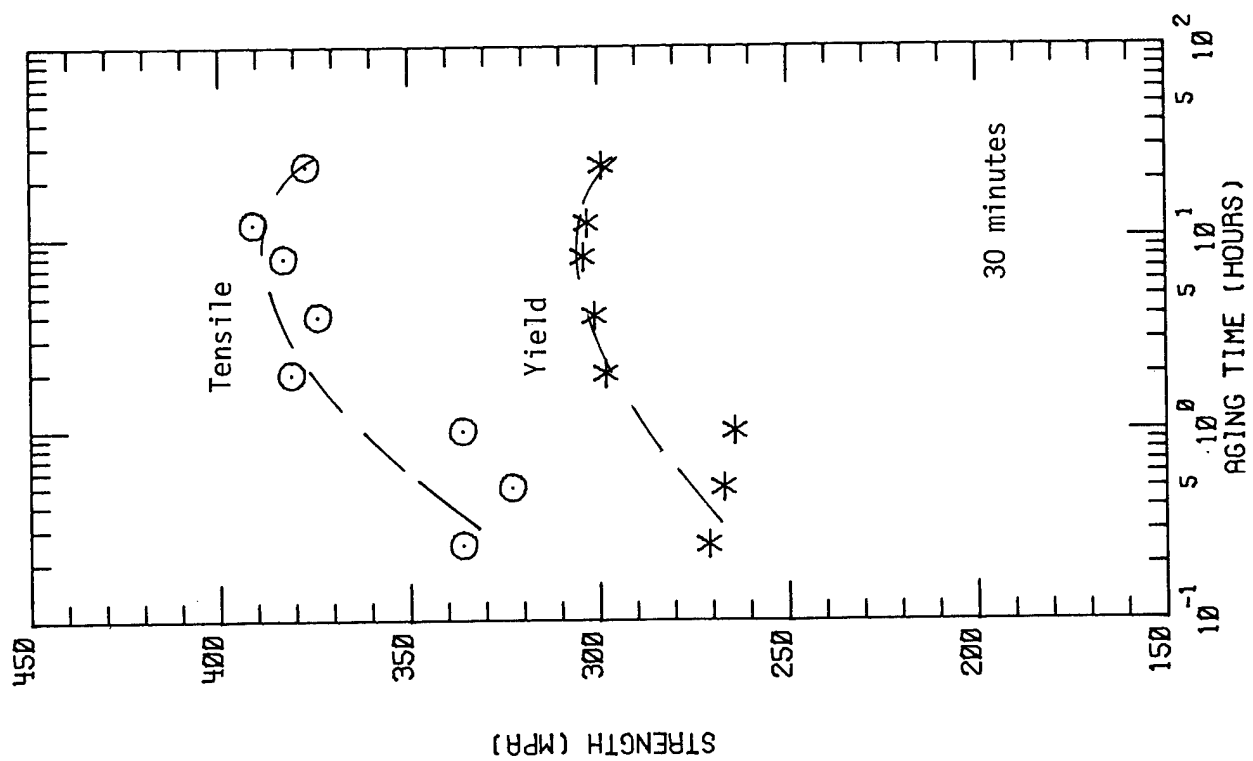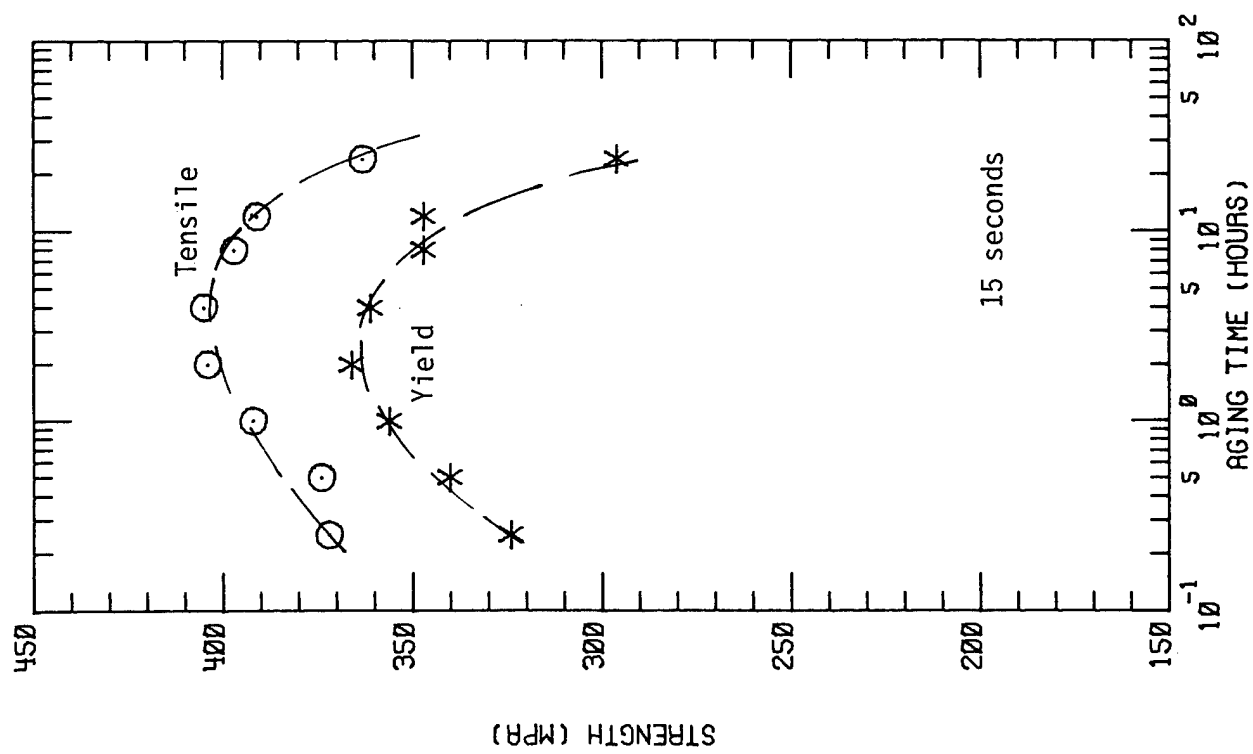
Figure 2-45. The Effect of Time at SHT in Al-Li-Zr Sheet.
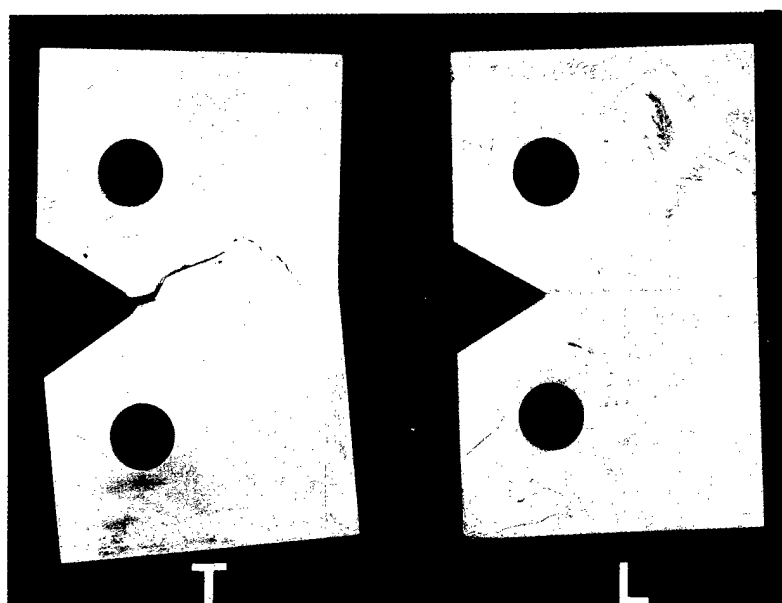
Figure 2-46. Al-Li-Zr Sheet Transverse and Longitudinal Specimens Showing the Behavior of the Crack Front as a Function of Specimen Orientation.

EP—
PL
100X

(b)

'2.25X

(a)
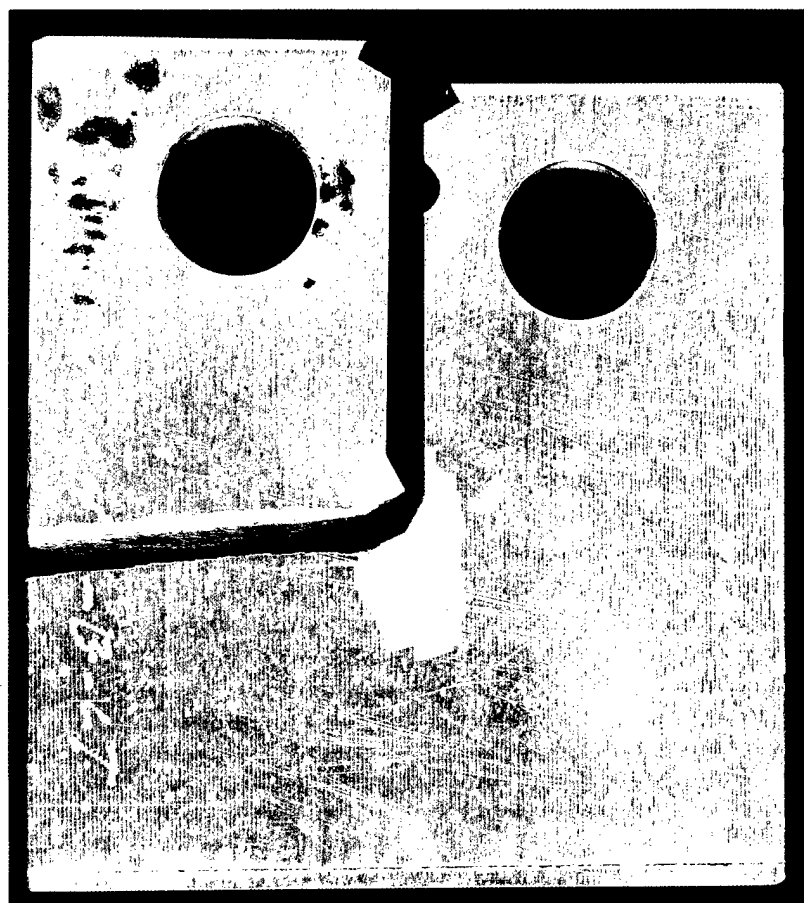
Figure 2-47.   (a) Macrograph Showing the Change in Crack
Direction of a Conventionally Cast Al-Li-Zr
Alloy Tested in the L-T Orientation. (b)
Micrograph Showing Grain Morphology of the
Specimen.
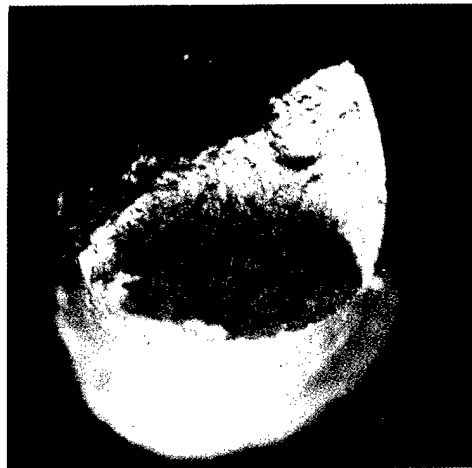
7.X   T
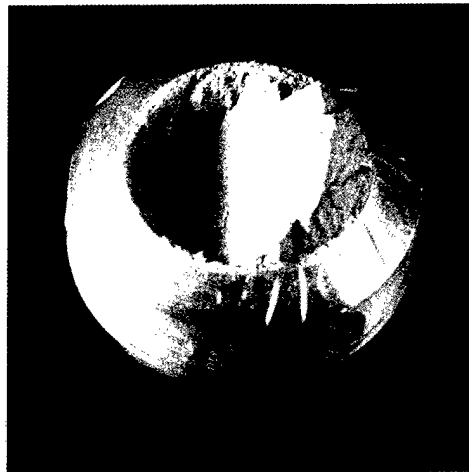
3.5 X   N-T

Figure 2-48.. Macrographs of Tensile and Notch-Tensile
Failures in Conventionally Cast Al-Li-Zr
Alloy Aged to Peak Strength.
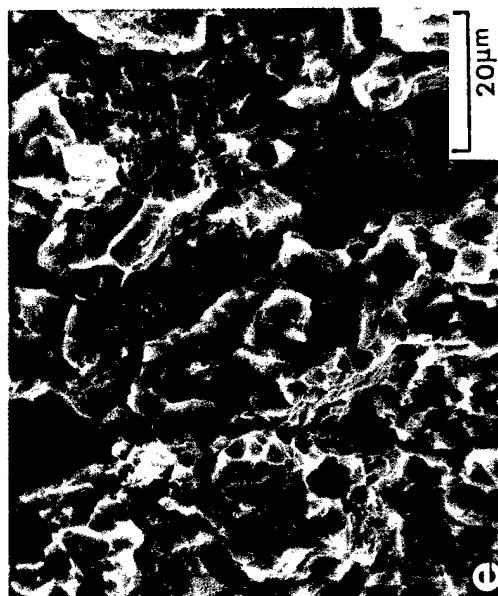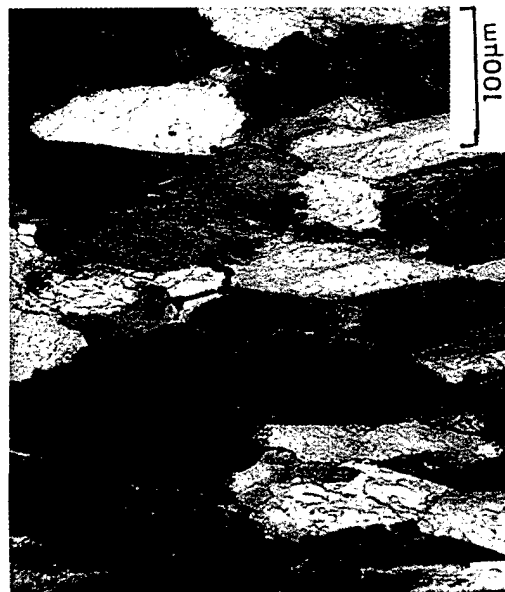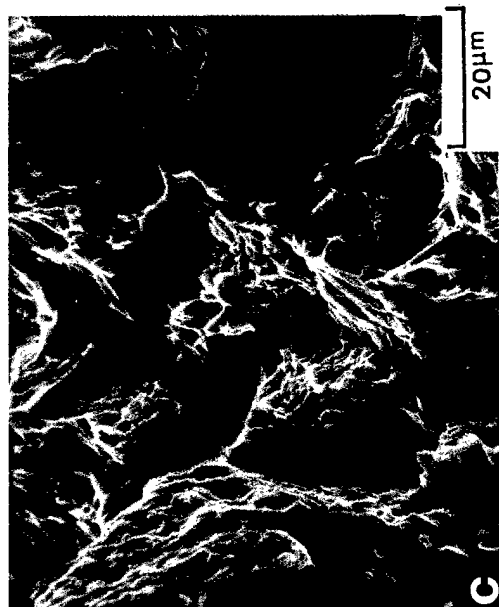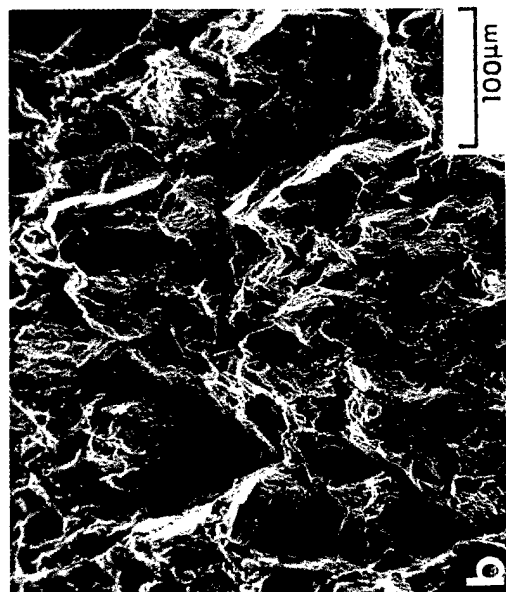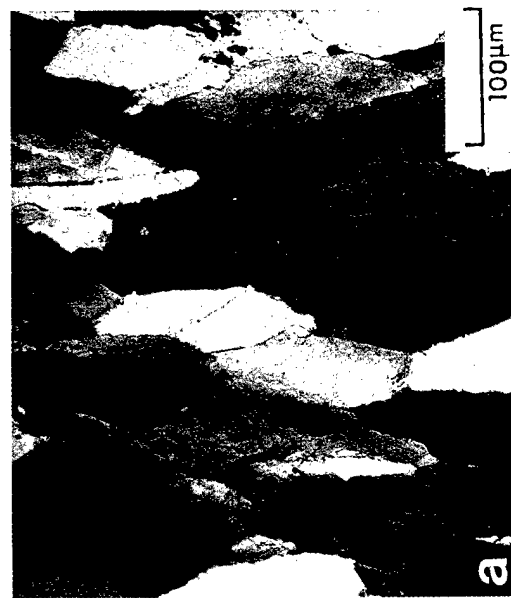
Figure 2-49. (a) Polished Surface Just Below Fracture of Peak Strength Al-Li-Zr, (b) and (c) SEM of Tensile Fracture in Peak Strength Condition, (d) Polished Surface Just Below Fracture of Overaged Al-Li-Zr, and (e) SEM of the Tensile Fracture.
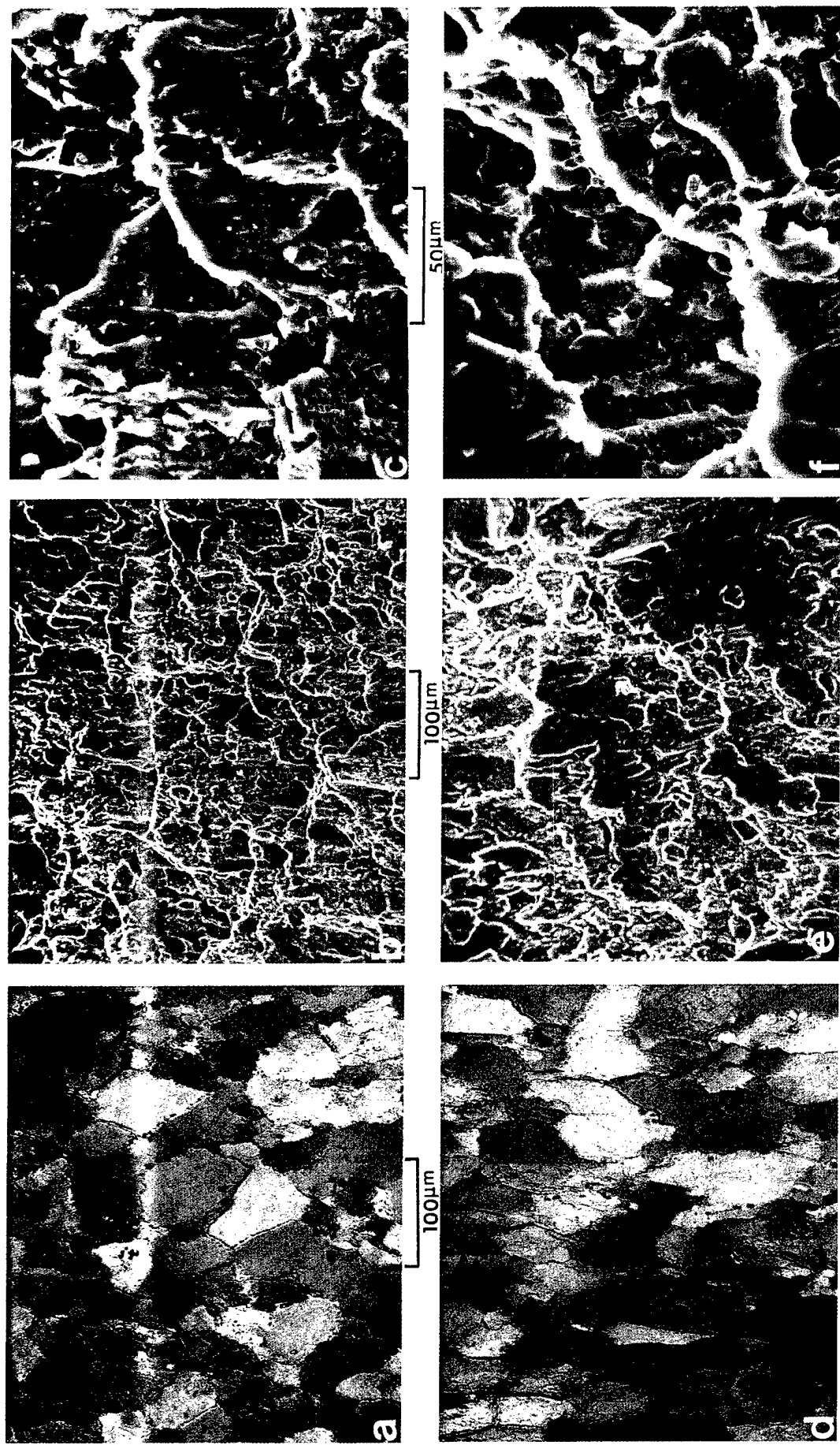
Figure 2-50. (a) Polished Surface Just Below Notch Tensile Fracture of Peak Strength Al–Li–Zr, (b) and (c) SEM of Notch Tensile Fracture in Overaged Condition, (d) Polished Surface Just Below Notch Tensile Fracture, (e) and (f) SEM of the Notch Tensile Fracture.

0.5µ
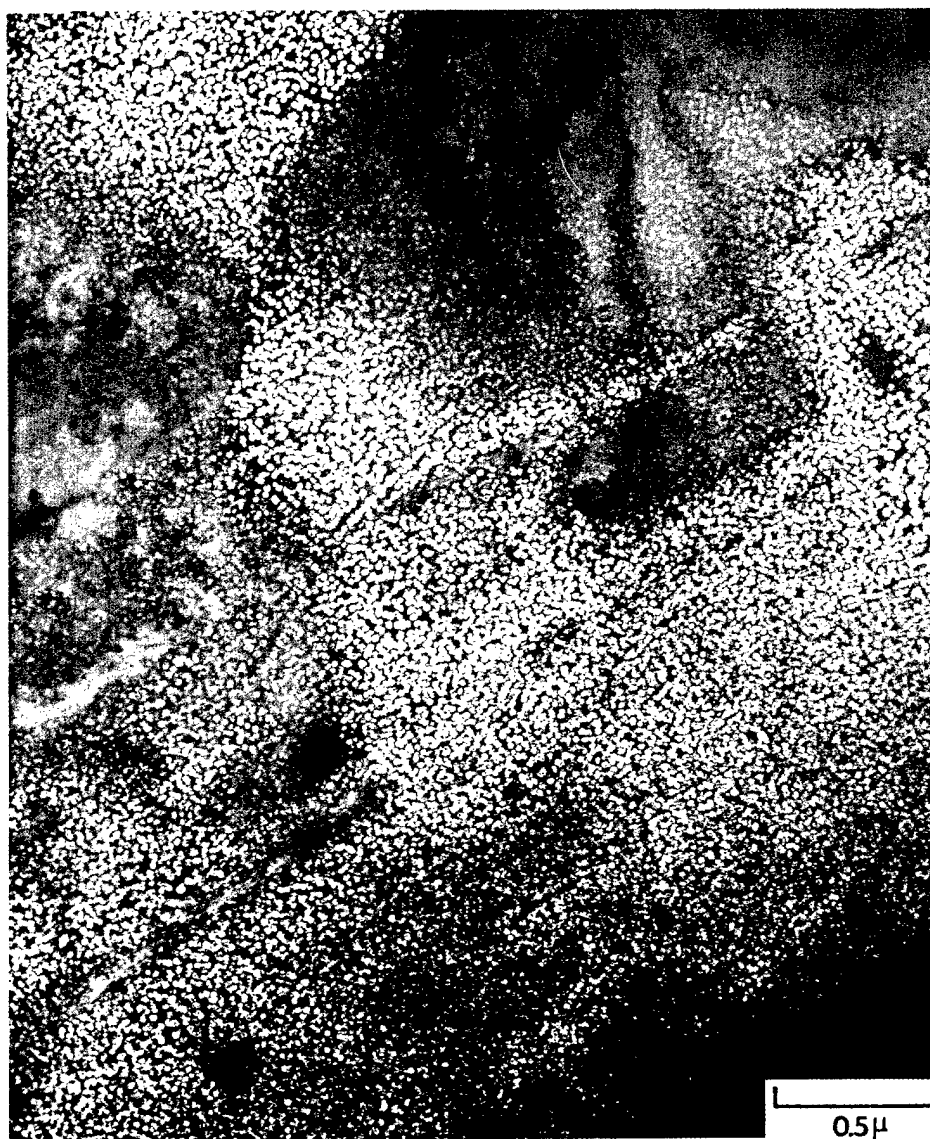
Figure 2-51. TEM of Specimen from Tensile Failure of Con-
ventionally Cast Al-Li-Zr Extrusion Aged 4
Hours at 200°C.

0.14m
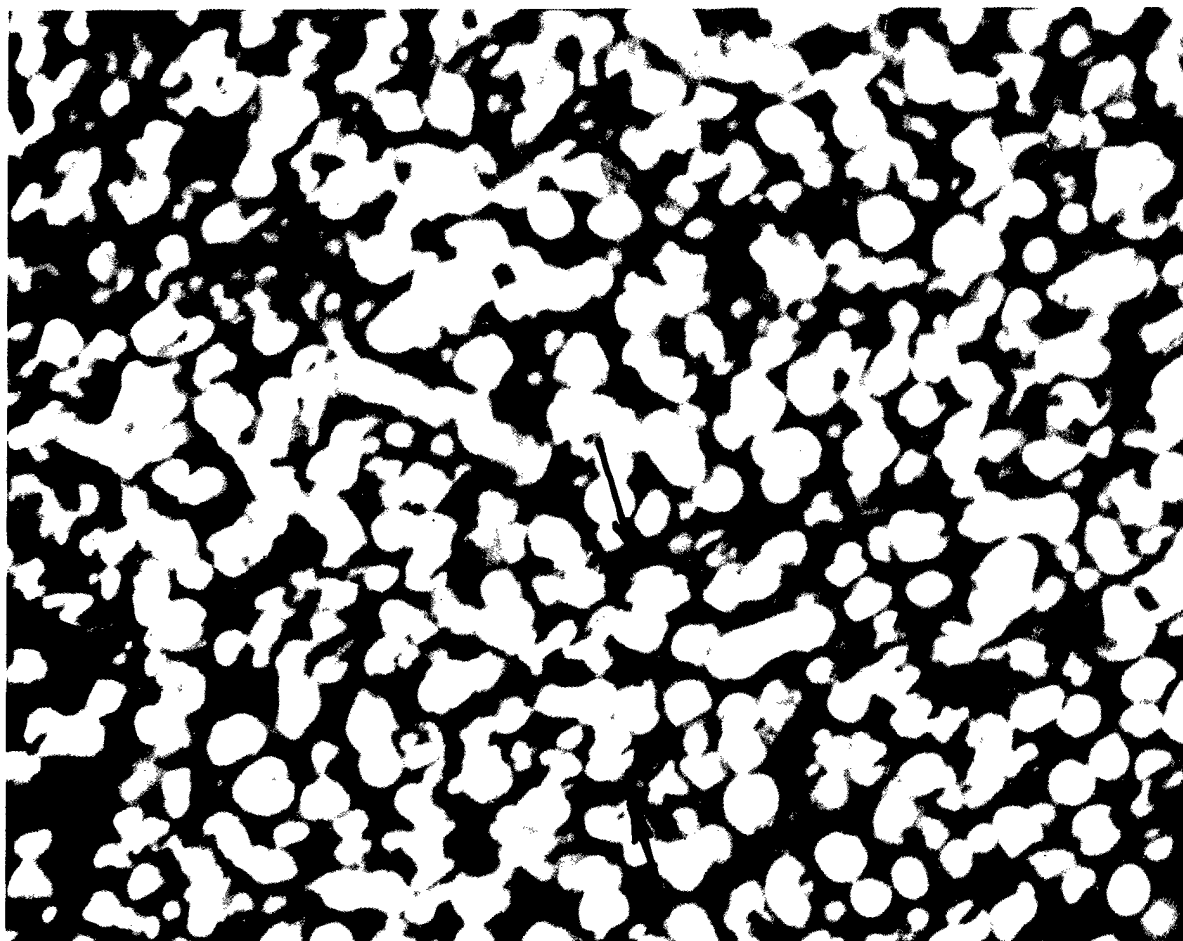
Figure 2-52. TEM of Specimen from Tensile Failure of
Conventionally Cast Al-Li-Zr Extrusion Aged
24 Hours at 200°C, CDF Image Using (100)
Al_3Li Reflection to Show Evidence of Dis-
location Shearing.
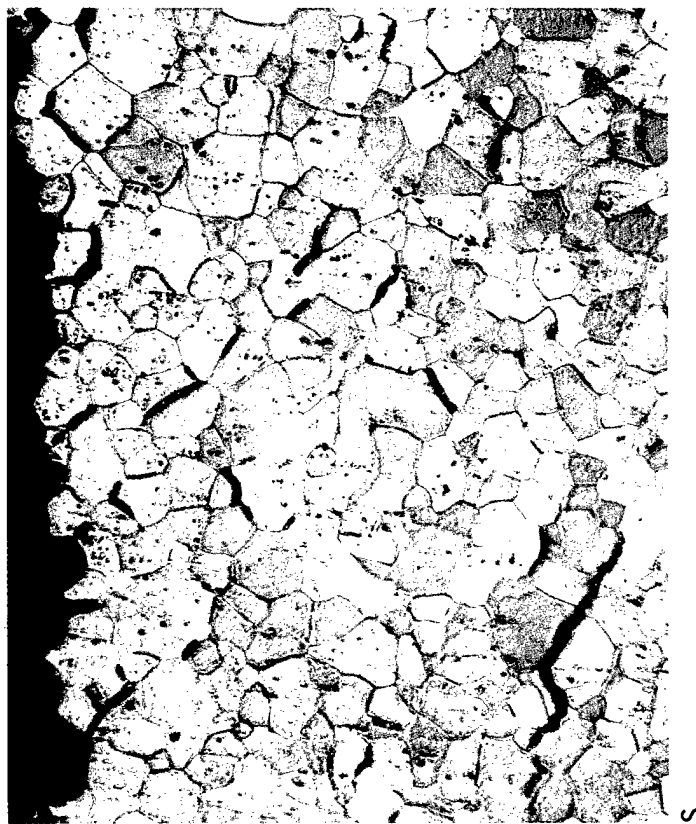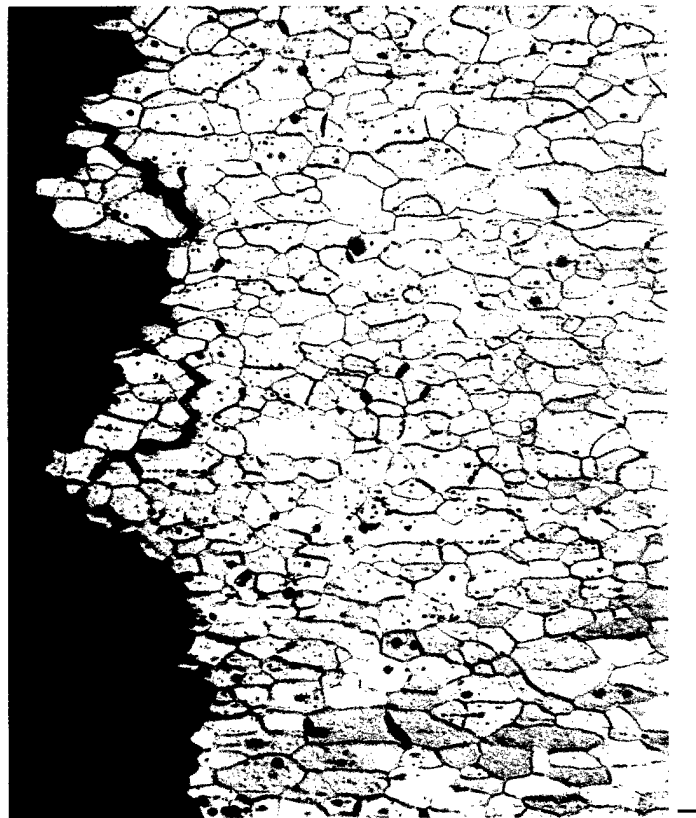
Figure 2-53.   Metallographic Sections of Al-Li-Mn Sheet
                Tensile Fracture.
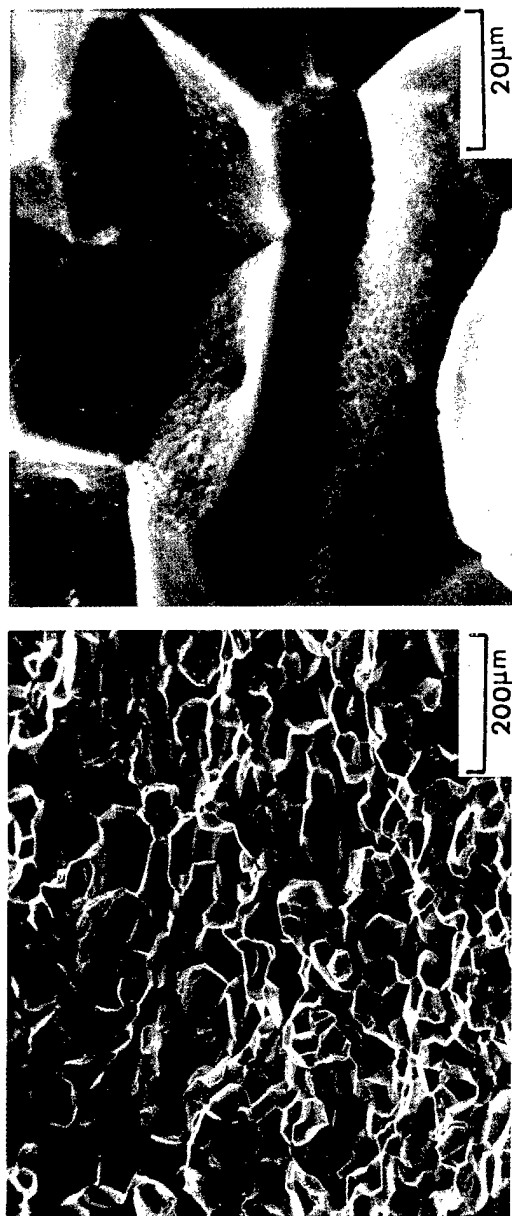
Figure 2-54. Fractographs of Al-Li-Mn Sheet Tensile Fractures, (a)-(c, 0.25 Hours at 200°C, and (d)-(e) 24 Hours at 200°C.
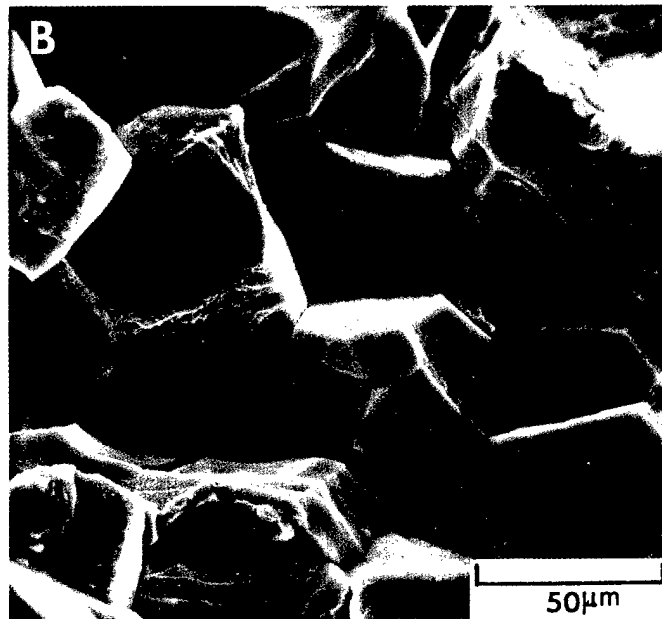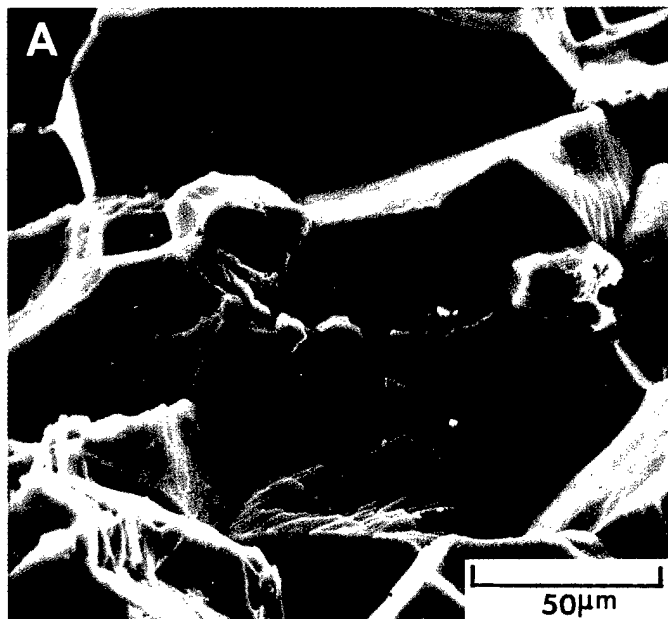
Figure 2-55. Fractographs of Al-Li-Mn Aged for (a) 2, (b) 4, and (c) 8 Hours at 200°C.
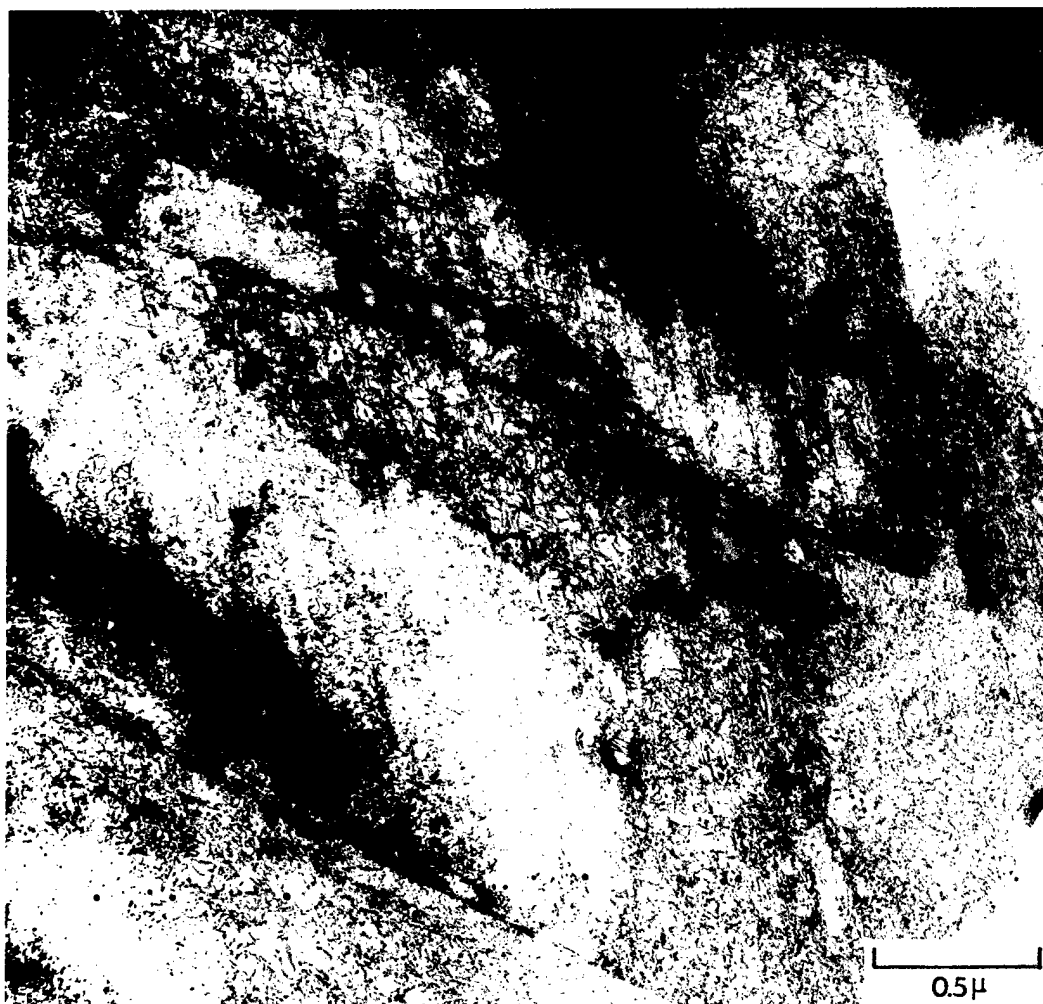
Figure 2-56.   Planar Deformation in Underaged Al-Li-Mn Sheet.
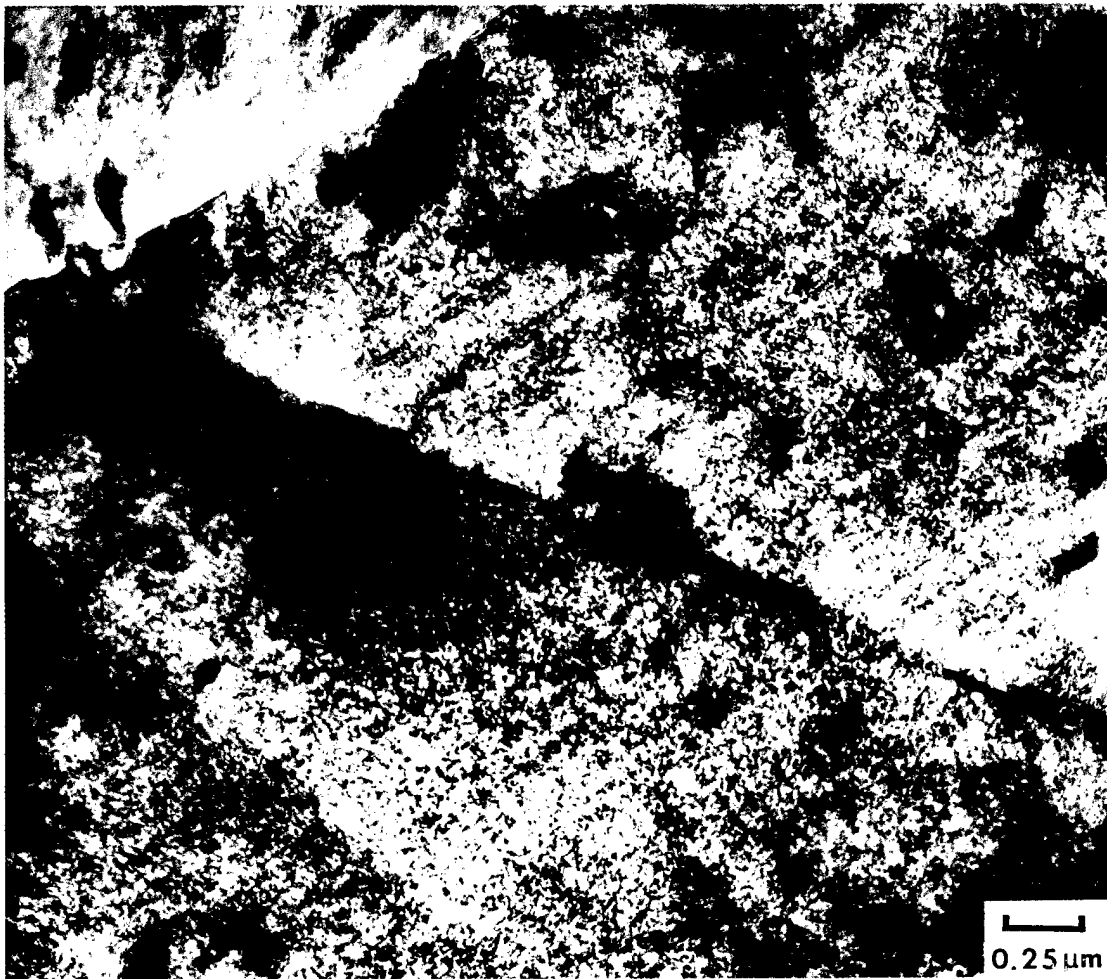
Figure 2-57. Planar Deformation in Underaged Al-Li-Mn Sheet.
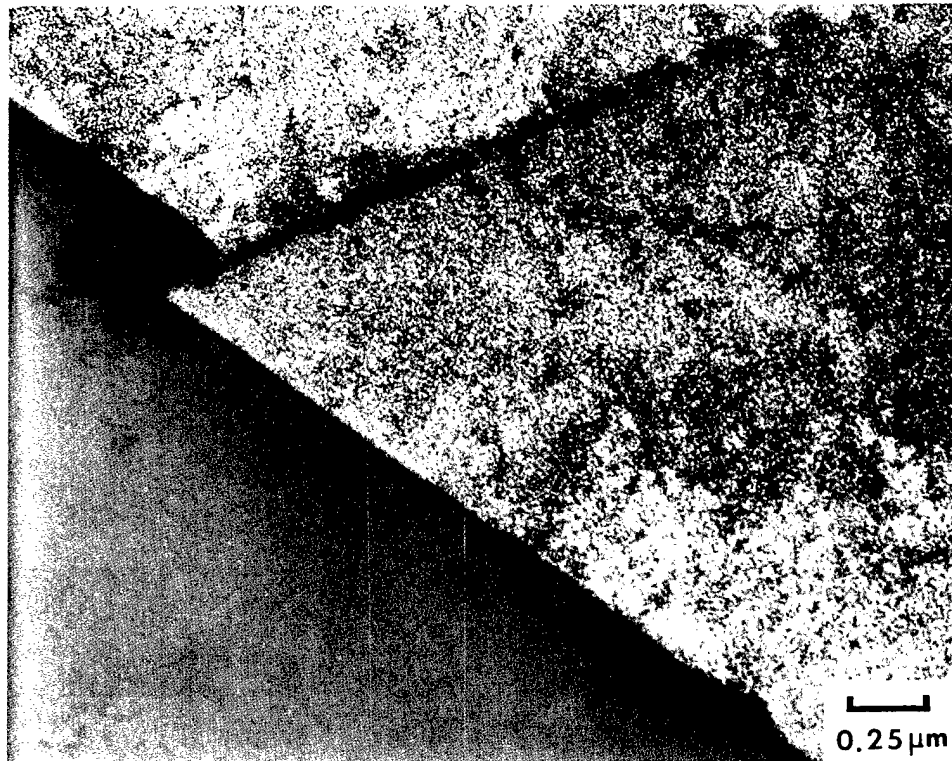
Figure 2-58. Intersection of Planar Slip Band with Grain Boundary Creating an Offset in the Boundary. CDF Image Using (100) Al₃Li Reflection.
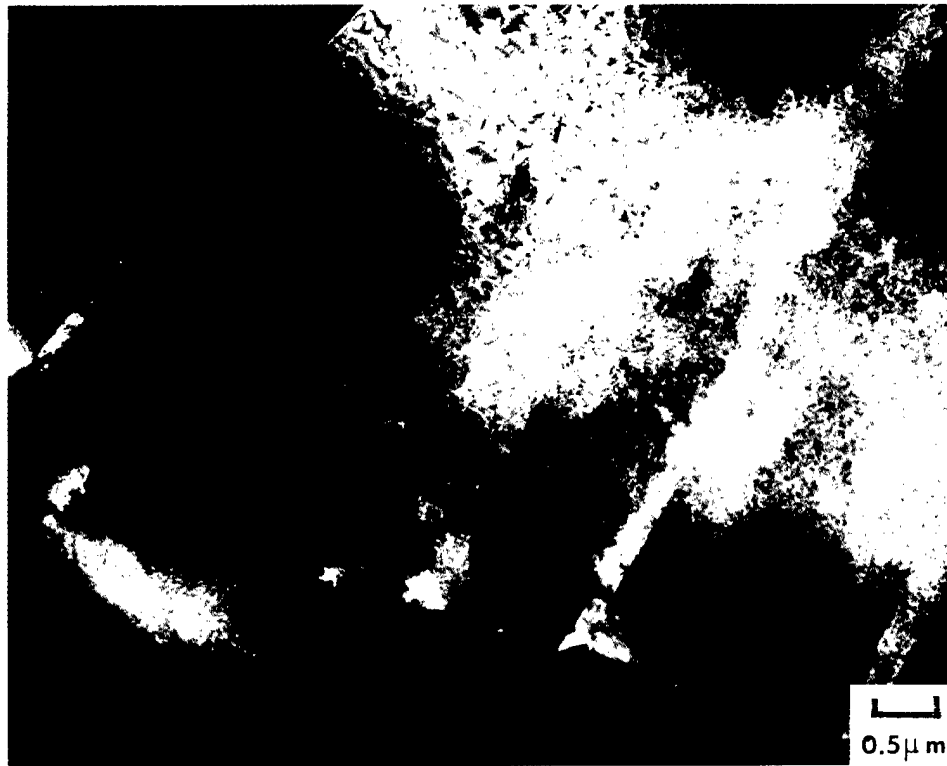
Figure 2-59. Intersection of Planar Slip Bands with Grain
Boundary. CDF Image Using (220) Aluminum
Reflection.
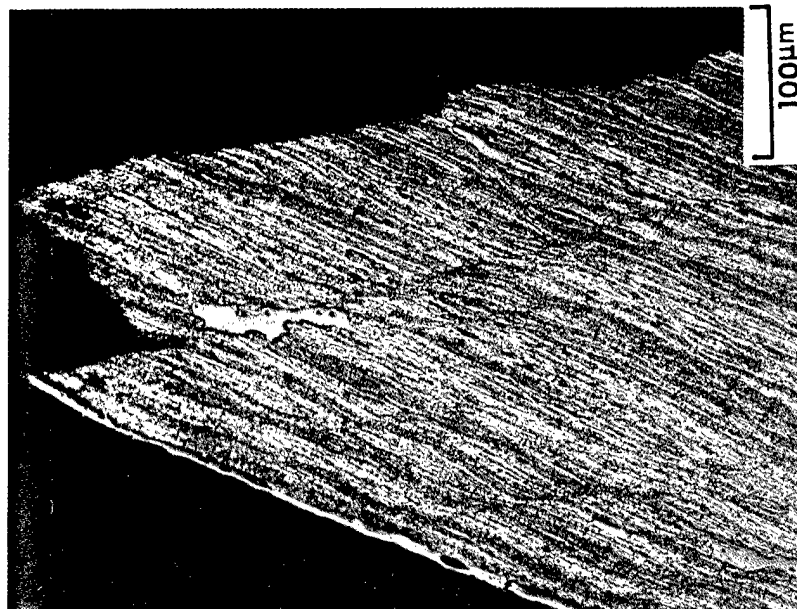
Figure 2-60. Longitudinal Section of a Tensile Failure in Al-Li-Zr Sheet.
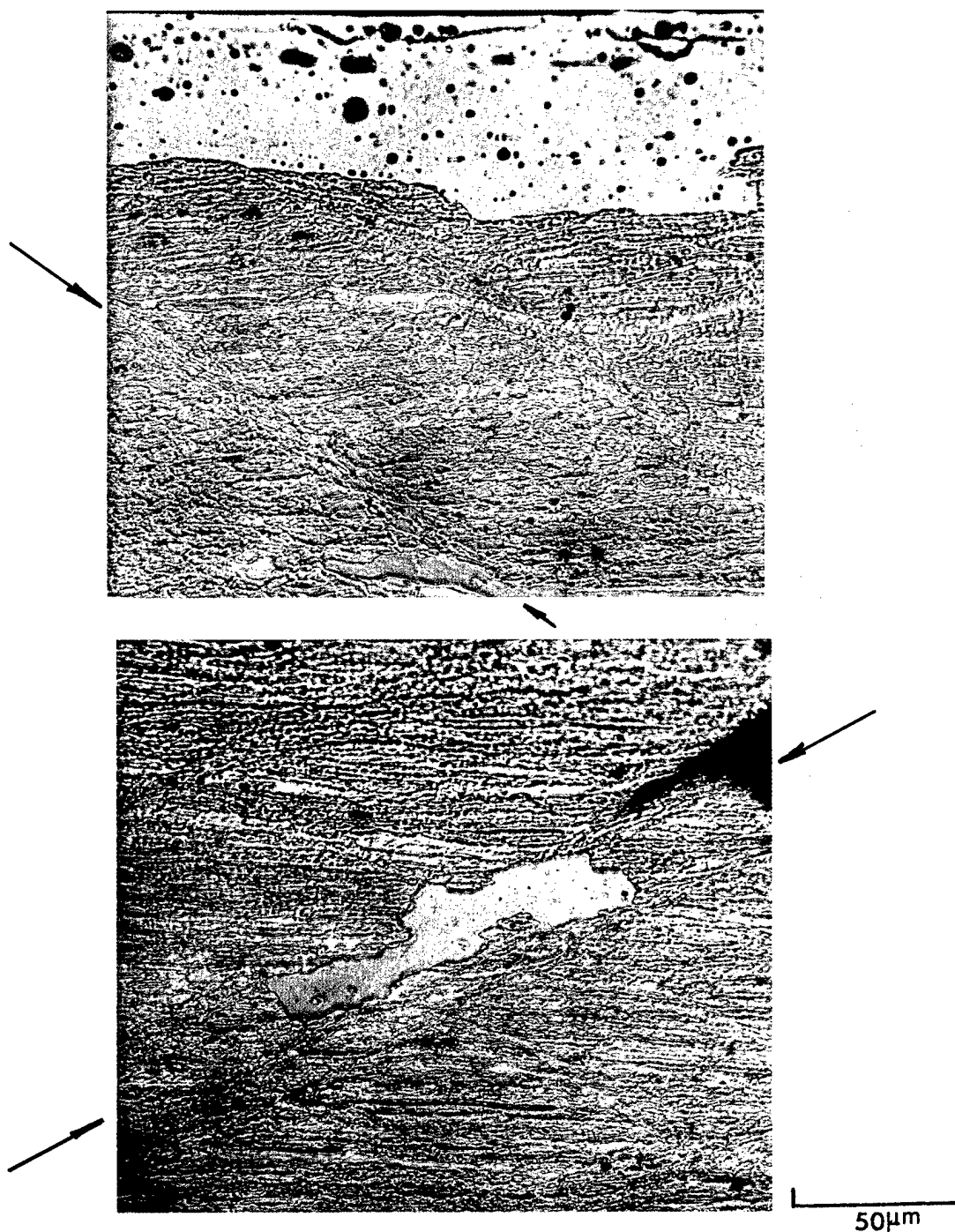
Figure 2-61.   Longitudinal Section of a Tensile Failure in
                Al-Li-Zr Sheet.   Evidence of small amount of
                recrystallization bands on deformation can
                be seen.
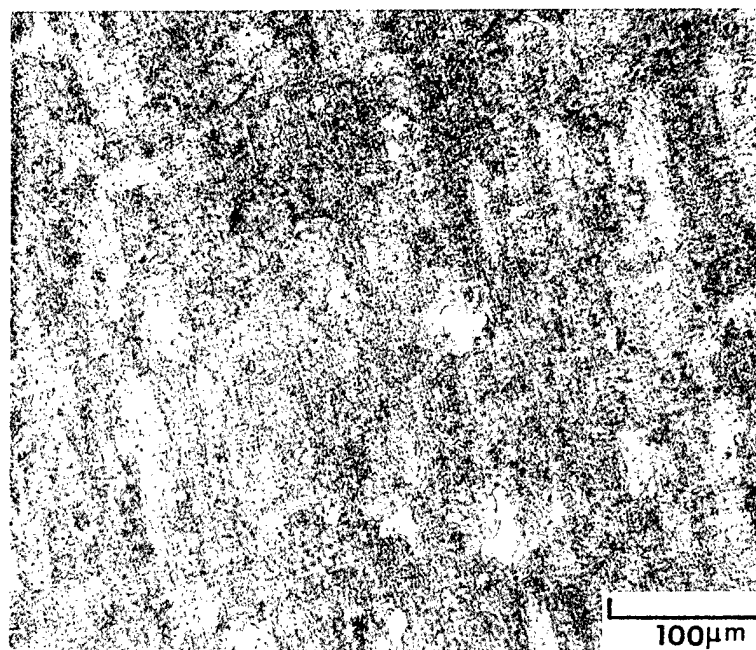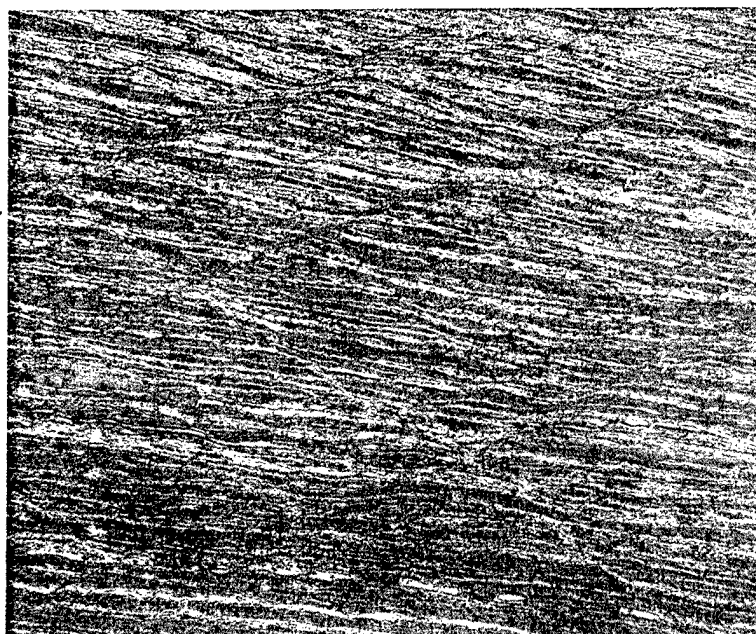
Figure 2-62. Surface and Longitudinal Section of Solution
              Heat Treated Al-Li-Zr Sheet. Deformation
              bands are evident.
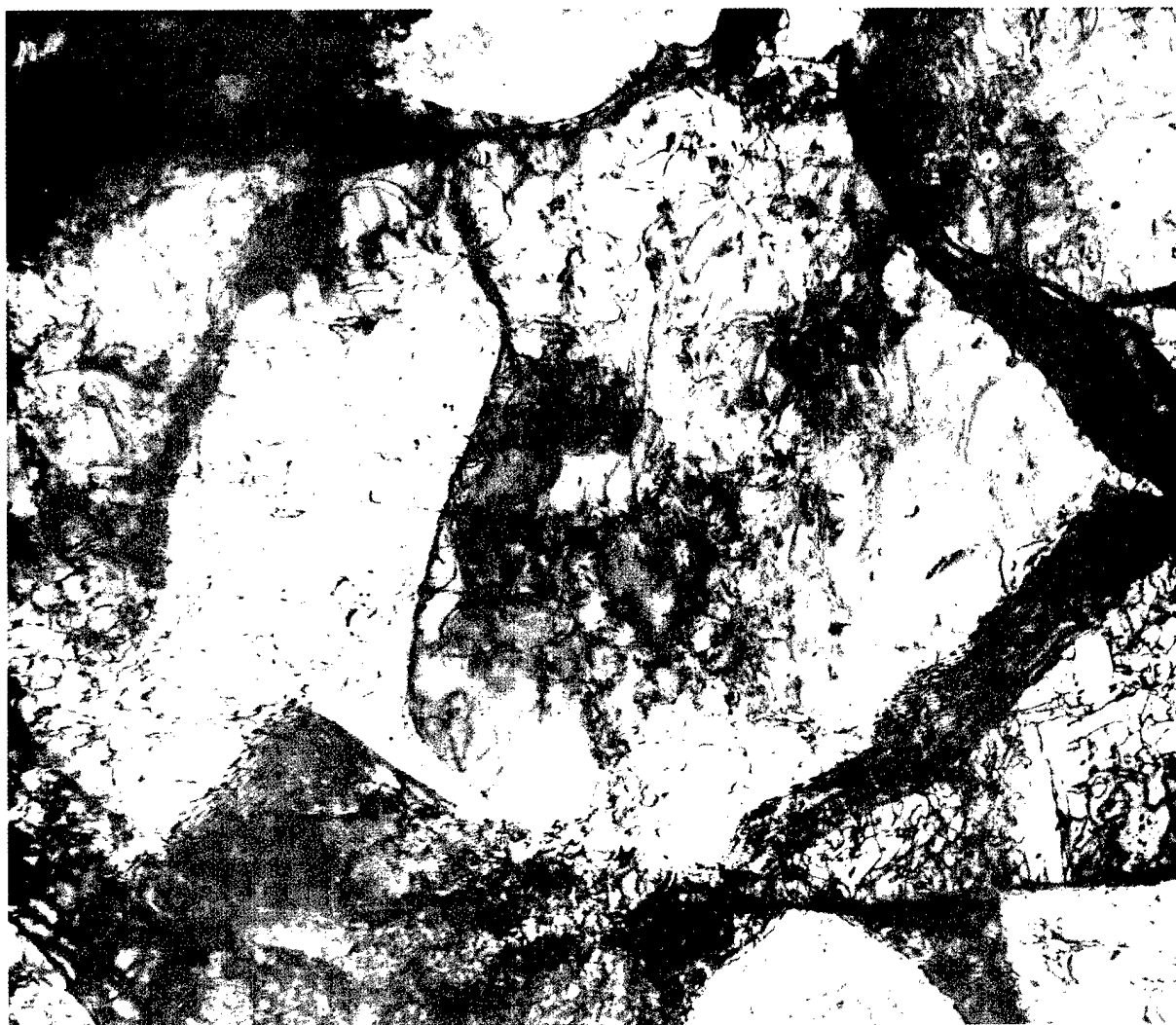
0.1μm

Figure 2-63. TEM of Al-Li-Zr Sheet Aged at 200°C for 0.25
Hours Pulled to Failure.

ALUMIUM
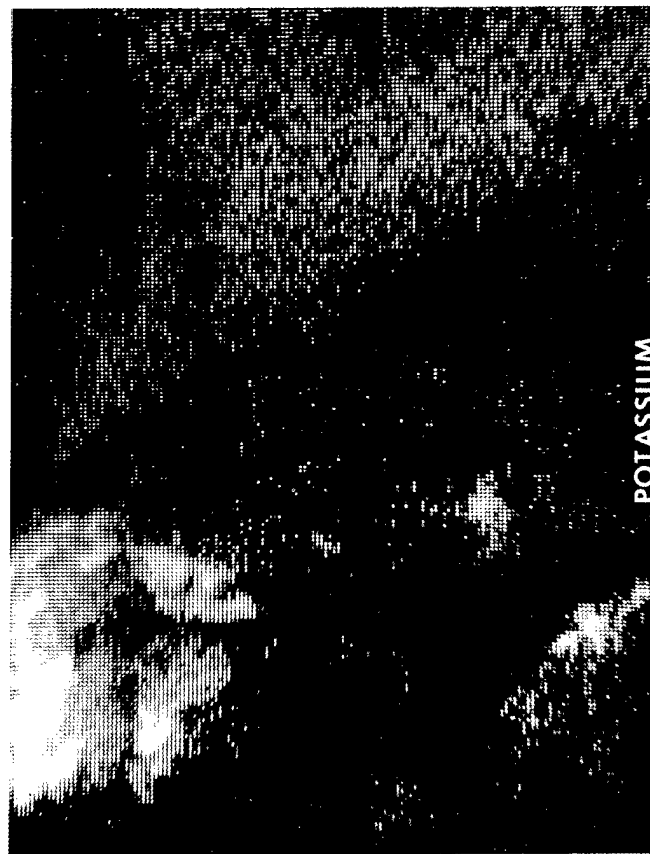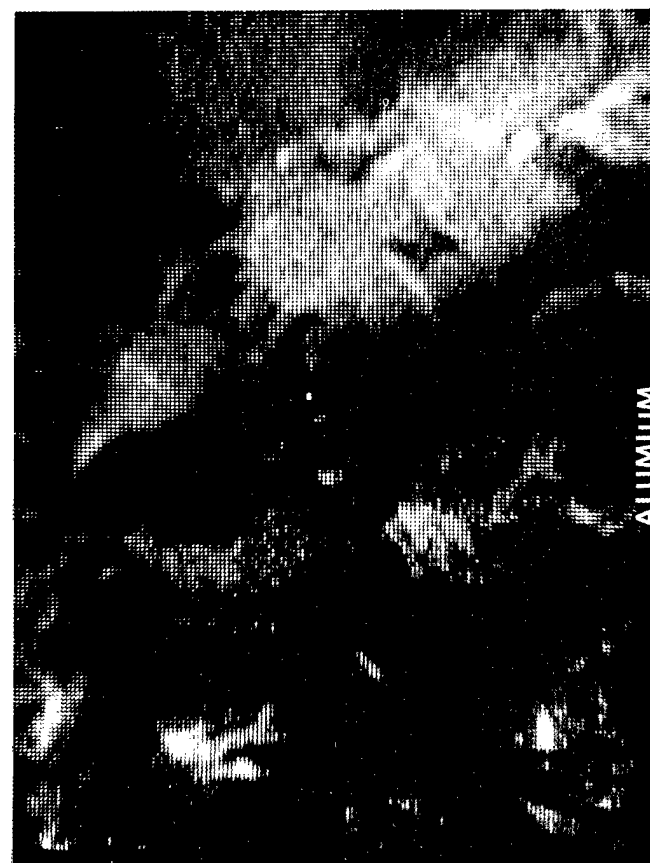
POTASSIUM

500X

Figure 2-64. (a) Scanning Electron Image and Scanning Auger Electron Images of (b) Potassium and (c) Aluminum on Fractured Al-Li-Zr Extrusion Aged to Peak Strength.
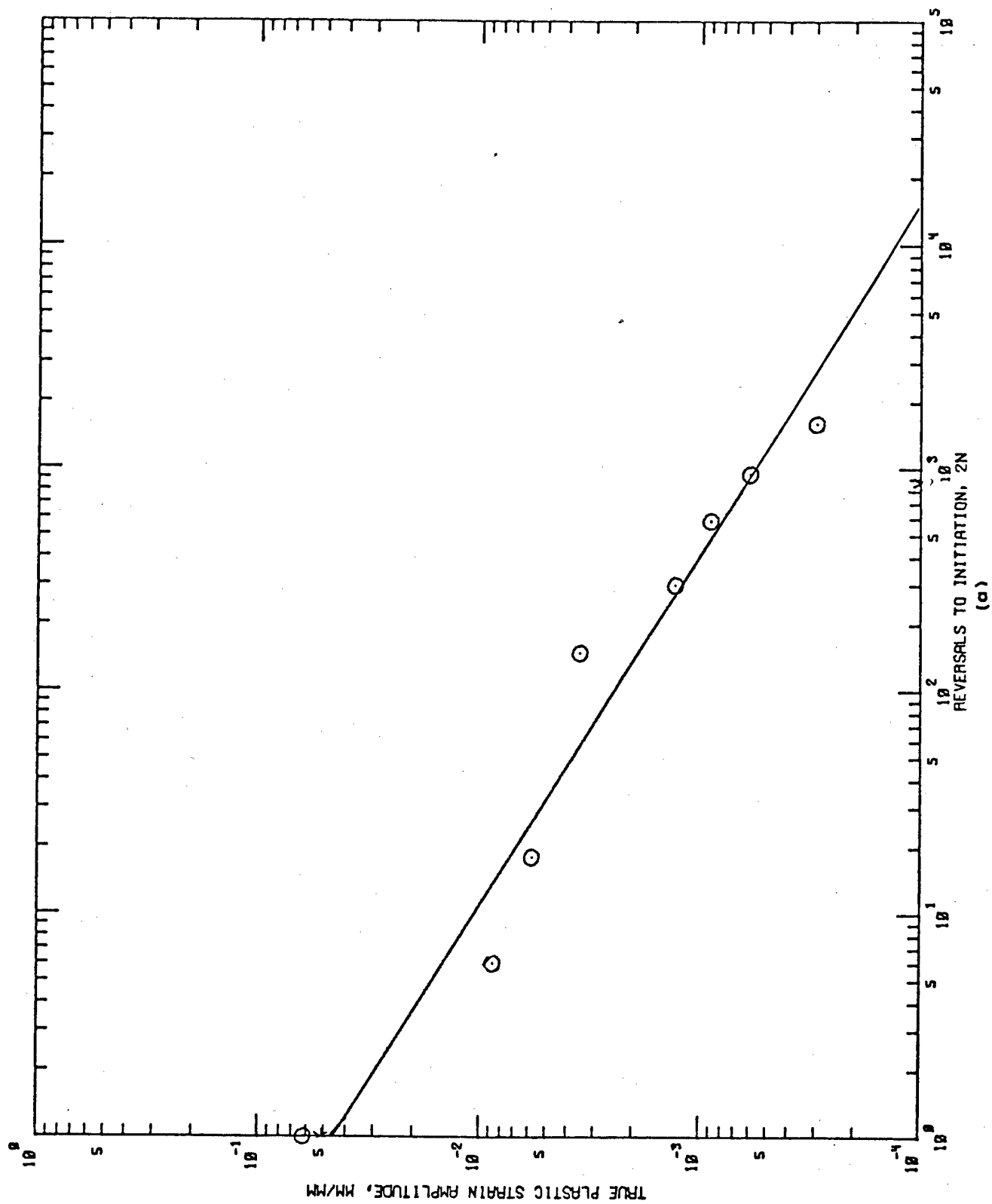
Figure 2-65. Coffin-Manson Plots of Specimens from Extrusions of (a) Al-Li-Mn Aged 4 hours at 200°C, (b) Aged 24 Hours at 200°C, (c) Al-Li-Zr Aged 4 Hours at 200°C, and (d) 24 Hours at 200°C.
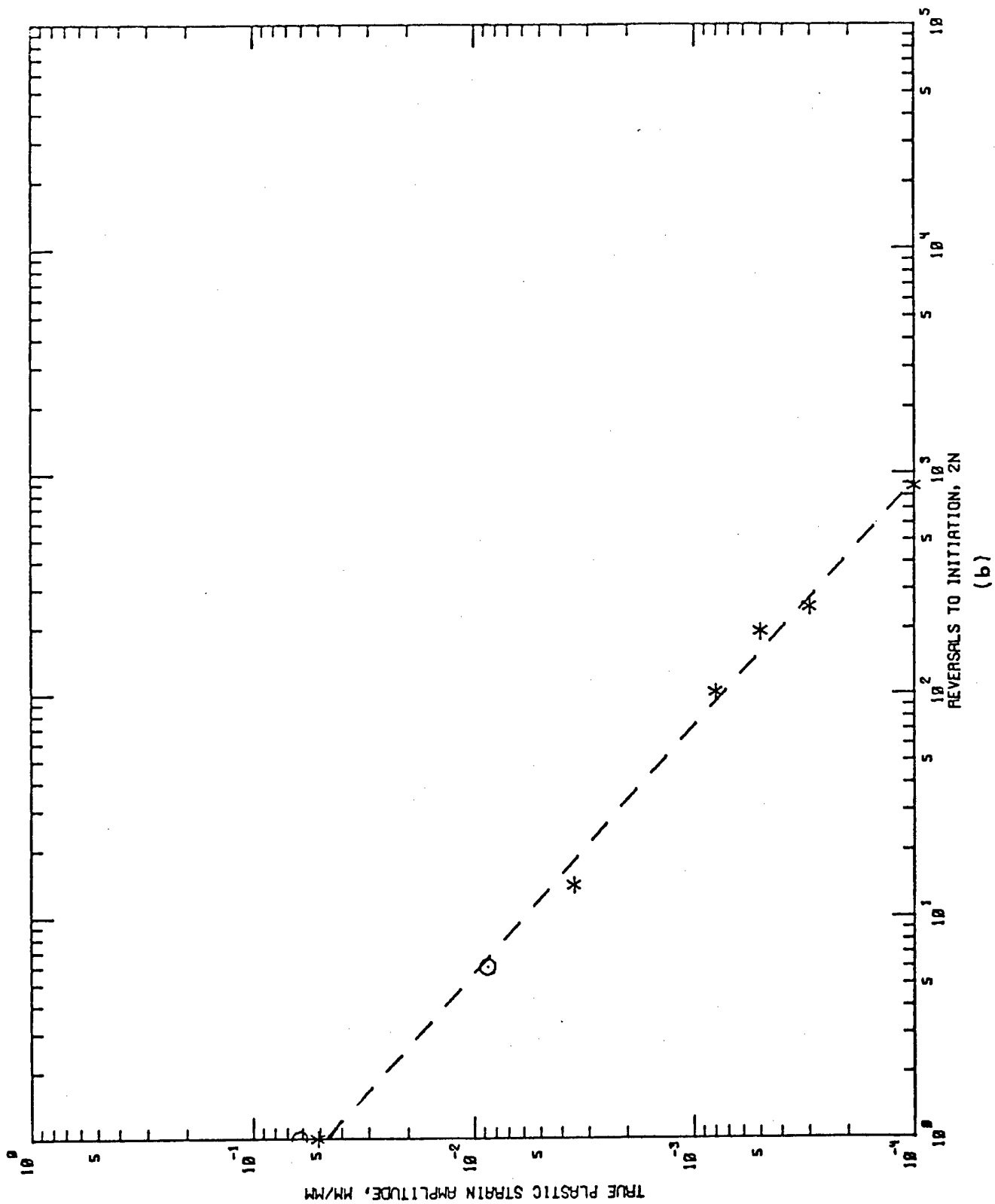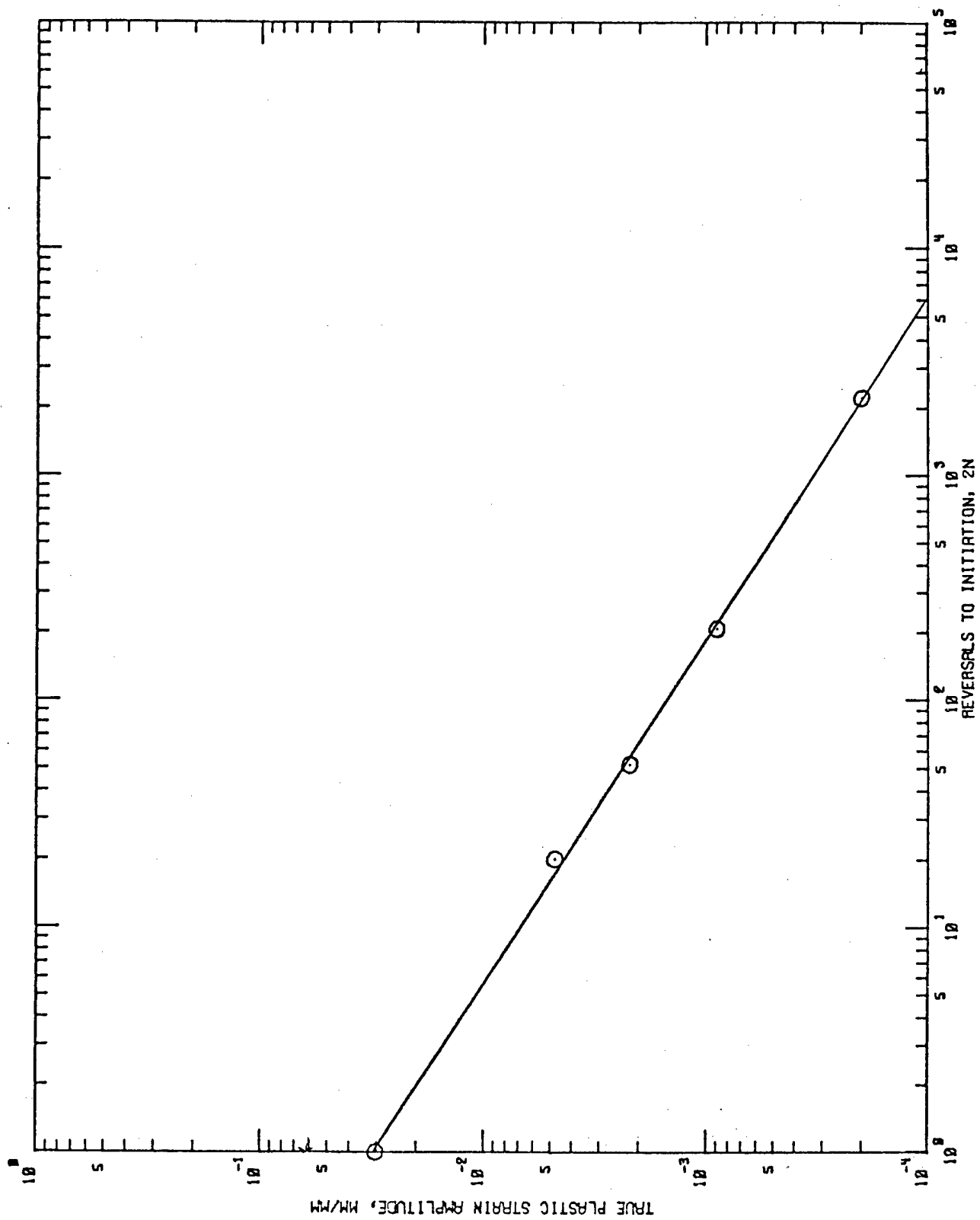
Figure 2-65. (Continued)

Figure 2-65. (Continued)
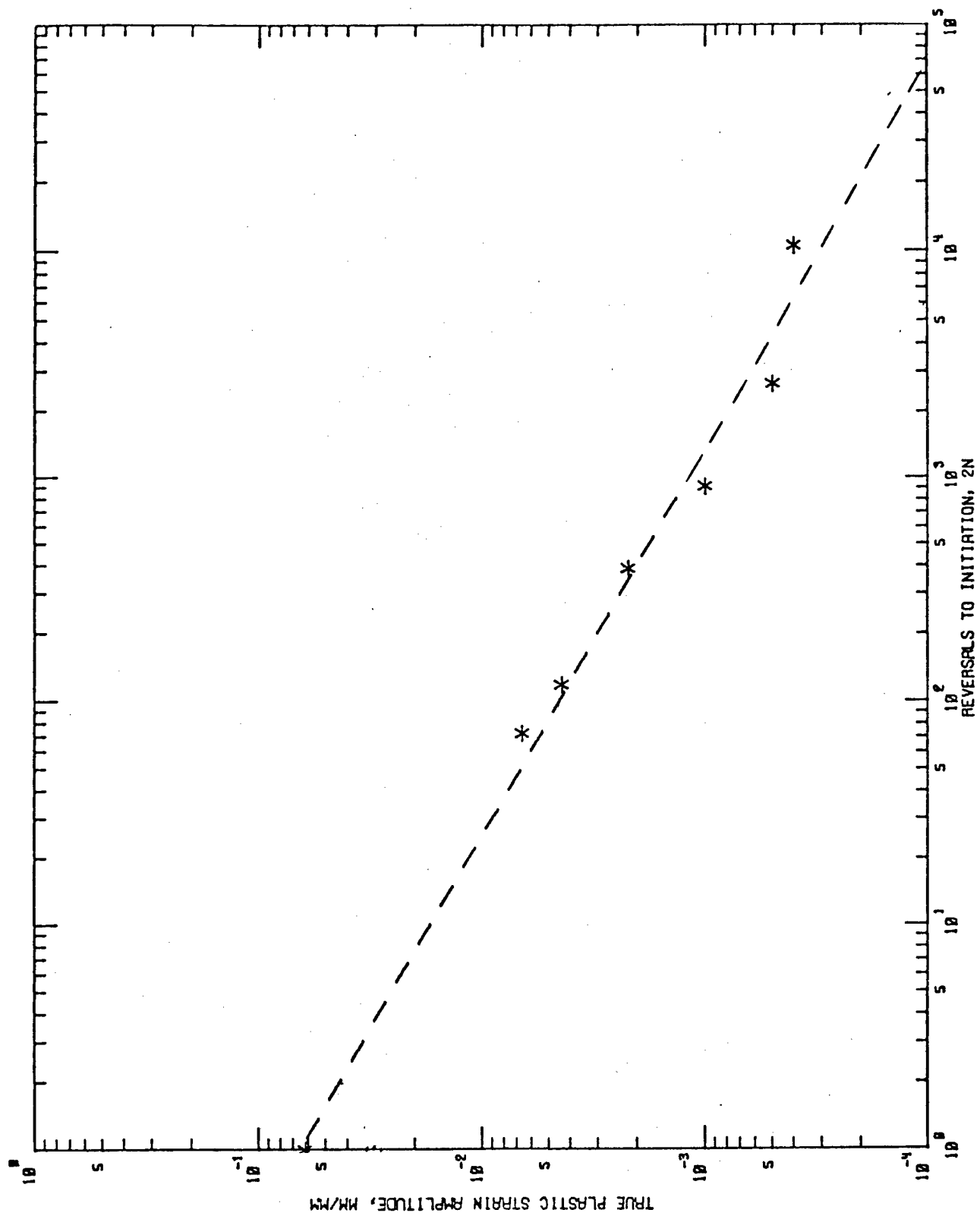
Figure 2-65. (Continued)
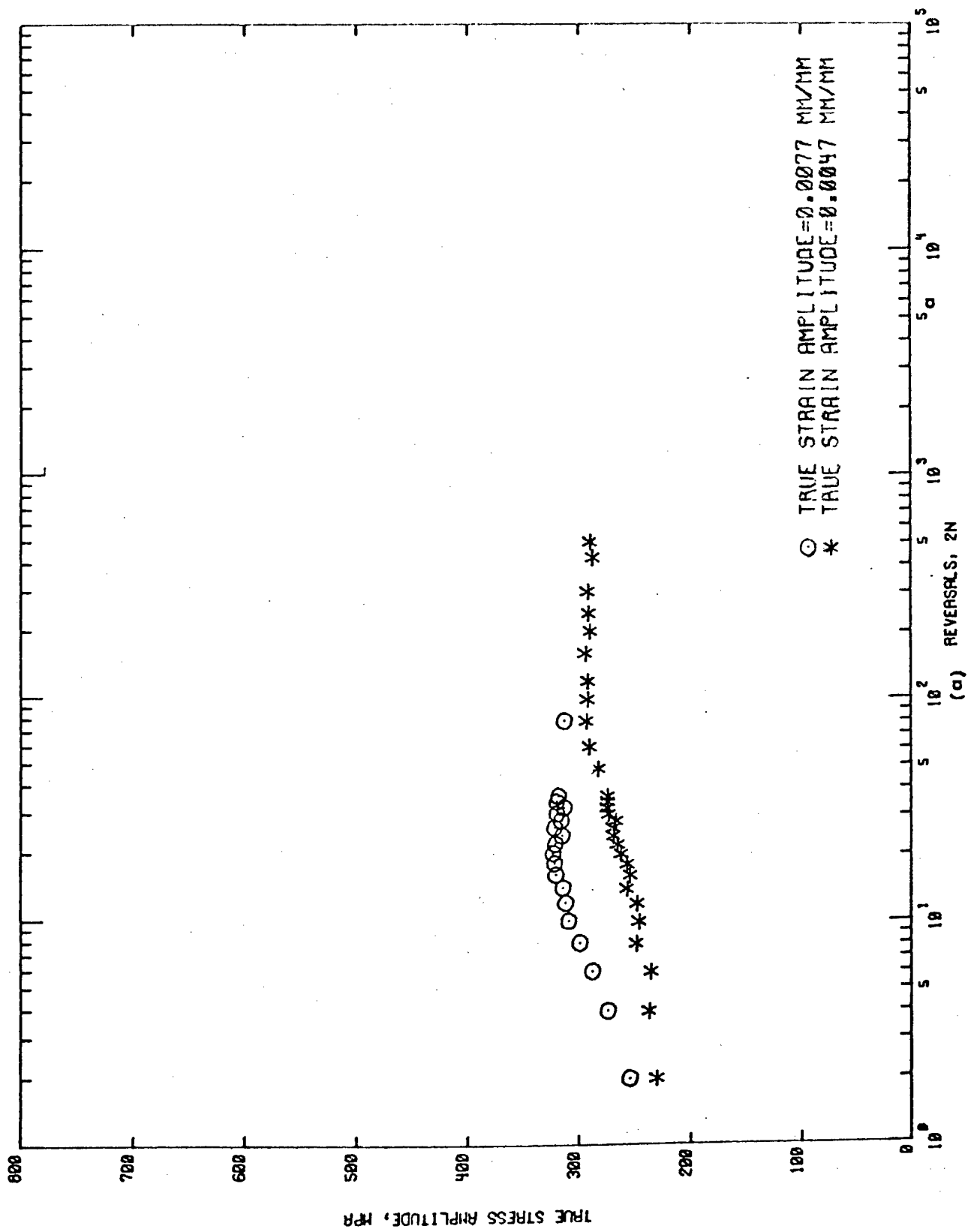
Figure 2-66. Cyclic Stress Responses of Specimens from
Extrusions of (a) Al-Li-Mn Aged 4 Hours at
200°C, (b) Aged 24 Hours at 200°C, (c) Al-Li-Zr
Aged 4 Hours at 200°C, and (d) 24 hours at
200°C.
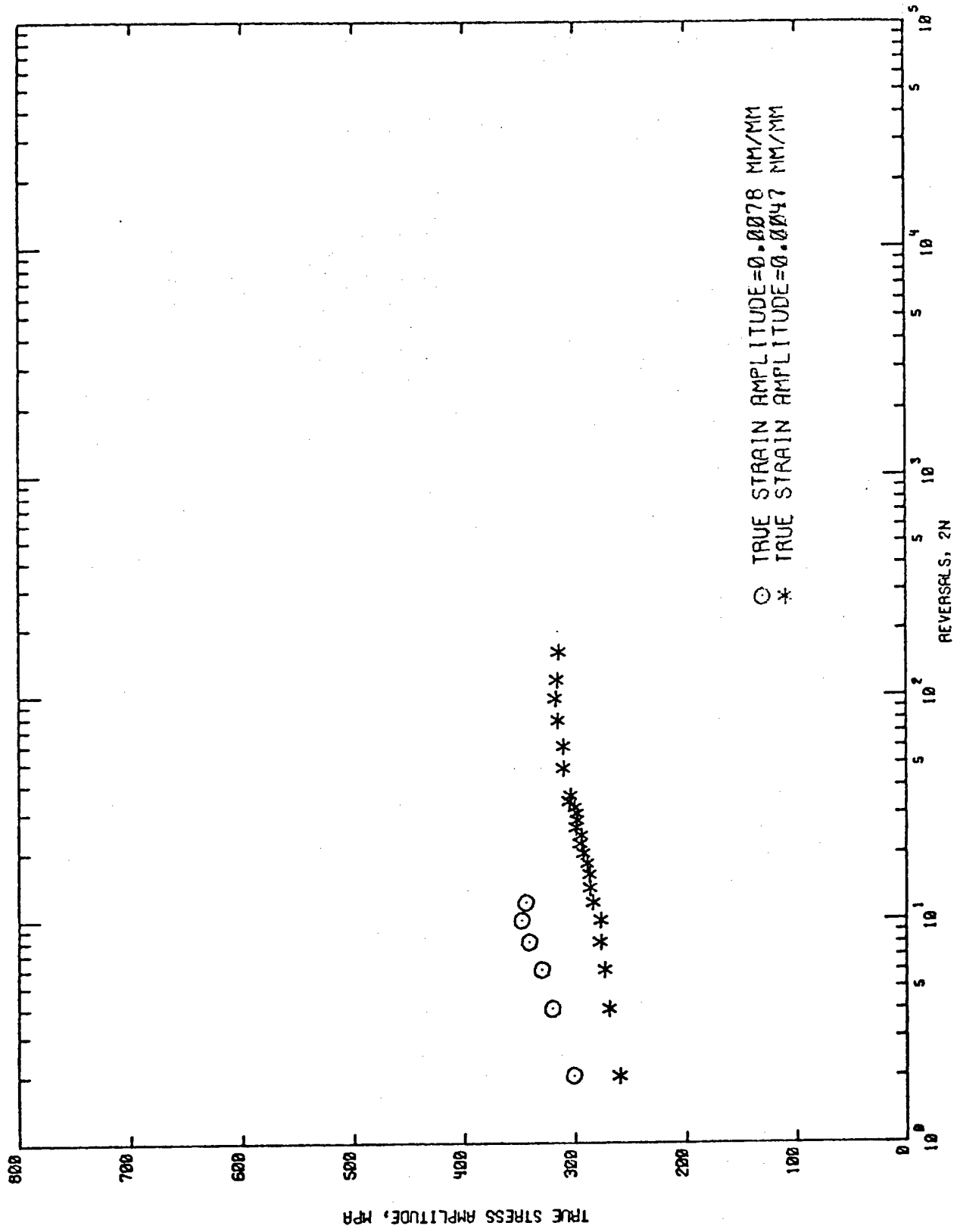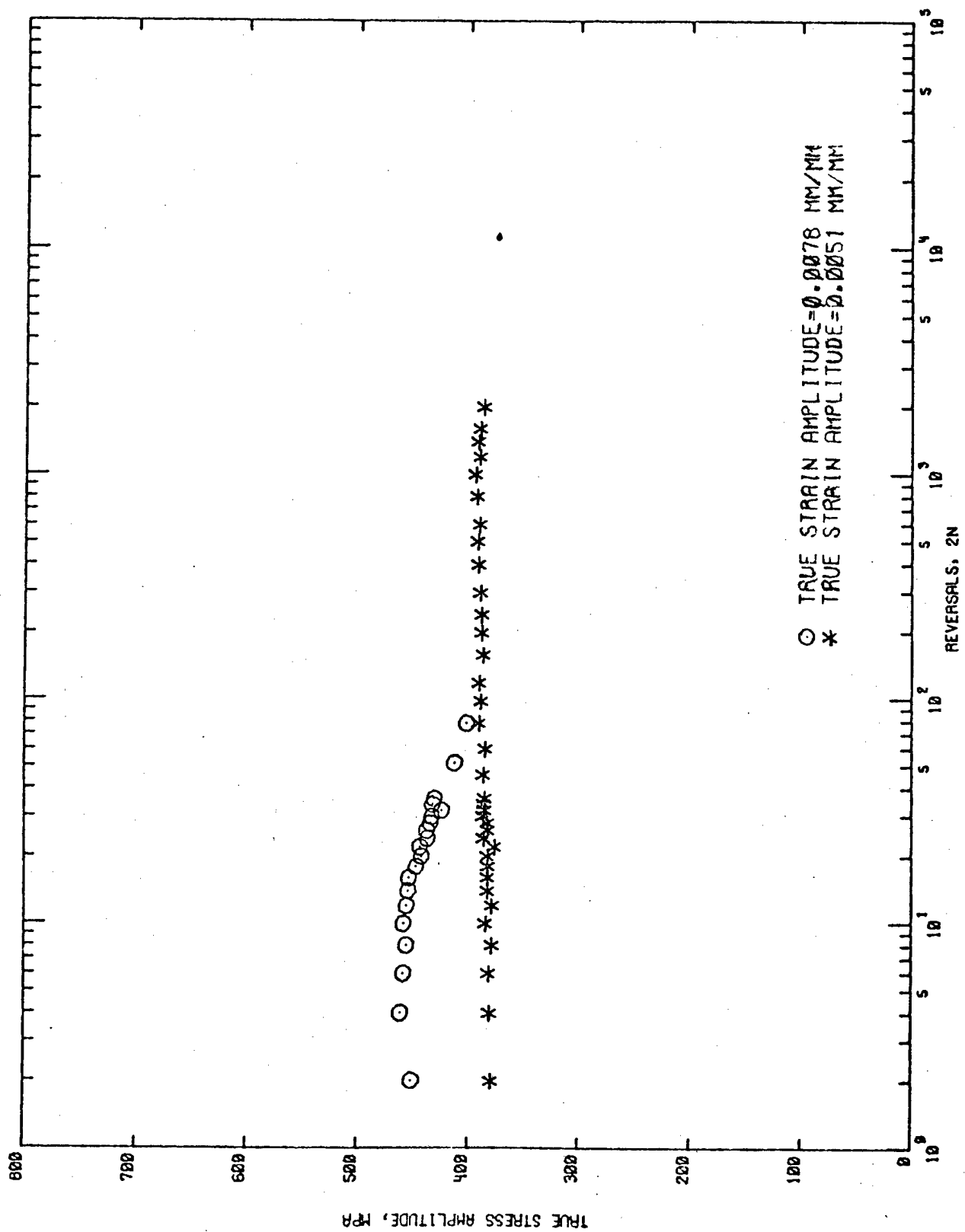
Figure 2-66. (Continued)

Figure 2-66. (Continued)
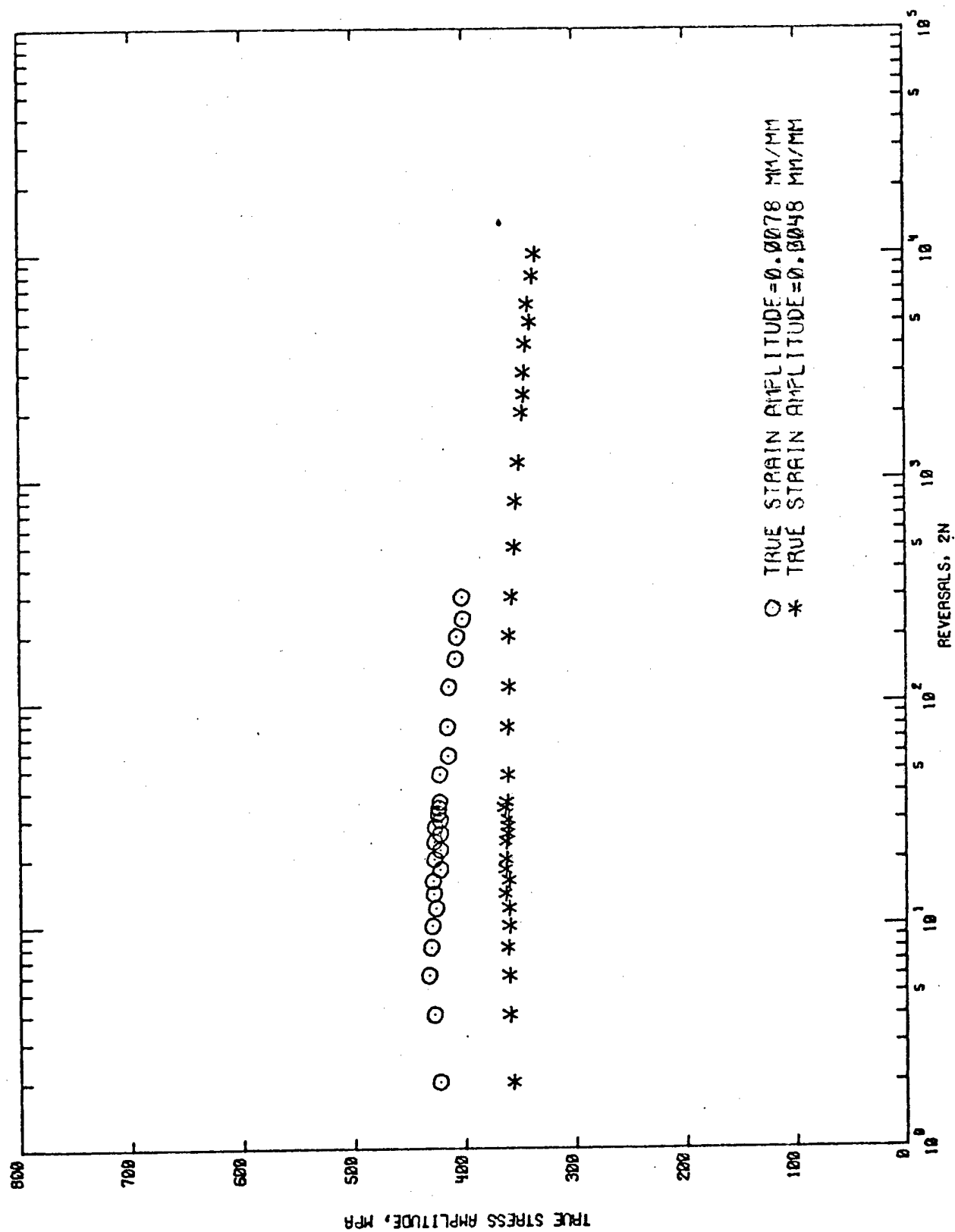
Figure 2-66.   (Continued)
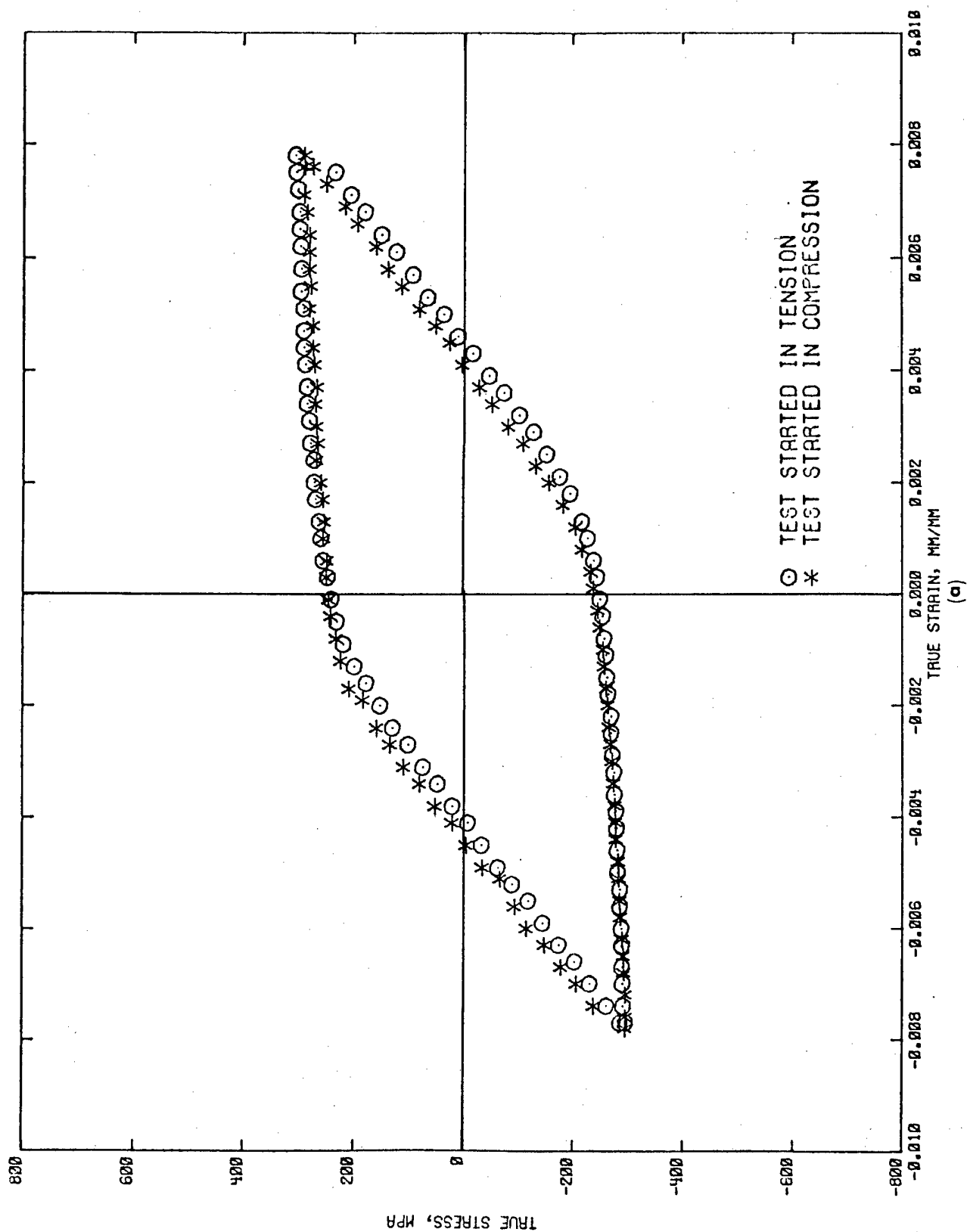
Figure 2-67. First Cycle Hysteresis Loop for (a) Al-Li-Mn
Aged 24 Hours at 200°C and (b) Al-Li-Zr Aged
24 Hours at 200°C.

TRUE STRESS, MPA

TRUE STRAIN, MM/MM

○ TEST STARTED IN TENSION
✳ TEST STARTED IN COMPRESSION

(b)
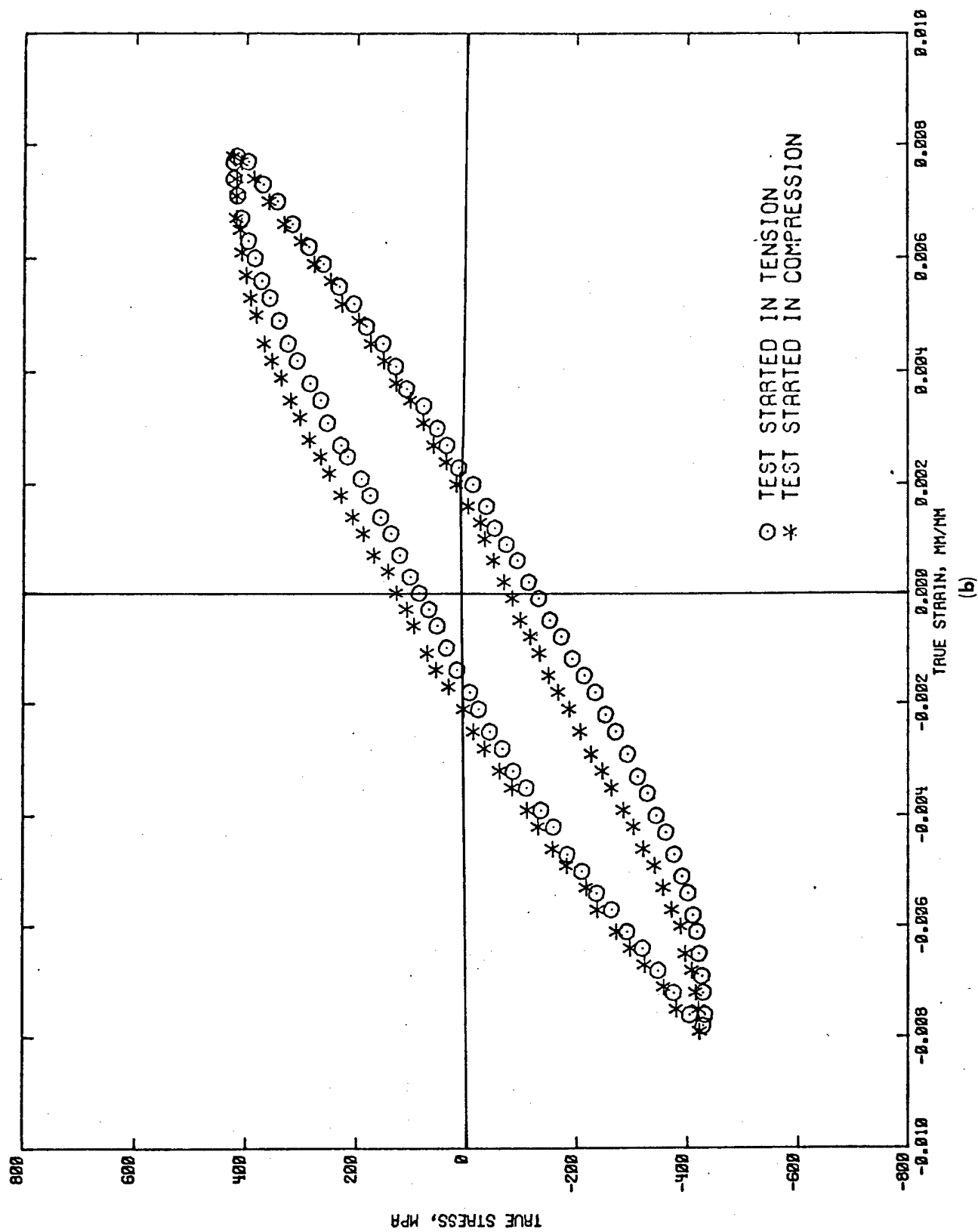
Figure 2-67. (Continued)
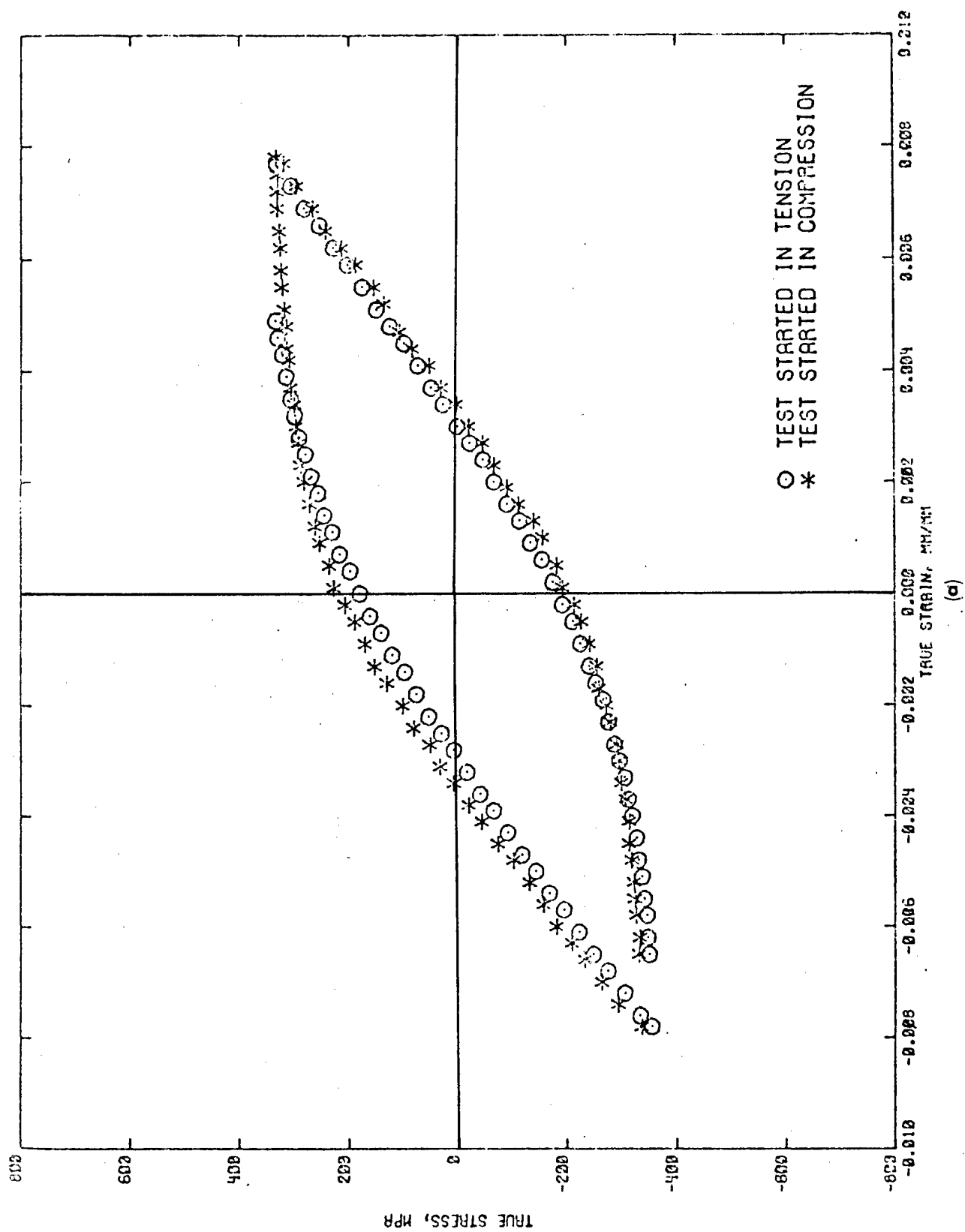
Figure 2-68. Half-Life Hysteresis Loop for (a) Al-Li-Mn Aged 24 Hours at 200°C and (b) Al-Li-Zr Aged 24 Hours at 200°C.

TRUE STRESS, MPA

TRUE STRAIN, MM/MM

⊙ TEST STARTED IN TENSION
✳ TEST STARTED IN COMPRESSION

(b)
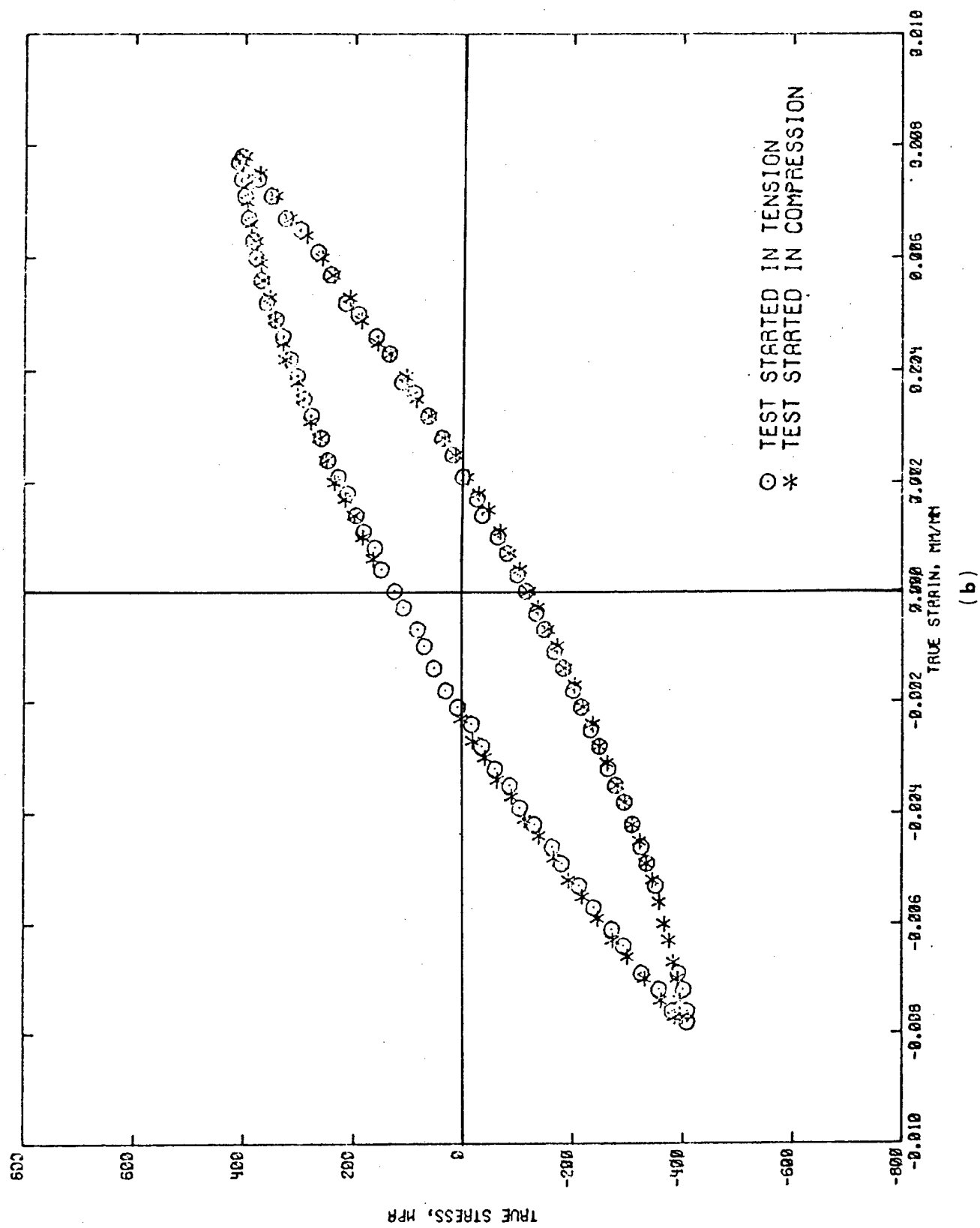
Figure 2-68. (Continued)

20X

100X

100X

Figure 2-69. SEM of Strain Control Fatigue Specimen of
Al-Li-Mn Aged 4 Hours at 200°C.

20X
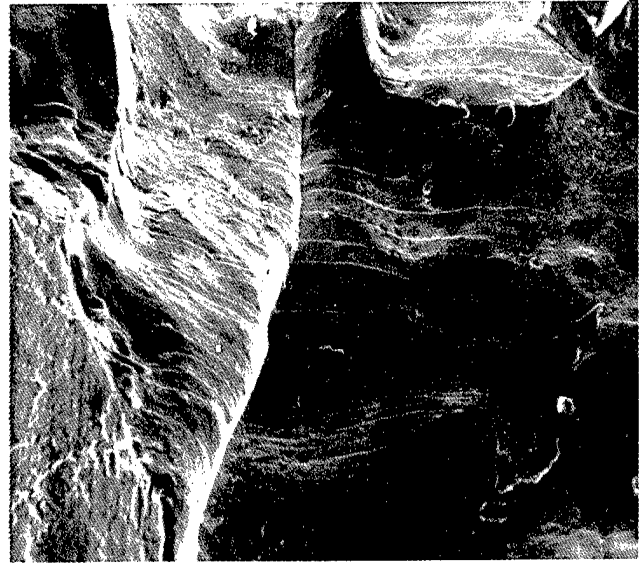
200X

100X
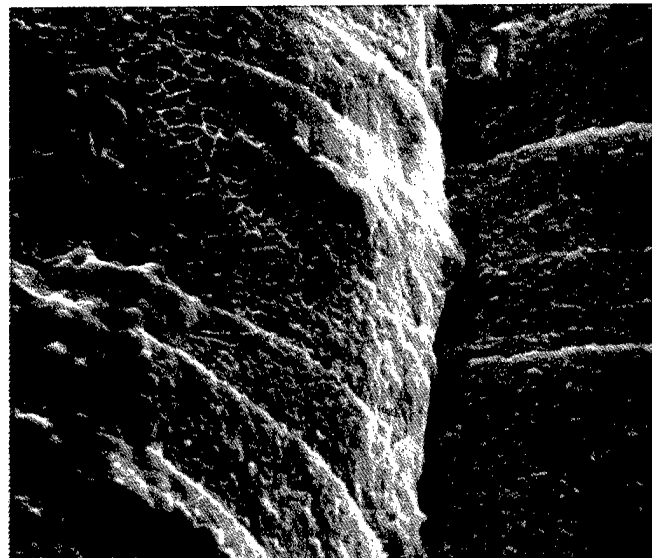
2000X

Figure 2-70. SEM of Strain Control Fatigue Specimen of
Al-Li-Mn Aged 24 Hours at 200°C.
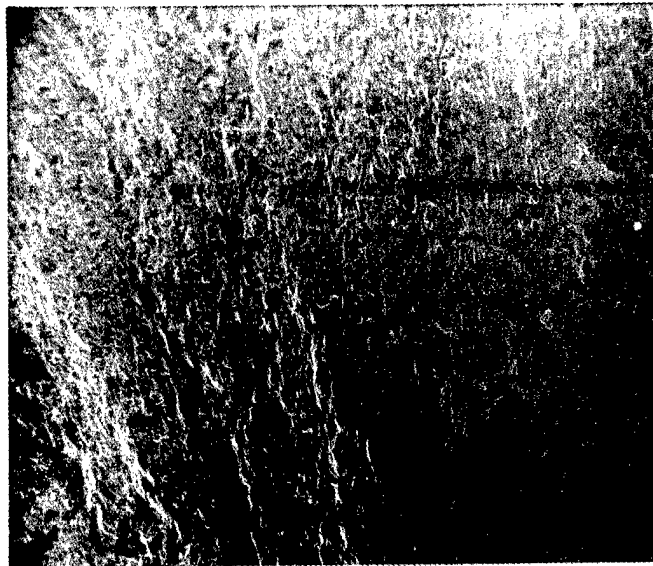
20X

200X

1000X

Figure 2-71. SEM of Strain Control Fatigue Specimen of
Al-Li-Zr Aged 4 Hours at 200°C.
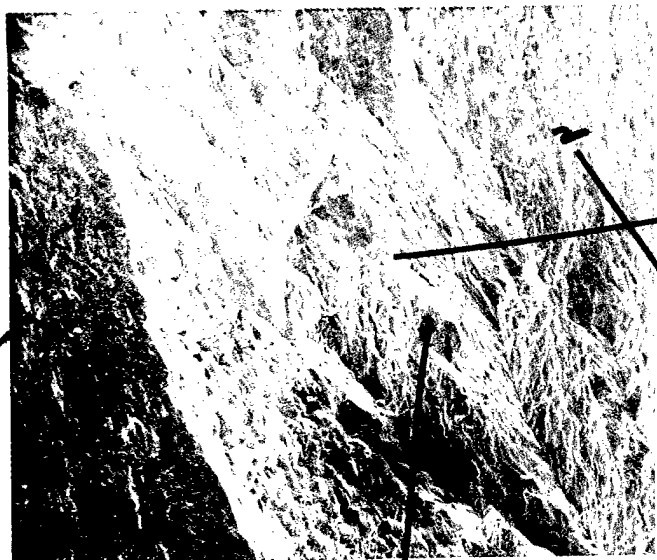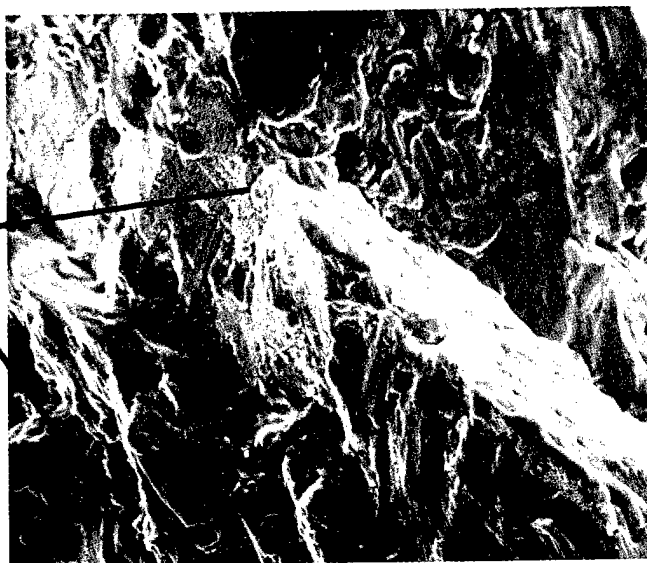
Figure 2-72. SEM of Strain Control Fatigue Specimen of
Al-Li-Zr Aged 24 Hours at 200°C.

(a)

(b)

LONG. 1.4X

Figure 2-73. Photographs Illustrating the Attack of Al-Li-Mn Extrusions in (a) 5% NaCl Spray and (b) MASTMAASIS After One Week Exposure.
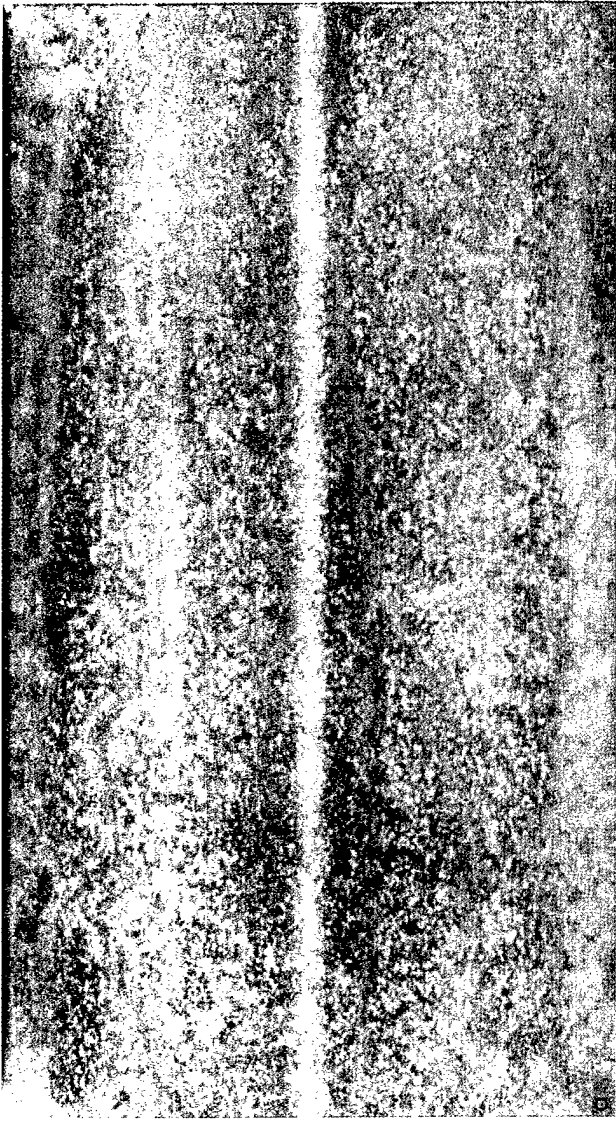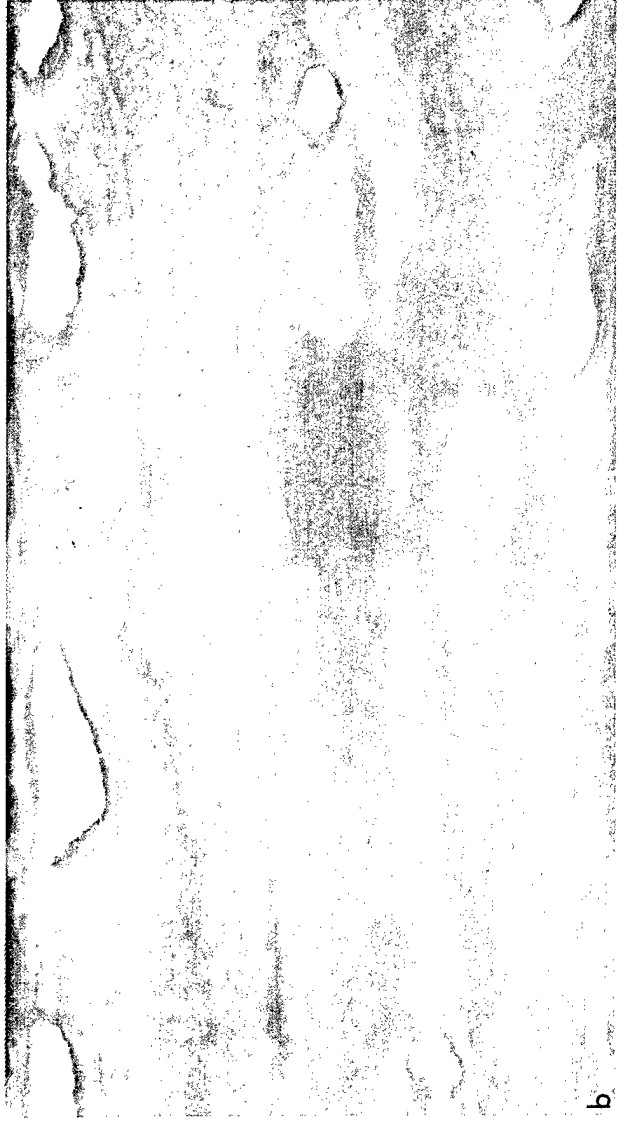
LONG. 14X

Figure 2-74. Photographs Illustrating the Attack of Al-Li-Zr Extrusions in (a) 5% NaCl Spray and (b) MASTMAASIS After One Week Exposure.

Appendix 2A

Evaluation of the Corrosion Performance of Al-Li Alloys

ABSTRACT

Al-Li-Zr and Al-Li-Mn alloy extrusions were evaluated for resistance to corrosion. Results indicate that although no significant changes in characteristic potentials were made by alloying with lithium, the alloys showed remarkably good resistance to intergranular, exfoliation, and pitting corrosion in three different electrolytes. Resistance to corrosion was particularly good in 3.5% NaCl solution. Results obtained in accelerated corrosion tests were confirmed and rationalized by laboratory testing.

MATERIALS

Alloys evaluated were of the following compositions:

(1) Al-2.78 Li-0.32 Mn (S. No. 454103A)

(2) Al-2.76 Li-0.14 Zr (S. No. 454104B)

Both extrusions were solution heat treated 1/2 hour at 551.5°C (1025°F), cold water quenched, and aged 24 hours at 200°C (392°F). The Al-Li-Mn alloy was fully recrystallized with a grain size of about 1 ASTM. The Al-Li-Zr alloy, on the other hand, was unrecrystallized.

EXPERIMENTAL

The following tests were conducted:

a. <u>Potentiokinetic Anodic Polarization Curves</u> in the following electrolytes: deaerated 3-1/2% NaCl (pH~6), deaerated MASTMAASIS solution (5% NaCl solution acidified to pH 3 with acetic acid) and deaerated ASSET solution (40 gms/lit NH_4Cl, 20 gms/lit NH_4NO_3 and 1.8 gms/lit ammonium tartrate). All curves were obtained at a speed of 20 mv/min after allowing 1/2 hour soak time to attain a steady corrosion potential.

b. <u>Solution Potential</u> measurements were made in standard $NaCl-H_2O_2$ solutions (53 gms/lit NaCl and 10 cc/lit 30% H_2O_2).

c. <u>Corrosion Potential</u> measurements were made as a function of exposure time in the three solutions mentioned earlier. Tests were continued for over 3 weeks, and the electrolytes were aerated by bubbling air.

d. <u>Potentiostatic Polarization</u> was made in the three electrolytes at potentials approximately 50 mv more active than the pitting potentials of the alloys in a given electrolyte (as determined from anodic polarization curves). Tests were continued for 72 to 96 hours, and currents recorded.

RESULTS AND DISCUSSION

a. <u>Potentiokinetic Anodic Polarization Curves</u> for the two alloys in three deaerated electrolytes are shown in Figures 1 - 6. The anodic behavior of the two alloys is identical in a given electrolyte, in that the ranges of passivity and the breakdown potentials are the same. They vary, as expected, from one electrolyte to another depending

upon their aggressiveness. In comparison with the more common
aluminum alloys in these electrolytes, the anodic behaviors of
these two extrusions do not vary appreciably. Bearing in mind
that breakdown potential and critical pitting potential, although
not the same, are reasonably close in high-chloride solutions, it
can be concluded that the resistance to pitting corrosion of these
alloys, measured solely on the basis of pitting potential values,
are not superior to the more common alloys. However, as is shown
later, defining resistance to pitting corrosion based on pitting
potential values could often be misleading.

   b. <u>Solution Potential</u> measurements for the two alloys were
made in standard electrolytes containing 53 gms/lit NaCl and
10 cc/lit 30% H_2O_2. Results are given in Table I. The values
obtained are similar to those for pure aluminum.

   c. <u>Variation of Corrosion Potential with Exposure Time</u>.
It is important to note that the values of pitting potentials, by
themselves, do not necessarily indicate the susceptibility to
pitting corrosion. A high (more noble) pitting potential does
not necessarily mean high pitting resistance. In order to
obtain information about the pitting corrosion susceptibility, it
is necessary to compare the pitting potential with the open circuit
(or corrosion) potential and its variation with exposure time.

   Pitting, under conditions of natural immersion, occurs only
when the corrosion potential is equal to or greater (more noble)
than the pitting potential of the alloy in that electrolyte. The
number and size of pits observed in a naturally immersed specimen can

be rationalized in terms of the potential difference $\Delta E = E_{CORR} - E_{Pitting}$. As mentioned earlier, for pits to nucleate under conditions of natural immersion, ΔE must be equal to or greater than zero for a certain length of time, and this time must at least be sufficient for pits to nucleate. Once pits nucleate, anodic polarization, in general, is progressively reduced and the corrosion potential drifts to more active values. When the corrosion potential becomes lower (more active) than the pitting potential, no new pits nucleate. The growth of existing pits, however, can be sustained at potentials lower than $E_{Pitting}$, i.e., when ΔE is negative. Although existing pits continue to grow at potentials more active than $E_{Pitting}$, the growth rate diminishes as E_{CORR} becomes more active, i.e., as ΔE becomes more negative.

The results obtained in this investigation are shown in Figure 7. It is obvious from the figure that in aerated MASTMAASIS and ASSET solutions, the corrosion potential remains close to the pitting potentials of these alloys in these electrolytes. The pitting potentials in these electrolytes are -670 mV$_{SCE}$ (ASSET) and -780 mV$_{SCE}$ (MASTMAASIS). In aerated 3-1/2% NaCl solution, however, the potential remains active compared to the pitting potential (-765 mV$_{SCE}$) and continues to more active values with exposure time. However, in the very initial stages of exposure ($\sim$3 to 4 hours), the corrosion potential does reach the pitting potential, as shown in Figure 8. But after the initial four hours, the potential drifts back to active values and ΔE ($= E_{CORR} = E_{Pitting}$) reaches very negative values.

From our understanding of the inter-relationship between pitting potentials and corrosion potentials, we would expect the Al-Li alloys to undergo pitting corrosion in aerated MASTMAASIS and ASSET solutions, simply because:

(a) the corrosion potential does become at least equal to the pitting potential, hence, pits can nucleate, and

(b) E ($= E_{CORR} - E_{Pitting}$) does not become too negative, and hence, pit growth can be sustained.

Figures 9 and 10, showing the nature and depth of attack during exposure to MASTMAASIS solution, illustrate the point. Although the extent of corrosion is little, pits do nucleate and grow. Similar corrosion was observed on specimens exposed to aerated ASSET solution.

However, no corrosion was observed on specimens exposed for over 3 weeks in aerated 3-1/2% NaCl. This is consistent with corrosion potential measurements in that pits probably did nucleate during the time E_{corr} was equal to $E_{pitting}$, but since E_{corr} became significantly more active than $E_{pitting}$, pit growth could not be sustained.

c. <u>Potentiostatic Polarization</u> experiments were conducted on these alloys to determine their susceptibility to intergranular and exfoliation corrosion. The alloys were polarized at potentials approximately 50 mv below (more active than) their pitting potentials in a given electrolyte (as obtained from anodic polarization curves), and held at that potential for 96 hours.

The objective of such a potentiostatic polarization tests
is to accentuate the galvanic differences between two phases, if
any, eventually leading to either intergranular or exfoliation
corrosion. Since the specimen is held below its breakdown
potential, no pitting occurs and the matrix remains passivated.
If we assume that the polarization characteristics of the two
phases (matrix and Al-Li precipitate) are different, then the
corrosion currents at a given potential for these two phases
would be different. Prolonged exposure at this potential would
then lead to intergranular and/or exfoliation corrosion provided
that the Al-Li precipitates are anodic to the matrix and that the
precipitate morphology is favorable for sustained localized
corrosion.

The results of potentiostatic polarization tests with Al-Li
alloys are shown in Figure 11. From the values of currents
obtained after about 70 hours testing (20-60 ua/cm^2), it is apparent
that neither alloy is susceptible to intergranular corrosion in
either ASSET or 3.5% NaCl solution.

The plot of current density against polarization time consists
of two parts. The first part, extending to as high as 20 hours,
may be construed as the incubation time necessary to establish
the galvanic potential difference between the different phases.
The rapid increase in current density in the second part of the
curve represents the corrosion current, and it is made up of both
the corrosion of the matrix and the precipitate. However, since

the polarization potential is below the breakdown potential of the matrix, the corrosion rate of the matrix is extremely low ($5-10$ μa/cm^2) and the bulk of this current is from the dissolution of the precipitates.

It is obvious that the currents are extremely low, especially so for Al-Li-Zr in 3.5% NaCl solution. This is consistent with the corrosion potential variation of this alloy in 3.5% NaCl solution. Since the corrosion potential drifts almost immediately below the pitting potential, it can be concluded that the anodic current from precipitate dissolution was extremely low. This fact is now confirmed by potentiostatic polarization. After about 70 hours of polarization, specimens showed only superficial damage.

CONCLUSIONS

(1) Although no significant change in pitting potential was affected by alloying with Li, the alloys tested showed extremely high resistance to pitting in NaCl solution.

(2) The alloys tested, Al-Li-Zr in particular, showed very high resistance to intergranular and exfoliation corrosion.

TABLE 2A-1

STANDARD SOLUTION POTENTIAL MEASUREMENTS FOR Al-Li
ALLOY EXTRUSIONS*

| Time (min.) | Potential (vs N/10 Calomel Electrode)** | | | |
| | Al-Li-Mn | | Al-Li-Zr | |
	#1	#2	#1	#2
5	-831	-834	-846	-852
10	-826	-830	-842	-846
15	-821	-824	-841	-843
20	-826	-822	-841	-841
25	-822	-820	-840	-841
30	-827	-824	-841	-842
60	-830	-820	-846	-846

*Solution contains 53 gm/lit NaCl and 10 cc/lit 30% H_2O_2.

**OmV (N/10 Calomel Electrode) = +81 mV (saturated calomel electrode)
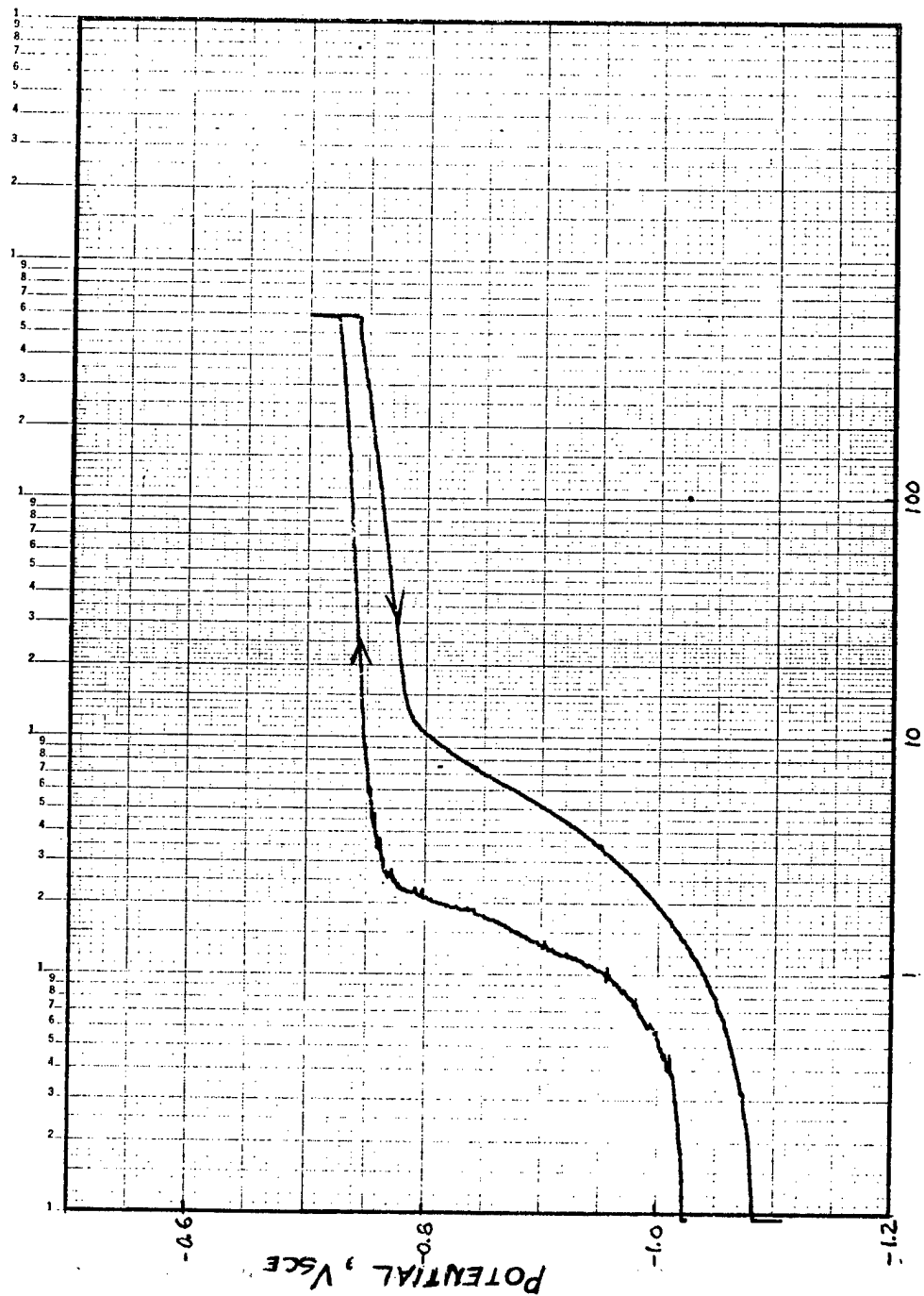
Figure 1. Anodic polarization curve for Al-Li-Zr alloy in deaerated 3 1/2% NaCl solution. Breakdown potential = -765 mVSCE.
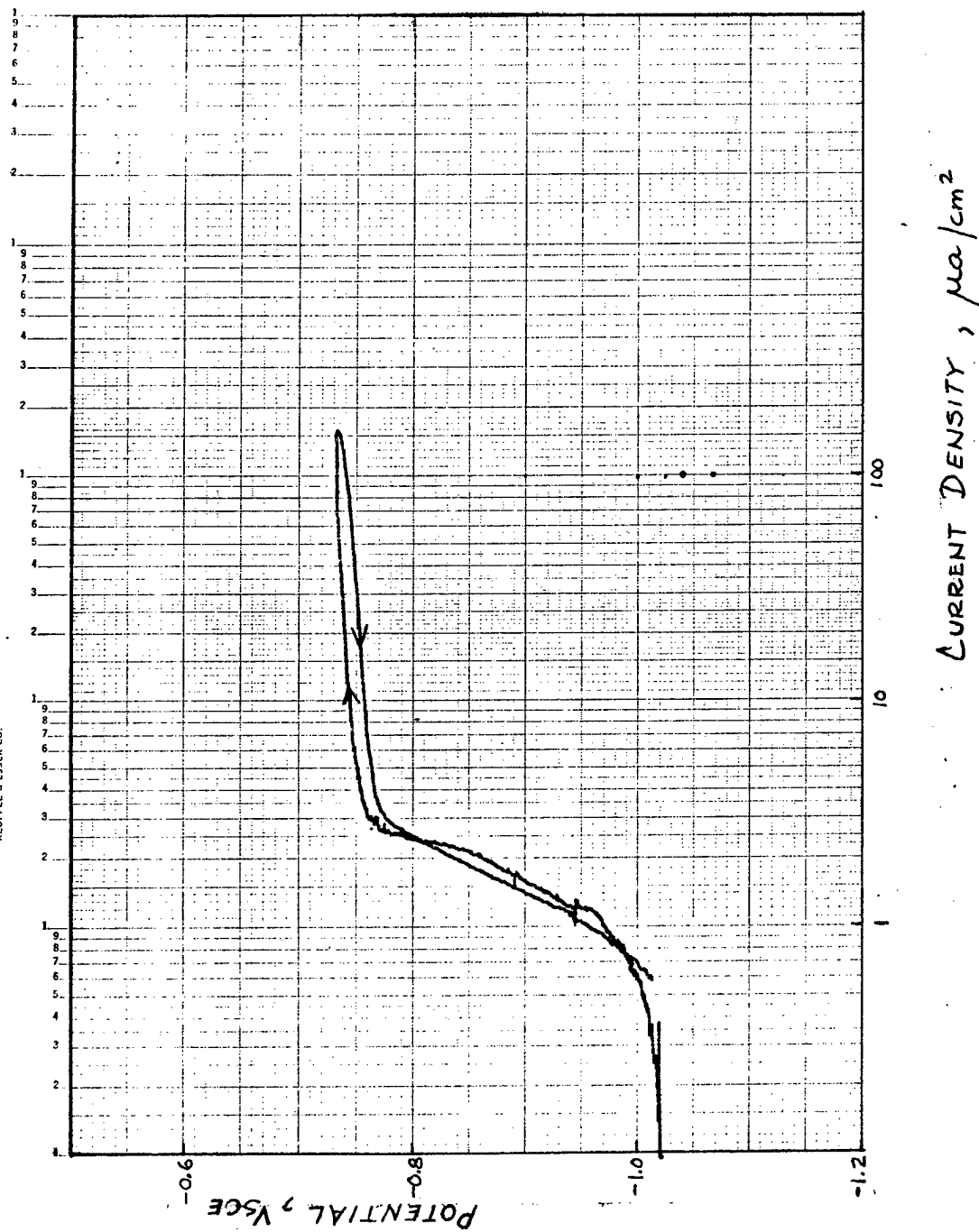
Figure 2. Anodic polarization curve for Al-Li-Mn alloy in deaerated 3 1/2% NaCl solution. Breakdown potential = -765 mV$_{SCE}$.
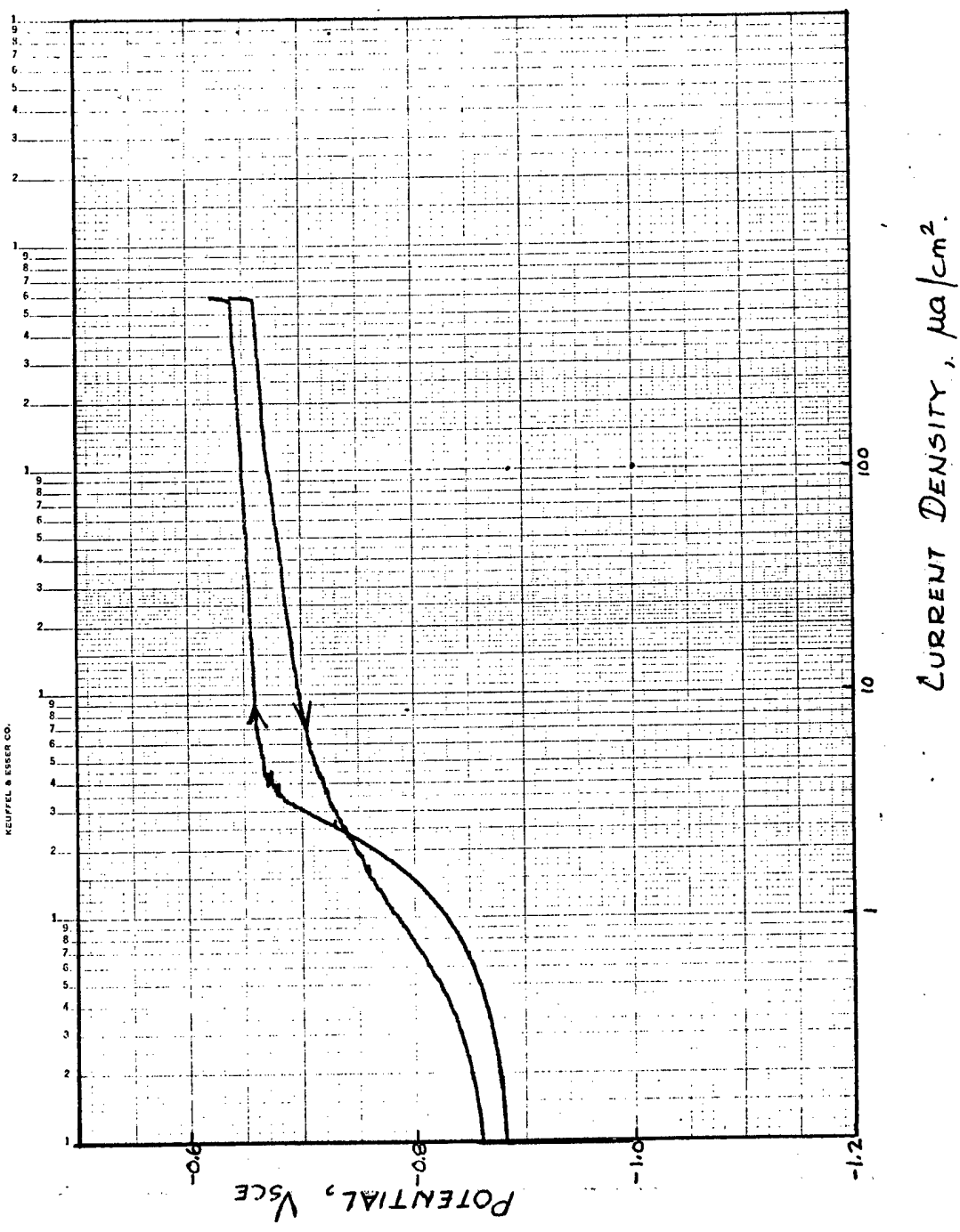
Figure 3. Anodic polarization curve for Al-Li-Zr alloy in deaerated ASSET solution (without H_2O_2). Breakdown potential = -670 mV_{SCE}.
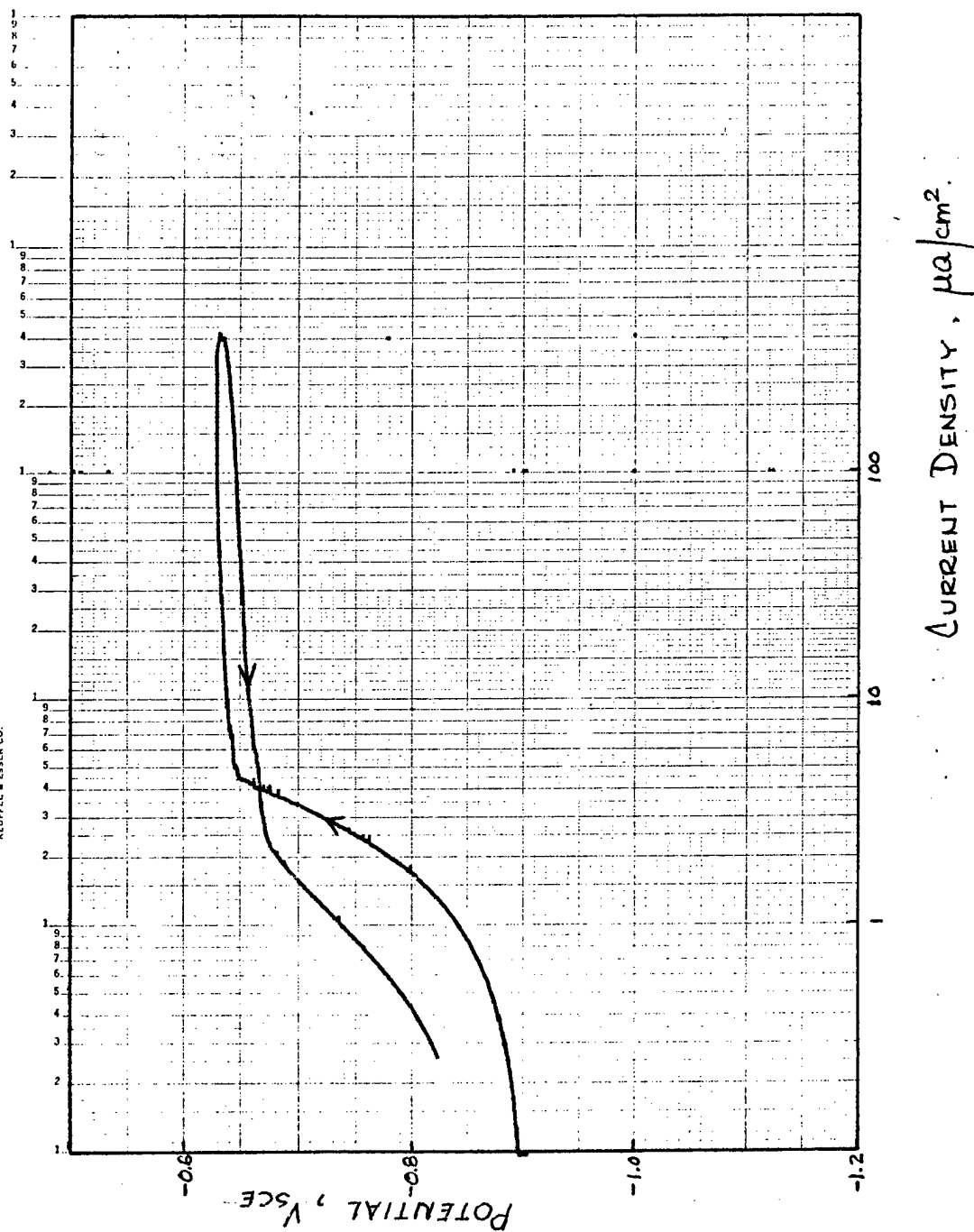
Figure 4.   Anodic polarization curve for Al-Li-Mn alloy in deaerated ASSET
solution (without H_2O_2).   Breakdown potential = -650 mV_{SCE}.
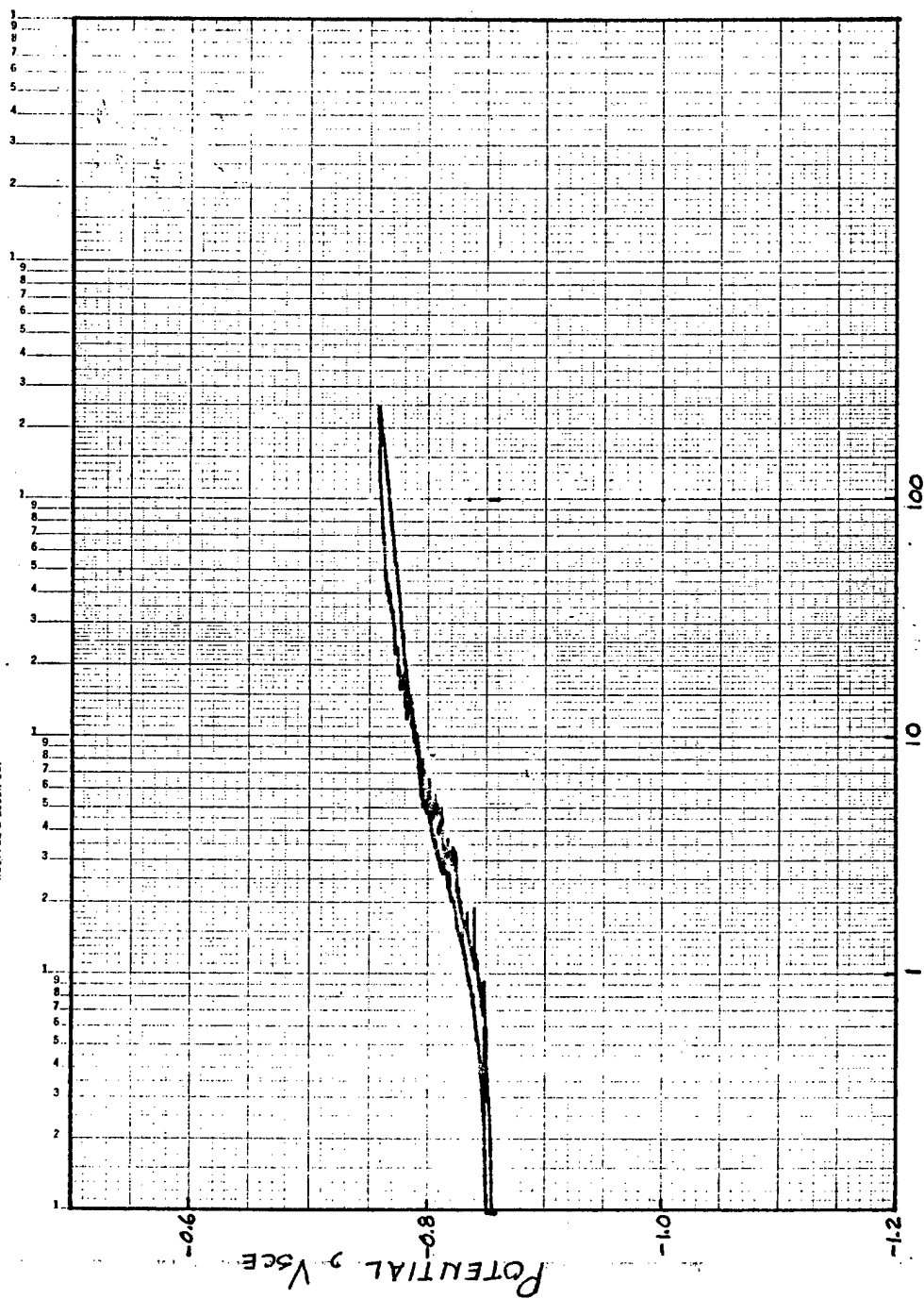
Figure 5. Anodic polarization curve for Al-Li-Zr alloy in deaerated MASTMAASIS solution. Breakdown potential = -800 mVSCE.
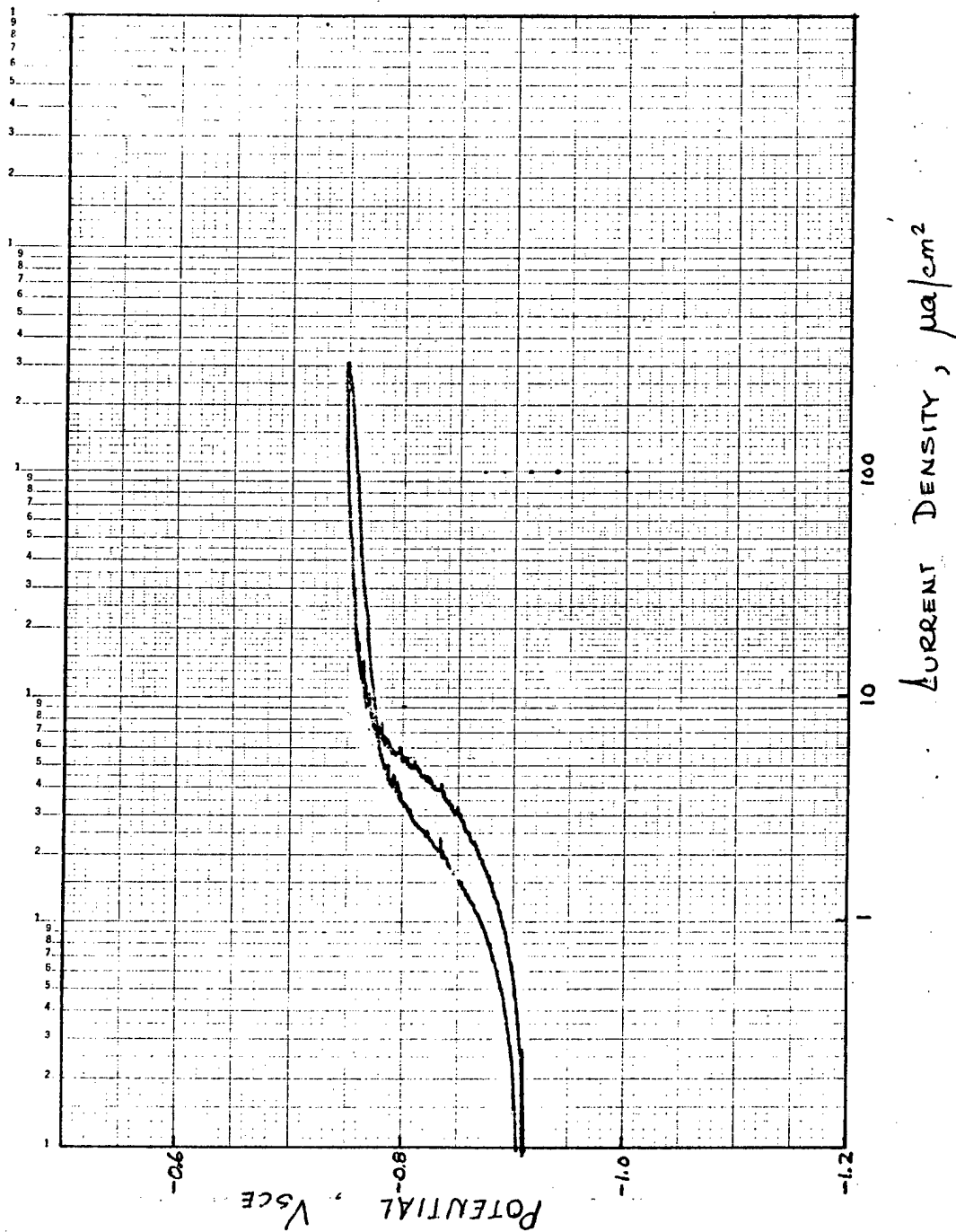
Figure 6. Anodic polarization curve for Al-Li-Mn alloy in deaerated MASTMAASIS solution. Breakdown potential = -790 mV$_{SCE}$.
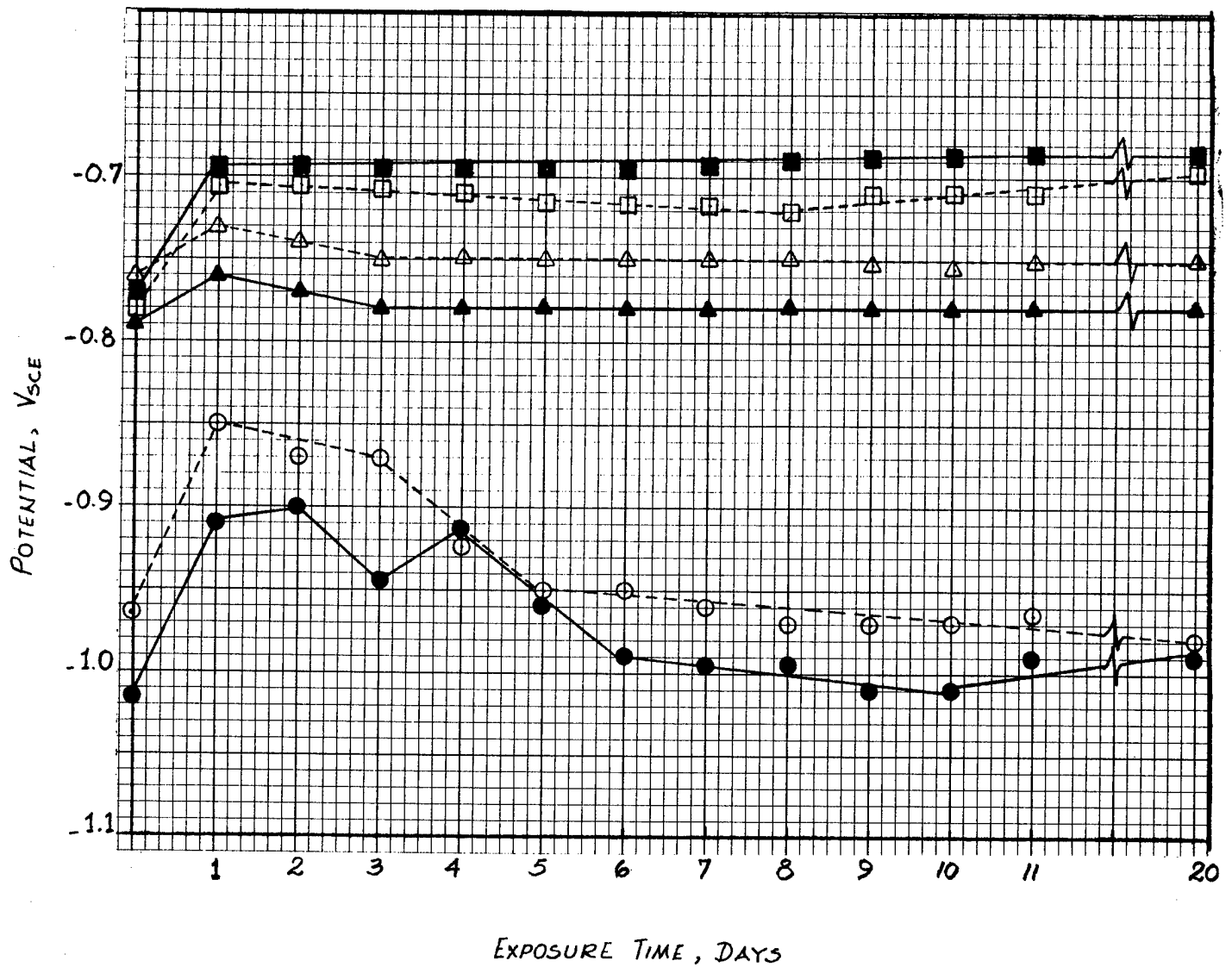
Figure 7. Variation of corrosion potential of Al-Li alloys in aerated 3 1/2% NaCl solution, MASTMAASIS solution and ASSET solution with exposure time.
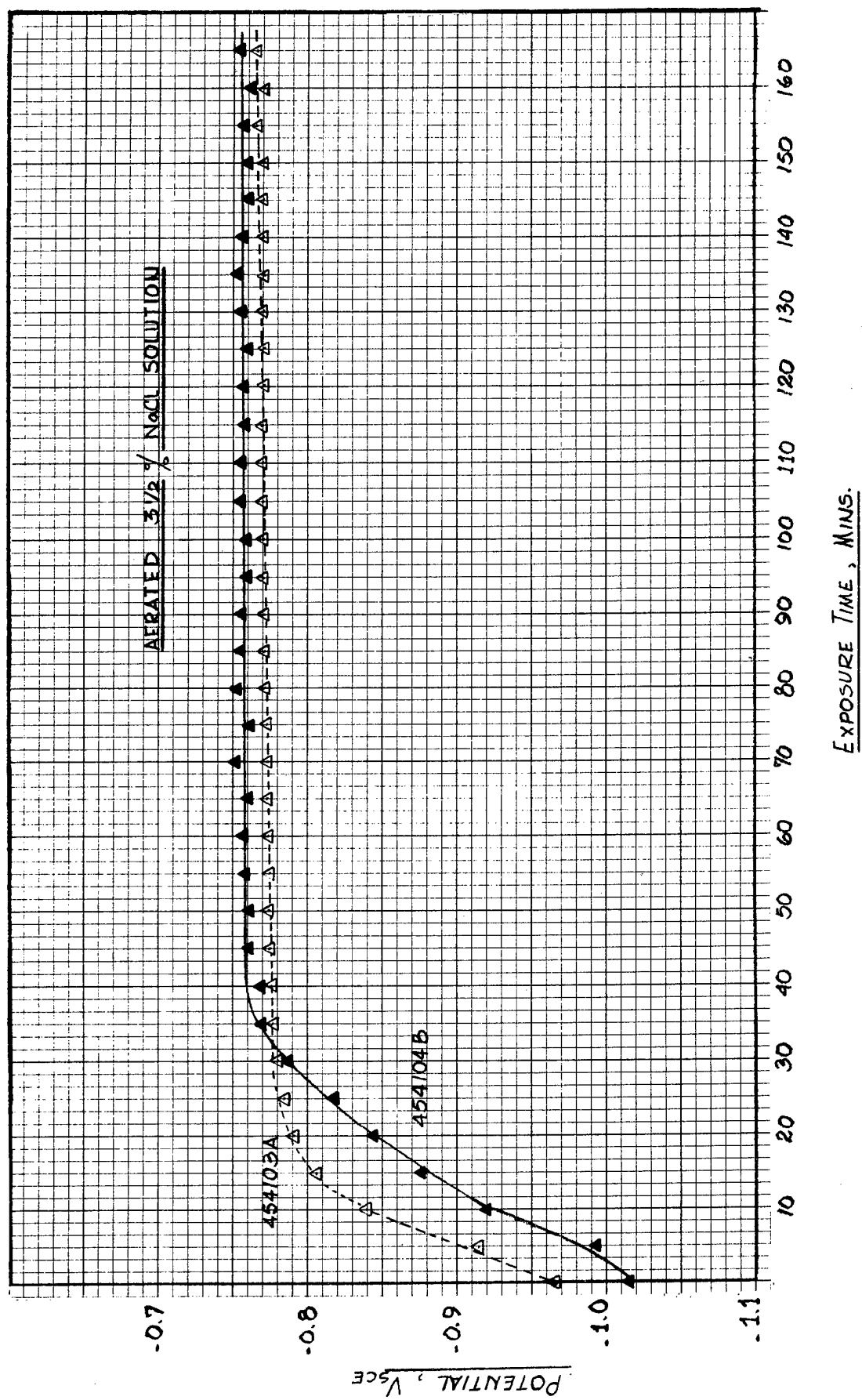
Figure 8. Variation of corrosion potential of Al-Li alloys in three aerated solutions during the initial hours of exposure.

Figure 9

a. As polished cross-section showing corrosion in
    Al-Li-Mn alloy (S. No. 454103A) after free corrosion
    in MASTMAASIS solution for 21 days.

    Neg. No. 206782A   Mag: 100X

b. As polished cross-section showing corrosion in Al-Li-Zr
    alloy (S. No. 454104B) after free corrosion in MASTMAASIS
    solution for 21 days.

    Neg. No. 206783A   Mag: 100X
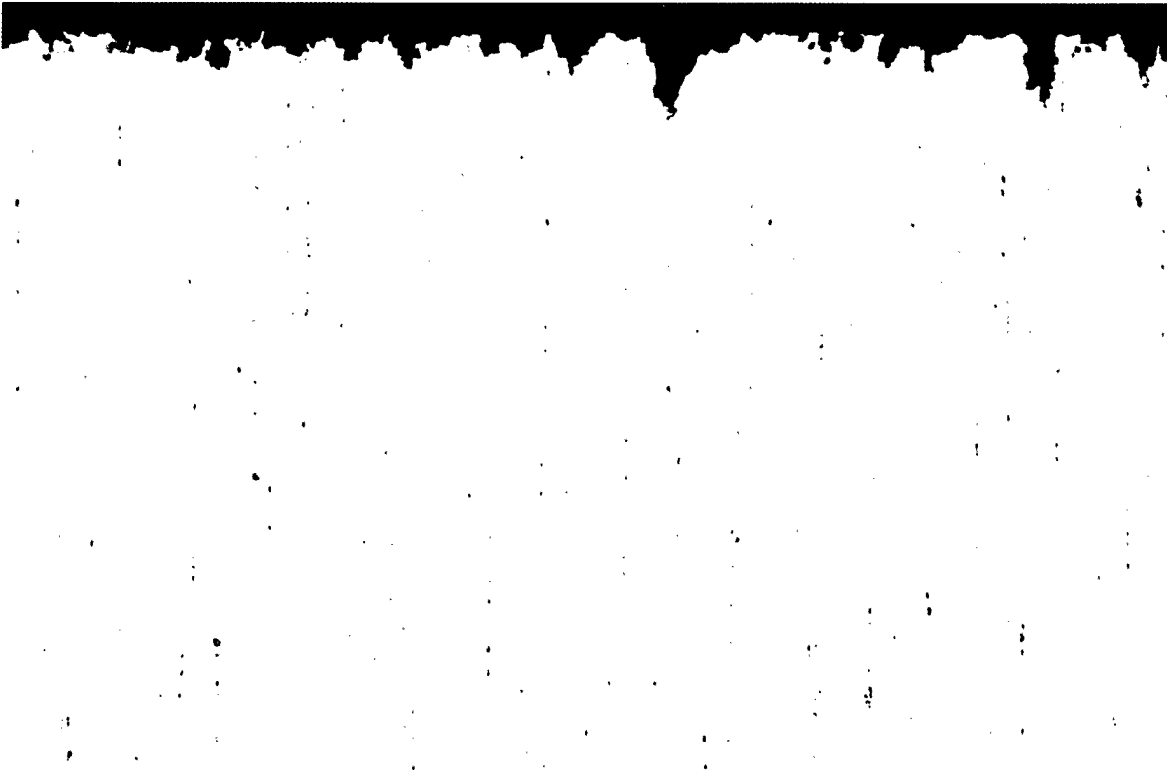
Figure 9a
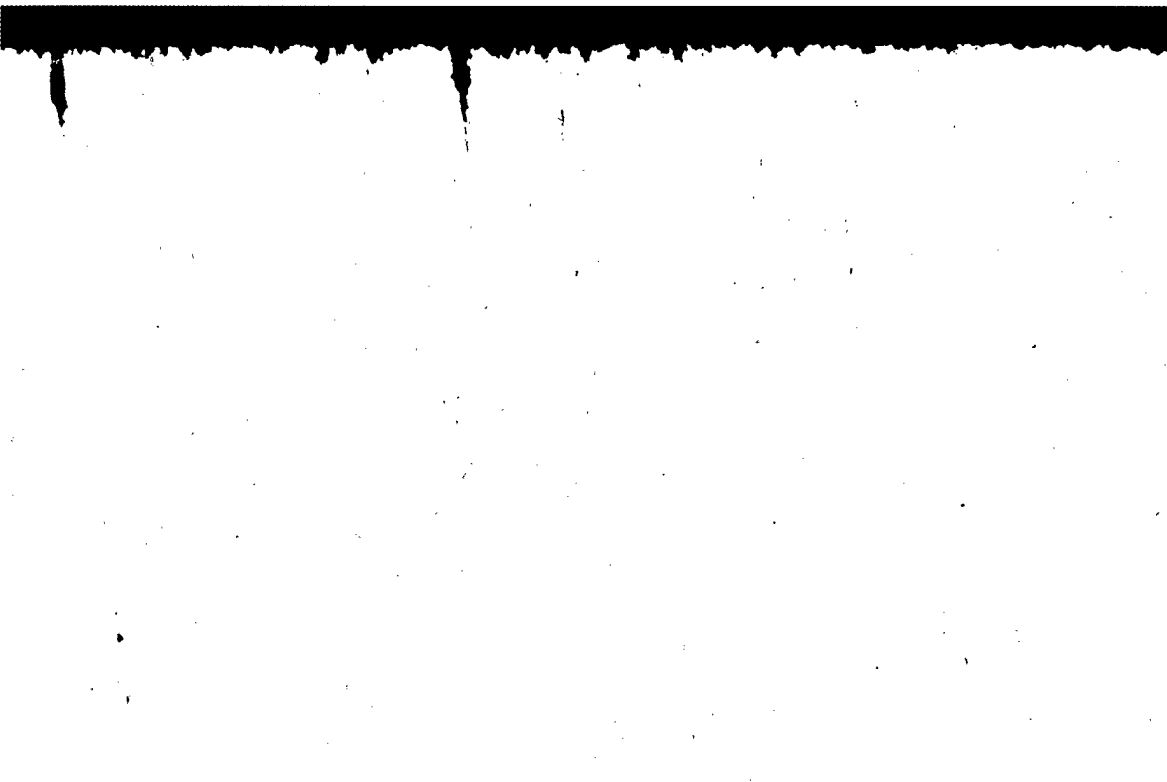
Figure 9b

Figure 10

a. Electropolished cross-section of Al-Li-Mn alloy
    (S. No. 454103A) after free corrosion in MASTMAASIS
    solution for 21 days (viewed under polarized light).

    Neg. No. 206780A   Mag: 100X

b. Electropolished cross-section of Al-Li-Zr alloy
    (S. No. 454104B) after free corrosion in MASTMAASIS
    solution for 21 days (viewed under polarized light).

    Neg. No. 206781A   Mag: 100X

Figure 10a

Figure 10b
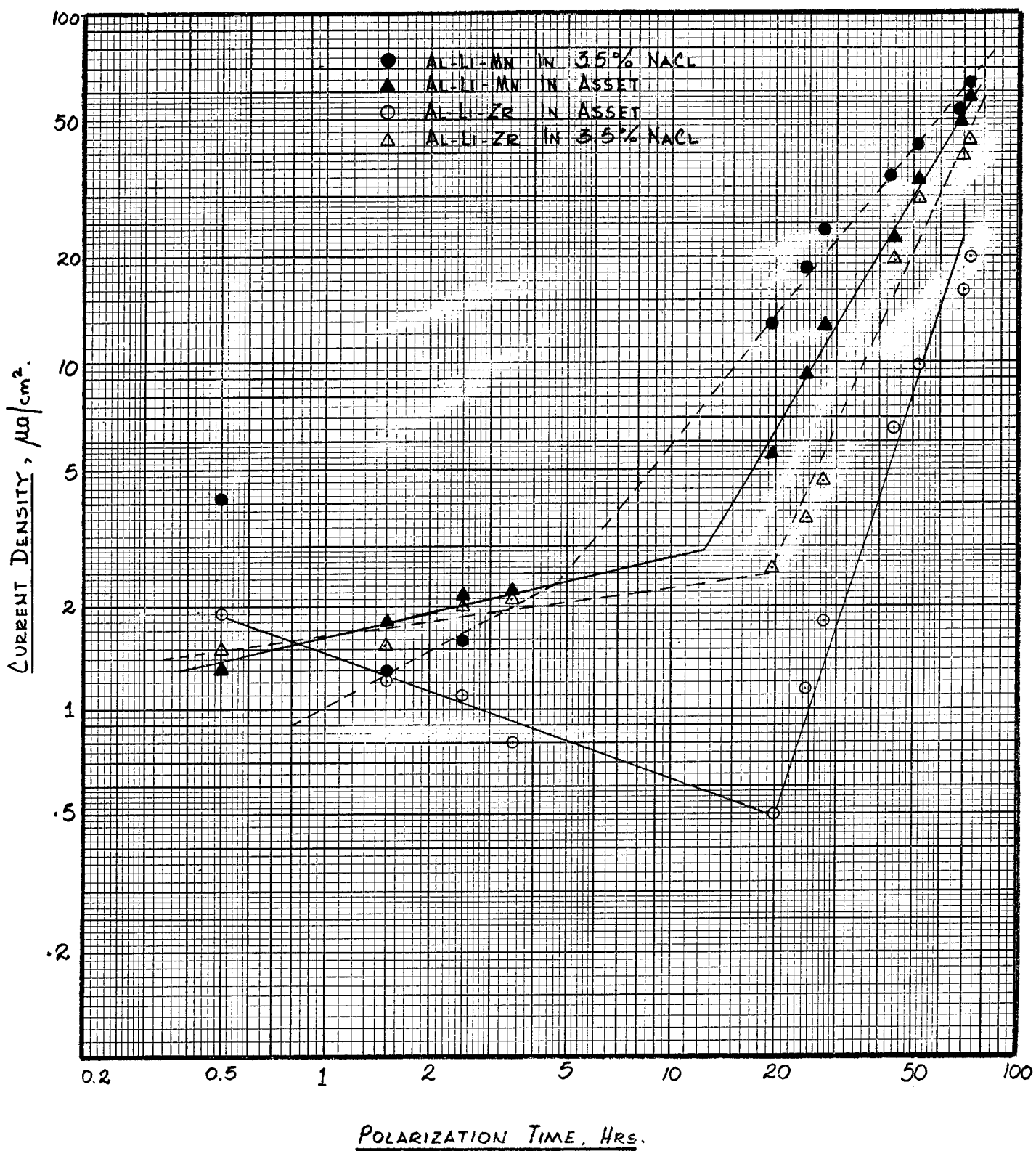
Figure 11. Variations of corrosion current during potentiostatic
polarization of Al-Li alloys in deaerated 3 1/2% NaCl
solution and deaerated ASSET solution.

LIST OF TABLES

CHAPTER 3

LIST OF FIGURES

CHAPTER 3

CHAPTER 3

Al-Cu-Li ALLOYS

Introduction

Because of the need for higher strength aluminum alloys, experiments were conducted on plant fabricated Al-Cu-Li plate. An alloy of this type (2020) has demonstrated its superiority in testing and service over other high-strength, commercial aluminum alloys in areas such as corrosion, stress-corrosion cracking, strength, elastic modulus, fatigue crack growth at low levels of stress intensity, and in smooth specimen, high cycle fatigue. However, in the peak strength temper, the fracture toughness was low enough to preclude its use for many applications. The low toughness combined with manufacturing difficulties contributed to its being withdrawn as a commercial material. During the last several years, however, much has been learned in the area of structure-toughness relationships. Consequently, a new look at an old problem was initiated.

Experimental

Plate, 2.5 cm thick, having composition listed in Table 3-1 was investigated. Two tempers were evaluated, the conventional T651 and an underaged one labeled T6X51. The heat treatment practices are summarized in Table 3-2.

Tensile properties and plane strain fracture toughness were determined for each temper, and optical metallography, phase identification by Guinier-deWolff and

electron microprobe, degree of recrystallization by pinhole X-ray method, and transmission electron microscopy (TEM) were performed as described in previous chapters.

Fatigue crack growth tests were conducted on each temper under low (<5%) and high (>90%) relative humidity conditions using tension-tension loading on a closed loop, electrohydraulic MTS test system at a frequency of 20 Hz. Edge notch, 3.9 x 8.9 x 0.64 cm (3.5 x 3.5 x 0.25") specimens oriented in the T-L* direction were tested. Crack growth measurements were made using an optical gridline technique where the crack was followed visually (5X magnification) as it traversed a series of reference gridlines photographically printed on the specimen surface. The stress intensity expression employed in determining the $\Delta a/\Delta N$ vs ΔK relationship is given by:

$$\Delta K = \frac{P\sqrt{a}}{BW} \, Y, \qquad\qquad (1)$$

where:

$\quad$ a = average crack length for two readings,

$\quad$ B = specimen thickness,

$\quad$ W = specimen width, load line to end of specimen,

$\quad$ P = load,

$\quad$ $Y = 29.6 - 185.5\left(\frac{a}{W}\right) + 655.7\left(\frac{a}{W}\right)^2 - 1017.0\left(\frac{a}{W}\right)^4 + 638.9\left(\frac{a}{W}\right)^5$.

---

*Where the direction of stress is perpendicular to the rolling direction and the crack growth direction is parallel to the rolling direction.

The response to cyclic loading in terms of average crack advance per cycle, $\Delta a/\Delta N$, as a function of stress intensity factor range, ΔK, was plotted on a log-log scale.

SEM was done on the fatigue crack growth specimens and TEM foils were prepared directly below the fracture surface where the high stress intensities were developed.

Flattened fracture specimens were analyzed for copper, iron, and silicon at regions of low ΔK, high ΔK, and a random plane.

Results

A three dimensional optical micrograph for the T6X51 structure is shown in Figure 3-1. The structure contained coarse, recrystallized grains. These findings were corroborated by the X-ray pinhole method. This degree of coarse grain structure is generally not observed in other high strength commercial aluminum alloy plate products.

A high volume fraction of constituent phases was observed optically and analyzed by the electron microprobe and by Guinier-deWolff X-ray diffraction methods. Back scattered electron and characteristic X-ray images for silicon, iron, and copper for a typical surface section are shown in Figure 3-2. These phases contained aluminum-copper-iron, aluminum-copper, and silicon. Guinier-deWolff results indicated the presence of Al_7Cu_2Fe, $Al_{20}Cu_2Mn_3$, and Al_2CuLi.

Bright field (BF) electron micrographs for the two tempers are shown in Figures 3-3 and 3-4. The

higher aging temperature and the longer time at temperature in the T6 condition produced slightly larger θ'' and δ' precipitates compared to the T6X temper. A foil oriented parallel to $(111)_{Al}$ revealed needle-like precipitates parallel to the $<100>_{Al}$. Small dislocation loops which accommodate the strain can also be seen (Figure 3-5). Slight tilting of the foil produced displacement fringe contrast (Figure 3-6). The θ'' precipitates are plate-like with the habit planes of the prcipitates on the cube plane of the matrix. Shape effect can be clearly seen in the selected area diffraction (SAD) pattern (Figure 3-7). Streaking parallel to the $<100>_{Al}$ and the $<010>_{Al}$ is a consequence of the plate-like nature of the θ''. Figure 3-8 is a central dark field (CDF) image using a δ' (100) super-lattice reflection. The small, spherical δ' precipitates are in contrast.

Tensile and plane strain fracture toughness properties for the two tempers are listed in Table 3-3. A small reduction in yield strength by underaging resulted in a substantial increase in fracture toughness. For comparision, typical values of 7075-T651 plate are given in Table 3-4.

Figures 3-9 through 3-12 show the results of the fatigue crack growth tests. Results in the two environments were similar. Since the yield and toughness of 7075-T651 is similar to that of this alloy in the T6X51 temper, its crack growth behavior under similar test conditions is included

for comparison. At all stress intensities, the crack growth rate was slower than that of 7075-T651, particularly in the high humidity environment.

Figures 3-13 and 3-14 are macrographs of the fractured Al-Cu-Li alloy specimens tested in dry (<5% R.H.) air. Figure 3-13 is a view normal to the fracture surface. A shiny surface, with octahedral facets, is present in the initial phases of the crack growth test. The shiny surface is indicative of Stage I crack growth which was observed in both specimens. The crack length for Stage I, however, was longer for the T6X51 temper than in the T651 temper. An edge view of the fatigue fracture shows that the growth of the crack was inclined at an angle of approximately 70° from the stress axis (Figure 3-14). The length of crack that was not normal to the stress axis was greater in the T6X51 temper. Figure 3-15 is a macrograph of the fractured Al-Cu-Li alloy specimens tested in the high humidity environment. This edge view of the fatigue fracture also shows the inclined crack growth behavior.

Results of examinations of the fracture surfaces using SEM and electron microprobe, and of areas adjacent to the fracture surface using optical and TEM, combined to give an understanding of the factors influencing fatigue crack growth of this alloy. Fractographic examinations (Figure 3-16) showed evidence in both tempers of all the fatigue fracture modes found in aluminum alloys; i.e., Stage I: crystallographic at low levels of ΔK; Stage II: striation

forming at intermediate levels of ΔK; and Stage III: ductile rupture or intergranular at the high levels of ΔK. The relative proportions in the underaged temper (Figure 3-16a, c, and e), however, were different for those in the peak aged temper (Figure 3-16b, d, and f).

The process of Stage I crack growth can be readily seen in Figures 3-16a and b, 3-17, and 3-18. The influence of grain structure on the fracture appearance in the Stage I region is revealed by a comparison of a fractograph (Figure 3-17a) with an optical micrograph taken of the polished fracture surface (Figure 3-17c). The distribution of facets on the fracture can be correlated with the grain size and shape. Optical micrographs of a surface section taken along the direction of crack growth in the low ΔK region show that the fracture path is not straight but changes from grain to grain (Figure 3-18). They also reveal numerous cracks below the main crack front.

Figure 3-16c shows the transition region from Stage II to Stage III in the underaged material. A higher magnification micrograph (Figure 3-19) shows the presence of ductile fatigue striations. However, a comparison with Figure 3-16d, peak aged material, shows a greater amount of overload area on the surface with a pronounced amount of intergranular failure.

The fracture process at a high level of ΔK is shown in Figure 3-16e for the underaged material and Figures

3-16f and 3-20 for the peak aged material. The underaged
material appears to have failed in the high ΔK region by
transgranular process as compared to the peak aged material
which appears to have failed in the high ΔK region by an
intergranular mechanism.

Table 3-5 summarizes the results of the chemical
analyses made using the electron microprobe on the flattened
fracture surfaces. A comparison of the relative amounts of
silicon, iron, and copper on the surfaces of the underaged
and peak strength materials at low and high levels of ΔK are
given. For reference, analysis results for a random plane
are included. In both aging conditions at low levels of ΔK,
the results were similar to one another and similar to the
analysis of a random plane; however, at high ΔK, there were
significant increases in the amounts of silicon, iron, and
copper present on the surface of the underaged material
compared to the random plane and to the peak strength
material.

Figures 3-21 through 3-23 are TEM's taken from a
foil prepared at the fracture surface in the rapid tensile
fracture region in the peak strength material. Intense
planar slip is observed. In Figures 3-21 and 3-22 large
offsets due to the intersection of the slip bands with a
subgrain boundary are clearly evident.

TABLE 3-1

REMELT ANALYSIS OF Al-Cu-Li PLATE
(WEIGHT PERCENT)

Cu	Li*	Mn	Cd	Fe	Si	Ti	Zn
4.24	1.24	0.49	0.19	0.16	0.09	0.05	0.01

*By Atomic Absorption.

TABLE 3-2

HEAT TREATMENT OF Al-Cu-Li PLATE

Temper	Solution Heat Treatment Temperature, °C (°F)	Time at Temperature, Hours	Artificial Aging Temperature, °C (°F)		Time at Temperature, Hours
T6X51*	516 (960)	1.5	149	(300)	15
T651**	516 (960)	6.0	160	(320)	18

*51 Stretch relieved approximately 1.5% after cold water quench.

**Typical for commercially produced product.

TABLE 3-3

LONG-TRANSVERSE MECHANICAL PROPERTIES OF Al-Cu-Li ALLOY

Temper	T.S., MPa	(ksi)	Y.S., MPa	(ksi)	El., %	Elastic Modulus, GPa	(ksi x 10^6)	Fracture Toughness, K_{Ic} MPa$\sqrt{m}$	(ksi$\sqrt{in.}$)
T6X51	555	(80.5)	505	(73.3)	8.0	76	(11.1)	29.2	(26.5)
T651	572	(83.0)	529	(76.8)	4.0	76	(11.1)	20.8	(18.9)

TABLE 3-4

LONG-TRANSVERSE MECHANICAL PROPERTIES OF 7075-T651 PLATE

Temper	T.S.*, MPa	(ksi)	Y.S.*, MPa	(ksi)	El.*, %	Elastic Modulus, GPa	(ksi x 10^6)	Fracture Toughness[+], K_{Ic} MPa$\sqrt{m}$	(ksi$\sqrt{in.}$)
T651	538	(78.0)	469	(68.0)	7.0	71	(10.3)	25.3	(23.0)

*Aluminum Association Guaranteed Values

[+]Average values for 7075-T651 from Alcoa Green Letter: Alloy 7050

TABLE 3-5

CHEMICAL ANALYSIS ON THE FLATTENED FRACTURE SURFACES

	Si	(%) Fe	Cu
Underaged			
Low ΔK	0.02	0.08	4.38
High ΔK	0.04	0.26	5.61
Random	0.02	0.07	4.78
Peak Aged			
Low ΔK	0.02	0.06	4.33
High ΔK	0.03	0.17	4.93
Random	0.02	0.07	4.73
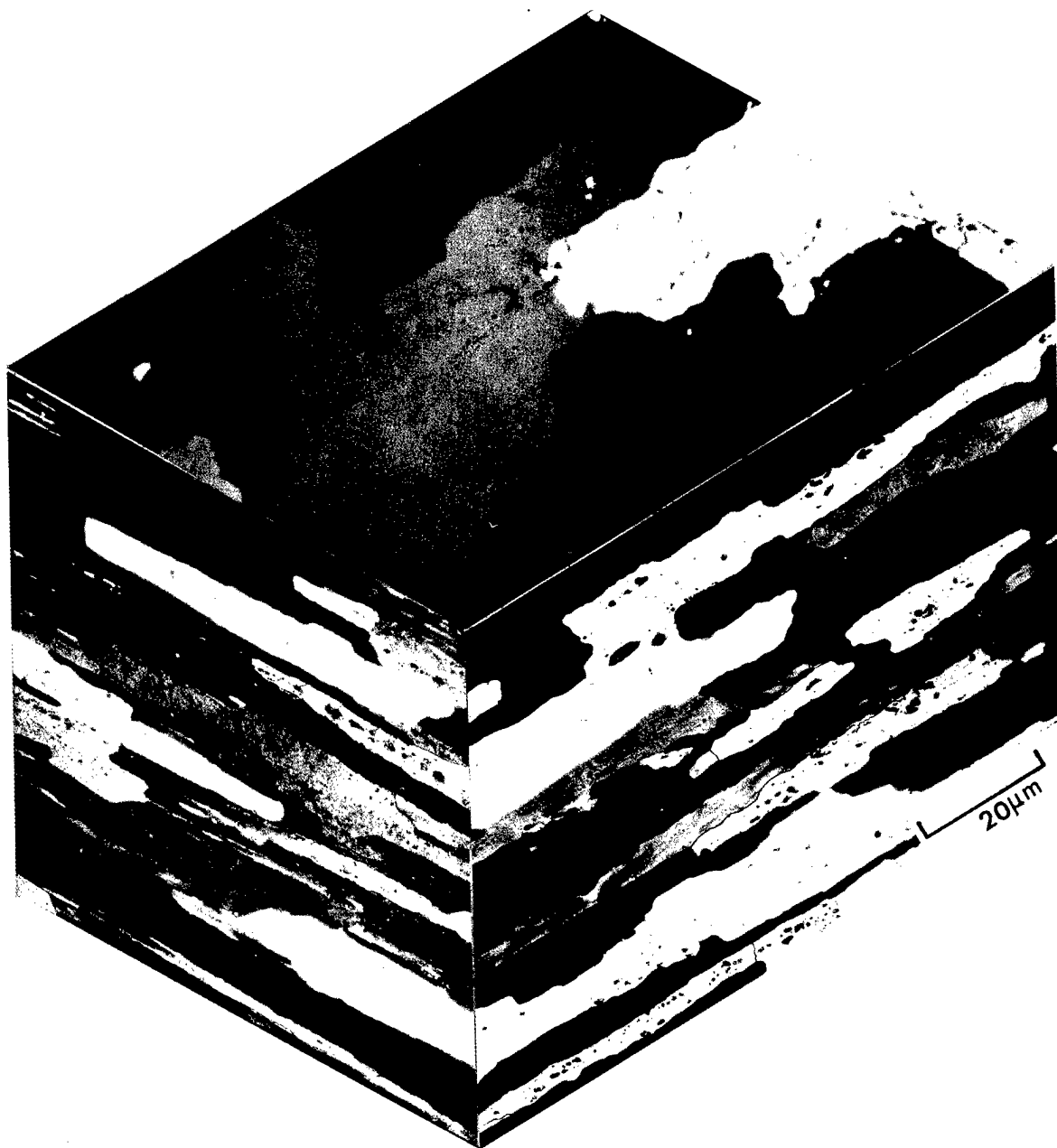
Figure 3-1. Photomicrograph Showing Grain Structure of
Al-Cu-Li-T6X51.   The structure is composed
of coarse, recrystallized grains (Electro-
polished-polarized light, 100X).
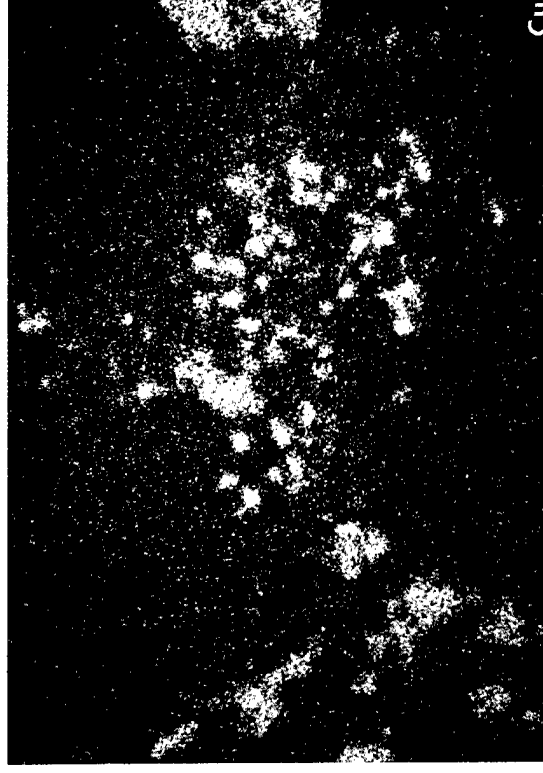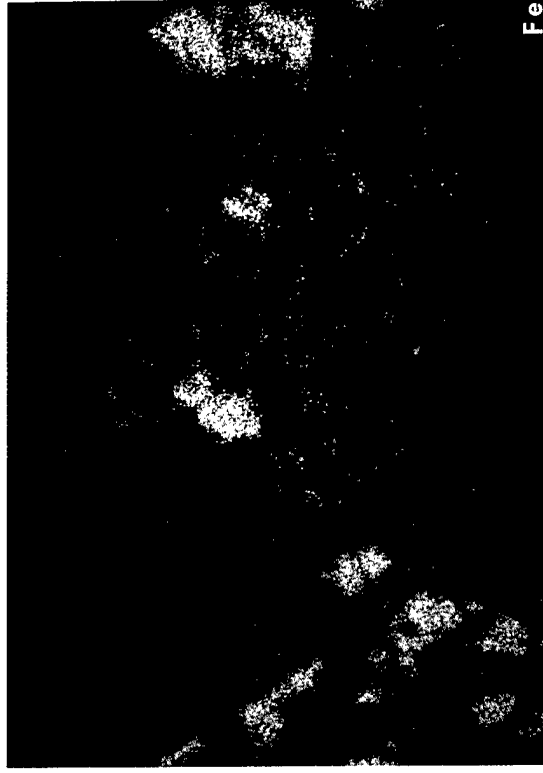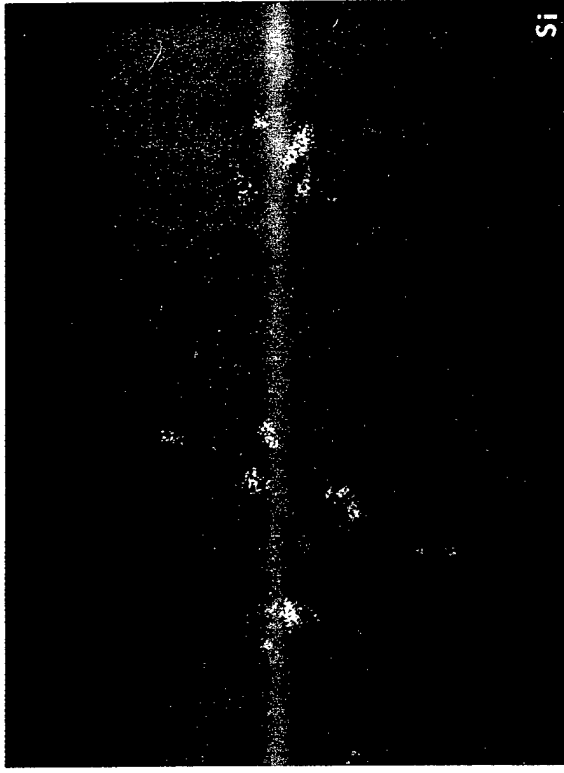
Figure 3-2. Back Scattered Electron (a), and Characteristic X-ray Images for (b) Silicon, (c) Iron, and (d) Copper in a Random Surface Section of Al-Cu-Li-T6X51.

0.2μ
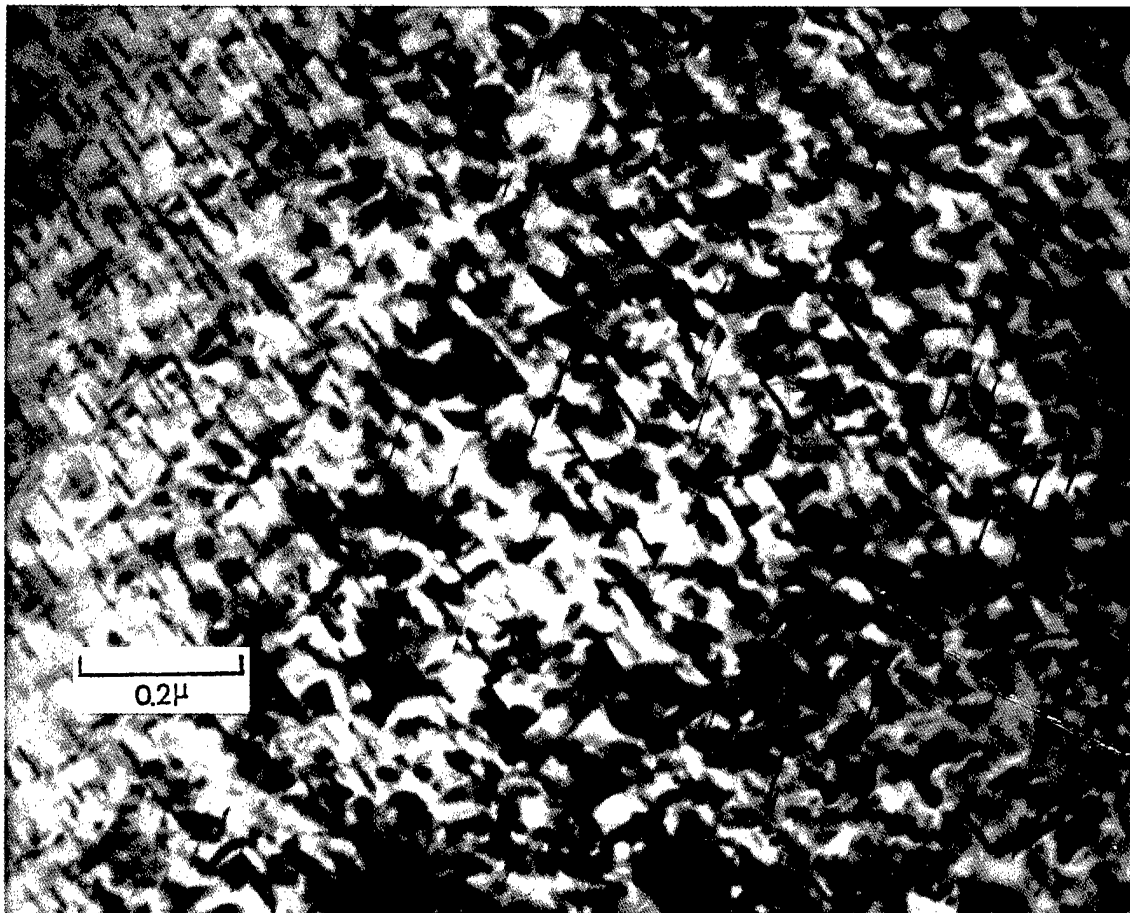
Figure 3-3.   Bright Field (BF) Electron Micrograph   of
           Al-Cu-Li-T6X51.
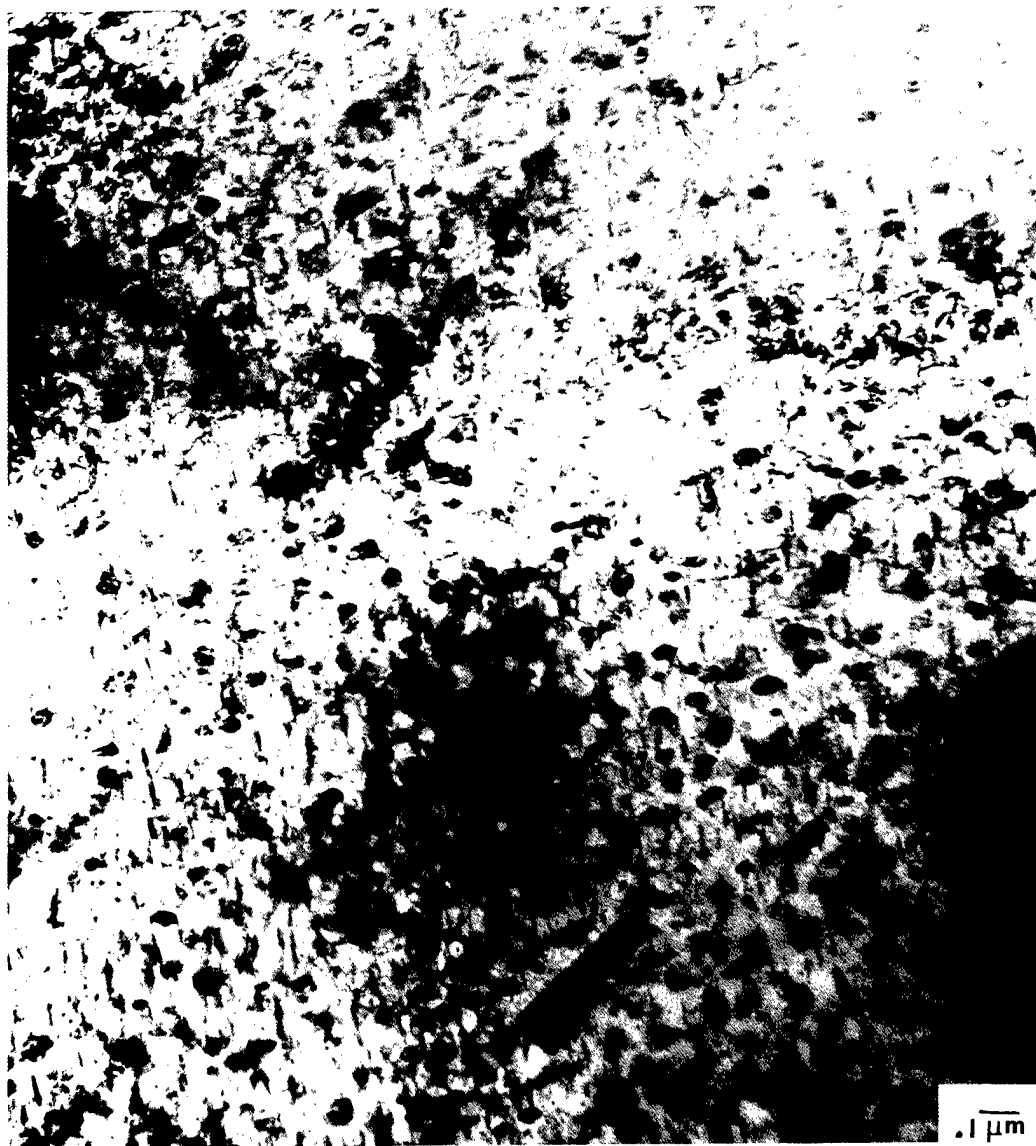
Figure 3-4. BF Electron Micrographs of Al-Cu-Li-T651.
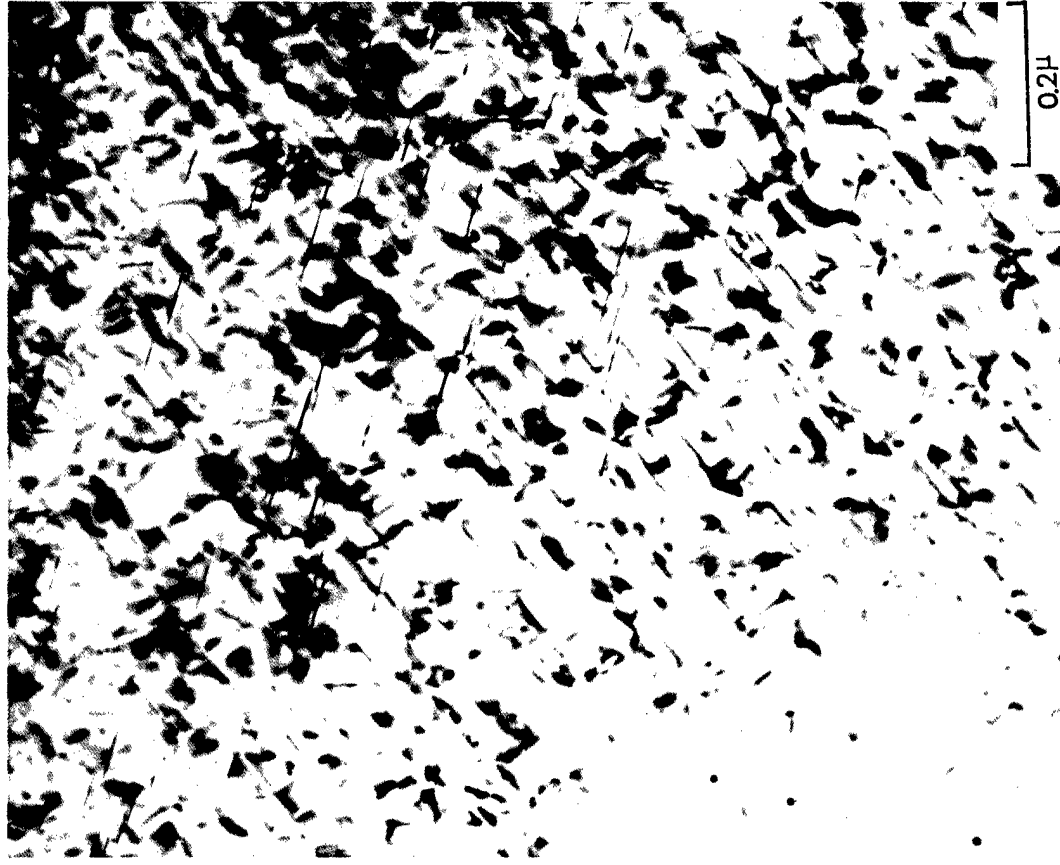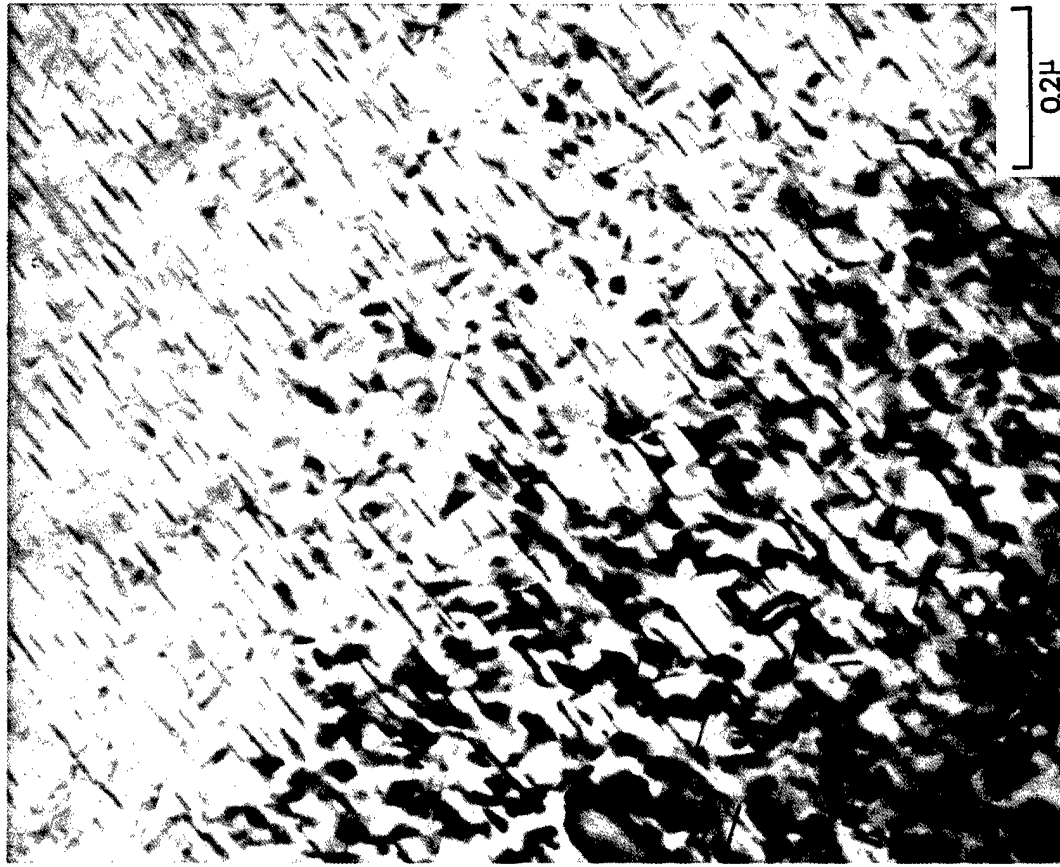
Figure 3-5 - BF Micrographs Taken in the Same Area but Slightly Tilted Illustrating the Needle-like Nature of the Al-Cu Precipitates. (Al-Cu-Li-T6X51)
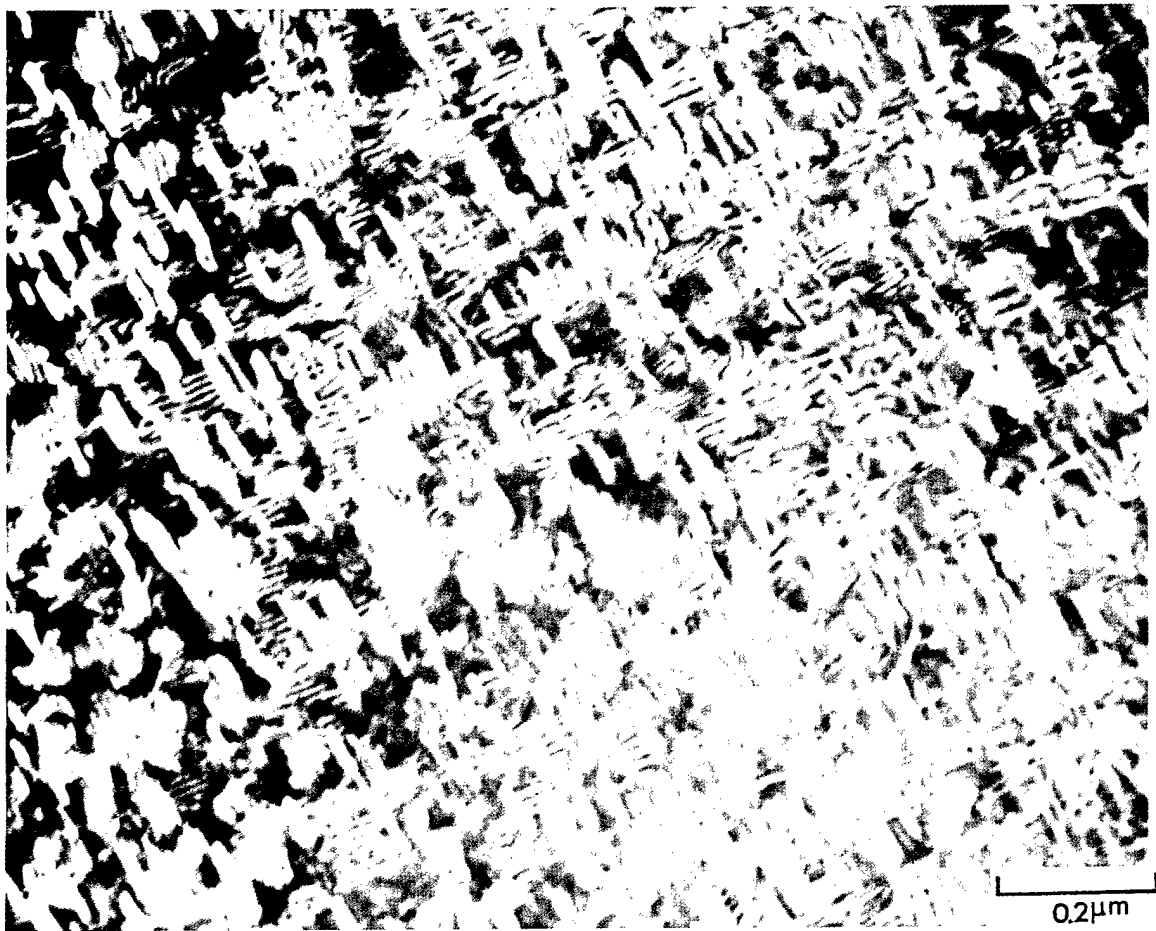
Figure 3-6. Slight Tilt of the Foil Such that the Planes
of the $(010)_{Al}$ and $(100)_{Al}$ are Inclined with
Respect to the Incident Beam to Produce
Characteristic Displacement Fringes.
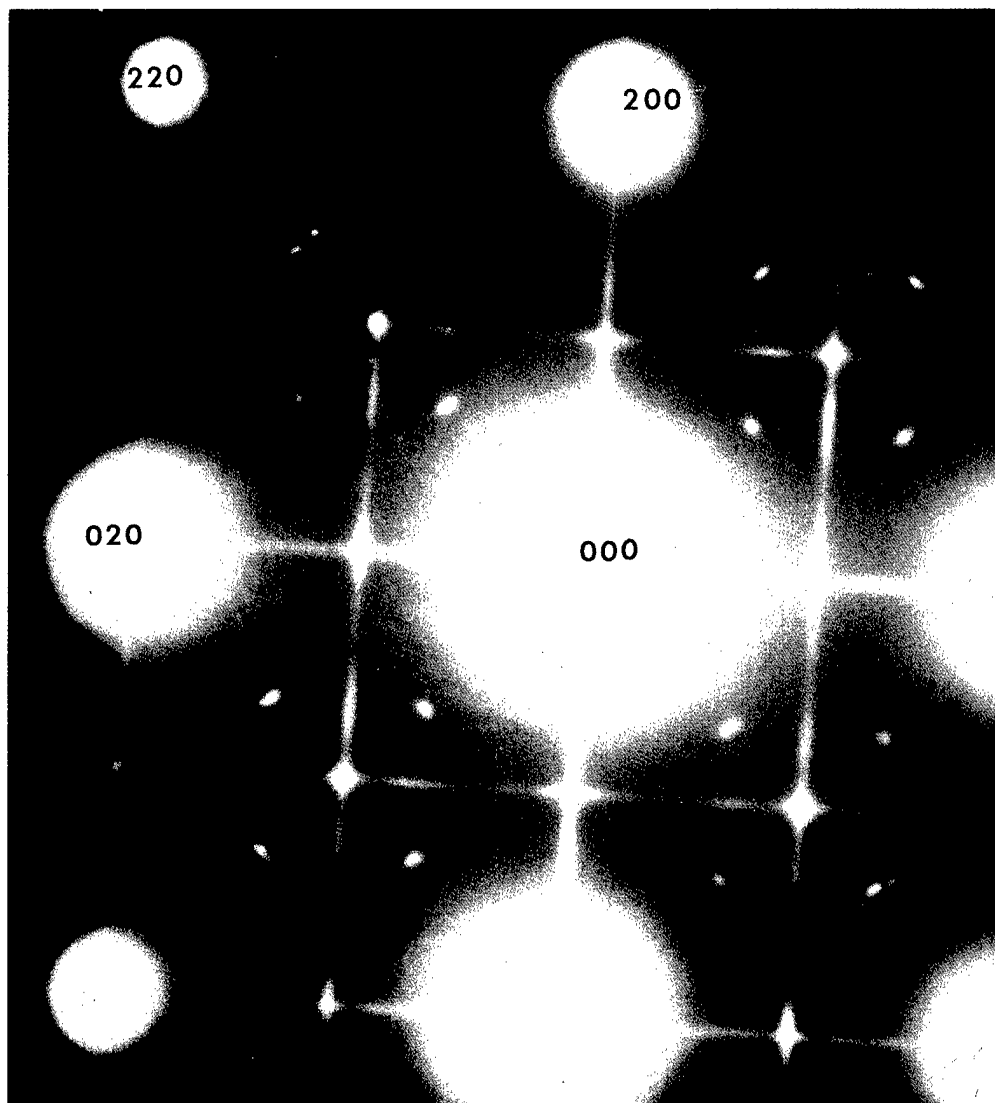
Figure 3-7. SAD Illustrating the Streaking Perpendicular to $(100)_{Al}$ and $(010)_{Al}$. Here the streaking is a consequence of the plate morphology of the θ'' precipitate.
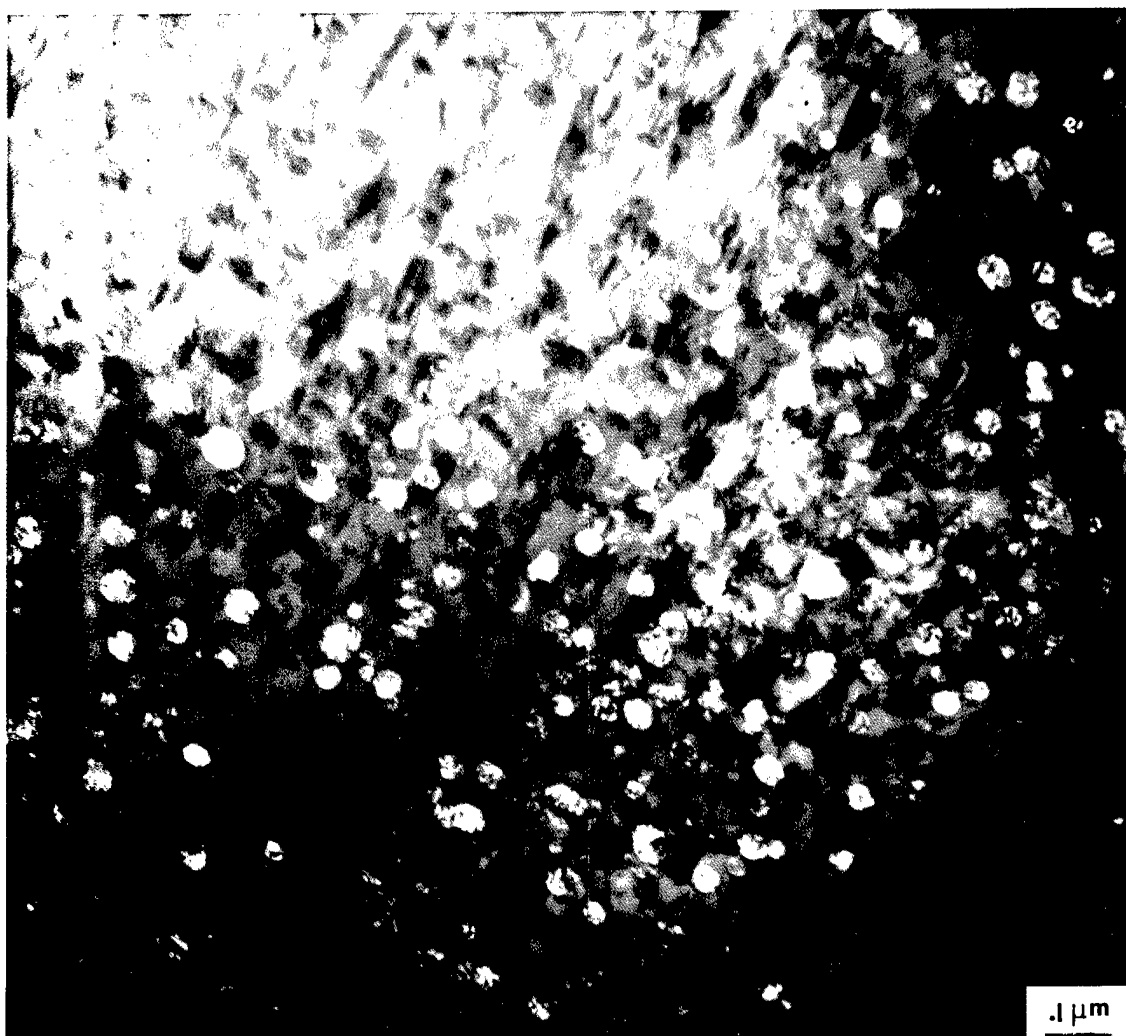
Figure 3-8. CDF Image Using δ′ (100) Superlattice
Reflection in the T651 Material.
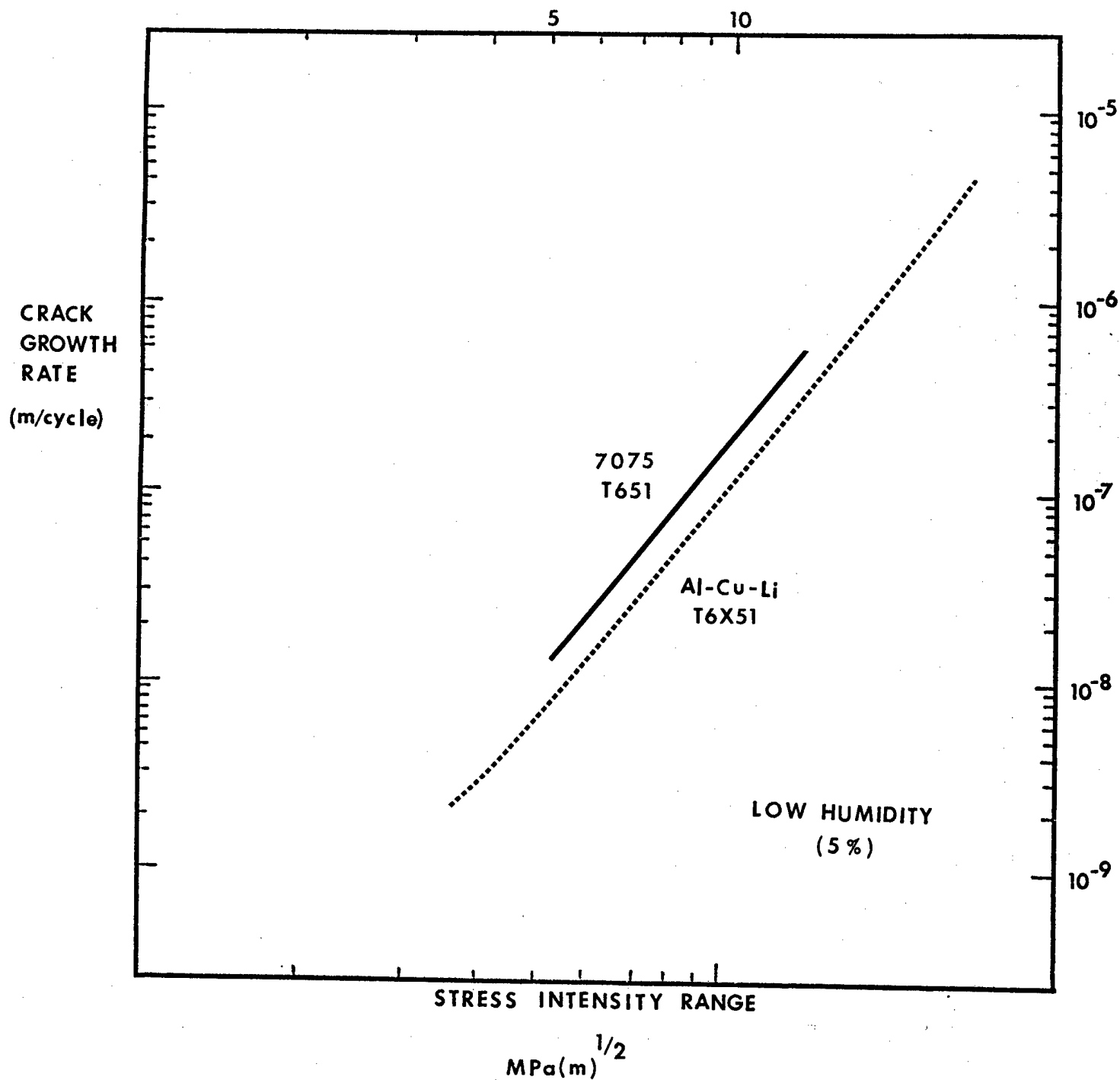
Figure 3-9. Fatigue Crack Growth Behavior of Al-Cu-Li-T6x51 in Low Humidity (<5%) Environment. Data for 7075-T651 under similar test conditions are included for comparison.[2]
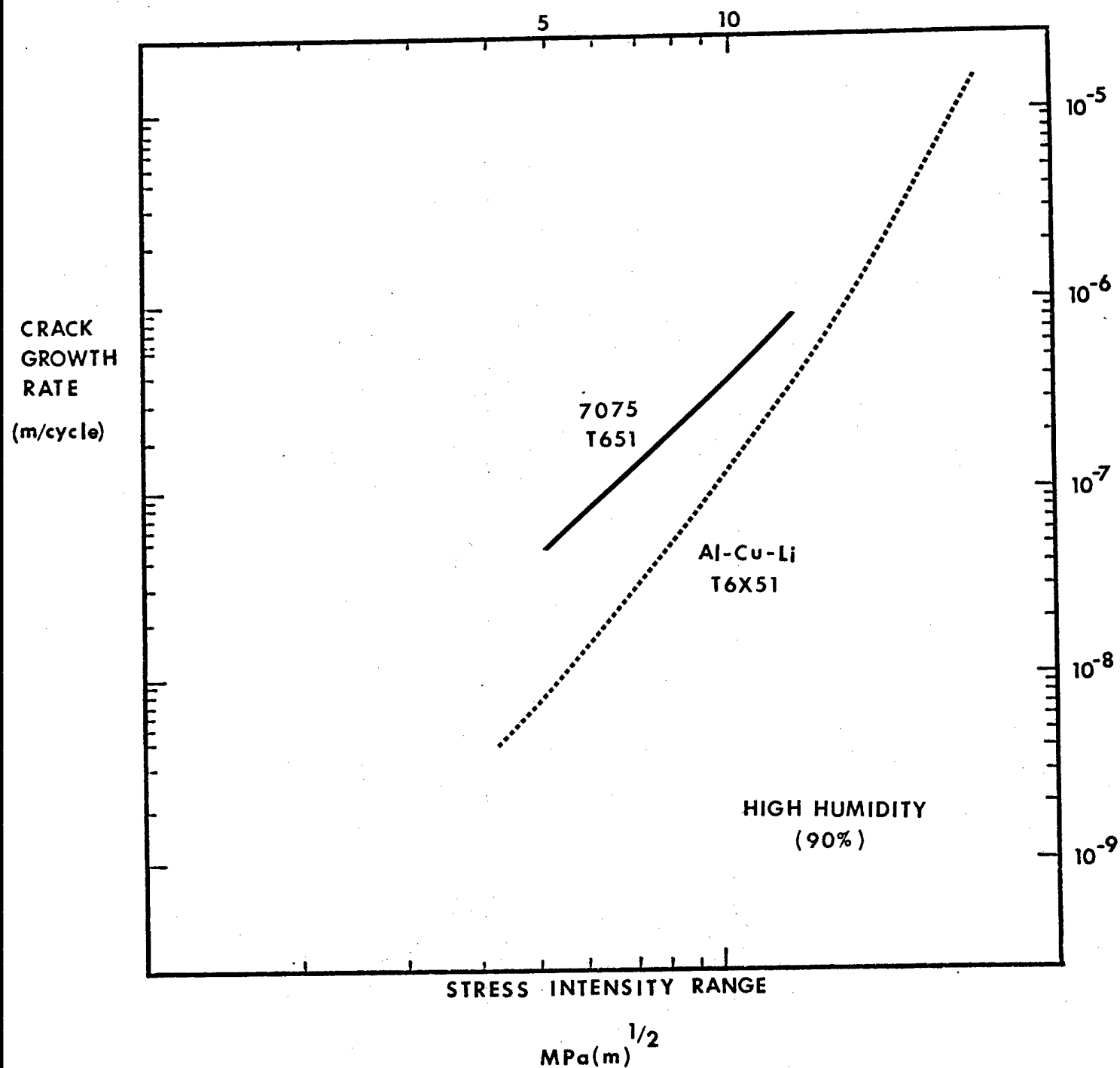
Figure 3-10. Fatigue Crack Growth Behavior of Al-Cu-Li-T6X51
in high humidity (>90%) Environment. Data for
7075-T651 under similar test conditions are
included for comparison.[2]
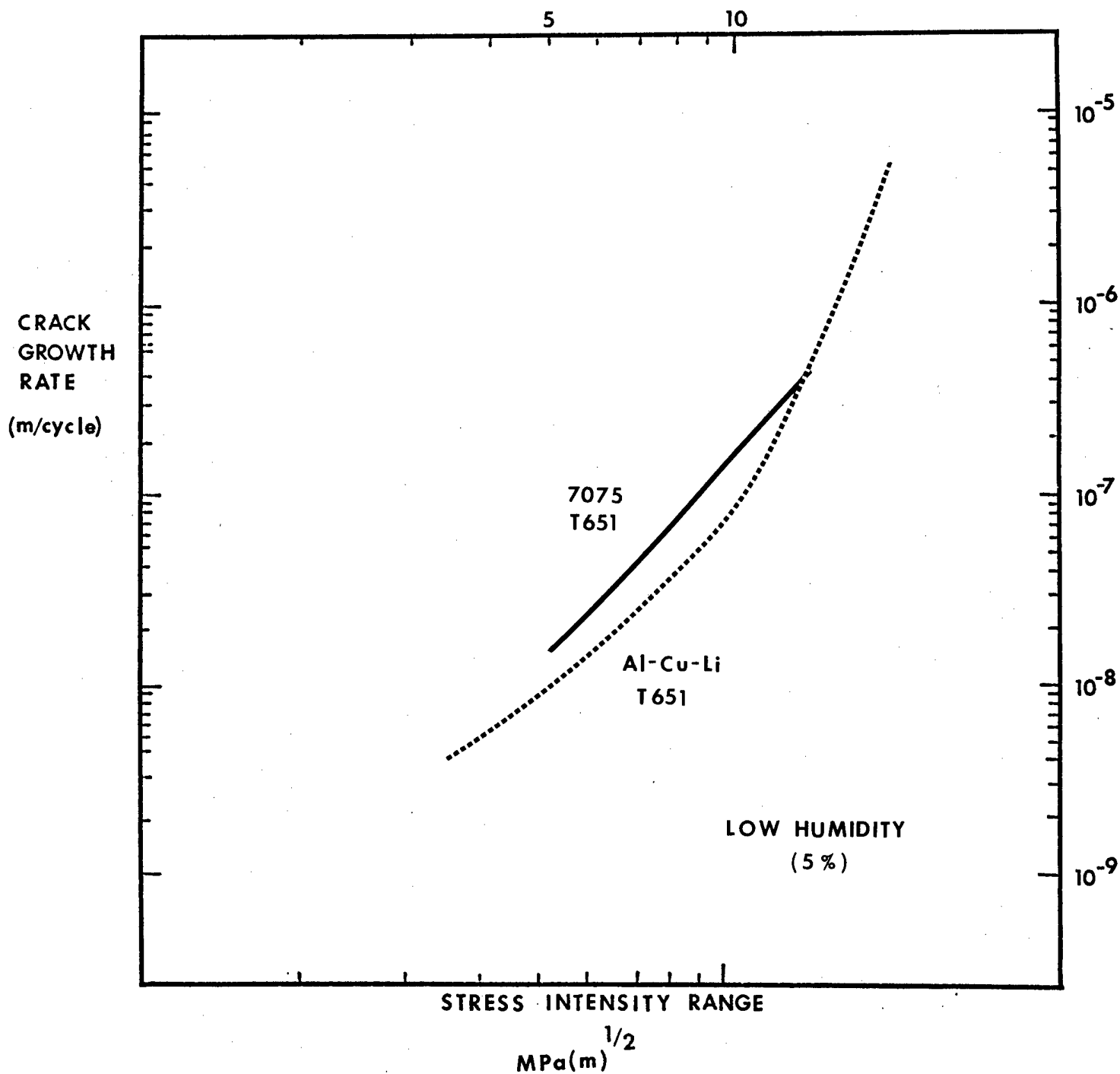
Figure 3-11.   Fatigue Crack Growth Behavior of Al-Cu-Li-T651
in Low Humidity (<5%) Environment. Data for
7075-T651 under similar test conditions are
included for comparison.[2]

CRACK
GROWTH
RATE

(m/cycle)

5   10

10^{-5}

10^{-6}

7075
T651

10^{-7}

Al-Cu-Li
T651

10^{-8}

HIGH HUMIDITY
(90%)

10^{-9}

STRESS INTENSITY RANGE

$MPa(m)^{1/2}$
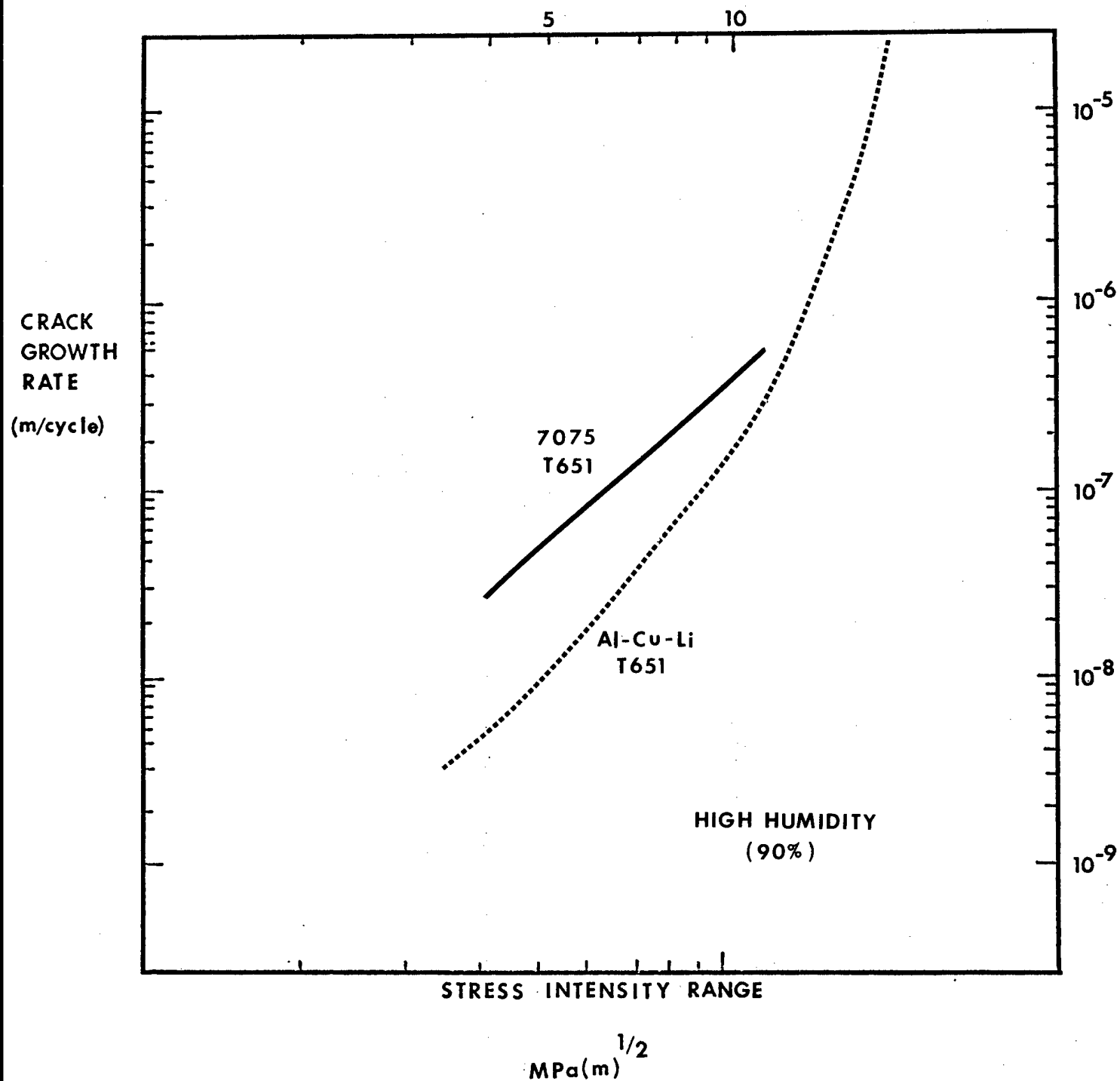
Figure 3-12.   Fatigue Crack Growth Behavior of Al-Cu-Li-T651
                in High Humidity (>90%) Environment. Data for
                7075-T651 under similar test conditions are
                included for comparison.[2]

T6X51

T651

Figure 3-13. Macrograph Normal to the Plane of Cracking
Showing Fatigue Fracture of Al-Cu-Li Alloy
Illustrating the Effect of Toughness on the
Extent of Stage I Crack Growth (Low Humidity,
<5%, Environment).
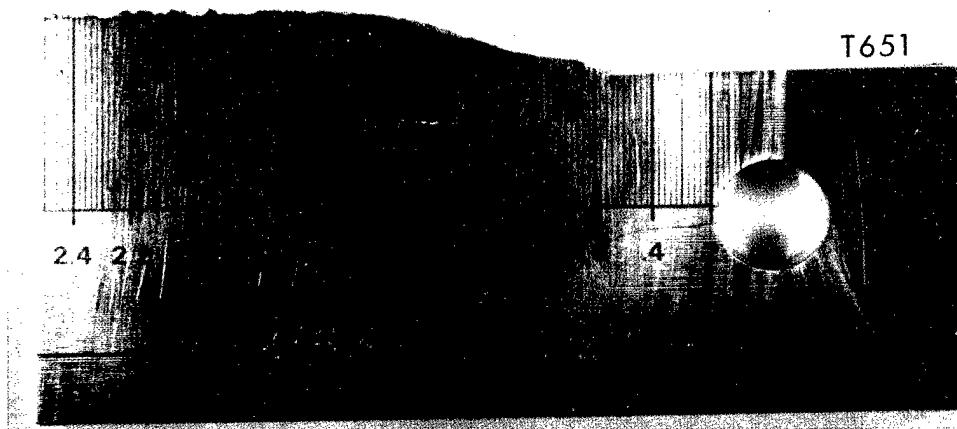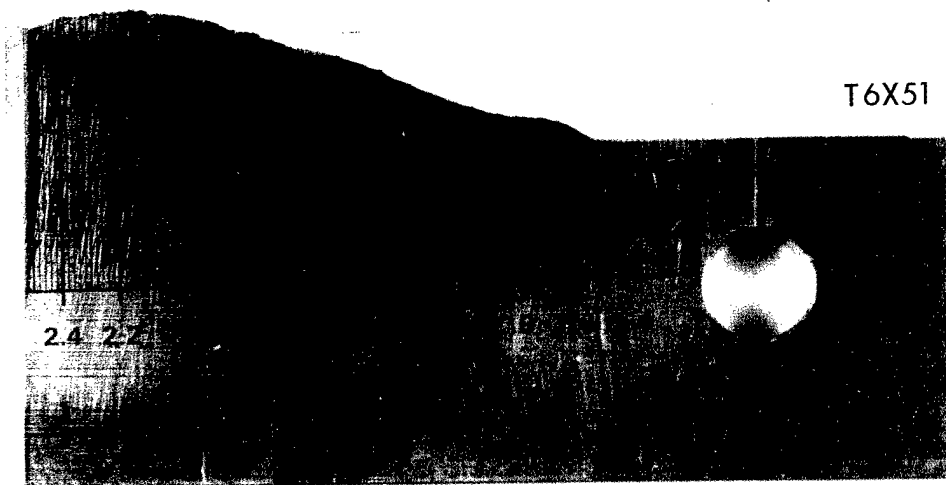
Figure 3-14. Macrograph Showing the Deviation of Crack Growth Direction. With increased toughness, lower yield strength, there was a corresponding increase in the extent of Stage I growth (low humidity, <5% environment).
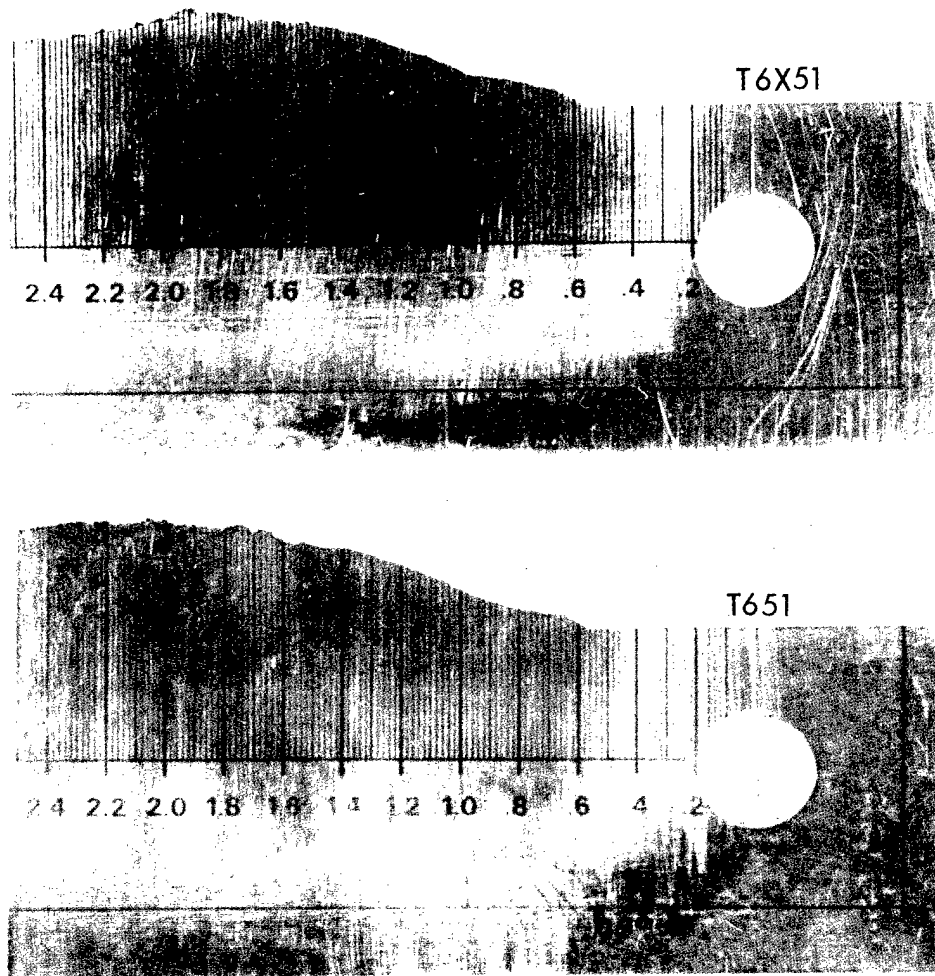
Figure 3-15. Macrograph Showing the Deviation of Crack Growth
              Direction (High Humidity, >90%, Environment).
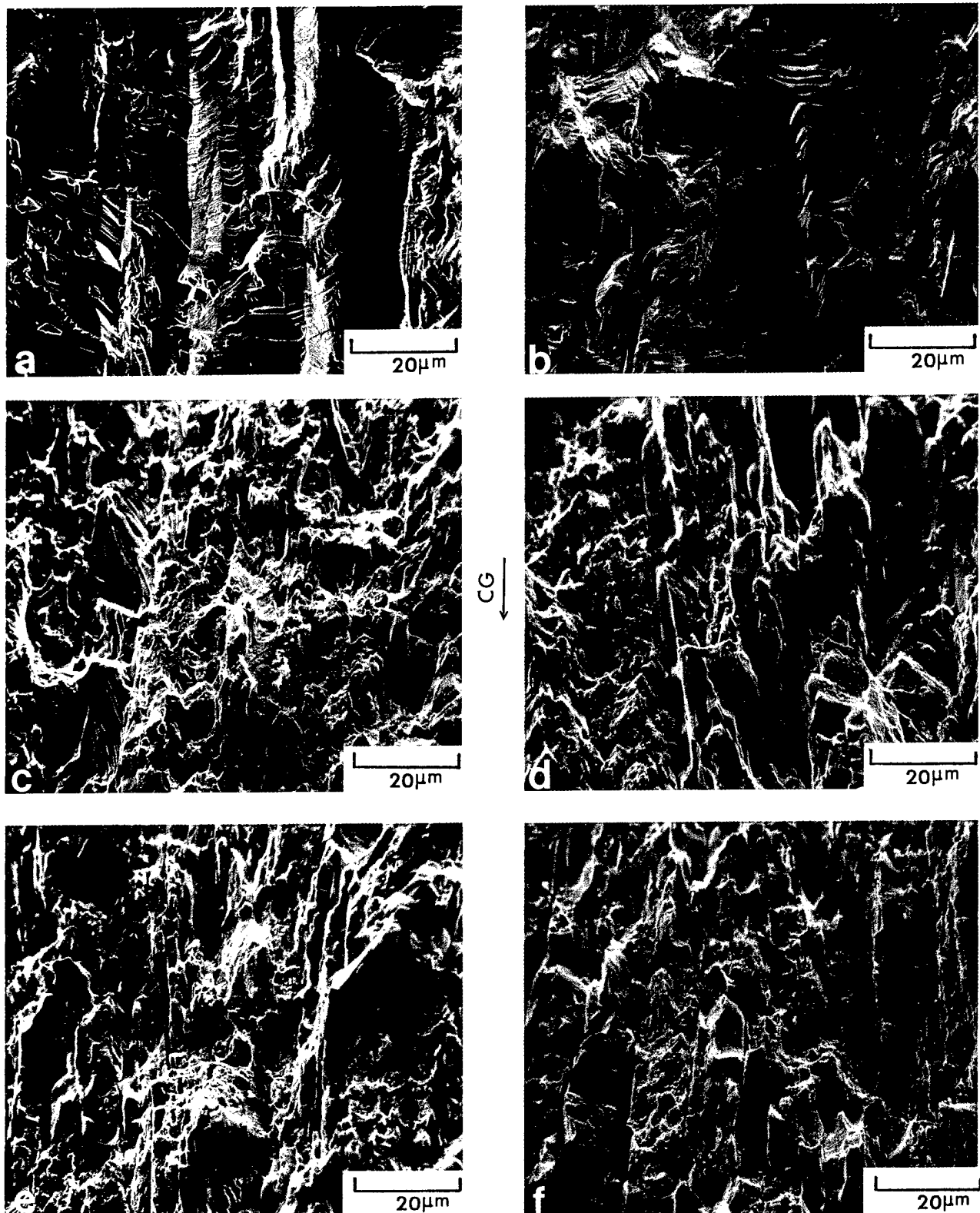
Figure 3-16.   Appearance of Stage I Crack Growth in (a) Al-Cu-Li-
T6X51 and (b) in Al-Cu-Li-T651 at the Same, Low
Level of ΔK; Transition in Stage II to Stage III
in (c) T6X51 Material, and Predominantly Stage
III in (d) T651 Material at the Same, Inter-
mediate Level of ΔK; and (e) Predominantly
Transgranular Failure in the T6X51, and (f)
Predominantly Intergranular Failure in the
T651 Material at the Same, High Level of ΔK.
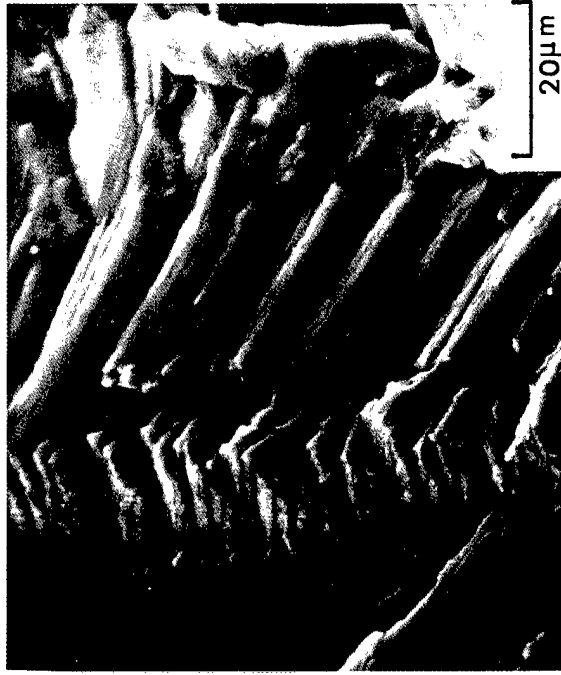
CG →
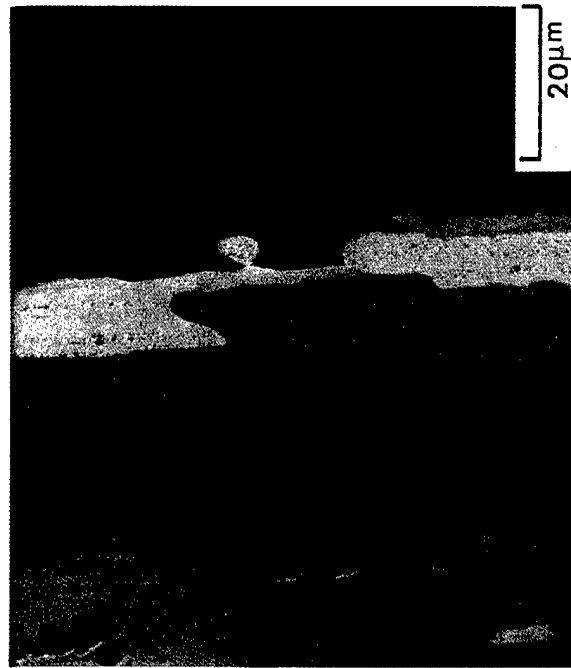
Figure 3-17. The Influence of Grain Structure on the Fracture Appearance in the Stage I Region is Revealed by Comparing the SEM Fractograph (a), with Optical Micrograph Taken of the Polished Fracture Surface (c); Higher Magnification (b) of the Fracture Surface.

CG →
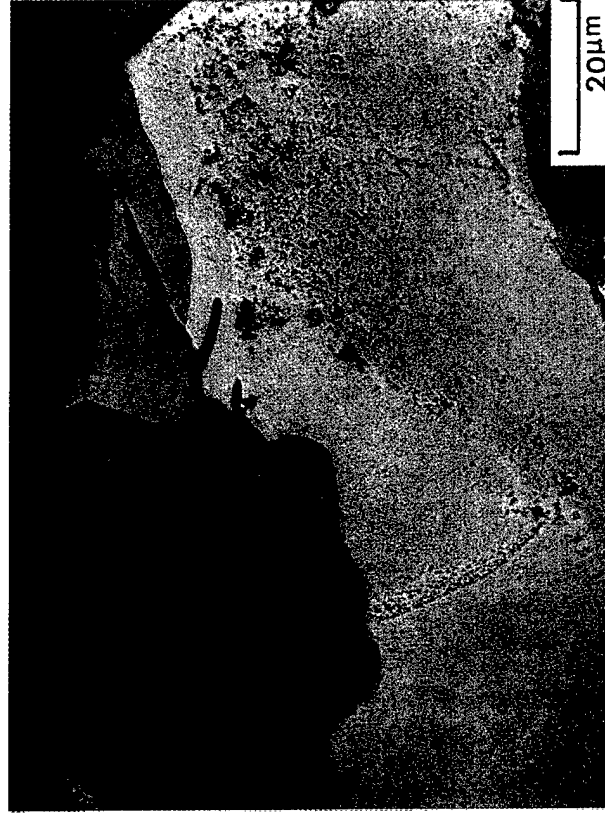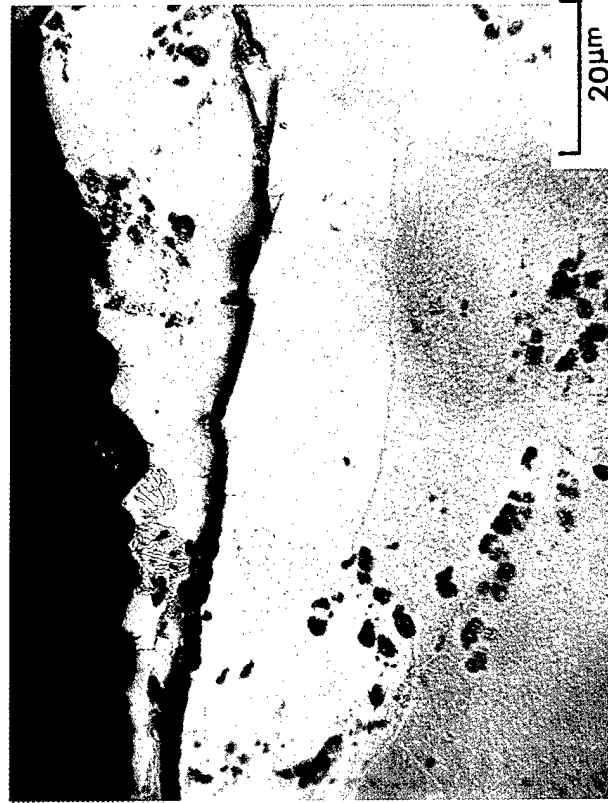
Figure 3-18. Optical Micrographs Along the Direction of Crack Growth in the Low ΔK Region Illustrating that the Fracture Path is not Straight but Changes from Grain to Grain.
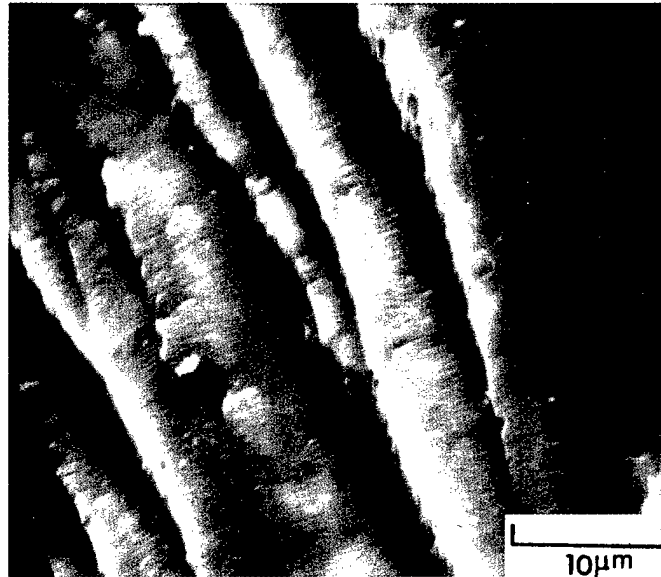
Figure 3-19. High Magnification Micrograph Showing the Presence
of Ductile Fatigue Striations at Intermediate
Levels of ∆K in the T6X51 Material.
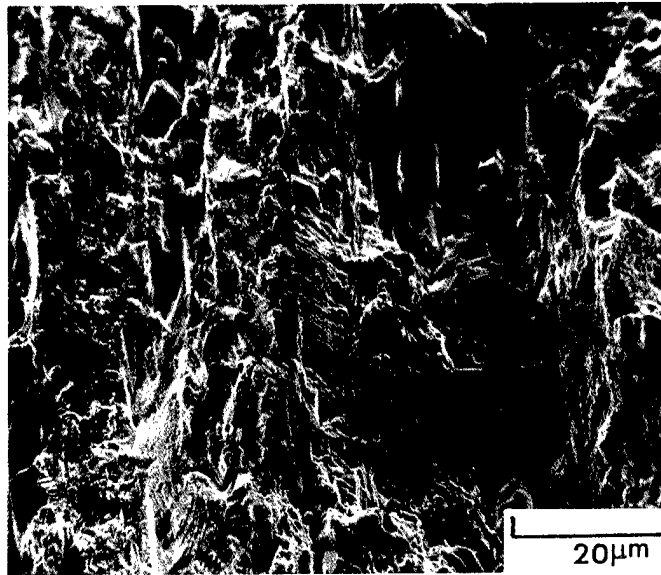
CG
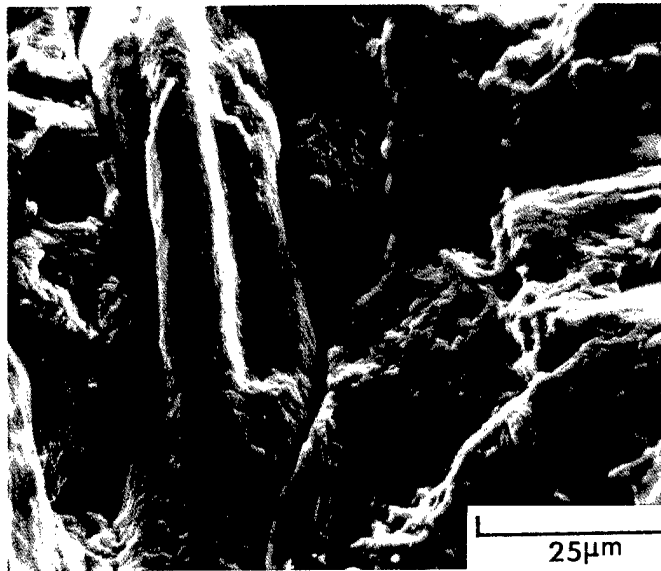
Figure 3-20.   SEM Showing the Intergranular Mode of Failure in the Peak Strength, T651, Material.

Figure 3-21.   Intense Planar Slip Developed in the High ΔK Region of a Crack Growth Specimen in the T651 Temper.

Figure 3-22.   Intense Planar Slip Developed in the High ΔK
               Region of a Crack Growth Specimen in the T651
               Temper.

Figure 3-23.   Intense Planar Slip Developed in the High ΔK
Region of a Crack Growth Specimen in the T651
Temper.

LIST OF TABLES

CHAPTER 4

CHAPTER 4

DISCUSSION AND SUMMARY

Aluminum-lithium alloys were successfully D.C. and vacuum cast. It was later shown that these methods produced unacceptable levels of dissolved gas, primarily hydrogen. The following consideration of melt preparation techniques shows where the likely sources of dissolved gases arise.

Conventional Casting

Hydrogen has a large solubility in molten aluminum. As a consequence, it is likely to be picked up by the melt. This free hydrogen principally arises through dissociation of water vapor contacting the melt. Normally, dissolved gases are removed by fluxing the melt with chlorine; however, lithium forms a stable chloride so chlorine fluxing must be done prior to lithium additions. Water, being a ubiquitous species, comes in contact with the melt during the addition of the lithium. Thus, each lithium addition after fluxing permits more gas uptake as the melt-salt surface is broken.

The results presented in the last contract showed increased hydrogen content with increased lithium additions.[1] In consideration of the previous discussion, these results do not necessarily demonstrate that lithium increases hydrogen solubility in molten aluminum but increasing the frequency of lithium additions might provide added opportunity for hydrogen uptake.

Vacuum Casting

In response to the problem of hydrogen uptake and the oxidation of lithium during casting, an attempt to

vacuum cast aluminum with high purity lithium was made.
Since the vapor pressure of lithium is low, the lithium did
not vaporize and condense on the walls of the vacuum system.
Prior to heating the aluminum and lithium, the system was
evacuated and back filled with argon several times to ensure
low partial pressure of oxygen before melting. Once the
batch was molten, the melt was poured into a chill mold.
The solidification was rapid enough to trap gas during
transfer, and an ingot with a very high gas content resulted.
The analysis of the trapped gas in the blister, Table 2-3 is
consistent with this discussion.

These results indicate that effort must be directed
toward reducing gas content to the level found in commercial
aerospace alloys.

P/M Alloys

Formation of insoluble phases such as oxides and
nitrides of lithium in the atomized powder would reduce the
amount of lithium available for precipitation hardening.
The atomizing atmosphere used was not sufficiently controlled
to produce a high quality product. Consequently, if a
powder metallurgy approach is to be taken in the future,
processes to minimize reaction of lithium with various
reactive gases must be developed. Further, experiments need
to be performed which will determine which gases will be
most reactive with lithium and thus be avoided.

Fabrication

As discussed in the previous contract, the contri-
bution of lithium to the high temperature flow stress is

small and, in most cases, alloying additions such as magnesium dominate the flow stress. Consequently, extrusion of the aluminum-lithium alloys required little press capacity. Moreover, the extrusions were high quality and had defect-free surfaces.

We have also demonstrated that Al-Li alloys can be forged and hot and cold rolled. The limited experience suggests that hot working temperatures should be maintained above the δ solvus. Cold rolling as-quenched Al-Li alloys up to a 92% reduction without an intermediate anneal can be accomplished without excessive edge cracking.

An alloy, such as the vacuum-cast alloy, which has excessive gas trapped in casting pores will be difficult to fabricate. When casting pores are filled with gas, they are compressed but cannot be healed during hot working. Thus, conditions such as blistering can occur during high temperature soaking operations.

Grain Structure

The Al-Li-Mn and Al-Li-Zr alloys both had a recovered structure after extrusion. However, the response of the grain structures to solution heat treatment was different and can be explained based on the nature of the interface between the matrix and the respective dispersoids.

During the recrystallization and growth process, a grain boundary sweeps through the matrix. The driving force, F_{Rex}, is related to the stored energy and must exceed the drag imposed by the precipitates.[2] Zener was the first to demonstrate that for a given volume fraction of

dispersoids, the radius of the particles control the drag of a grain boundary migrating under a fixed driving force.[3] Thus, the particles limit the maximum attainable grain size during growth.

Figure 4-1 is a schematic illustrating a spherical precipitate and a migrating grain boundary. When the force of migration is greater than the drag force imposed by the precipitate, the boundary will move; conversely, when the drag force exceeds the migration force, grain growth will cease. The drag force of a single particle on a boundary can be approximated by:

$$F = \pi r \sigma \sin 2\theta,$$

where σ is the grain boundary energy and r is the radius of the particle. The maximum drag force will occur when $\theta = 45°$, thus,

$$F = \pi r \sigma.$$

For a matrix containing N particles per unit volume randomly distributed, the volume fraction, f, is defined as:

$$f = \frac{4}{3}\pi r^3 N.$$

A boundary of unit area will intersect all particles that lie within a volume having a radius, 2r, that is 2rN particles. Therefore, the number of particles intersecting a unit area of grain boundary is then:

$$n = 3f/2\pi r^2.$$

Then, the total retarding force, F_{Retar}, per unit area is:

$$F_{Retar} = nF = \frac{3}{2} \frac{f}{r} \cdot$$

Consequently, the retardation to growth is directly proportional to the volume fraction and inversely proportional to the size of the precipitates.

At the solution heat treatment temperature used in this program, a significant amount of manganese can be taken back into solution, thus reducing the volume fraction of $MnAl_6$. Consequently, solution heat treatment of the Al-Li-Mn extrusions resulted in a coarse grained, recrystallized product. In the case of the heavily deformed Al-Li-Mn sheet, the extensive amount of cold work (92% reduction) and the rapid heatup to the solution heat treatment temperature in the molten metal produced a finer grain size than in the extruded material.

The nature of the interfaces and the structures of the manganese and the zirconium precipitates are different. The manganese dispersoids (Al_6Mn and $Al_{12}Mn_3Si$) are incoherent with the matrix and are rod-like. Significant mechanical fibering aligns the precipitates parallel to the metal flow. The Al_3Zr precipitates, on the other hand, are coherent and spherical. They have a definite orientation relationship to the matrix, cube/cube.[4] Like the Al_3Li precipitates, Al_3Zr have the ordered Ll2 structure. The similarities between the metastable strengthening precipitate and the orientation

relationship between the Al_3Zr and the matrix are perhaps key features in interpreting the role of Al_3Zr dispersoids on the recrystallization behavior.

As pointed out in the previous discussion, the recrystallization behavior depends upon both the volume fraction and the radius of the particle; however, the nature of the dispersoid/matrix interface must also be taken into consideration. When a grain boundary migrates through the matrix, a change in orientation of the matrix will in general result (Figure 4-2). In Al-Zr alloy, this change in orientation will lead to the development of an incoherent interface between the matrix and the Al_3Zr precipitate.[5] Therefore, an additional component to the drag on the grain boundary must be considered. The magnitude of the drag will be proportional to the misorientation.

The orientation dependence can aid in the explanation of the resistance to recrystallization of the extrusion, but how do we account for the maintenance of an unrecrystallized structure in Al-Li-Zr sheet which was heavily deformed? Since both Al_3Li and Al_3Zr are isostructural, two possibilities may be used to explain the effect of the small amount of zirconium. The first is that lithium may modify the solubility of zirconium in aluminum, thus producing a higher volume fraction of Al_3Zr. The second possibility is that lithium may substitute for zirconium, thus giving a higher volume fraction of dispersoid.

The coherent interface and the high volume fraction of Al_3Zr can account for the observation that recrystallization is difficult in the Al-Li-Zr system.

Development of Strength: The Effect of Precipitates

The strength of an alloy is related to the resistance to the motion of dislocations. Plastic deformation in aluminum and most of its alloys occurs by the motion of unit dislocation moving on close packed planes, {111}, and in close packed directions.

The increase in flow stress of a precipitation hardening alloy is due to the interaction of dislocations with zones and precipitates. Coherent and partially coherent precipitates may be penetrated by dislocations since the slip systems of the precipitates and the matrix are generally coincident. The strength and microdeformation characteristics of a precipitation hardening alloy will thus depend upon the degree of coherency, size, spacing, uniformity in the distribution of the precipitates, and the crystallographic structure of the the precipitate. The crystal structure of the metastable precipitate, Al_3Li, in the Al-Li alloys is different than the structure of the hardening precipitates of commercial aluminum alloys. In the Al-Li system, the metastable phase is the ordered, Ll_2-type (Cu_3Au) structure. The relationship between the Ll_2 lattice and an FCC lattice is shown in Figure 4-3.

There are two unique types of lattice sites in this structure. The A sites are located on the faces of the

cube. Since each face is shared by one other unit cell, the six A sites contribute a total of three lattice points per unit cell volume. The B sites are located at the corners of the cube. Each site is shared by eight adjacent unit cells, and thus the total number of B lattice sites per unit cell volume is one. This arrangement leads to an A_3B structure. Initially, the four sites are equivalent. However, once a B site is established, the A sites are automatically defined since the structure must be consistent with the composition.

A {100} section through a region of alloy which contains aluminum matrix and Al_3Li precipitates is shown in Figure 4-4. The open circles represent Al and the closed circles represent Li.

In an alloy system such as Al-Li, when the particles are sheared by the dislocations, the difference between the physical properties of the precipitates and those of the matrix determine deformation mode. In addition, precipitate radius and volume fraction control the magnitude of the flow stress. For sheared precipitates, the following are the four possible mechanisms for hardening:[6]

1. Lattice mismatch,

2. Modulus difference,

3. Peierls-force mismatch, and

4. Antiphase boundary energy.

The following relationship shows how coherency strain, ε_c, introduced by the difference between the lattice parameters of the precipitate and the matrix contributes to the strength:[7]

$$\Delta\sigma_{\epsilon_c} = \frac{6G(rf)^{1/2}}{|\vec{b}|} \epsilon_c^{3/2},$$

where: G = shear modulus, and

$|\vec{b}|$ = the magnitude of the Burgers' vector.

The strength is weakly dependent on particle radius, r, and volume fraction, f, but is dominated by coherency strain. In the case of Al-Li, the mismatch has been shown to be small, so the contribution of ϵ_c is minimal.

The following expression reveals how differences in elastic moduli increase strength:[8]

$$\Delta\sigma_E = \frac{0.8G|\vec{b}|}{\lambda_p} \left(1 - \frac{E_M^2}{E_p^2}\right)^{1/2},$$

where: E_M = modulus of matrix,

E_p = modulus of precipitate, and

λ_p = interparticle spacing.

The elastic moduli of Al-Li alloys are higher than moduli of other precipitation hardening aluminum alloys. As discussed in a section to follow, the high moduli of the alloys are attributed to the high modulus of the Al_3Li precipitate. Thus, elastic modulus differences appear to contribute to the strength of Al-Li alloys.

A strength increase has also been shown to be due to differences in the Peierls-force (the drag on a dislocation)

between the matrix and precipitate.[9] The increase has been

shown to be of the form:

$$\Delta\sigma_{P.F.} = (5.2)\frac{f^{1/3}r^{1/2}}{G^{1/2}\vec{b}^2}\left[\sigma_p - \sigma_m\right],$$

where: σ_p = flow stress of precipitate, and

σ_m = flow stress of matrix.

This hardening mechanism has been shown to account for as

much as one-third of the strength in certain superalloys

when the lattice mismatch is very small.[10] The contribution

of this mechanism to the Al-Li system has not been determined.

Lastly, a strength increase has been shown to

occur when the particles are ordered.[9] This relationship

follows:

$$\Delta\sigma_{APB} = \frac{0.56f^{1/3}r^{1/2}}{G^{1/2}\vec{b}^2}\left[\gamma_{APB}\right]^{3/2},$$

where: γ_{APB} = antiphase boundary energy.

Thus, strength is moderately dependent on r and f, and

strongly dependent on the antiphase boundary energy. The

motion of a unit dislocation in an ordered lattice will not

recreate the structure in its wake, so disorder, in the form

of an antiphase boundary, will result (Figure 4-5).[11] To

eliminate the extra energy necessary to create the antiphase

boundary, motion of an identical pair of unit dislocations

is required (Figure 4-6).[12] The dislocations are connected by

a strip of antiphase boundary. The separation of the two dislocations is determined by a balance between the force imposed by the structure to maintain its order and the repulsive force between the two dislocations of the same sign. Thus, when the dislocations move as pairs, there will be no net change in order behind the dislocation pair. These unit dislocations are referred to as superlattice dislocations.

An important manifestation of this hardening mechanism is the tendency toward strain localization. Once slip has occurred on a plane, the area of the APB is decreased, thus further favoring deformation on that plane. Localized slip has been shown to occur in all the alloys and tempers investigated. The presence of super lattice dislocations along with the observation of planar slip supports the importance of this mechanism in Al-Li alloys.

Thus, in aluminum-lithium alloys, strong contributions to strength and deformation mechanisms are the results of:

1. an ordered precipitate structure, and
2. the difference in elastic modulus between the precipitate and the matrix.

Experiments would have to be designed to determine the exact contributions of the different effects to the increase in yield strength.

Artificial Aging

Measurements of the equilibrium spacing between the superlattice dislocations in an Al-3% Li single crystal

gave an estimate of the antiphase boundary energy of Al_3Li

on the (111) planes.[13] A value of 195 erg/cm was

determined. These authors used this value to arrive at an

estimate of 537°C for the critical temperature of ordering.

This temperature is above the δ' solvus temperature determined

by Williams and Edington.[14] As a consequence of the pre-

dicted high critical temperature for ordering, it would appear

that Al_3Li should decompose directly from the supersaturated

solid solution as an ordered structure and would not disorder

on heating, but rather dissolve.

The stability of δ' and its direct formation from

the solid solution rather than sequential decomposition

through clustering reactions to some intermediate precipitates

can account for the direct aging results in this program.

Whereas, in the Al-Zn-Mg system, the following reaction

scheme has been shown:

$$\text{supersaturated solid solution} \longrightarrow \text{G.P. zones} \longrightarrow \eta' \longrightarrow \eta,$$
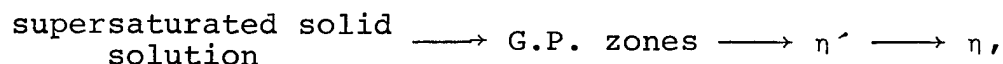
or the more complicated sequence in the Al-Cu system:

$$\text{supersaturated solid solution} \longrightarrow \text{G.P.I} \longrightarrow \theta'' \longrightarrow \theta' \longrightarrow \theta.$$
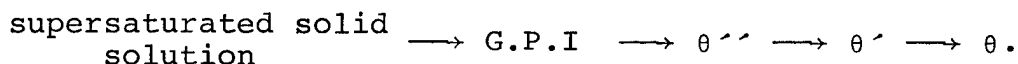
Each phase in the aging sequence has a range of stability,

and different distributions of precipitates can occur,

leading to significantly different mechanical properties.

Since the homogeneous decomposition process produces δ' directly, a variety of artificial aging conditions in a high solute lithium alloy resulted in similar structures and properties. For example, the quench aging and conventional aging produced identical notch-tensile/yield strength behavior. Moreover, the hardness results suggest that the aging is isokinetic and depends, therefore, only on an integral of time and temperature.

Effect of Grain Structure on Mechanical Properties

Although strength and ductility are directly related to the morphology of the metastable precipitates, contributions to these properties may also have their origins in the grain structure. Four grain structures were produced in this program. Two were fully recrystallized, one coarse and the other fine, and two were unrecrystallized. As discussed earlier, the alloy containing manganese recrystallized while the alloy containing zirconium tended to remain unrecrystallized in both extrusion and sheet forms; however, when recrystallization occurred in the Al-Li-Zr sheet, the grain size tended to be coarse and associated with shear bands which developed during cold rolling. The limited data in this program suggested that both the degree of recrystallization and grain size had a systematic effect on both strength and ductility. Table 4-1 compares the yield strength and ductility in the four structures investigated. A low degree of recrystallization resulted in

higher strength and slightly lower ductility and a coarse grain size tended to lower both strength and ductility.

Within this investigation, we have shown the existence of planar slip and a discussion of the consequences of this. Localized shear and the interrelationship between the localized deformation and grain structure on the mechanical properties of Al-Li alloys must now be considered. We will use the concept of dislocation pileups to phenomenologically account for the deformation behavior in Al-Li alloys.

There are two logical paths which develop the framework necessary to qualitatively relate grain size to deformation behavior in polycrystalline materials.[15] One model utilizes the concept of dislocation "pileups" at grain boundaries and the second considers the effect of grain size on dislocation density.

In the dislocation pileup model, a slip band which is formed within a favorably oriented grain will terminate at a grain boundary. In order for the shear displacement associated with this impinging slip band to be accommodated plastically at the adjacent grain, the stress concentration must be sufficient to nucleate slip along the trace of the shear zone in the adjacent grain. This can be expressed mathematically in the simplified form:

$$n(\tau - \tau_o) \geq m\tau_c,$$

where, τ is the applied shear stress, τ_o a back stress, m the average Schmid orientation factor, n a stress concentration

factor, and τ_c is the critical resolved shear stress necessary to nucleate slip in the adjacent grain. The stress concentration factor, n, can be considered to be a pileup of n dislocations and n becomes proportional to the grain diameter, ℓ. The stress concentration at a distance, r, ahead of the pileup may be approximated by $(\ell/r)^{1/2}$, which leads to the expression:

$$\tau = \tau_o + n\tau_c \sigma^{1/2} \cdot \ell^{-1/2}.$$

The above equation can be rewritten in terms of tensile stresses and the form follows the familiar empirical Hall-Petch relationship:

$$\sigma = \sigma_o + k\ell^{-1/2}.$$

In the second approach, stress concentrations at the grain boundaries are not treated explicitly but the flow stress is written in terms of dislocation density having the following form:

$$\sigma = \sigma_o + \alpha\mu|\vec{b}| \sqrt{\rho},$$

where σ_o is a lattice friction term, α a numerical constant, μ the shear modulus, and ρ the dislocation density. Numerous TEM investigations have experimentally verified the qualitative inverse relationship between dislocation density and grain size.[16-19] The inverse dependence has been explained by considering grain boundary ledges as sources for dislocations, and the number of dislocations generated/unit of strain is then proportional to the grain boundary surface area. Consequently a Hall-Petch type relationship again emerges.

When there are sufficient slip systems available to satisfy the macroscopic criteria of Von Mises and Taylor, as in the case of face centered cubic materials, microscopic phenomena become more apparent. For example, one must consider the distribution of dislocations and cross slip probability. Most aluminum alloys show only a weak dependence of grain size on mechanical properties and this can be interpreted in light of the microstructural significance of the slope, k, in the Hall-Petch relationship. We must, therefore, attempt to understand why Al-Li alloys behave differently.

Alloys in which systematic variations in stacking fault energy (SFE) can be made by alloying have shed much light on the influence of microstructure on the deformation behavior, specifically, the effect of cross slip probability and the change in k that results when cross slip is not viable.[15] For example, in pure copper and up to certain concentrations of aluminum, the deformation can be characterized by wavy slip and a subgrain structure results after deformation. However, beyond a critical level of aluminum, the deformation changes from wavy slip to planar glide. The dislocations occur in coplanar arrays, and the slip bands are straight and finely spaced. Planar glide arises as a result of reduced cross slip. When the deformation was more planar, k was also shown to be larger than in pure copper. Figure 4-7 shows the variation in the Hall-Petch slope ratio with electron-atom ratio for several copper alloys.

Schematically, this effect is shown in Figure 4-8
where the stress-strain plots are depicted for wavy and planar
slip as a function of grain size, ℓ.[15]

Alternatively, changes in cross slip probability can
be made by varying the degree of long range order in ordered
alloy systems.[12,20-22] With increasing degree of order, there is
a corresponding decrease in the cross slip probability and the
slope, k, increases with increasing order.

The dramatic effect of order in the FeCo-V system
on deformation behavior and consequent effect on such proper-
ties as the reduction in area at 25°C will serve as an
illustration (Figure 4-9). As a consequence of the ordering
reaction, there is a discontinuous change in ductility. (S =
0 is disordered and S = 1 is ordered.) TEM investigations con-
firmed that disordered FeCo-V deformed by wavy glide, but when
fully ordered the deformation occurred by planar glide bands.
Also, SEM showed a change in fracture mode from ductile shear
with no evidence of micro-cleavage at S = 0 to complete cleavage
at S = 1.

To appreciate the effect of planar slip on the
influence of both k and ultimately on the fracture behavior, a
simple model will be outlined. Figure 4-10 illustrates a grain
boundary in a material undergoing deformation.[15] A slip band
in grain A has been nucleated and is terminating at the boundary
between A and B. The rate at which the grain boundary displace-
ment is occurring, $\dot{D}$, is related to the mobile dislocation
density, ρ, the average velocity, $\bar{v}$, which is governed by the

resolved shear stress, the average mean free path, ℓ, which
is at a maximum equal to the grain diameter and the magnitude
of the Burger's vector, $|\vec{b}|$. This can be expressed as:

$$\dot{D} = \rho \bar{v} \ell |\vec{b}|.$$

The total relaxation rate, $\dot{R}$, in grain B bounded by r is
governed by the sum of the individual rates on each of the
slip systems to satisfy local strain compatibility require-
ments. These include ρ, a dislocation multiplication factor,
M, and the average Schmid factor, m. For n operative slip
systems, this becomes:

$$\dot{R} = \frac{r}{m} \sum_n M_n \rho_n |\vec{b}| \bar{v}_n.$$

In addition to the applied shear stress, the microscopic specimen
of dimension, r, is subjected to a shear stress, $\Delta\tau$, which is
a function of the difference between $\dot{D}$ and $\dot{R}$. If $\dot{D}$ is not
significantly greater than $\dot{R}$, then $\Delta\tau$ is not a significant
obstacle, and $\Delta\tau$ is very near zero. On the other hand, if
$\dot{R}$ is much less than $\dot{D}$, then $\Delta\tau$ is quite large. As the effective
strain increases, $\dot{R}$ eventually increases and the rate of change
of $\Delta\tau$ with increasing strain reduces. Schematically, this can
be represented by Figure 4-15. Wavy slip, significant cross
slip, results in $\dot{R} \rightarrow \dot{D}$ and thus the local increase in $\Delta\tau$ at the
boundary is small. However, for planar glide, $\dot{R} << \dot{D}$, and
locally $\Delta\tau$ is large. Reducing the ability to cross slip
reduces $\dot{R}$.

Using this simple model we have a way of qualitatively
assessing the significance of the localized deformation and the

fracture behavior. When the δ´ particles are sheared by the dislocations (shearing occurs up to peak strength), the ordered particles require superlattice dislocations and thus cross slip probability is reduced. The rate, $\dot{R}$, of accommodation at a grain boundary is low and locally $\overline{\Delta\tau}$ becomes large. Consequently, any reduction in strength in the grain boundary region will have deleterious effect on the fracture behavior.

Segregation of Tramp Elements

In *Situ*. Auger analysis of fractured Al-Li and Al-Mg-Li alloys consistently showed the presence of large quantities of sodium, potassium, and sulfur on the fracture surfaces. These elements were probably introduced to the aluminum as impurities in the lithium. Unlike lithium, these elements have virtually no solubility in aluminum. Figure 4- 12 shows, for example, the Al-Na phase diagram.[23] The low solubility of sodium, potassium, and sulfur in aluminum may lead to unwanted segregation in the grain boundaries.

In support of the observations made in this research, recent work has shown the deleterious effect of sodium on the ductility of Al-Li alloys.[24] They found that when the bulk sodium concentration was in excess of 0.004%, the ductility and impact toughness were low. These investigators also showed that additions of iron, silicon, and bismuth neutralized the effect of sodium on the fracture behavior. Tables 4-2 and 4-3 contain the compositions and the effects of composition on the mechanical properties of Al-Mg-Li alloys, respectively.[24]

Sodium and potassium form a liquid phase in aluminum at temperatures lower than either the solution heat treatment or the artificial aging temperatures used in this investigation. Consequently, it would not be unreasonable to expect these elements to find their way along grain boundaries, and because of the very low solubility of the liquid, form a thin film along the boundaries. This concept would support the observation that small quantities of these species reduce ductility.[25]

The effect of elements such as Fe, Si, and Bi probably have their origins in the formation of intermetallic compounds with low volume fractions. Silicon, for example, moves the liquid immiscibility gap to higher percentages of sodium in the Al-Na system and forms a ternary compound having the approximate formula $AlNaSi_{1.25}$.

Though a causal effect between the tramp elements and the fracture behavior have not been established in this program, it does seem reasonable to expect that any lowering of the grain boundary strength would seriously affect the toughness of a material, especially those which deform by planar slip.

Grain Boundary Precipitation

Precipitation within the matrix region of Al-Li alloys occurs by homogeneous decomposition with uniform nucleation up to the grain boundaries. Growth measurements of the matrix precipitates as a function of isothermal aging

time showed that the growth of δ´ was diffusion controlled and that precipitate growth followed the classical coarsening equation:

$$R = kt^{1/3}.$$

Along with the growth of the metastable precipitates, a PFZ also developed and the growth also followed a similar relationship, which can be written:

$$\left(\frac{w}{2}\right) = kt^{1/3},$$

where, $\frac{w}{2}$ is the PFZ half width in micrometers, and t is the aging time in seconds. In the grain boundary region, δ´ particles preferentially coarsen and their rate of growth is significantly faster than within the matrix.

In a recent investigation, Williams and Edington observed a discontinuous precipitation reaction at grain boundaries in binary Al-Li alloy systems.[26] The discontinuous reaction is also a coarsening reaction, and the existence of the reaction depends to a large extent on the stability of the grain boundaries. In the alloys investigated in this program, zirconium and manganese were added to reduce grain boundary migration. Consequently, rather than observing a coarsening reaction by discontinuous precipitation, simple coarsening of individual precipitates close to the grain boundaries occurred. Based on the experimental observations, a model for the PFZ development and the effect of the PFZ on mechanical properties will be discussed.

The TEM investigations showed that the matrix precipitates were spherical throughout the aging sequences investigated. The largest precipitate diameter measured was approximately 0.18 μm and even at that size, the interface dislocations were not observed. Williams and Edington measured the strain associated with δ´ and found it to be quite small.* The observations in this research of precipitate morphology and the absence of interface dislocations would support their findings.

Nucleation can occur either homogeneously or heterogeneously. In the Al-Li system, coherent, spherical precipitates which form from the supersaturated solid solution occur by homogeneous decomposition. Due to the small misfit one would suspect that the barrier to homogeneous decomposition is small. This has been experimentally substantiated by the difficulty in suppressing the precipitation reaction. Specimens quenched and examined a short time after quenching (less than 10 minutes at room temperature) in the electron microscope showed evidence of δ´ reflections. The supersaturation is thus relieved efficiently by homogeneous nucleation. Also, incoherent, (AlLi) precipitates were not observed on grain boundaries.

Once nucleation has occurred, the precipitates grow and eventually small precipitates grow at the expense of the larger precipitates. The size distribution shifts to larger

---

*The matrix α/δ´ misfit parameter was determined to be −0.08+0.02%.[14]

radii during growth. The growth rate was shown in this research
(which confirmed the earlier work of Noble and Thompson[27]) to be
controlled by volume diffusion and the theoretical equation:

$$\bar{r}^3 - \bar{r}_o^3 = kt,$$

predicts the coarsening rate. In this equation, $\bar{r}$ is the
average particle radius at time, t, $\bar{r}_o$ is the average particle
radius at the onset of coarsening. The rate constant, k, is
given by:

$$k = \frac{2\gamma D C_e v_n^2}{\rho_o^2 RT},$$

where γ is the interfacial free energy of the particle/matrix
interface, D is the coefficient of diffusion of the solute in
the matrix, C_e is the concentration of solute in equilibrium
with a particle of infinite size, v_n is the molar volume of the
precipitate, ρ_c is a numerical constant related to the distri-
bution of particle sizes and RT have their usual meaning.

The precipitates growing in the matrix and the grain
boundary regions are similar and, to a reasonable approximation,
all the terms with the exception of the diffusion coefficient
in the expression for k can be written as a single constant, C.
Then the equation for growth becomes:

$$\bar{r}^3 - \bar{r}_o^3 = CDt.$$

The rate of growth is then determined by the diffusion of
solute. From this it becomes clear that since D at grain
boundaries, D_{GB}, is much greater than D in the matrix, D_m,

the ultimate size of the particle r_{GB} will be proportionately
larger than r_m. Thus, the PFZ occurs as a consequence of
preferential ripening of δ' along the grain boundaries by
enhanced diffusion.

Influence of PFZ's on Ductility and Fracture

Room temperature behavior can be affected by the
presence of a PFZ.[28] A large PFZ tends to facilitate inter-
granular failure with small reductions in area, and growth of
voids at large precipitates. Voids nucleate and grow near the
onset of macroscopic instability. Final fracture occurs when
sufficient matrix flow permits the voids to link up.

In the Al-Li alloys investigated, PFZ's widened during
aging and concurrent with the PFZ gowth, δ' particles in the
grain boundary region coarsened. With increased aging time, the
spacings between the large precipitates were reduced and likewise
the amount of matrix flow necessary to link up the voids was also
reduced. Thus, the ductility continuously decreased.

SEM and TEM observations confirmed this model. At
short aging times, before grain boundary coarsening began, the
failure was intergranular with slip offsets on the grain facets.
As aging proceeded, the offsets were progressively replaced by
dimples which formed around the coarse grain boundary pre-
cipitates.

In the Al-Mg-Li alloy system recently investigated,[1,29]
we observed the presence of coarse, Al_2MgLi precipitates on
the grain boundaries. Further, increasing the magnesium

increased the amount of grain boundary precipitation. Also, the TEM investigations conducted in this program showed the presence of a depleted zone in the Al-Mg-Li system.

Fatigue Crack Growth - Al-Cu-Li Alloys

The development of the high strength in an Al-Cu-Li alloy is a consequence of the co-precipitation of $CuAl_2$-type and Al_3Li-type metastable precipitates. The Al_2Cu precipitates significantly add to the strength, while Al_3Li not only adds to the strength but affects the deformation process and controls properties such as elastic modulus. The excellent fatigue performance of Al-Cu-Li alloys is in part due to the presence of the coherent, ordered Al_3Li precipitates. The presence of the ordered precipitates reduces the probability of cross slip, thereby making the slip more reversible. It is the irreversibility of slip which ultimately leads to failure.

A second important feature of Al-Cu-Li alloys is that crack growth proceeds along certain crystallographic planes (Stage I crack growth). Thus, the orientation of a growing fatigue crack is controlled by the orientation of the grain in which it is propagating. Consequently, by decreasing the grain size, an increase in fatigue crack growth resistance would be expected.

In the peak strength temper, the fracture process was shown to be by intergranular failure. Due to the presence of the ordered precipitates, there is a tendency toward

localization of strain. Once slip has occurred on one plane, the area of an APB is decreased, thus further favoring deformation on that plane. The localized deformation will produce large stress concentrations at grain boundaries and will therefore initiate failure at the grain boundaries.

The change in failure from transgranular to intergranular can be rationalized on the basis of increased strength of the matrix. At peak strength, nucleation of flow across a boundary becomes more difficult and if large stress concentrations continue to build on one side of the grain, the boundary may separate before yielding can occur in an adjacent grain. Thus, due to the tendency to develop intense localized deformation, peak strength tempers might be undesirable because of low fracture toughness.

The Al-Cu-Li alloys used in this investigation consisted of coarse, recrystallized grains, with a high volume fraction of constituent particles. Both of these microstructural features have been shown in other high-strength alloys to adversely affect fracture toughness. Through control of grain size and constituent level, fracture toughness may be increased in tempers which fail by a transgranular failure mechanism.

A further important characteristic of the Al-Cu-Li alloys is the relative insensitivity of crack growth rates to moisture extremes used in this investigation. Two moisture levels, <5% and >95% were used. In the case of the low relative humidity, the crack growth rate of Al-Cu-Li in both tempers was

slightly better than 7075-T651 at intermediate ΔK levels.[30] However, in high humidity, the crack growth resistance of Al-Cu-Li was significantly better than 7075-T651. The increased difference between the two alloys is attributed to the insensitivity of Al-Cu-Li alloys to moisture and the extreme sensitivity of 7075-T651 to moisture. The mechanism for the insensitivity of Al-Cu-Li to moisture has not been established.

SCF in Al-Li Alloys

The results of the SCF tests on the Al-Li-Mn and Al-Li-Zr alloys showed that the plastic strain-life plots followed the Coffin-Manson relationship over the entire strain range investigated. TEM of fatigue specimens at high and low plastic strain amplitude showed the presence of intense planar slip. Therefore, the Coffin-Manson behavior should be applicable over the entire range.

SCF lives are in general related to the monotonic ductility. For example, reviewing many alloy systems, Herztberg concluded that more ductile materials which possess high cyclic strain hardening exponents have greater resistance in the SCF regime.[31] The low ductility of the Al-Li alloys manifests itself throughout the plastic strain regime. Improvements in SCF will occur when there is an increase in the ductility and toughness.

Modulus

The stability of the Al_3Li and its spontaneous formation can be used to explain the high elastic modulus and the

change in modulus with aging. Once the alloy is quenched, the ordered precipitates form directly and grow with increased time. With short time aging, the structure of Al-Li alloys consists of a uniform distribution of small, closely spaced, coherent domains of ordered Al_3Li having a high modulus of elasticity. Consequently, the modulus of the precipitates contributes strongly to the modulus of the alloy. As aging progresses, especially beyond peak strength, the separation between the areas of order and the matrix becomes larger. Therefore, the contribution of the matrix to modulus becomes progressively more important.

TABLE 4-1

CHEMCIAL COMPOSITION FOR INVESTIGATING THE EFFECT OF Na ON FRACTURE[24]

No. of Melt	Chemical composition, wt.%						
	Mg	Li	Zr	Fe	Si	Na	Bi
1	5.4	2.1	0.14	0.25	0.20	0.0032	--
2	5.3	2.0	0.13	0.04	0.04	0.0031	--
3	5.3	2.0	0.13	0.04	0.04	0.0076	--
4	5.3	2.1	0.13	0.04	0.04	0.0036	0.04
5	5.5	2.2	0.14	0.03	0.22	0.0032	--
6	5.5	2.1	0.13	0.03	0.03	0.0040	--
7	5.5	2.1	0.14	0.28	0.03	0.0042	--

TABLE 4-2

MECHANICAL PROPERTIES OF CONTROLLED COMPOSITIONS[24]

No. of Melt	Longitudinal direction					Transverse direction		
	UTS, kg/mm^2	$\sigma_{0.2}$, kg/mm^2	δ,%	kgm/cm^2	K_{Ic}, $kg/mm^{3/2}$	UTS, kg/mm^2	$\sigma_{0.2}$, kg/mm^2	δ,%
1	49.0	30.0	17.6	0.3	84.5	38.6	29.9	6.0
2	44.0	25.6	17.7	--	92.0	--	--	--
3	43.4	25.3	17.0	--	77.0	--	--	--
4	44.1	25.5	18.4	--	109.5	--	--	--
5	46.3	30.0	11.3	1.6	109.0	32.1	26.0	2.5
6	46.7	27.5	17.2	0.7	89.5	38.2	27.8	6.0
7	48.3	30.4	13.8	1.3	109.2	41.0	26.0	8.1
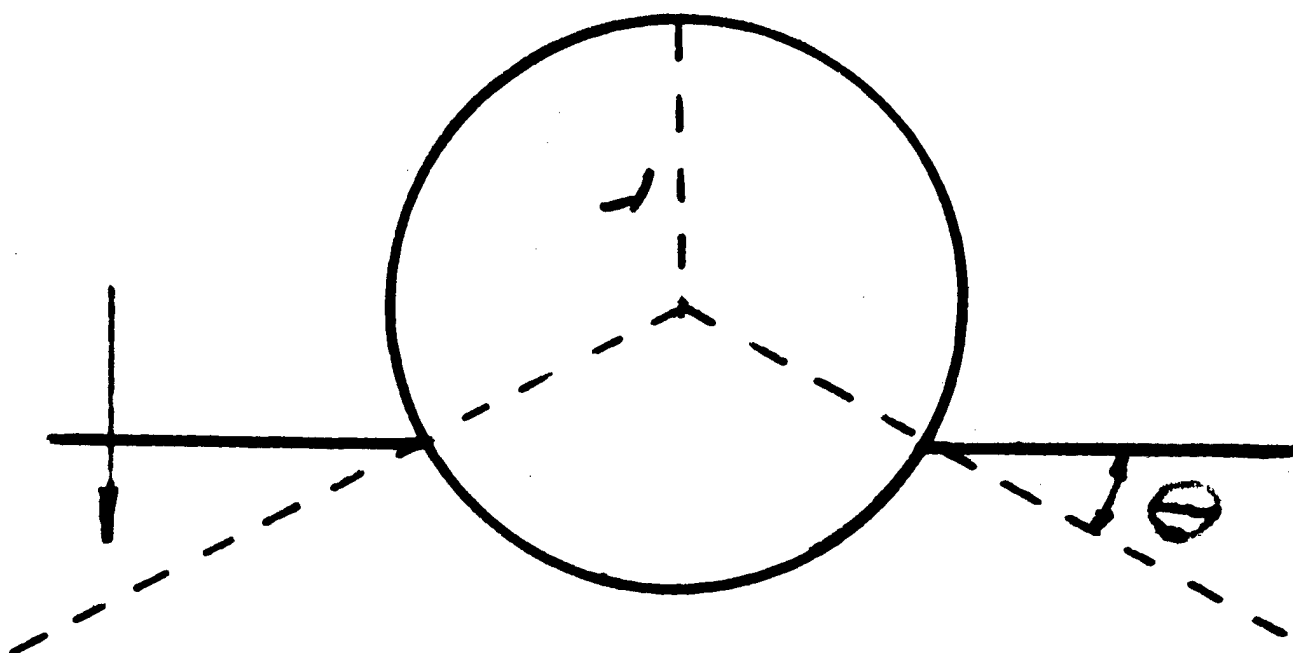
4-1   Interaction of a Migrating Grain Boundary with
an Incoherent Particle.

COHERENT PRECIPITATES

MIGRATING GRAIN BOUNDRY

INCOHERENT PRECIPITATES
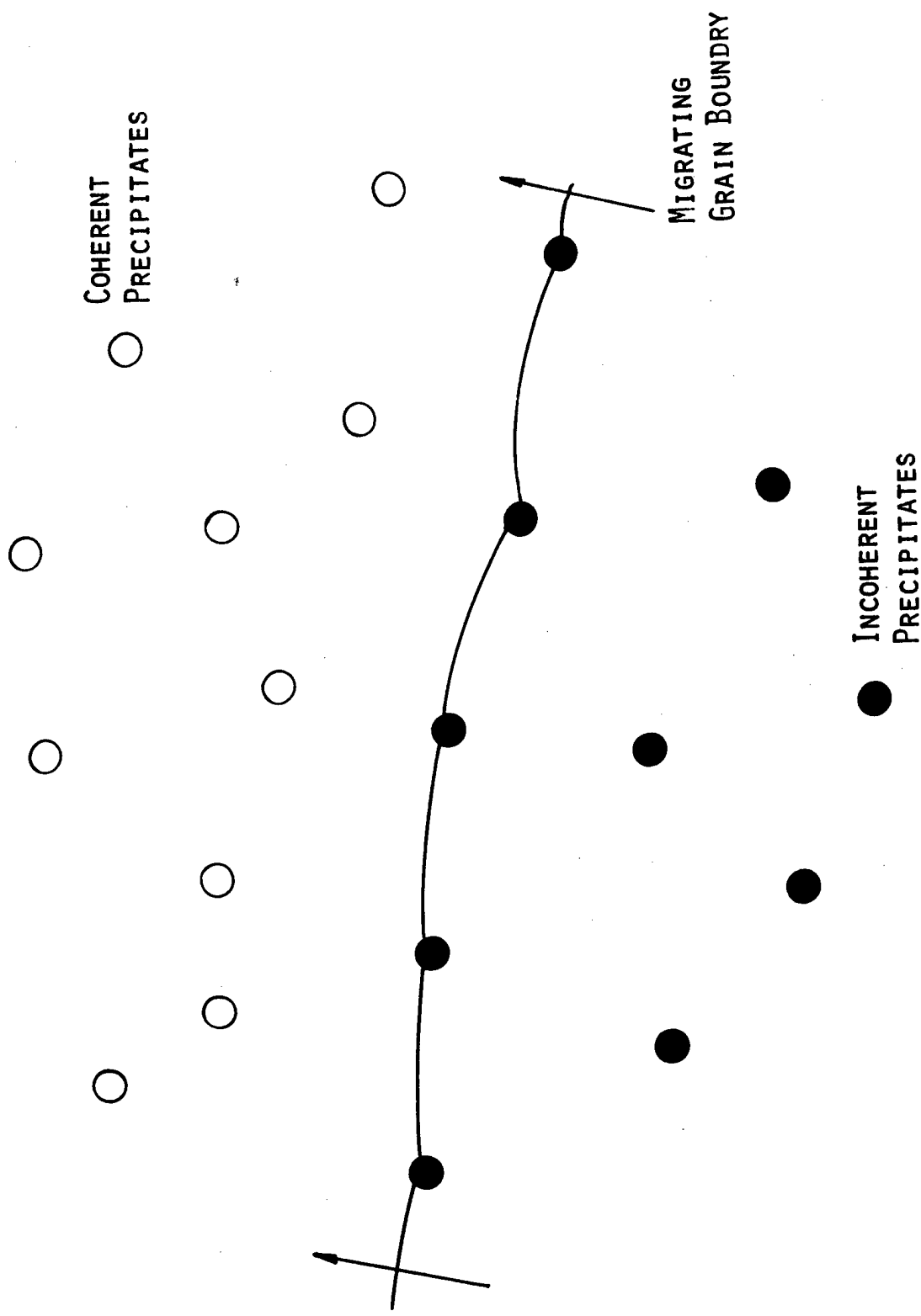
4-2   Interaction of a Migrating Grain Boundary with Coherent Precipitates.
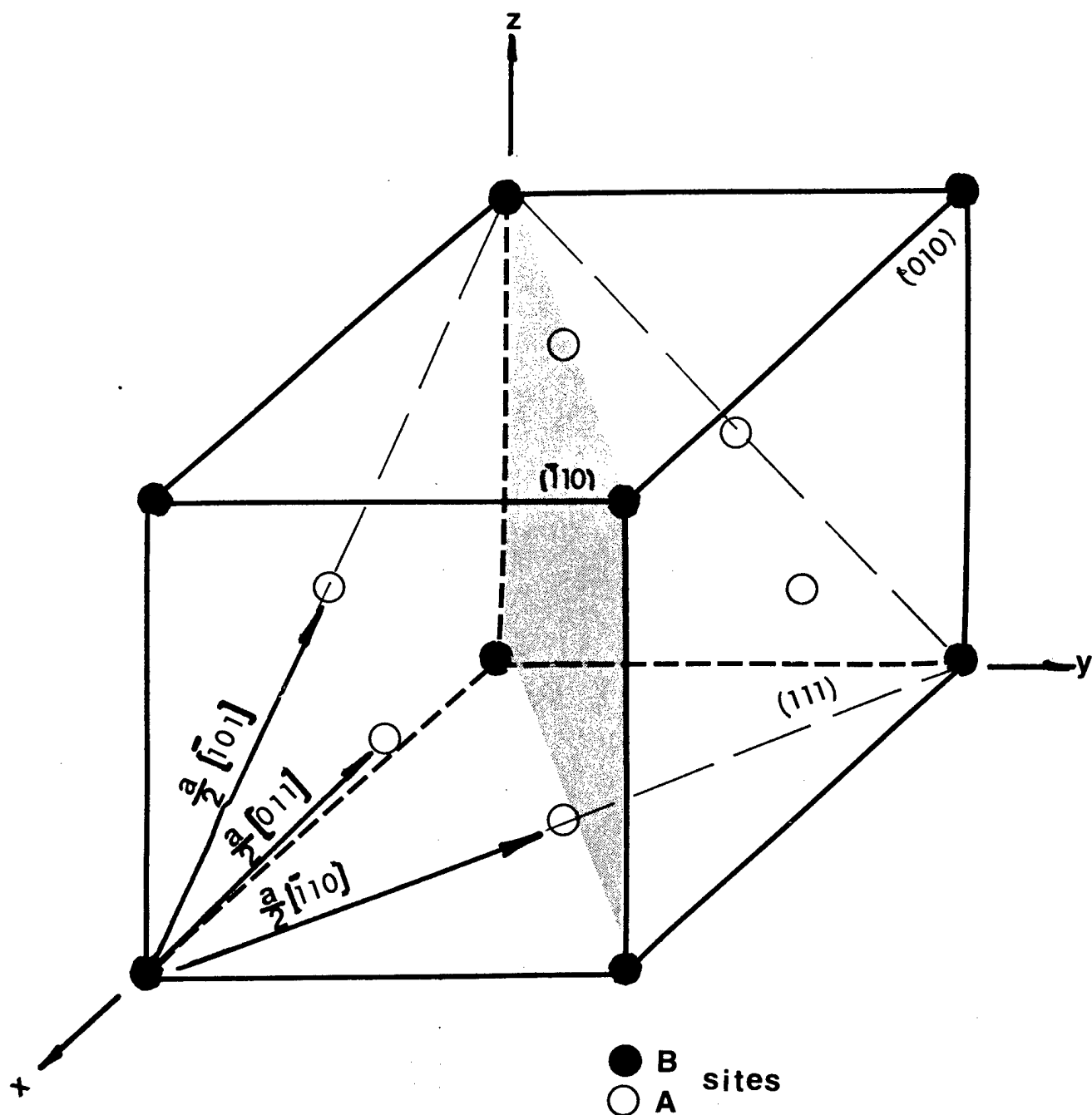
4-3   Definition of Atomic Positions in the Face-Centered,
        Cubic (FCC) Lattice.

{100}

Al ◯
Li ● SITES
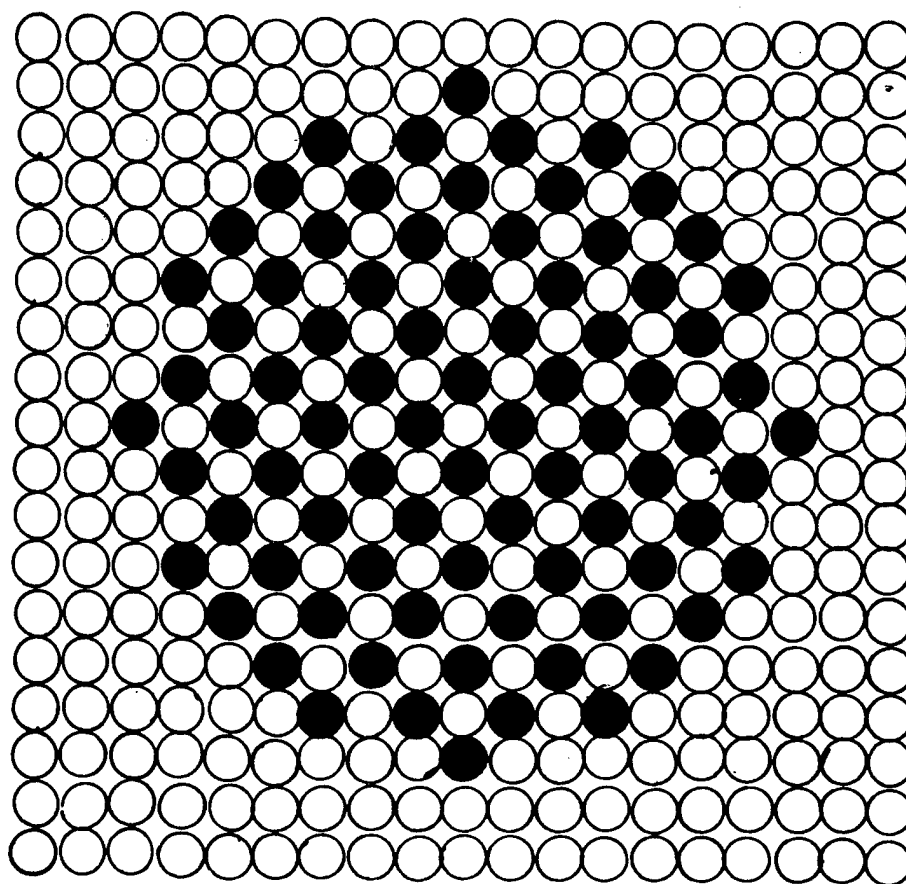
4-4 A {100} Section Through a Region of Alloy Which
Contains Aluminum Matrix and Al_3Li Precipitate.

ORDERED LI₂
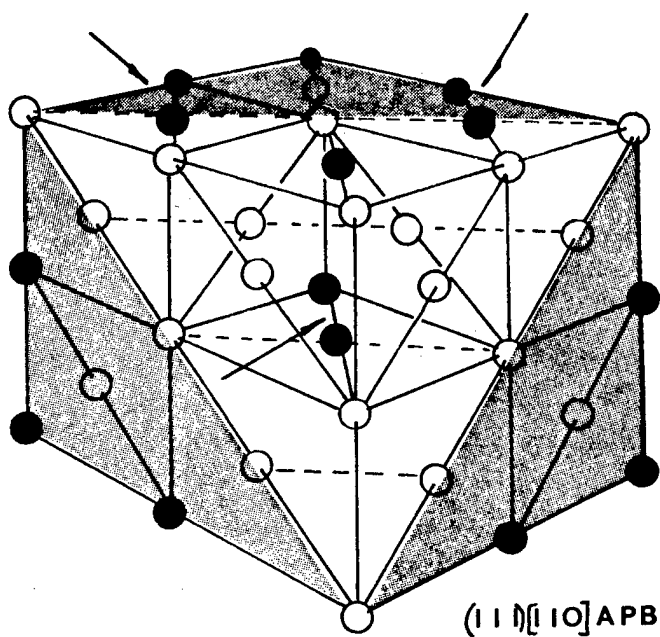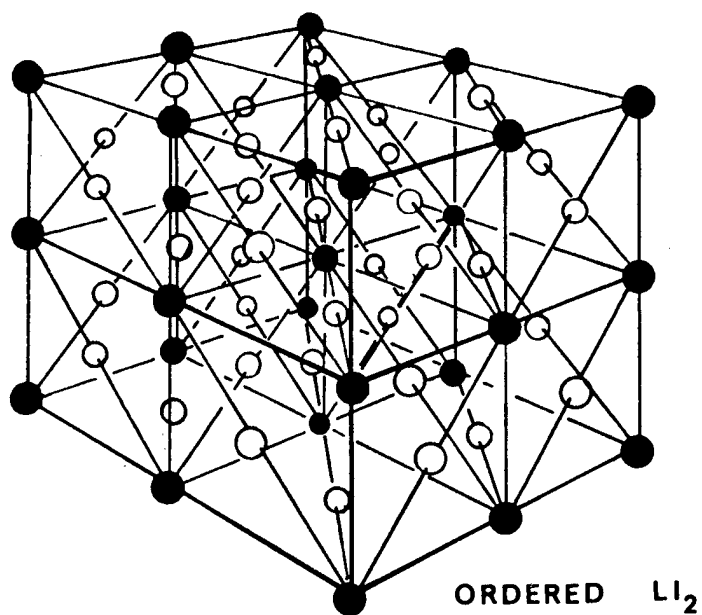
(1 1 1)[1 1 0] APB

4-5   (a) The Ordered Cu₃Au, Ll₂ Structure. (b) (111)
       [110] Antiphase Boundary in the Ll₂ Structure.
       Brackets show the creation of unlike neighbors.
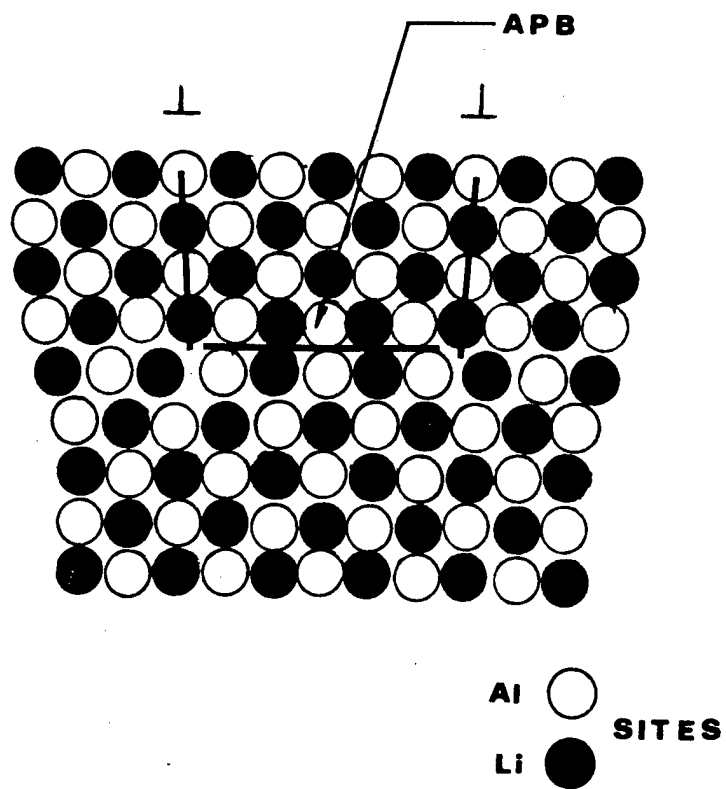
4-6   A (100) Section Through a Region of Ordered Alloy
      Illustrating the Pair-Wise Motion of Dislocations.
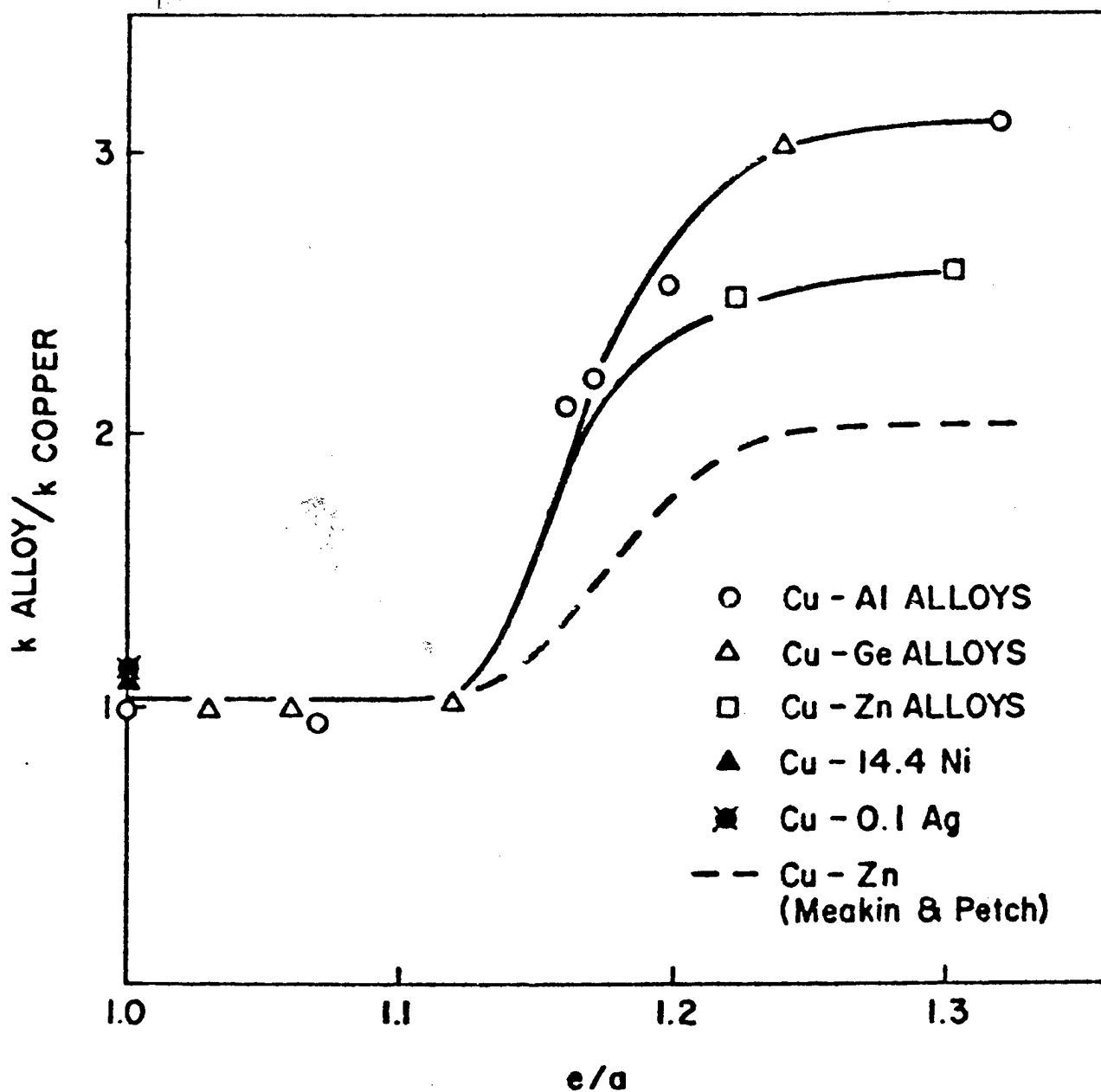
4-7   Variation of Petch Slope Ratio with Electron-
       Atom Ratio for Several Copper Alloys.

DIFFICULT CROSS SLIP

ℓ_1

ℓ_2

ℓ_3

ℓ_1 ℓ_2

ℓ_3

EASY CROSS SLIP

σ

10^{-4}

10^{-2}

ϵ_ρ

4-8   Schematic of Stress Strain Curves of Wavy and Planar Slip Mode Materials of Different Sizes, $l_3 > l_2 > l_1$.
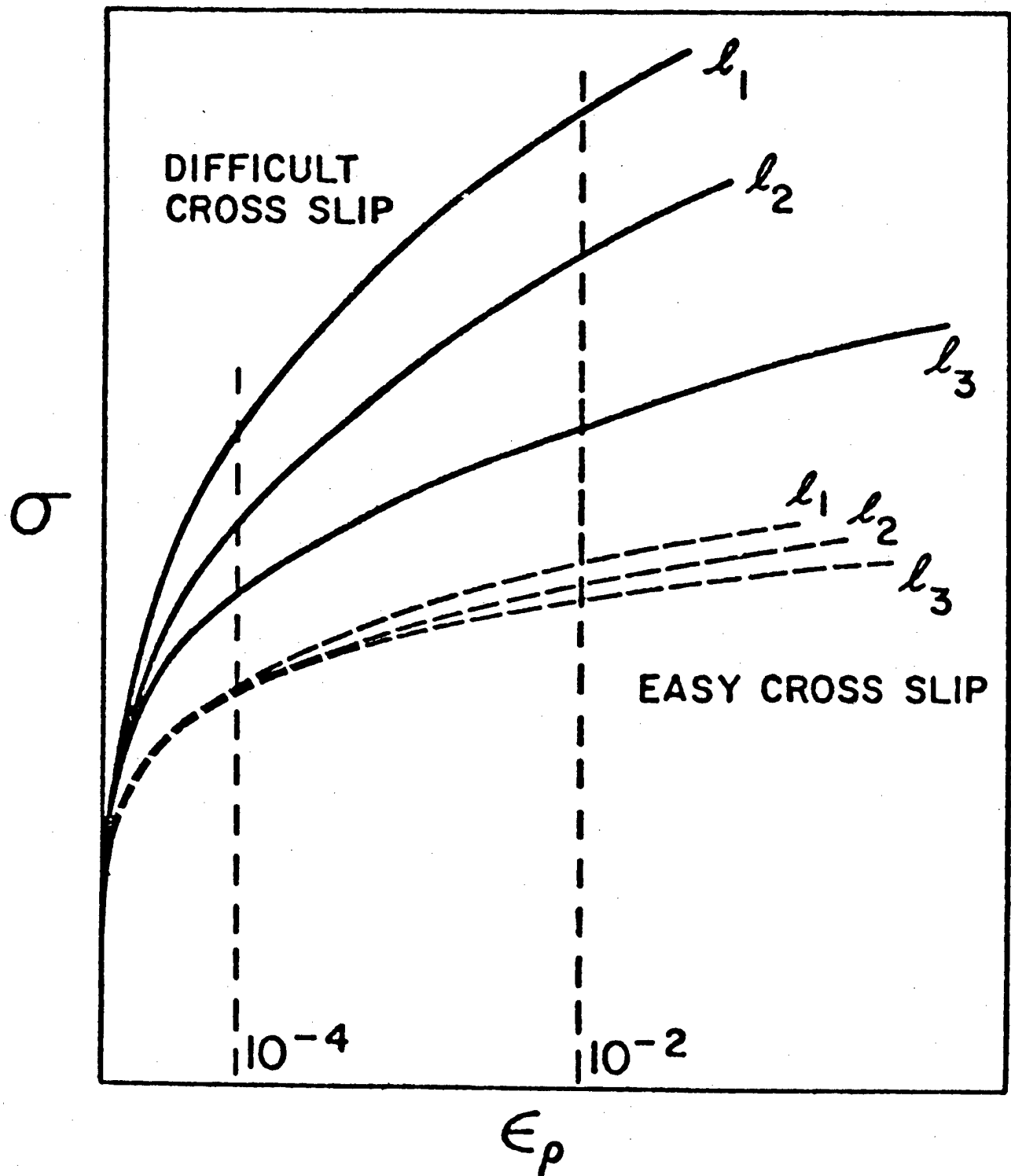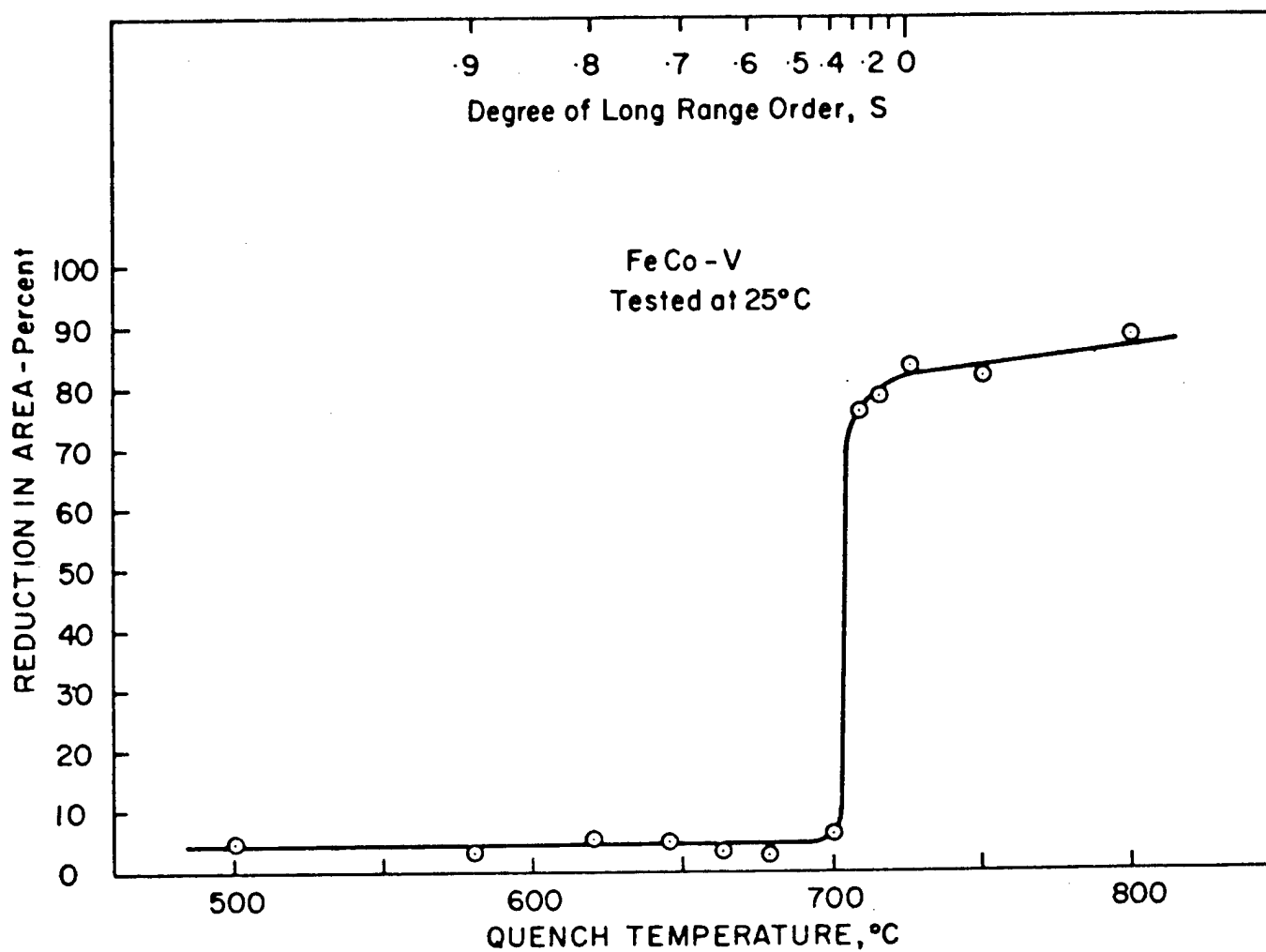
4-9   The Influence of Long-Range Order on Ductility
       of FeCo-V at 25°C.

$$\dot{D} = \rho \cdot b \cdot \overline{v} \cdot \ell \qquad \dot{R} = \frac{r}{m} \sum_{1,2,3} M \cdot \rho \cdot b \cdot \overline{v}$$
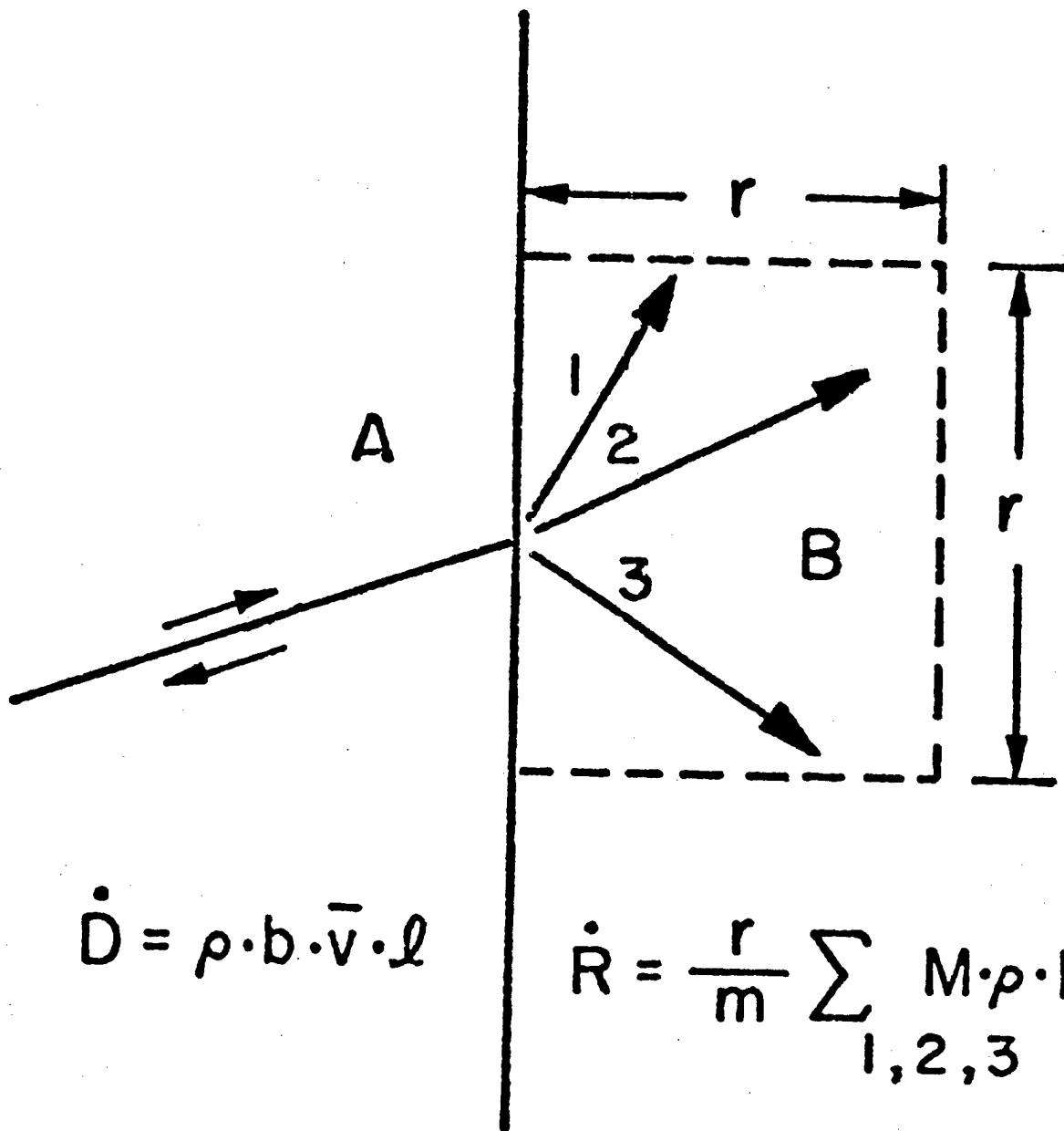
4-10   Glide Band in Grain A Imposes a Shear Displacement
        at a Rate $\dot{D}$ Upon a Region of Dimension γ in Grain
        B. The overall relaxation rate $\dot{R}$ depends on the
        rate at which the required number of accommodation
        slip bands nucleate and spread.
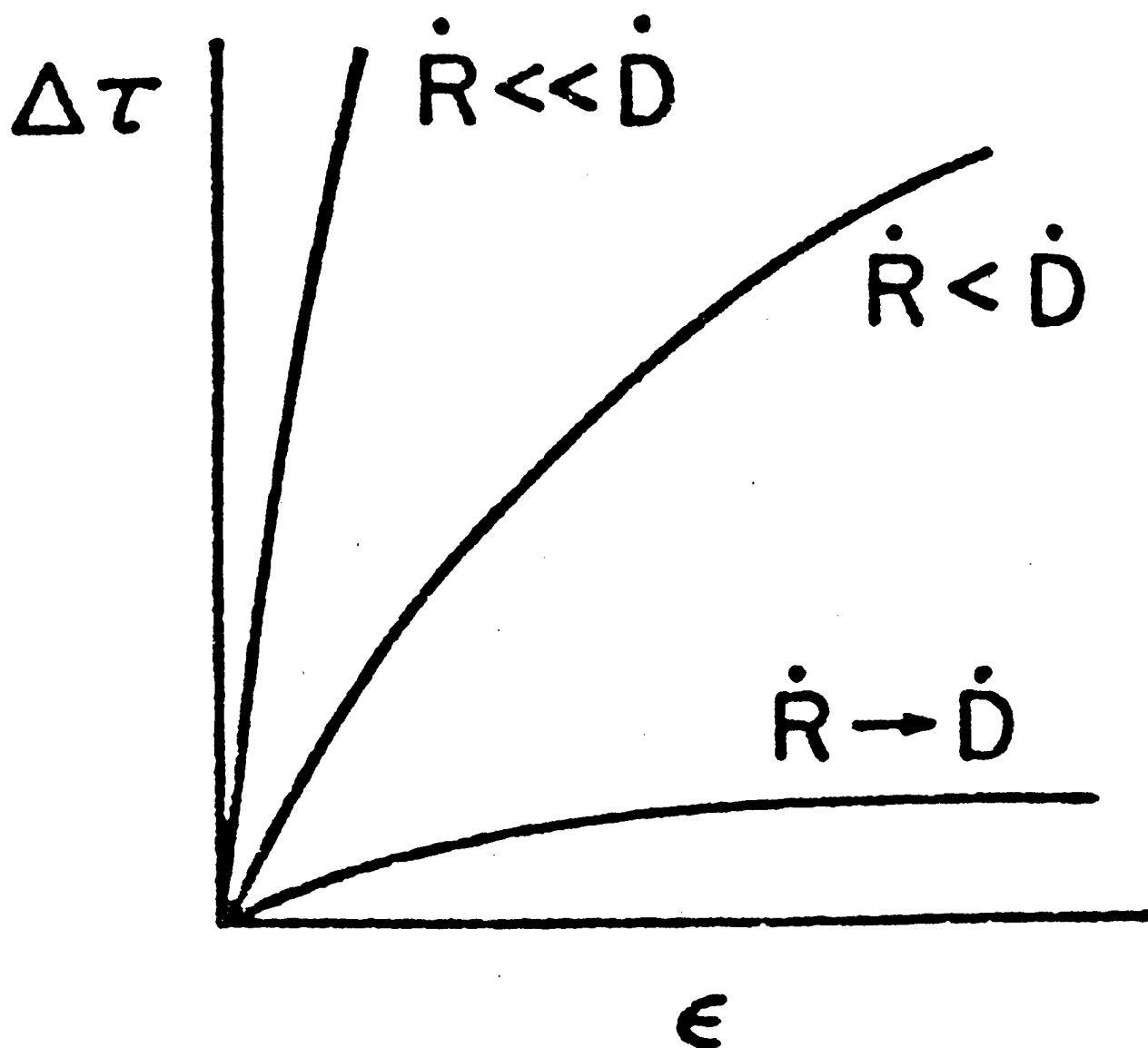
4-11   The Local Shear Stress-($\Delta\tau$) Strain Curves of the Region Bounded by γ in Grain B of Figure 4-10 for Cases where $\dot{R} \approx \dot{D}$, $\dot{R} << \dot{D}$.

ATOMIC PERCENTAGE SODIUM

The figure shows the Al-Na phase diagram in the Al-rich region, with °C on the left axis (658.6 to 660.6) and °F on the right axis (1218 to 1221). The top axis is Atomic Percentage Sodium (.02 to .22) and the bottom axis is Weight Percentage Sodium (AL .02 to .20). Phase regions labeled: L_1, $(Al) + L_1$, $(Al) + L_2$, $L_1 + L_2$, (Al). The horizontal line is at 659°, and $<.003$ is marked near the (Al) region.

WEIGHT PERCENTAGE SODIUM

4-12   The Al-Na Phase Diagram in the Al-Rich Region.

REFERENCES

1. T. H. Sanders, Jr., Final Report, Naval Air Development Center Contract No. N62269-74-C-0438, for Naval Air Systems Command.

2. R. W. Cahn, in Recrystallization Grain Growth and Textures, ASM Seminar, p 99 (1966).

3. C. Zener, quoted by C. S. Smith, Trans. AIME, 175, 151 (1948).

4. N. Ryan, Acta Metallurgical, 17, 269 (1969).

5. N. Ryan, Aluminium, 53, 193 (1977).

6. R. F. Decker, Met. Trans., 4, 2495 (1973).

7. V. Gerold and H. Haberkorn, Phys. Status Solidi, 16, 675 (1966).

8. K. C. Russell and L. M. Brown, Acta Met., 20, 969 (1972).

9. H. Gleiter and E. Hornboyer, Mater. Sci. Eng., 2, 285 (1967-68).

10. S. M. Copley and B. H. Kear, Trans. TMS-AIME, 239, 977 (1967).

11. P. A. Flinn., Trans. AIME, 218, 145 (1960).

12. N. S. Stoloff and R. G. Davies, "The Mechanical Properties of Ordered Alloys," Progress in Materials Science, Vol. 13, No. 1, Bruce Chalmers, ed., (1966).

13. M. Tamura, T. Mori, and T. Nakamura, J. JIM, 34, 919 (1970).

14. D. B. Williams and J. W. Edington, Metal Science, 9, 529 (1975).

15. T. L. Johnston and C. E. Feltner, Met. Trans., 1, 1161 (1970).

16. D. G. Brandon and J. Nutting, J. Iron Stell Inst., 196, 160 (1960).

17. A. H. Keh and S. Weissman, Electron Microscopy and Strength of Crystals, G. Thomas and J. Washburn, eds., J. Wiley and Sons, New York, p 231 (1963).

18. J. E. Bailey and P. B. Hirsch, Phil. Mag., 5, 485 (1960).

19. J. E. Bailey, Phil. Mag., 8, 223 (1963).

20. M. J. Marcinkowski and R. M. Fisher, Trans. TMS-AIME, 233, 293 (1965).

21. T. L. Johnston, R. G. Davies, and N. S. Stoloff, Phil. Mag., 12, 305 (1965).

22. A. C. Arko and Y. H. Liu, Met. Trans., 2, 1875 (1971).

23. W. L. Fink, L. A. Willey, and H. C. Stumpf, AIME TP 2339, (1948).

24. Yu. M. Vaynblat, B. A. Kopelivich, and Yu. G. Gol'der, "The Physics of Metals and Metallography," 42, 104 (1976).

25. H. W. L. Phillips, Inst. Metals Monograph Series No. 25.

26. D. B. Williams and J. W. Edington, Acta Met., 24, 323 (1976).

27. B. Noble and G. E. Thompson, Metal Science Journal, 5, 114 (1971).

28. P. P. P. Pizzo, "An Investigation of the Effects of Precipitate Free Zones on the Mechanical Behavior of An Aluminum-Zinc-Magnesium Alloy," Ph.D. Thesis, Stanford University (1975).

29. T. H. Sanders and E. S. Balmuth, Metal Progress, 113, 37 (1978).

30. W. G. Truckner, J. T. Staley, R. J. Bucci, and A. B. Thakker, "Effects of Microstructure on Fatigue Crack Growth of High Strength Aluminum Alloys," U.S. Air Force Materials Laboratory Report AFML-TR-76-169, October 1976.

31. R. W. Hertzberg, Deformation and Fracture Mechanics of Engineering Materials, John Wiley & Sons, N.Y., p 457 (1976).

DISTRIBUTION LIST

(6 + balance)
Mr. E. S. Balmuth
AIR-52031G
Naval Air Systems Command
Washington, DC   20361

Commander
Naval Air Development Center (Code 606)
Warminster, PA   18974

Naval Sea Systems Command (Code 035)
Department of the Navy
Washington, DC   20360

Naval Ships Research &
 Development Center
Code 2812
Annapolis, MD   21402

Naval Ships Research &
 Development Center
Washington, DC   20007
Attn: Mr. Abner R. Willner
        Chief of Metals Research

Commander
Naval Surface Weapons Center
Metallurgy Division
White Oak, Silver Spring, MD   20910
Attn: Dr. D. Divecha

Director
Naval Research Laboratory
Code 6380
Washington, DC   20390

Director
Naval Research Laboratory
Code 6490
Washington, DC   20390

Director
Naval Research Laboratory
Code 8430
Washington, DC   20390

Naval Surface Weapons Center
Dahlgren Laboratory, Code DG-33
Dahlgren, VA   22448

Office of Naval Research
The Metallurgy Program
Code 471
Arlington, VA   22217

Dr. T. R. McNelley
Dept. of Mechanical Engineering
(Code 59)
Naval Postgraduate School
Monterey, CA   93940

Wright-Patterson Air Force Base
Dayton, OH   45433
Attn: W. Griffith, AFML/LLS

Wright-Patterson Air Force Base
Dayton, OH   45433
Attn: B. Kosmal, AFML/LTM

Wright-Patterson Air Force Base
Dayton, OH   45433
Attn: AFML/MXA

Wright-Patterson Air Force Base
Dayton, OH   45433
Attn: H. Koenigsberg, FTD/PDIT

DCASMA Pittsburgh
1610-S Federal Building
1000 Liberty Avenue
Pittsburgh, PA   15222

Army Materials & Mechanics
 Research Center
Watertown, MA   02172
Attn: Dr. A. Gorum

Wright-Patterson Air Force Base
Dayton, OH   45433
Attn: AFML/LLN

NASA Ames Research Center
Materials and Physical Sciences Branch
MS 230-3
Moffett Field, CA   94035

Commanding Officer
Office of Army Research
P.O. Box 12211
Triangle Park, NC 27709
Att: Metallurgy & Ceramics Program

U.S. Army Armament R&D
 Command(ARRADCOM)
Dover, NJ 07801
Attn: Dr. J. Waldman
       DRDAR-SCM-P
       Bldg. 3409

National Aeronautics & Space
 Administration
(Code RWM)
600 Independence Ave., S.W.
Washington, DC 20546

National Aeronautics & Space
 Administration
Langley Research Center
Materials Div., Langley Station
Hampton, VA 23365
Attn: Mr. H. F. Hardrath
       STOP 188M

National Aeronautics & Space
 Administration
George C. Marshall Space Flight
 Center
Huntsville, AL 35810
Attn: M. W. Brennecke
       EH23 Bldg. 4612

National Academy of Sciences
Materials Advisory Board
Washington, DC 20418
Attn: Dr. J. Lane

U.S. Energy Research & Development
 Administration
Savannah River Operations Office
P.O. Box A
Aiken, SC 29801
Attn: N. J. Donahue
       Reactor Materials

Director
National Bureau of Standards
Washington, DC 20234
Attn: Dr. E. Passaglia

Battelle Memorial Institute
505 King Avenue
Columbus, OH 43201
Attn: Stephen A. Rubin, Mgr.
       Information Operations

IIT Research Institute
Metals Research Department
10 West 35th Street
Chicago, Illinois 60616
Attn: Dr. N. Parikh

General Dynamics Convair Div.
P.O. Box 80847
San Diego, CA 92138
Attn: Jack Christian, Code 643-10

Kaman Aerospace Corporation
Old Windsor Road
Bloomfield, CT 06001
Attn: Mr. M. L. White

Rockwell International
Columbus Division
Columbus, OH 43216
Attn: Fred Kaufman, Dept. 75
       Group 521

Rockwell International
Rocketdyne Division
Canoga Park, CA 91305
Attn: Dr. Al Jacobs
       Group Scientist
       Materials Branch

Rockwell International
Los Angeles Division
International Airport
Los Angeles, CA 90009
Attn: Gary Keller
       Materials Applications

Lockheed Palo Alto Research
 Laboratories
Materials Science Laboratory
3251 Hanover Street
Palo Alto, CA 94303
Attn: Dr. D. Webster
       Bldg. 201 Org. 52-31

Lockheed California Company
P.O. Box 551
Burbank, CA 91503
Attn: Mr. J. M. VanOrden
       Dept. 74-71
       Bldg. 221, Plt. 2

Lockheed-Georgia Company
Marietta, GA 30060
Attn: E. Bateh
       Dept. 72-26, Zone 285

Lockheed Missile & Space Corp.
Box 504
Sunnyvale, CA 94088
Attn: Mr. G. P. Pinkerton
       Dept. 81-23

Mr. R. H. Gassner
MS 1-18
Douglas Aircraft Company
Long Beach, CA 90846

Sikorsky Aircraft
Div. of United Technologies, Inc.
Stratford, CT 06497
Attn: Materials & Processes Dept.

Grumman Aerospace Corp.
Plant 12
Bethpage, NY 11714
Attn: R. Heitzmann

Bell Helicopter Co.
A Textron Division
P.O. Box 482
Fort Worth, TX 76101
Attn: M. A. Green

United Technology Center
P.O. Box 358
Sunnyvale, CA 94088
Attn: George Kreici

Hughes Helicopters
Division Summa Corporation
Centinela & Teale Sts
Culver City, CA 90230
Attn: T. Matsuda

Norman A. Nielson
Engineering Technology Laboratories
E. I. Dupont de Nemours
Wilmington, DE 19898

Massachusetts Institute of Technology
Dept of Metallurgy & Materials Science
Cambridge, MA 02139
Attn: Dr. N. J. Grant

Dr. J. Williams
Dept. of Metallurgy & Materials Science
Carnegie-Mellon University
Pittsburgh, PA 15213

The Franklin Institute Research
 Laboratories
Twentieth & Parkway
Philadelphia, PA 19103
Attn: Technical Director

Martin Marietta Aluminum
Attn: Mr. Paule E. Anderson (M/C 5401)
19200 South Western Avenue
Torrance, CA 90509

Dept of Metallurgical Engineering
Drexel University
32nd & Chestnut Streets
Philadelphia, PA 19104

Mr. W. Spurr
The Boeing Company
12842 72nd Ave., N.E.
Kirkland, WA   98033

Dr. John A. Sehey
Dept. of Materials Engineering
University of Illinois at
 Chicago Circle
Box 4348
Chicago, IL   60680

Dr. J. C. Chesnutt
Rockwell International
P.O. Box 1085
1027 Camino Dos Rios
Thousand Oaks, CA   91360

Pratt & Whitney Aircraft Group
Div. of United Technologies
Florida Research & Development Ctr.
P.O. Box 2691
West Palm Beach, FL   33402

Martin Marietta Corporation
P.O. Box 5837
Orlando, FL   32805
Attn: Dr. Richard C. Hall
        Mail Point 275

Dr. D. L. Davidson
Southwest Research Institute
8500 Culebra Road
P.O. Drawer 28510
San Antonio, TX   78284

Boeing-Vertol Company
Boeing Center
P.O. Box 16858
Philadelphia, PA   19142
Attn: Mr. J. M. Clark

The Boeing Company
Commercial Airplane
ORG. 6-8733, MS77-18
P.O. Box 3707
Seattle, WA   98124
Attn: Cecil E. Parsons

Northrop Corporation
Aircraft Division
Dept. 3771-62
3901 West Broadway
Hawthorne, CA   90250
Attn: Mr. Allen Freedman

Vought Corporation
P.O. Box 5907
Dallas, TX   75222
Attn: Mr. A. Hohman

McDonnell Aircraft Co
P.O. Box 516
St. Louis, MO   63166
Attn: Mr. H. Turner
        Materials & Processes Dev.
        General Engineering Div.

Grumman Aerospace Corp
Research Dept
Bethpage, NY   11714
Attn: Dr. P. Adler

Detroit Diesel Allison Division
General Motors Corporation
Materials Laboratories
Indianapolis, IN   46206

General Electric Company
Aircraft Engine Group
Materials & Processes Technology Labs
Evendale, OH   45215

Dr. Charles Gilmore
Tompkins Hall
George Washington University
Washington, DC   20006

Mr. Michael Hyatt
The Boeing Company
P.O. Box 707
Seattle WA   98124

General Electric Co.
Corporate Research & Development
Bldg. 36-441
Schenectady, NY 12345
Attn: Dr. J. H. Westbrook, Mgr
      Materials Information Services

General Electric Company
Corporate Research & Development
P.O. Box 8
Schenectady, NY 12301
Attn: Dr. D. Wood

Westinghouse Electric Company
Materials & Processing Laboratories
Beulah Road
Pittsburgh, Pa 15235
Attn: Don E. Harrison

Dr. D. B. Williams
Dept. of Metallurgy & Materials Science
Whitaker Lab - #5
Lehigh University
Bethlehem, PA 18015

General Dynamics Corp
Convair Aerospace Division
Fort Worth Operation
P.O. Box 748
Fort Worth, TX 76101
Attn: J. M. Shults
      MZ 2860

Dr. D. Matlock
Dept. of Metallurgical Engineering
Hill Hall
Colorado School of Mines
Golden, CO 80401

Brush Wellman, Inc
17876 St. Clair Avenue
Cleveland, OH 44110
Attn: Mr. Bryce King

Mr. H. S. Rubenstein
6803 Lemon Rd
McLean, VA 22101

General Electric
Missile & Space Division
Materials Science Section
P.O. Box 8555
Philadelphia, PA 91901

Kawecki Berylco Industries
Attn: Dr. B. Brillhart
P.O. Box 1462
Reading, PA 19603

ERDA Division of Reactor Develop-
ment & Technology
Washington, DC 20545
Attn: Mr. J. M. Simmons, Chief
      Metallurgy Section

Dr. F. N. Mandigo
Olin Metals Research Laboratories
91 Shelton Avenue
New Haven, CT 06515

Kaiser Aluminum & Chemical Corp
Aluminum Division Research Center
for Technology
P.O. Box 870
Pleasonton, CA 94566
Attn: T. R. Pritchett

Reynolds Metals Company
Metallurgical Research Division
4th & Canal Sts
Richmond, VA 23261
Attn: Dr. G. E. Spangler

Dr. E. A. Starke, Jr.
School of Chemical Engineering &
Metallurgy
Georgia Institute of Technology
Atlanta, GA 30332

General Electric Co
1000 Western Ave
Lynn, MA 01910
Attn: Mr. John Shai

AFOSR-NE
Bldg. 410
Bolling AFB
Washington, DC 20332
Attn: Dr. A. H. Rosenstein

Charles Gure
Wyman Gordon Co.
Worcester St.
North Grafton, MA 01536

Dr. W. C. Setzer, Director
Metallurgy & Surface Technology
Consolidated Aluminum Corp.
P.O. Box 14448
St. Louis, MO 63178

Librarian
Bendix Aircraft Brake & Strut/
 Energy Controls Divisions
717 N. Bendix Drive
South Bend, IN 46620

Chief, Materials Engineering Dept.
Dept. 93-03-503-4
AiResearch Manufacturing Co. of Arizona
402 S. 36th St.
P.O. Box 5217
Phoenix, AZ 85010

Mr. Brian Taylor
Dept. 94
Manufacturing Development Division
General Motors Technical Center
Warren, MI 48090

Mr. Charles W. Fox
Technical Director
Homogeneous Metals, Inc.
P.O. Box 752
Herkimer, NY 13350

Dr. R. Geisendorfer
Battelle Northwest
Bldg. 306W, Area 300
Richland, WA 99352

AVCO-Lycoming
550 S. Main St.
Stratford, CT 06497
Attn: Mr. L. Fiedler

W. E. Ely
Mgr, Materials & Technology
B. F. Goodrich
Engineered Systems Division
P.O. Box 340
Troy, Ohio 45373

Mr. A. Shames
Mgr of Manufacturing Technology
Fairchild Republic
Conklin St.
Farmingdale, NY 11735

Dr. R. Mehrabian
Dept. of Metallurgy & Mining
 Engineering
University of Illinois at Urbana-
 Champaign
Urbana, IL 61801

C. R. Whitsett
McDonnell Douglas Research Laboratories
McDonnell Douglas Corp
P.O. Box 516
St. Louis, MO 63166

Dr. E. Von Reuth
DARPA
1400 Wilson Blvd
Arlington, VA 22209

United Technologies Research Labs
East Hartford, CT 06108
Attn: Mr. Roy Fanti

Autonetics Division of Rockwell
 International
P.O. Box 4173
Anaheim, CA 92803
Attn: Mr. A. G. Gross, Jr.
        Dept. 522-92

Dr. J. W. Edington
Dept of Mechanical & Aerospace
 Engineering
University of Delaware
Newark, DE 19711

Dr. Ruoff, Chairman
Dept of Materials Science & Engineering
Bard Hall
Cornell University
Ithaca, NY 14853

Dr. D. J. Duquette
Materials Engineering Dept
RPI
Troy, NY 12181

Dr. M. Fine
Northwestern University
Dept. of Materials Sciences
Evanston, IL 60201

Dr. C. Laird
Dept of Metallurgy & Materials Science
University of Pennsylvania
Philadelphia, PA 19174

Mr. Edward W. Kernan
Federal Preparedness Agency
Room 5230
18th & F St., N.W.
Washington, DC 20405

Dr. H. Marcus
Dept. of Mechanical Engineering
University of Texas
Austin, TX 78712

Dr. A. J. McEvily
Dept. of Metallurgy
University of Connecticut
Storrs, CT 06268

Dr. R. Pelloux
Dept. of Metallurgy
MIT
Cambridge, MA 02100

Commander
Naval Air Systems Command
Air-954 (2 copies)
Washington, DC 20361

(12 copies)
Defense Documentation Center
Cameron Station
Alexandria, VA 22314
  VIA: Commander
        Naval Air Development Center
        Code 606
        Warminster, PA 18974

(3 copies)
Commander
Naval Air Development Center
Attn: Code 8131
Warminster, PA 18974

D-7